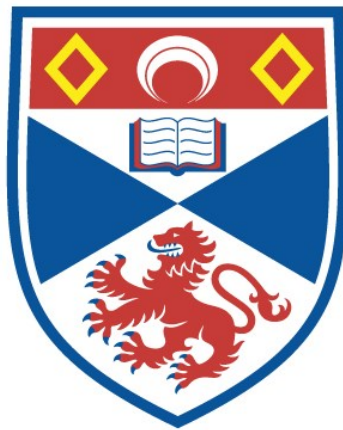


# Tensor network simulations of open quantum systems

Dainius Kilda

A thesis submitted for the degree of PhD  
at the  
University of St Andrews



2020

Full metadata for this thesis is available in  
St Andrews Research Repository  
at:

<https://research-repository.st-andrews.ac.uk/>

Identifier to use to cite or link to this thesis:

DOI: <https://doi.org/10.17630/10023-19584>

This item is protected by original copyright

This item is licensed under a  
Creative Commons Licence

<https://creativecommons.org/licenses/by-nc-nd/4.0>

## **Candidate's declaration**

I, Dainius Kilda, do hereby certify that this thesis, submitted for the degree of PhD, which is approximately 77,000 words in length, has been written by me, and that it is the record of work carried out by me, or principally by myself in collaboration with others as acknowledged, and that it has not been submitted in any previous application for any degree.

I was admitted as a research student at the University of St Andrews in August 2015.

I received funding from an organisation or institution and have acknowledged the funder(s) in the full text of my thesis.

Date

Signature of candidate

## **Supervisor's declaration**

I hereby certify that the candidate has fulfilled the conditions of the Resolution and Regulations appropriate for the degree of PhD in the University of St Andrews and that the candidate is qualified to submit this thesis in application for that degree.

Date

Signature of supervisor

## **Permission for publication**

In submitting this thesis to the University of St Andrews we understand that we are giving permission for it to be made available for use in accordance with the regulations of the University Library for the time being in force, subject to any copyright vested in the work not being affected thereby. We also understand, unless exempt by an award of an embargo as requested below, that the title and the abstract will be published, and that a copy of the work may be made and supplied to any bona fide library or research worker, that this thesis will be electronically accessible for personal or research use and that the library has the right to migrate this thesis into new electronic forms as required to ensure continued access to the thesis.

I, Dainius Kilda, confirm that my thesis does not contain any third-party material that requires copyright clearance.

The following is an agreed request by candidate and supervisor regarding the publication of this thesis:

## **Printed copy**

Embargo on all of print copy for a period of 2 years on the following ground(s):

- Publication would preclude future publication

**Supporting statement for printed embargo request**

This thesis contains unpublished material. Publication would preclude future publication of this material.

**Electronic copy**

Embargo on all of electronic copy for a period of 2 years on the following ground(s):

- Publication would preclude future publication

**Supporting statement for electronic embargo request**

This thesis contains unpublished material. Publication would preclude future publication of this material.

**Title and Abstract**

- I agree to the title and abstract being published.

Date

Signature of candidate

Date

Signature of supervisor

## **Underpinning Research Data or Digital Outputs**

### **Candidate's declaration**

I, Dainius Kilda, understand that by declaring that I have original research data or digital outputs, I should make every effort in meeting the University's and research funders' requirements on the deposit and sharing of research data or research digital outputs.

Date

Signature of candidate

### **Permission for publication of underpinning research data or digital outputs**

We understand that for any original research data or digital outputs which are deposited, we are giving permission for them to be made available for use in accordance with the requirements of the University and research funders, for the time being in force.

We also understand that the title and the description will be published, and that the underpinning research data or digital outputs will be electronically accessible for use in accordance with the license specified at the point of deposit, unless exempt by award of an embargo as requested below.

The following is an agreed request by candidate and supervisor regarding the publication of underpinning research data or digital outputs:

Embargo on all of electronic files for a period of 2 years on the following ground(s):

- Publication would preclude future publication

### **Supporting statement for embargo request**

This thesis contains unpublished material. Publication would preclude future publication of this material.

### **Title and Description**

- I require an embargo on the title and description

Date

Signature of candidate

Date

Signature of supervisor

# Abstract

The nonequilibrium effects of dissipation and drive play a key role in an immense variety of nanoscale and mesoscale quantum systems. To understand the behaviour of open quantum systems, we need accurate methods that capture the influence of the environment on the system, while managing the exponentially large Hilbert space required to describe the system. Tensor network algorithms offer an efficient way to approach this challenge. In this thesis, we develop and apply tensor network techniques to study the dynamics and steady states of various open quantum systems.

The first part of the thesis focuses on the driven dissipative many body physics in coupled cavity arrays described by Born-Markov master equations. We extend transfer matrix product operator methods to Liouvillian dynamics, and utilize them to compute dynamical correlation functions and fluorescence spectrum of an infinite coupled cavity array in 1D. We also investigate thermalization, and observe the emergence of a quasi-thermal steady state with a negative effective temperature. In another study, we use infinite projected entangled pair state (iPEPS) methods to compute steady states of coupled cavity lattices in 2D. We find that a straightforward adaptation of iPEPS to Liouvillian dynamics is unstable, contradicting a recent publication in the field.

The second part investigates more general systems involving strong couplings and structured environments that induce non-Markovian dynamics. We develop a powerful time-evolving matrix product operator (TEMPO) algorithm that builds on Feynman-Vernon influence functional formalism, and uses matrix product states (MPS) to represent the temporal non-Markovian correlations efficiently. We apply TEMPO to study the localization phase transition of the spin-boson model and the dynamics of two spatially separated two-level systems coupled to a common environment. Finally, we propose the Toblerone TEMPO algorithm, which extends TEMPO to many-body systems interacting with general bosonic environments.

## Publications

Parts of this thesis have been published in the following journals:

*Fluorescence spectrum and thermalization in a driven coupled cavity array.* Dainius Kilda and Jonathan Keeling. Physical Review Letters, 122, 043602 (2019).

*Efficient non-Markovian quantum dynamics using time-evolving matrix product operators.* Aidan Strathearn, Peter Kirton, Dainius Kilda, Jonathan Keeling, and Brendon Lovett. Nature Communications, 9, 3322 (2018).

## Acknowledgements

First of all, I would like to express my gratitude to Jonathan Keeling for his excellent supervision and mentorship. I have learnt much from him, and would like to thank him for his generous support, his illuminating ideas in our projects, and for all the enriching discussions with him. It has also been a great pleasure to work with Brendon Lovett, and I am especially grateful for his advice, kindness, and continuous encouragement.

I would also like to say a big thank you to all of my fantastic fellow group members and colleagues during my time here in St. Andrews. It is too difficult to name everyone, but here is my special thanks to Artēm, Aidan, Gerald, Roberta – and Kristín, whose yummy cakes kept the spirits high when times were tough. Thanks also to Sofia, and thanks to Coen and Jude for being amazing housemates.

Outside of my life in St. Andrews, I am very grateful to my friends since my days in Cambridge, especially Themis, Gabija, and all the K-blockers: Caspian, Laco, Cristina, Sai, Xue, Andrea, Emilis. Andreas Nunnenkamp and Themis, who were great and inspiring teachers, have both given me insights that still guide me through the impasses in my research endeavours and in life.

Finally, and most importantly, I would like to thank my family: Remigija, Raimondas, Aidas, for always supporting me, and Juoduliukas, for always being so fluffy. I also thank my Japanese family: Yuko, Tadaki, Yuki, Ayako and Asako for welcoming me into their lives and for always cheering me on.

This thesis would have never seen daylight without Yui, who means everything to me.

## Funding

This work was supported by the EPSRC CM-CDT (grant EP/L015110/1).

This work was supported by the University of St. Andrews (School of Physics and Astronomy).

## Research Data/Digital Outputs access statement

Digital outputs underpinning this thesis are available at <https://doi.org/10.17630/2ffcdde0-57f0-48b5-bc2c-817f03cb2756>

# Contents

<b>I</b>	<b>Introduction and background</b>	<b>1</b>
	Introduction	3
<b>1</b>	<b>Open quantum systems</b>	<b>7</b>
1.1	Open system theory . . . . .	7
1.1.1	System and environment . . . . .	7
1.1.2	Master equation formalism . . . . .	10
1.1.3	Influence functional formalism . . . . .	15
1.1.3.1	Influence functional formalism with multiple baths	19
1.2	Driven dissipative coupled cavity arrays . . . . .	22
1.2.1	Quantum simulation with photonic systems . . . . .	22
1.2.2	From cavity QED to coupled cavity arrays . . . . .	23
1.2.3	Photon blockade . . . . .	25
1.2.4	Experimental realizations and circuit QED . . . . .	25
1.2.5	Review of theoretical results: collective behaviour in coupled cavity arrays . . . . .	28
1.2.6	Theoretical methods . . . . .	29
1.3	Non-Markovian dynamics . . . . .	31
1.3.1	The spin-boson model . . . . .	34
<b>2</b>	<b>Tensor networks</b>	<b>37</b>
2.1	Fundamentals . . . . .	37
2.1.1	Tensor diagrams . . . . .	37
2.1.2	Entanglement and the area law . . . . .	40
2.2	Matrix product states . . . . .	45
2.2.1	Matrix product operators . . . . .	50
2.2.2	MPS-MPO multiplication . . . . .	52
2.2.3	TEBD algorithm . . . . .	53
2.2.4	Liouvillian time evolution . . . . .	57
2.3	Projected entangled pair states . . . . .	60
2.3.1	Corner transfer matrix method . . . . .	62
2.3.2	iPEPS algorithm: simple update . . . . .	66
2.3.3	iPEPS algorithm: full update . . . . .	69



<b>II</b>	<b>Driven dissipative coupled cavity arrays</b>	<b>73</b>
<b>3</b>	<b>Fluorescence spectrum and thermalization in 1D</b>	<b>75</b>
3.1	Introduction . . . . .	75
3.2	Calculating two-time correlations in the thermodynamic limit . . .	77
3.3	Thermalization and the fluctuation dissipation theorem . . . . .	82
3.4	The Driven Dissipative XY Model . . . . .	85
3.5	Steady state correlations . . . . .	86
3.6	Fluorescence spectrum . . . . .	88
3.7	Spin-wave calculations . . . . .	92
3.7.1	Calculating correlation functions . . . . .	92
3.7.2	Temperature of individual bosonic modes . . . . .	96
3.7.3	Fluctuation dissipation relation in linear theories . . . . .	98
3.8	Momentum-resolved fluorescence spectrum . . . . .	99
<b>4</b>	<b>Computing steady states in 2D</b>	<b>103</b>
4.1	Introduction . . . . .	103
4.2	Implementation of iPEPO algorithm . . . . .	106
4.3	Benchmarking with ground state calculations . . . . .	109
4.4	Steady states of the dissipative XYZ model . . . . .	112
4.5	Conclusions . . . . .	119
<b>III</b>	<b>Non-Markovian dynamics</b>	<b>121</b>
<b>5</b>	<b>Time-evolving matrix product operators</b>	<b>123</b>
5.1	Introduction . . . . .	123
5.2	Quasi-adiabatic propagator path integrals . . . . .	125
5.3	Time-evolving matrix product operators . . . . .	130
5.4	Benchmarking TEMPO . . . . .	134
5.5	TEMPO results . . . . .	138
5.5.1	The localization phase transition . . . . .	138
5.5.2	Environment-mediated energy transfer . . . . .	142
<b>6</b>	<b>Toblerone tensor networks</b>	<b>147</b>
6.1	Introduction . . . . .	147
6.2	TEMPO in the process tensor framework . . . . .	149
6.2.1	Rearranging the TEMPO network . . . . .	149
6.2.2	The process tensor approach . . . . .	153
6.3	Toblerone TEMPO algorithm . . . . .	158
6.4	Toblerone simulation results . . . . .	164
<b>IV</b>	<b>Conclusions</b>	<b>169</b>
<b>7</b>	<b>Conclusions and future work</b>	<b>171</b>
7.1	Conclusions . . . . .	171

7.2	Future work . . . . .	173
<b>V</b>	<b>Appendices</b>	<b>177</b>
<b>A</b>	<b>Supplementary non-Markovian calculations</b>	<b>179</b>
A.1	Reaction Coordinate Mapping . . . . .	179
A.2	Independent boson model . . . . .	181
A.3	Many-body independent boson model . . . . .	183
<b>VI</b>	<b>Bibliography</b>	<b>187</b>
	<b>Bibliography</b>	<b>189</b>

# Part I

## Introduction and background



# Introduction

No system can be perfectly isolated from its environment, and will always experience some form of interaction like heat transfer or exchange of particles with the surrounding medium. Any quantum system that can be measured will also come into contact with an external measurement device. As a consequence, any real world system is, in principle, an open system. In many cases, we either study systems that have already established a thermal equilibrium state with their surroundings, or the presence of environment only introduces a weak relaxation mechanism that is negligible over the timescales of interest. One then never has to worry about the surroundings and treating these systems as isolated systems is an excellent approximation. However, in other cases the interaction with environment can fundamentally change the physics of the system. Of particular interest to us are the dissipative and the driven dissipative systems where it brings the open system far away from the thermodynamic equilibrium. The equilibrium statistical mechanics no longer applies here, and one needs to seek alternatives to describe the nonequilibrium behaviour. Under these conditions, the equilibrium particle statistics and the equilibrium form of the fluctuation-dissipation theorem are no longer valid, while the detailed balance condition and the time reversal symmetry are broken [1, 2]. Driving a system out of equilibrium can thus stabilize new states of matter that are not possible in equilibrium [3, 4].

Many examples of driven nonequilibrium systems exist in the familiar classical world around us and have been studied extensively. They range from the models of traffic in city streets or noisy dynamics of financial markets, to the flocking and swarming behaviour of living organisms and the cell migration in morphogenesis during the embryonic development [5–9]. The unifying feature among many of these systems (often called active matter) is the presence of a dissipative environment (e.g. due to the surrounding fluid particles exerting a drag force), and an internally generated drive (e.g. by consuming food obtained from the surroundings) to produce the energy for self-propelled motion. This driven dissipative behaviour leads to surprising nonequilibrium phenomena such as spontaneous assembly of colloids or bacteria with no attractive forces, active fluids that flow spontaneously with no externally applied forces, and condensation of fluid particles without any cohesive interactions [5, 6, 10].

The research of dissipative and driven dissipative nonequilibrium physics is playing an increasingly important role in the quantum world. In the last few decades, incredible advances in quantum coherent control and measurement have enabled us to probe and manipulate nanoscale and mesoscale quantum systems with unprecedented accuracy [11–14]. There is now a growing number of actively investigated

experimental platforms, for instance superconducting circuits [15, 16], micromechanical resonators [17, 18], quantum dots [19, 20], trapped ions [21, 22], cold atoms in optical cavities [23], exciton-polaritons in microcavities [24], and many others. In such experiments, a controlled quantum system interacts with a large uncontrolled environment. For example, the basic building blocks of quantum computing architectures, such as qubits and quantum dots, are subject to external thermal noise and decoherence, quantum optical systems experience photon loss into external reservoir of electromagnetic modes, and electronic excitations in organic molecules interact with vibrational modes of the molecular scaffold. The progress in the ongoing development of quantum technology – such as quantum computing [25–27], quantum enhanced metrology [28, 29], or possible renewable energy sources based on molecular light harvesting [30–32] – relies heavily on our ability to understand the sources of noise and build mathematical models describing the mechanisms of dissipation. Many of these examples, in fact, involve large ensembles of interacting systems and inevitably deal with collective effects out of equilibrium. It is clear that traditional theoretical techniques describing collective behaviour in equilibrium [2], that have dominated condensed matter physics over the last century, are no longer appropriate here – and our understanding of quantum matter driven out of equilibrium remains far more limited. Indeed, driven dissipative systems pose many intriguing questions regarding nonequilibrium states of matter, quantum transport, relaxation dynamics, quantum phase transitions far from equilibrium, and engineering of novel quantum states. Similarly to the aforementioned classical active matter, they can display collective phases of matter not possible in a thermal equilibrium setting: a few prominent examples include condensation of photons and exciton-polaritons [24, 33, 34], optically-induced superconductivity [35], dissipatively stabilized photonic Mott insulators [36], and nonequilibrium time crystals [37].

Understanding the nonequilibrium effects of dissipation and drive in open quantum systems, and developing more effective modelling techniques is therefore of paramount importance from both the fundamental and technological perspective, which presents a formidable challenge to theoretical physics. In fact, even the very simplest models can quickly become insoluble by analytical means when interaction with environment is introduced. Consider, for example, a two-level system surrounded by a large number of oscillators – as we will see later, this turns a straightforward textbook problem into one still posing significant hurdles for modern numerical algorithms. Various approaches have been proposed and applied with varying degrees of success, including master equation and path integral based computational techniques, some of which we will build upon in this thesis. The numerical modelling of open quantum systems, both many-body and few-body, faces the same principal problem as the simulations of quantum matter in equilibrium: the number of parameters required to describe a quantum state grows exponentially with system size, commonly known as ‘the curse of dimensionality’. The primary goal of any computational method is finding ways to reduce or bypass this exponential scaling.

My work will focus on developing one class of such computational techniques based on tensor networks. Tensor network algorithms have been highly successful at simulating strongly correlated matter in one dimension and, to some extent, in

two dimensions [38, 39]. They rely on the idea of parameterizing a quantum many body state by a network of interconnected tensors, and exploiting the structure of correlations or entanglement in the system to discard the information about irrelevant parts of the Hilbert space, thereby leading to a drastic reduction in the dimensionality of the problem. Tensor network techniques have originally been designed in the context of isolated quantum systems, to target the low-lying states of their model Hamiltonians with local interactions. Nevertheless, they are now entering the realm of open quantum systems and have already shown their potential in computing both the dissipative quantum dynamics and the nonequilibrium steady states [40–46]. In this thesis, we will develop tensor network methods to pursue two main directions. The first one will focus on simulating the effects of drive and dissipation in quantum optical many body systems, particularly the arrays of coupled nonlinear optical cavities. In the second one, we will tackle problems with more general system-environment interactions that induce non-Markovian dynamics.

More specifically, this thesis is organized as follows. Part I provides the background relevant to this thesis. Chapter 1 introduces the relevant concepts and theoretical tools, and reviews the state-of-the-art. Chapter 2 describes tensor network techniques that will form the computational basis of this work.

Part II focuses on driven dissipative many body physics in coupled cavity arrays. These systems are characterized by a weak coupling to an unstructured environment of electromagnetic modes and are well described by Born-Markov master equations with many body Hamiltonians. Here we will address two major unsolved problems in the field, discussed in Chapters 3 and 4. In Chapter 3, we calculate dynamical correlation functions and fluorescence spectra of an infinite coupled cavity array in 1D. We achieve this by extending matrix product operator techniques to compute two-time correlations in open quantum systems. We then demonstrate the information available from the fluorescence spectrum, and investigate thermalization in driven systems. In particular, we observe that blue-detuned driving stabilizes a quasi-thermal steady state with a negative effective temperature and a maximum-energy order. Chapter 4 deals with two-dimensional coupled cavity lattices in the thermodynamic limit, with a goal of extending the infinite projected entangled pair state (iPEPS) methods to study the nonequilibrium steady states of open quantum systems in 2D.

Part III investigates more general types of system-environment interaction featuring strong couplings and structured environments. These conditions lead to non-Markovian dynamics where a system retains the memory of its past states, causing the weak coupling approximations and time-local master equations break down. In Chapter 5 we develop a powerful time-evolving matrix product operator (TEMPO) algorithm that builds on Feynman-Vernon influence functional formalism and employs matrix product states to represent the temporal non-Markovian correlations efficiently. We demonstrate the power of this approach by studying the localization phase transition of the spin-boson model and the dynamics of two spatially separated two-level systems coupled to a common environment. Chapter 6 builds on the ideas of Chapter 5 to pursue the ambitious goal of extending TEMPO algorithm to many body lattice systems interacting with non-Markovian environments. To this end, we propose the Toblerone tensor network algorithm that

is capable of treating non-Markovian memory effects and many body correlations simultaneously.

## Units

We work in natural units where the reduced Planck constant  $\hbar = 1$  and the Boltzmann constant  $k_B = 1$ .



# Chapter 1

## Open quantum systems

### 1.1 Open system theory

#### 1.1.1 System and environment

On the conceptual level, we can define an open system as follows. Let us take a collective set of degrees of freedom that we call “universe” and divide it into two parts: the “interesting part” that we call a “system”, and the “remaining part” that we call an “environment”. The main motivation for such partitioning is that the environment is often very large and intractable, and a complete mathematical model of the “universe” is far too complicated. For example, the environment may consist of infinitely many degrees of freedom, which will require an infinite number of equations of motion. A more fruitful approach is to focus instead on the system of interest that lives in a reduced state space formed by a restricted set of physical variables, and build a mathematical model that incorporates the influence of environment on the behaviour of the system. We usually think of environment as a collection of phonons in a crystal, modes of electromagnetic field, or a reservoir of fermionic states. In many cases, the microscopic details of environment will not be accessible and we will have to resort to a phenomenological description. One common approach is to take a system-environment Hamiltonian where the environment is represented as a collection of harmonic oscillators. The main idea then is to integrate out the reservoir degrees of freedom and obtain a formally exact expression for the reduced density matrix of the system. More concretely, we define an open quantum system as the system  $S$  coupled to environment  $B$ . The total composite system  $S + B$  is then the universe, which we assume to be an isolated system governed by the Hamiltonian dynamics. In contrast, the state of  $S$  will evolve depending both on its internal dynamics and its interaction with  $B$ . This  $S - B$  interaction leads to system-environment correlations, and the evolution of  $S$  can no longer be described by the Hamiltonian dynamics [1]. We elaborate on this statement below. In general, the composite wavefunction of  $S + B$  is given by

$$|\Psi\rangle = \sum_{ij} c_{ij} |i_S\rangle |j_B\rangle = \sum_k \lambda_k |k_S\rangle |k_B\rangle \quad (1.1)$$

where in the second equality we have applied the Schmidt decomposition. Schmidt values  $\lambda_k$  correspond to probabilistic weights  $\sum_k \lambda_k^2 = 1$  of each state  $k$ . The number

of Schmidt values required to express the composite state  $|\Psi\rangle$  of the two subsystems  $S, B$  quantifies the amount of entanglement between the two subsystems. The entanglement is maximized when all Schmidt values  $\lambda_k$  and hence all probabilistic weights  $\lambda_k^2$  are equal: the state  $|\Psi\rangle$  is then maximally entangled. We can only express the composite state  $S + B$  as a product state  $|\Psi\rangle = |1_S\rangle |1_B\rangle$  of  $S$  and  $B$  if the  $S - B$  entanglement is zero, corresponding to  $\lambda_{k=1} = 1$ ,  $\lambda_{k>1} = 0$  in Eq. (1.1). Generally, the density matrix of the total system  $S + B$  is defined in terms of the pure state  $|\Psi\rangle$ :

$$\rho = |\Psi\rangle \langle \Psi| = \sum_{kq} \lambda_k \lambda_q |k_S, k_B\rangle \langle q_B, q_S| \quad (1.2)$$

The reduced density matrix of system  $S$  is then

$$\rho_S = \text{Tr}_B(\rho) = \sum_k \lambda_k^2 |k_S\rangle \langle k_S| \quad (1.3)$$

where we trace out the degrees of freedom of the environment  $B$ . This is a fundamental property of bipartite entanglement: after tracing out the information about  $B$ , the reduced system  $S$  will be described by a statistical mixture of pure states, to an extent determined by the amount of bipartite entanglement between  $S$  and  $B$ . One can quantify the bipartite entanglement itself using the von Neumann entanglement entropy [1]:

$$S = -\text{Tr}(\rho \ln \rho) = -\sum_k \lambda_k^2 \ln \lambda_k^2 \quad (1.4)$$

which is determined by the number of Schmidt values and by the distribution of  $\lambda_k^2$  probabilistic weights over the spectrum of Schmidt states  $k$ .

It follows that for a non-zero  $S - B$  entanglement the open system  $S$  cannot be represented by a single pure state wavefunction, and so we can no longer apply the familiar unitary time evolution to compute its dynamics. Instead, we will deal with a reduced density matrix  $\rho_S$  as the principal entity describing the state of  $S$  that undergoes non-unitary Liouvillian dynamics, generated by a Liouvillian superoperator that we will introduce shortly. Let us start with the von Neumann equation of motion for the total system  $S + B$ :

$$\partial_t \rho = -i [H, \rho] \quad (1.5)$$

whose full Hamiltonian is

$$H = H_S + H_B + V \quad (1.6)$$

$H_S$  and  $H_B$  are the Hamiltonians of system  $S$  and bath  $B$  respectively, while  $V$  is the system-bath interaction Hamiltonian. For convenience, we switch to the interaction picture by transforming all operators as  $X \rightarrow e^{i(H_S+H_B)t} X e^{-i(H_S+H_B)t}$ , which gives the equation of motion for a transformed density matrix

$$\partial_t \rho = \mathcal{L}(t) \rho(t) \quad (1.7)$$

Here we have defined the Liouvillian superoperator that generates the dynamics:

$$\mathcal{L}(t) = -i [V(t), \bullet] \quad (1.8)$$

The Liouvillian time evolution can be formally written as

$$\rho(t) = \overleftarrow{\mathcal{T}} \exp \left( \int_0^t dt' \mathcal{L}(t') \right) \rho(0) \quad (1.9)$$

with time-ordering operator  $\overleftarrow{\mathcal{T}}$ . Our main interest, however, is the dynamics of the reduced density matrix  $\rho_S(t)$  of the system  $S$ . We will assume that the time evolution starts in a state such that  $S$  and  $B$  are initially uncorrelated:

$$\rho(0) = \rho_S(0) \otimes \rho_B(0) \quad (1.10)$$

i.e. we switch on dissipation at  $t = 0$  and let the correlations build up as we evolve in time. If we evolve a system that has a finite memory time for a sufficiently long timespan  $t \rightarrow \infty$ , the initial condition becomes effectively infinitely far away in the past and thus is no longer relevant. In practice, the  $t \rightarrow \infty$  limit corresponds to the steady states and the late time dynamics, after the initial state has been ‘forgotten’. For a transient evolution at early times, the assumption Eq. (1.10) is more restrictive and corresponds to an experiment where we prepare our system in a known initial state that is not entangled with the bath at  $t = 0$ . We refer an interested reader to Ref. [1] for a discussion on non-factorizing initial conditions. In addition to Eq. (1.10), we will assume that the bath is initially in the thermal equilibrium state

$$\rho_B(0) = \frac{e^{-\beta H_B}}{Z} \quad (1.11)$$

Using Eq. (1.9), this allows us to write the formal solution for the time evolution of  $\rho_S(t)$ :

$$\rho_S(t) = \text{Tr}_B (\rho(t)) = G(t) \rho_S(0) \quad (1.12)$$

where the propagator  $G(t)$  is given by

$$G(t) = \text{Tr}_B \left[ \overleftarrow{\mathcal{T}} \exp \left( \int_0^t dt' \mathcal{L}(t') \right) \rho_B(0) \right] = \left\langle \overleftarrow{\mathcal{T}} \exp \left( \int_0^t dt' \mathcal{L}(t') \right) \right\rangle_B \quad (1.13)$$

Later in this section, we will introduce two different theoretical methods that will allow us to extract the dynamics of the reduced density matrix  $\rho_S(t)$  in Eq. (1.12). The first one is the Lindblad master equation, well-suited for describing quantum optical systems in Chapters 3 and 4, while the second one is a much more general Feynman-Vernon influence functional approach that we will use to tackle non-Markovian dynamics in Chapters 5 and 6.

Overall, an important message from the discussion above is that even if  $S$  and  $B$  are initially prepared in a product state, their interaction will create a buildup of entanglement between  $S$  and  $B$  as we evolve in time. The decay of the initial pure state of  $S$  into a mixture of states given by  $\rho_S$  is termed decoherence. A common example of the physical process behind decoherence is dissipation: the emission of energy from a system  $S$  into an environment  $B$  causes the loss of quantum information from system into its surroundings, and leads to a dynamical destruction of quantum coherence in  $S$ . An important concept to mention here is the irreversibility of  $S$  dynamics. If environment  $B$  has a finite number of degrees of freedom then

there will exist a timescale on which recurrences take place and the dynamics will be reversible. On the other hand, if  $B$  consists of an infinite continuum of modes, the recurrence times will become infinite and the  $S$  dynamics will be irreversible. We often call the latter type of environment a bath. In this work, we will primarily focus on environments that can be modelled as a bath.

### 1.1.2 Master equation formalism

This subsection will introduce a framework for describing the driven dissipative dynamics of quantum optical systems. Here we model the environment as a heat bath of harmonic oscillators with optical frequencies, and by tracing out the bath degrees of freedom we will derive the Lindblad master equation that governs dynamics of the reduced density matrix of the system for weak couplings (Born approximation) and unstructured memoryless environments (Markovian approximation) [1]. We start with the von Neumann equation of motion transformed to the interaction picture Eq. (1.7) and formally solve it for  $\rho(t)$ :

$$\rho(t) = \rho(0) + \int_0^t d\tau \mathcal{L}(\tau)\rho(\tau) \quad (1.14)$$

Substituting Eq. (1.14) into Eq. (1.7) and tracing out the environment degrees of freedom with  $\text{Tr}_B$  yields a formal equation of motion for the reduced density matrix  $\rho_S(t) = \text{Tr}_B(\rho(t))$  of the system:

$$\partial_t \rho_S(t) = \text{Tr}_B(\mathcal{L}(t)\rho(0)) + \int_0^t d\tau \text{Tr}_B(\mathcal{L}(t)\mathcal{L}(\tau)\rho(\tau)) \quad (1.15)$$

We now make Born approximation, which says that the bath is very large and virtually unaffected by the system:  $\rho_B(t) \approx \rho_B(t=0) = \rho_B$ . Since we have assumed a separable initial state Eq. (1.10), the system and the bath are uncorrelated at  $t=0$ . At times  $t > 0$ , correlations build up between  $S$  and  $B$  and the full  $S+B$  density matrix becomes  $\rho(t) = \rho_S(t) \otimes \rho_B + \rho_{\text{corr}}(t)$ , where  $\rho_{\text{corr}}(t) \sim O(V)$  is the part of  $\rho(t)$  induced by  $S-B$  interaction Hamiltonian  $V(t)$ . We will make a stronger assumption that the coupling between the system and the environment is weak, and neglect terms higher than the second order in  $S-B$  interaction in Eq. (1.15), where  $\mathcal{L}(t) = -i[V(t), \bullet]$ . This approximation implies that one can correctly calculate the system dynamics by assuming that  $\rho(t) \approx \rho_S(t) \otimes \rho_B$ : the dynamics that started in a product state will remain in the product state for as long as the bath experiences a negligible influence from the  $S-B$  interaction. Therefore, Born approximation allows us to separate the time evolution of  $S$  and  $B$  degrees of freedom. Another simplification we can make is eliminating the first term on RHS of Eq. (1.15). For a separable initial state Eq. (1.10) we have

$$\text{Tr}_B(\mathcal{L}(t)\rho(0)) = \text{Tr}_B(\mathcal{L}(t)\rho_B)\rho_S(0) = \langle \mathcal{L}(t) \rangle_B \rho_S(0) \quad (1.16)$$

Assuming that  $S-B$  interaction takes a generic, linearly coupled form of

$$V(t) = \sum_{\alpha} A_{\alpha}(t) \otimes B_{\alpha}(t) \quad (1.17)$$

where  $A_\alpha(t)$  and  $B_\alpha(t)$  are Hermitian operators of system and bath respectively and index  $\alpha$  runs over different operators, we can write

$$\begin{aligned} \langle \mathcal{L}(t) \rangle_B &= -i \text{Tr}_B ([V(t), \rho_B]) = -i \text{Tr}_B (V(t) \rho_B) = \\ &= -i \sum_{\alpha} A_{\alpha}(t) \otimes \text{Tr}_B (B_{\alpha}(t) \rho_B) = -i \sum_{\alpha} A_{\alpha}(t) \otimes \langle B_{\alpha}(t) \rangle_B \end{aligned} \quad (1.18)$$

We can shift the bath operators by  $B_{\alpha}(t) \mapsto B_{\alpha}(t) - \langle B_{\alpha}(t) \rangle_B$  which gives  $\langle \mathcal{L}(t) \rangle_B = 0$  and thus  $\text{Tr}_B (\mathcal{L}(t) \rho(0)) = 0$  in Eq. (1.15). Using the assumptions discussed above and changing variables  $\tau \mapsto t - \tau$  in the main equation of motion Eq. (1.15) we find:

$$\partial_t \rho_S(t) = \int_0^t d\tau \langle \mathcal{L}(t) \mathcal{L}(t - \tau) \rangle_B \rho_S(t - \tau) \quad (1.19)$$

and substituting the  $S - B$  interaction Hamiltonian Eq. (1.17) into Eq. (1.19) gives:

$$\partial_t \rho_S(t) = \int_0^t d\tau \sum_{\alpha, \beta} \langle B_{\alpha}^{\dagger}(t) B_{\beta}(t - \tau) \rangle_B [A_{\alpha}^{\dagger}(t), [A_{\beta}(t - \tau), \rho_S(t - \tau)]] \quad (1.20)$$

In the next step, we make the Markovian approximation, which assumes that bath correlations  $C(\tau) = \langle B_{\alpha}^{\dagger}(t) B_{\beta}(t - \tau) \rangle_B$  for bath operators  $B_{\alpha}(t)$  decay away on a timescale  $\tau_B$  much faster than the characteristic timescale  $\tau_S$  of the system relaxation dynamics:  $\tau_B \ll \tau_S$ . This implies that any information flowing from  $S$  to  $B$  decays away very fast, before it had time to flow back from  $B$  to  $S$ . In other words, the bath  $B$  is Markovian: it retains no memory of the system dynamics. Hence the system dynamics is also Markovian: its time evolution at time  $t$  depends only on the state of system  $S$  at time  $t$  but not on its past states, so that we can set  $\rho(\tau) \approx \rho(t)$  in Eq. (1.20). In addition, a short bath correlation time  $\tau_B \ll \tau_S$  means that the memory kernel  $C(\tau)$  decays away very fast, and the integrand disappears for  $\tau \gg \tau_B$ . Therefore, we can extend the effective integration limit to infinity:  $\int_0^t \rightarrow \int_0^{\infty}$ . The equation of motion Eq. (1.20) now reads:

$$\partial_t \rho_S(t) = \int_0^{\infty} d\tau \sum_{\alpha, \beta} \langle B_{\alpha}^{\dagger}(t) B_{\beta}(t - \tau) \rangle_B [A_{\alpha}^{\dagger}(t), [A_{\beta}(t - \tau), \rho_S(t)]] \quad (1.21)$$

The bath correlation time  $\tau_B$  is determined by the bandwidth  $\Delta$  of the bath spectral density:  $\tau_B \sim 1/\Delta$ . It follows that a Markovian bath with  $\tau_B \ll \tau_S$  must have an approximately flat spectral density, with an effectively infinite bandwidth  $\Delta \gg 1/\tau_S$  over the range of frequencies of interest. In quantum optical systems, bath correlation time is set by the bandwidth  $\Delta$  of the spectral density of the electromagnetic bath  $\tau_B \sim 1/\text{THz}$  while system dynamics timescale is set by photon lifetime in a cavity  $\tau_S \sim 1/\text{MHz}$ . This implies  $\tau_B \ll \tau_S$  and the Markovian approximation is well justified. More generally, Markovian behaviour arises when our environment  $B$  is unstructured and has a flat density of states. Later in this section we will discuss a more general treatment of open quantum systems where this is not the case and the dynamics is non-Markovian.

To make further progress, we will express the  $S - B$  interaction Hamiltonian Eq. (1.17) in terms of the eigenoperators of the system Hamiltonian  $H_S$ . Let us first project a system operator  $A_\alpha$  onto the eigenspace of  $H_S$ :

$$\tilde{A}_\alpha(\omega) = \sum_{\epsilon' - \epsilon = \omega} \langle \epsilon' | A_\alpha | \epsilon \rangle | \epsilon' \rangle \langle \epsilon | \quad (1.22)$$

where  $|\epsilon\rangle, |\epsilon'\rangle$  are the eigenstates of  $H_S$  and  $\epsilon, \epsilon'$  are the corresponding eigenvalues. The sum runs over all pairs of energy levels with a given difference  $\omega = \epsilon' - \epsilon$ . It follows straightforwardly from Eq. (1.22) that  $\tilde{A}_\alpha(\omega)$  are the eigenoperators of  $H_S$ , satisfying  $[H_S, \tilde{A}_\alpha(\omega)] = -\omega \tilde{A}_\alpha(\omega)$ . We can decompose a system operator  $A_\alpha$  into

$$A_\alpha = \sum_{\omega} \tilde{A}_\alpha(\omega) \quad (1.23)$$

where each  $\tilde{A}_\alpha(\omega = \epsilon' - \epsilon)$  mediates a transition from the energy level  $\epsilon$  to the energy level  $\epsilon'$ . One can easily verify Eq. (1.23) by substituting Eq. (1.22) and summing over all the energy differences  $\omega = \epsilon' - \epsilon$ . Switching to the interaction picture  $A_\alpha \rightarrow A_\alpha(t) = e^{i(H_S + H_B)t} A_\alpha e^{-i(H_S + H_B)t}$  we obtain

$$A_\alpha(t) = \sum_{\omega} \tilde{A}_\alpha(\omega) e^{-i\omega t} = \sum_{\omega} \tilde{A}_\alpha^\dagger(\omega) e^{i\omega t} \quad (1.24)$$

where we have used  $A_\alpha(t) = A_\alpha^\dagger(t)$ . To simplify Eq. (1.21), we first exploit the mathematical identity  $[A, [B, C]] = [A, BC] + \text{H.c.}$  for Hermitian operators  $A, B, C$ :

$$[A_\alpha^\dagger(t), [A_\beta(t - \tau), \rho_S(t)]] = [A_\alpha^\dagger(t), A_\beta(t - \tau) \rho_S(t)] + \text{H.c.} \quad (1.25)$$

Plugging Eqs. (1.24) and (1.25) into Eq. (1.21) then gives:

$$\begin{aligned} \partial_t \rho_S(t) &= \\ &= - \int_0^\infty d\tau \sum_{\alpha, \beta} \sum_{\omega, \omega'} \langle B_\alpha^\dagger(t) B_\beta(t - \tau) \rangle_B e^{i\omega t} e^{-i\omega'(t - \tau)} [\tilde{A}_\alpha^\dagger(\omega), \tilde{A}_\beta(\omega') \rho_S(t)] + \text{H.c.} \\ &= \sum_{\alpha, \beta} \sum_{\omega, \omega'} J_{\alpha\beta}(\omega') e^{i(\omega - \omega')t} \left( \tilde{A}_\beta(\omega') \rho_S(t) \tilde{A}_\alpha^\dagger(\omega) - \tilde{A}_\alpha^\dagger(\omega) \tilde{A}_\beta(\omega') \rho_S(t) \right) + \text{H.c.} \end{aligned} \quad (1.26)$$

where we have defined the bath spectral density matrix:

$$J_{\alpha\beta}(\omega) = \int_0^\infty d\tau e^{i\omega\tau} \langle B_\alpha^\dagger(\tau) B_\beta(0) \rangle_B \quad (1.27)$$

with two-time correlators  $\langle B_\alpha^\dagger(\tau) B_\beta(0) \rangle_B = \text{Tr}_B (B_\alpha^\dagger(t) B_\beta(t - \tau) \rho_B)$  and used the fact that since the bath does not evolve, the correlators are homogeneous in time:  $\langle B_\alpha^\dagger(t) B_\beta(t - \tau) \rangle_B = \langle B_\alpha^\dagger(\tau) B_\beta(0) \rangle_B$ .

We now make the secular (rotating wave) approximation that neglects the non-resonant, fast-rotating terms. The typical timescale of *intrinsic* evolution of a quantum optical system is  $\tau_{S0} = 1/|\omega - \omega'| \sim 1/\text{THz}$ , set by optical frequencies. For weak  $S - B$  coupling rates, it will be much faster than the system relaxation

timescale  $\tau_S \sim 1/\text{MHz}$  in the presence  $S-B$  interactions discussed above:  $\tau_{S0} \ll \tau_S$ . The non-resonant exponentials will then oscillate very rapidly and average to zero. Therefore, we neglect the contributions from  $\omega \neq \omega'$  terms in Eq. (1.26):

$$\partial_t \rho_S(t) = \sum_{\alpha, \beta} \sum_{\omega} J_{\alpha\beta}(\omega) \left( \tilde{A}_\beta(\omega) \rho_S(t) \tilde{A}_\alpha^\dagger(\omega) - \tilde{A}_\alpha^\dagger(\omega) \tilde{A}_\beta(\omega) \rho_S(t) \right) + \text{H.c.} \quad (1.28)$$

It is convenient to split  $J_{\alpha\beta}(\omega)$  in Eq. (1.27)

$$J_{\alpha\beta}(\omega) = \frac{1}{2} \gamma_{\alpha\beta}(\omega) + i \Gamma_{\alpha\beta}(\omega) \quad (1.29)$$

into the dissipative term:

$$\gamma_{\alpha\beta}(\omega) = J_{\alpha\beta}(\omega) + J_{\beta\alpha}^*(\omega) = \int_{-\infty}^{\infty} d\tau e^{i\omega\tau} \langle B_\alpha^\dagger(\tau) B_\beta(0) \rangle_B \quad (1.30)$$

and the Lamb shift term:

$$\Gamma_{\alpha\beta}(\omega) = \frac{1}{2i} (J_{\alpha\beta}(\omega) - J_{\beta\alpha}^*(\omega)) \quad (1.31)$$

Substituting Eq. (1.29) into Eq. (1.28), and transforming back to Schrödinger picture we get:

$$\begin{aligned} \partial_t \rho_S(t) = & -i [H_S + H_{LS}, \rho_S(t)] \\ & + \sum_{\alpha, \beta} \sum_{\omega} \gamma_{\alpha\beta}(\omega) \left( \tilde{A}_\beta(\omega) \rho_S(t) \tilde{A}_\alpha^\dagger(\omega) - \frac{1}{2} \left\{ \tilde{A}_\alpha^\dagger(\omega) \tilde{A}_\beta(\omega), \rho_S(t) \right\} \right) \end{aligned} \quad (1.32)$$

with the Lamb shift Hamiltonian  $H_{LS} = \sum_{\alpha\beta} \sum_{\omega} \Gamma_{\alpha\beta}(\omega) \tilde{A}_\alpha^\dagger(\omega) \tilde{A}_\beta(\omega)$  which leads to renormalization of the system energy levels due to  $S-B$  interaction, and is negligible in the weak coupling regime we are considering [1]. Hence,  $H_{LS}$  will be neglected in further steps of the derivation. We next diagonalize the dissipation matrix  $\gamma_{\alpha\beta}(\omega) = \sum_p U_{\alpha p} \gamma_p(\omega) U_{p\beta}^\dagger$  in Eq. (1.32) and define  $\hat{A}_\alpha(\omega) = \sum_p U_{\alpha p} a_p(\omega)$  in terms of new operators  $a_p$ :

$$\partial_t \rho_S(t) = -i [H_S, \rho_S(t)] + \sum_p \sum_{\omega} \gamma_p(\omega) \mathcal{D}[a_p(\omega)] \rho_S(t) \quad (1.33)$$

where the dissipative superoperator is

$$\mathcal{D}[a] \bullet = \left( a \bullet a^\dagger - \frac{1}{2} \{a^\dagger a, \bullet\} \right) \quad (1.34)$$

This is the Lindblad master equation that governs the time evolution of the reduced density matrix  $\rho_S(t)$  under Born-Markov and secular approximations.

In this thesis, we will often be interested in quantum optical problems where the bath  $B$  is a continuum of harmonic oscillator modes of electromagnetic field described by  $H_B = \sum_{\mathbf{k}\lambda} \omega_{\mathbf{k}} b_{\mathbf{k}\lambda}^\dagger b_{\mathbf{k}\lambda}$  with bath creation and annihilation operators  $b_{\mathbf{k}\lambda}^\dagger, b_{\mathbf{k}\lambda}$  for each mode  $\mathbf{k}$  that has polarization  $\lambda$ . In such case we can derive a more

specific form of bath correlators. In the expression Eq. (1.30), bath operators now correspond to Cartesian components  $i, j$  of electromagnetic field  $B_\alpha(t) \rightarrow E_j(t)$  and so we have:

$$\gamma_{ij}(\omega) = \int_{-\infty}^{\infty} d\tau e^{i\omega\tau} \langle E_i(\tau) E_j(0) \rangle \quad (1.35)$$

We next expand the  $E_j(t)$  field in terms Fourier modes in a large box of volume  $V$  with periodic boundary conditions. These modes are labelled by the wavevector  $\mathbf{k}$  and two corresponding transverse unit polarization vectors  $\mathbf{e}_{\mathbf{k}\lambda}$ :

$$E_j(t) = \sum_{\mathbf{k}\lambda} \sqrt{\frac{2\pi|\omega_{\mathbf{k}}|}{V}} e_{\mathbf{k}\lambda}^j \left( i b_{\mathbf{k}\lambda} e^{-i\omega_{\mathbf{k}}t} - i b_{\mathbf{k}\lambda}^\dagger e^{i\omega_{\mathbf{k}}t} \right) \quad (1.36)$$

The bath modes have the following defining properties:

$$\omega_{\mathbf{k}} = c|\mathbf{k}|, \quad \mathbf{k} \cdot \mathbf{e}_{\mathbf{k}\lambda} = 0, \quad \mathbf{e}_{\mathbf{k}\lambda} \cdot \mathbf{e}_{\mathbf{k}\lambda'} = \delta_{\lambda\lambda'}, \quad \sum_{\lambda} e_{\mathbf{k}\lambda}^i e_{\mathbf{k}\lambda}^j = \delta_{ij} - \frac{k_i k_j}{|\mathbf{k}|^2} \quad (1.37)$$

where  $k_{i,j}$  are the Cartesian components  $i, j$  of  $\mathbf{k}$ . The bath mode correlations are:

$$\langle b_{\mathbf{k}\lambda}^\dagger b_{\mathbf{q}\lambda'} \rangle = \delta_{\mathbf{k}\mathbf{q}} \delta_{\lambda\lambda'} N(\omega_{\mathbf{k}}) \quad \langle b_{\mathbf{k}\lambda} b_{\mathbf{q}\lambda'}^\dagger \rangle = \delta_{\mathbf{k}\mathbf{q}} \delta_{\lambda\lambda'} (N(\omega_{\mathbf{k}}) + 1) \quad \langle b_{\mathbf{k}\lambda} b_{\mathbf{q}\lambda'} \rangle = 0 \quad (1.38)$$

where  $N(\omega_{\mathbf{k}}) = \frac{1}{e^{\omega_{\mathbf{k}}/T} - 1}$  is the Bose-Einstein distribution that gives the average number of photons populating each mode  $\mathbf{k}$ . Substituting Eqs. (1.36)-(1.38) into Eq. (1.35) and treating the sum over bath modes as a continuum  $\sum_{\mathbf{k}} \rightarrow \int d\Omega \int \frac{|\mathbf{k}|^2 d|\mathbf{k}|}{(2\pi)^3/V}$  then yields:

$$\gamma_{ij}(\omega) = \int d\Omega \int d\omega_{\mathbf{k}} \frac{\omega_{\mathbf{k}}^3}{(2\pi)^2 c^3} \left( \delta_{ij} - \frac{k_i k_j}{|\mathbf{k}|^2} \right) \int_{-\infty}^{\infty} d\tau \left( (N(\omega_{\mathbf{k}}) + 1) e^{i(\omega - \omega_{\mathbf{k}})\tau} + N(\omega_{\mathbf{k}}) e^{i(\omega + \omega_{\mathbf{k}})\tau} \right) \quad (1.39)$$

Integrating we find the rate of excitation transfer between  $S$  and  $B$ :

$$\gamma_{ij}(\omega) = \delta_{ij} \frac{4\omega^3}{3c^3} \begin{cases} N(\omega) + 1 & \text{for } \omega > 0 \text{ emission from S to B} \\ N(-\omega) & \text{for } \omega < 0 \text{ absorption from B to S} \end{cases} \quad (1.40)$$

The problems of our interest will often involve an optical field trapped in a cavity with a single mode  $\omega = \omega_c$  and hence  $a_p(\omega = \omega_c) = a_p$  in Eq. (1.33). At optical frequencies  $\omega_c \gg T$ , i.e. the energy scale of thermal fluctuations in the heat bath is far lower than characteristic energy scales of the system so we can consider the bath temperature to be effectively zero  $T = 0$  with  $N(\omega) \approx 0$ . The heat bath  $B$  then corresponds to a continuum of unoccupied radiation modes at  $T = 0$ , and we have  $\gamma_{ij}(\omega_c) = \delta_{ij} \frac{4\omega_c^3}{3c^3}$ . The spectral density matrix then has a single eigenvalue  $\gamma_{k=1}(\omega_c) = \gamma = \frac{4\omega_c^3}{3c^3}$ . The Lindblad master equation Eq. (1.33) reduces to

$$\partial_t \rho_S(t) = -i [H_S, \rho_S(t)] + \gamma \mathcal{D}[a] \rho_S(t) \quad (1.41)$$

where  $a^\dagger, a$  are now creation and annihilation operators of the cavity field, and  $\gamma$  is the rate of photon loss from the cavity.



### 1.1.3 Influence functional formalism

Having introduced Lindblad master equation, we next describe a more general approach that does not rely on Born and Markov approximations. Instead of deriving a non-Markovian master equation, this approach builds on the Feynman path integral formulation of quantum dynamics, and is known as the Feynman-Vernon influence functional formalism [47]. By integrating out the environment degrees of freedom, we will obtain a path integral expression for the dynamics of the reduced density matrix of an open system. Here, all the effects of the environment are contained in the influence functional that is nonlocal in time and thus captures non-Markovian correlations between distant points of time evolution. While Lindblad master equation is going to be our main tool for modelling quantum optical systems in Chapters 3 and 4 characterized by weak couplings and Markovian dynamics, the influence functional approach will form the basis of our algorithms for simulating non-Markovian systems in Chapters 5 and 6 where such approximations no longer apply. In our derivation we consider a class of models described by the Hamiltonian

$$H = H_S + H_B, \quad H_B = H_{B0} + V \quad (1.42)$$

where the system is described by a generic Hamiltonian  $H_S$  and the environment is a bosonic bath that consists of a large number of harmonic modes, with a Hamiltonian given by

$$H_{B0} = \sum_k \left( \frac{p_k^2}{2m_k} + \frac{m_k \omega_k^2 q_k^2}{2} \right) = \sum_k \omega_k b_k^\dagger b_k \quad (1.43)$$

where  $b_k^\dagger$ ,  $b_k$  are the creation and annihilation operators of the mode  $k$ . Each harmonic mode  $k$  has the frequency  $\omega_k$ , mass  $m_k$ , momentum  $p_k$ , and displacement  $q_k$  from the equilibrium position. Since the interaction between the system and each individual bath mode is inversely proportional to the volume of the bath, the coupling strength of each individual mode to the system will be small [1]. Therefore we will assume that the system operator  $X$  couples linearly to each mode  $k$  via the coupling constant  $g_k$ . The system-bath interaction is then given by the Hamiltonian

$$V = X \sum_k \left( g_k b_k + g_k^* b_k^\dagger \right) = XB \quad (1.44)$$

where we have defined the collective bath operator

$$B = \sum_k \left( g_k b_k + g_k^* b_k^\dagger \right) \quad (1.45)$$

for later convenience. As before, we work in the interaction picture with respect to  $H_S + H_{B0}$ ; the interaction picture Hamiltonian is then  $V(t) = X(t)B(t)$ . Liouvillian dynamics of the total system  $S + B$  density matrix is governed by the equations of motion Eqs. (1.7), (1.8) with the Liouvillian superoperator given by

$$\mathcal{L}(t) = -i [X(t)B(t), \bullet] \quad (1.46)$$

Our derivation starts from the formal result in Eqs. (1.12), (1.13) introduced in Section 1.1.1, assuming the separable initial condition Eq. (1.10) with the bath

initially in the thermal equilibrium state Eq. (1.11). Since the initial bath density matrix  $\rho_B = e^{-\beta H_{B0}}/Z$  is Gaussian in bath operators  $q_k$  and  $p_k$ , as seen from Eq. (1.43), we can write the propagator Eq. (1.13) as a cumulant expansion that terminates after only two terms:

$$\begin{aligned} G(t) &= \left\langle \overleftarrow{\mathcal{T}} \exp \left( \int_0^t dt' \mathcal{L}(t') \right) \right\rangle_B \\ &= \exp \left[ \int_0^t dt' \langle \mathcal{L}(t') \rangle_{B,C} + \frac{1}{2} \int_0^t dt' \int_0^t dt'' \langle \mathcal{L}(t') \mathcal{L}(t'') \rangle_{B,C} \right] \end{aligned} \quad (1.47)$$

Here

$$\langle \mathcal{L}(t') \rangle_{B,C} = \langle \mathcal{L}(t') \rangle_B \quad (1.48)$$

and

$$\langle \mathcal{L}(t') \mathcal{L}(t'') \rangle_{B,C} = \langle \overleftarrow{\mathcal{T}} \mathcal{L}(t') \mathcal{L}(t'') \rangle_B - \langle \mathcal{L}(t') \rangle_B \langle \mathcal{L}(t'') \rangle_B \quad (1.49)$$

are the first and second order cumulants. Since we can always shift bath operators such that  $\langle q_k \rangle_B = 0$ ,  $\langle p_k \rangle_B = 0$ , the Liouvillian average can be taken as  $\langle \mathcal{L}(t) \rangle_B = 0$ . The propagator Eq. (1.47) then becomes:

$$G(t) = \exp \left[ \frac{1}{2} \int_0^t dt' \int_0^t dt'' \langle \overleftarrow{\mathcal{T}} \mathcal{L}(t') \mathcal{L}(t'') \rangle_B \right] \quad (1.50)$$

We now make use of the following property of the time ordering operator  $\overleftarrow{\mathcal{T}}$

$$\langle \overleftarrow{\mathcal{T}} \mathcal{L}(t') \mathcal{L}(t'') \rangle_B = \langle \mathcal{L}(t') \mathcal{L}(t'') \rangle_B \theta(t' - t'') + \langle \mathcal{L}(t'') \mathcal{L}(t') \rangle_B \theta(t'' - t') \quad (1.51)$$

and substitute the Liouvillian Eq. (1.46) into the propagator Eq. (1.50) to find

$$G(t) = e^{\phi(X)} \quad (1.52)$$

in terms of the influence phase superoperator

$$\phi(X) = - \int_0^t dt' \int_0^{t'} dt'' \text{Tr}_B [X(t') B(t'), [X(t'') B(t''), \rho_B \bullet]] \quad (1.53)$$

After some algebraic rearrangements, the influence phase Eq. (1.53) takes the following form

$$\phi(X_a, X_c) = - \int_0^t dt' \int_0^{t'} dt'' (C_{\text{Re}}(t' - t'') X_c(t') X_c(t'') + i C_{\text{Im}}(t' - t'') X_c(t') X_a(t'')) \quad (1.54)$$

which involves the commutator and anticommutator superoperators  $X_c = [X, \bullet]$ ,  $X_a = \{X, \bullet\}$ . We have also defined the bath autocorrelation function

$$C(t - t') = \langle B(t) B(t') \rangle_B = C_{\text{Re}}(t - t') + i C_{\text{Im}}(t - t') \quad (1.55)$$

whose real part  $C_{\text{Re}}(t - t')$  and imaginary part  $C_{\text{Im}}(t - t')$  we derive below. The correlators  $C_{\text{Re}}(t - t')$  and  $C_{\text{Im}}(t - t')$  are also known as the noise and dissipation

kernels respectively. The collective bath operator Eq. (1.45) in the interaction picture reads

$$B(t) = \sum_k \left( g_k b_k(t) + g_k^* b_k^\dagger(t) \right) = \sum_k \left( g_k b_k e^{-i\omega_k t} + g_k^* b_k^\dagger e^{i\omega_k t} \right) \quad (1.56)$$

The  $b_k^\dagger$ ,  $b_k$  operators of bath modes  $k$  obey the bosonic commutation and anticommutation relations:

$$\left\langle \left[ b_k, b_{k'}^\dagger \right] \right\rangle = \delta_{kk'} \quad (1.57)$$

and

$$\left\langle \left\{ b_k, b_{k'}^\dagger \right\} \right\rangle = \left\langle \left\{ b_k^\dagger, b_{k'} \right\} \right\rangle = (2N(\omega_k) + 1) \delta_{kk'} \quad (1.58)$$

where  $N(\omega) = \frac{1}{e^{\omega/T} - 1}$  is the Bose-Einstein distribution (the temperature is measured in units of  $k_B = 1$ ). The imaginary part of  $C(t - t')$  is then

$$\begin{aligned} C_{\text{Im}}(t - t') &= \frac{1}{2i} \langle [B(t), B(t')] \rangle_B \\ &= \frac{1}{2i} \sum_k \left( g_k g_{k'}^* \left\langle [b_k, b_{k'}^\dagger] \right\rangle e^{-i\omega_k(t-t')} + g_k^* g_{k'} \left\langle [b_k^\dagger, b_{k'}] \right\rangle e^{i\omega_k(t-t')} \right) \\ &= \frac{1}{2i} \sum_k |g_k|^2 \left( e^{-i\omega_k(t-t')} - e^{i\omega_k(t-t')} \right) \\ &= - \sum_k |g_k|^2 \sin(\omega_k(t - t')) = - \int_0^\infty d\omega J(\omega) \sin(\omega(t - t')) \end{aligned} \quad (1.59)$$

where we have defined the general form of bath spectral density:

$$J(\omega) = \sum_k |g_k|^2 \delta(\omega - \omega_k) \quad (1.60)$$

Similarly, the real part of  $C(t - t')$  is

$$\begin{aligned} C_{\text{Re}}(t - t') &= \frac{1}{2} \langle \{B(t), B(t')\} \rangle_B \\ &= \frac{1}{2} \sum_k \left( g_k g_{k'}^* \left\langle \{b_k, b_{k'}^\dagger\} \right\rangle e^{-i\omega_k(t-t')} + g_k^* g_{k'} \left\langle \{b_k^\dagger, b_{k'}\} \right\rangle e^{i\omega_k(t-t')} \right) \\ &= \frac{1}{2} \sum_k (2N(\omega_k) + 1) |g_k|^2 \left( e^{-i\omega_k(t-t')} + e^{i\omega_k(t-t')} \right) \\ &= \sum_k |g_k|^2 \coth\left(\frac{\omega_k}{2T}\right) \cos(\omega_k(t - t')) = \int_0^\infty d\omega J(\omega) \coth\left(\frac{\omega}{2T}\right) \cos(\omega(t - t')) \end{aligned} \quad (1.61)$$

Finally, combining Eqs. (1.59) and (1.61) in Eq. (1.55) gives the bath autocorrelation function:

$$C(t) = \int_0^\infty d\omega J(\omega) \left[ \coth\left(\frac{\omega}{2T}\right) \cos(\omega t) - i \sin(\omega t) \right] \quad (1.62)$$

The next step of our derivation is to express the formal solution of the Liouvillian dynamics Eq. (1.12) as a Feynman path integral for propagation along the Keldysh-Schwinger contour [48, 49]. Without losing generality, we choose to work in the basis where the system operator  $X$  is diagonal – i.e. using the basis states  $|x\rangle, |x'\rangle$  that are the eigenstates of  $X$ . This means that the system coordinates are measured by the eigenvalues of  $X$ :  $x(t) = \langle x(t)|X|x(t)\rangle$  and  $x'(t) = \langle x'(t)|X|x'(t)\rangle$  for any time  $t$  during the propagation. The path integral is evaluated along the forward and backward time evolution trajectories measured respectively by  $x$  and  $x'$  – the coordinates  $x, x'$  are allowed to be different on the forward and the backward branches of the contour. Here we discuss a continuous integral, considering a problem where the eigenvalues of  $X$  form a continuous basis, for instance the position space if  $X$  is a position operator. In Chapter 5 we will return to consider the case of a discrete eigenbasis of  $X$  that occurs for any finite dimensional Hilbert space.

Let us first write Eq. (1.12) with the propagator Eq. (1.52) and the influence phase Eq. (1.54)

$$\rho_S(t) = e^{\phi(X_a, X_c)} \rho_S(0) \quad (1.63)$$

in the basis of the final points  $x_N, x'_N$  of time evolution after time  $t$ :

$$\rho_S(x_N, x'_N, t) = \langle x_N(t) | e^{\phi(X_a, X_c)} \rho_S(0) | x'_N(t) \rangle \quad (1.64)$$

We next insert identity resolutions  $I = \int Dx |x\rangle \langle x|$ ,  $I = \int Dx' |x'\rangle \langle x'|$  for the forward and backward contours:

$$\rho_S(x_N, x'_N, t) = \int Dx \int Dx' \langle x_N(t) | \left( e^{\phi(X_a, X_c)} |x\rangle \langle x'| \right) | x'_N(t) \rangle \rho_S(x, x', 0) \quad (1.65)$$

To evaluate  $\langle x_N(t) | \left( e^{\phi(X_a, X_c)} |x\rangle \langle x'| \right) | x'_N(t) \rangle$ , we note that the commutator and anticommutator superoperators  $X_{a,c}$  obey the following equalities:

$$\begin{aligned} \langle z | \left( X_{a,c} |y\rangle \langle y'| \right) | z' \rangle &= \langle z | X | y \rangle \langle y' | z' \rangle \pm \langle z | y \rangle \langle y' | X | z' \rangle = \\ &= \langle z | y \rangle \langle y' | z' \rangle (y \pm y') \end{aligned} \quad (1.66)$$

The switch from the superoperator form to the path integral form is then achieved by replacing

$$X_{a,c}(t) \rightarrow x^\pm(t) = x(t) \pm x'(t) \quad (1.67)$$

in the influence phase Eq. (1.54), which gives

$$\phi(x^+, x^-) = - \int_0^t dt' \int_0^{t'} dt'' x^-(t') (C_{\text{Re}}(t' - t'') x^-(t'') + i C_{\text{Im}}(t' - t'') x^+(t'')) \quad (1.68)$$

expressed in terms of the sums  $x^+(t)$  and differences  $x^-(t)$  of the  $X$  eigenvalues. The influence phase Eq. (1.68) represents non-Markovian interactions that are mediated

by the bath correlation function  $C(t)$ , also known as the memory kernel. As a result, we find

$$\rho_S(x_N, x'_N, t) = \int Dx \int Dx' \langle x_N(t)|x \rangle \langle x'|x'_N(t) \rangle e^{\phi(x+x', x-x')} \rho_S(x, x', 0) \quad (1.69)$$

Switching back from the interaction picture to the Schrödinger picture, the remaining inner products become

$$\langle x_N(t)|x \rangle \langle x'|x'_N(t) \rangle = \langle x_N| \left( e^{t\mathcal{L}_S} |x \rangle \langle x'| \right) |x'_N \rangle \quad (1.70)$$

with the system Liouvillian  $\mathcal{L}_S = -i[H_S, \bullet]$ . This yields the final result

$$\rho_S(x_N, x'_N, t) = \int Dx \int Dx' \langle x_N| \left( e^{t\mathcal{L}_S} |x \rangle \langle x'| \right) |x'_N \rangle I(x, x') \rho_S(x, x', 0) \quad (1.71)$$

Eq. (1.71) is the path integral representation of the time-evolved reduced density matrix  $\rho_S(t)$ , which corresponds to integrating over the contributions of all the reduced system trajectories  $x, x'$ . Here, the system-environment interaction enters through the influence functional

$$I(x, x') = e^{\phi(x+x', x-x')} \quad (1.72)$$

that conveniently packages the non-Markovian memory effects of the environment into a single object. The influence phase  $\phi(x+x', x-x')$  is given by Eq. (1.68), as before. This concludes our discussion of the Feynman-Vernon influence functional formalism. We will meet this topic again in Chapter 5 where we will describe how it can be recast as a practical numerical technique for solving non-Markovian dynamics.

### 1.1.3.1 Influence functional formalism with multiple baths

The influence functional theory presented above was derived for a system interacting with a single harmonic bath. We next describe influence functional formalism for a system coupled to multiple independent baths. In particular, we will consider a multipartite system of  $M$  particles, where each particle interacts with its own bath. We start with the same Hamiltonian Eq. (1.42) where  $H_{B0}$  now contains  $M$  harmonic baths:

$$H_{B0} = \sum_{j=1}^M H_{B0,j} \quad (1.73)$$

and each bath  $j$  is given by the Hamiltonian  $H_{B0,j}$ , identical to Eq. (1.43):

$$H_{B0,j} = \sum_k \left( \frac{p_{k,j}^2}{2m_{k,j}} + \frac{m_{k,j}\omega_{k,j}^2 q_{k,j}^2}{2} \right) = \sum_k \omega_{k,j} b_{k,j}^\dagger b_{k,j} \quad (1.74)$$

Here,  $b_{k,j}^\dagger, b_{k,j}$  are the creation and annihilation operators of the mode  $k$  for a bath  $j$ . Each harmonic mode  $k$  of a bath  $j$  has the frequency  $\omega_{k,j}$ , mass  $m_{k,j}$ ,

momentum  $p_{k,j}$ , and displacement  $q_{k,j}$  from the equilibrium position. The system-bath interaction is then given by the Hamiltonian

$$V = \sum_{j=1}^M V_j \quad (1.75)$$

and  $V_j$  describes the interaction of a particle  $j$  with a bath  $j$ :

$$V_j = X_j \sum_k \left( g_{k,j} b_{k,j} + g_{k,j}^* b_{k,j}^\dagger \right) = X_j B_j \quad (1.76)$$

where the system operator  $X_j$  corresponding to a particle  $j$  couples linearly to each mode  $k$  in a bath  $j$  via the coupling constant  $g_{k,j}$ . For convenience, we have defined the collective bath operator:

$$B_j = \sum_k \left( g_{k,j} b_{k,j} + g_{k,j}^* b_{k,j}^\dagger \right) \quad (1.77)$$

for each bath  $j$ . As before, we work in the interaction picture with respect to  $H_S + H_{B0}$ ; the interaction picture Hamiltonian is then  $V(t) = \sum_{j=1}^M V_j(t) = \sum_{j=1}^M X_j(t) B_j(t)$ . Liouvillian dynamics of the total system  $S + B$  density matrix is governed by the equations of motion Eqs. (1.7), (1.8) and the Liouvillian superoperator is given by

$$\mathcal{L}(t) = \sum_{j=1}^M \mathcal{L}_j(t) \quad (1.78)$$

where

$$\mathcal{L}_j(t) = -i [X_j(t) B_j(t), \bullet] \quad (1.79)$$

As in the case of a single bath, our derivation builds on the formal result in Eqs. (1.12), (1.13), assuming the factorizing initial condition Eq. (1.10) with the bath initially in the thermal equilibrium state Eq. (1.11):

$$\rho_B = \prod_{j=1}^M \rho_{B,j} \quad (1.80)$$

where

$$\rho_{B,j} = e^{-\beta H_{B0,j}} / Z_j \quad (1.81)$$

Using the above equations Eqs. (1.73), (1.75), (1.78), (1.80) for a setting with multiple baths, we can write Eq. (1.13) as

$$G(t) = \left\langle \overleftarrow{\mathcal{T}} \exp \left( \int_0^t dt' \mathcal{L}(t') \right) \right\rangle_B = \prod_{j=1}^M \left\langle \overleftarrow{\mathcal{T}}_j \exp \left( \int_0^t dt' \mathcal{L}_j(t') \right) \right\rangle_{B,j} = \prod_{j=1}^M G_j(t) \quad (1.82)$$

where the propagator

$$G_j(t) = \left\langle \overleftarrow{\mathcal{T}}_j \exp \left( \int_0^t dt' \mathcal{L}_j(t') \right) \right\rangle_{B,j} \quad (1.83)$$

corresponds to the influence of a bath  $j$  on the system. As before,  $\rho_B$  is Gaussian in bath operators  $q_{k,j}$  and  $p_{k,j}$ , and so we can write the propagator Eq. (1.82) as a cumulant expansion that terminates after only two terms, similarly to Eq. (1.50) in Sec. 1.1.3. Repeating the same steps as in Eqs. (1.50)-(1.54) of Sec. 1.1.3 for a single bath, we obtain the equation

$$\rho_S(t) = \prod_{j=1}^M e^{\phi(X_a^{(j)}, X_c^{(j)})} \rho_S(0) \quad (1.84)$$

analogous to Eq. (1.63). Here, we have expressed the time evolution of the reduced density matrix  $\rho_S(t)$  using the influence phase  $\phi(X_a^{(j)}, X_c^{(j)})$  given by Eq. (1.54), as before. The commutator and anticommutator superoperators are now defined as  $X_c^{(j)} = [X_j, \bullet]$ ,  $X_a^{(j)} = \{X_j, \bullet\}$ , in terms of the system operator  $X_j$  corresponding to a particle  $j$  that couples to a bath  $j$ .

We choose again to work in the basis where the system operators  $X_j$  are diagonal for each  $j$  – using the basis states  $|x\rangle = |x^{(1)}, x^{(2)}, \dots, x^{(M)}\rangle$  that are the eigenstates of  $X_j$ . Here, the coordinate  $x^{(j)} = \langle x(t) | X_j | x(t) \rangle$  of each particle  $j$  in the system is an eigenvalue of the system operator  $X_j$  at time  $t$  during the propagation. The system coordinates are then measured by a set of  $M$  eigenvalues  $x = \{x^{(j)}\}_1^M$ . Proceeding along the same lines as in Sec. 1.1.3, we will next express Eq. (1.84) as a Feynman path integral for propagation along the Keldysh-Schwinger contour. Similarly to Sec. 1.1.3, we write Eq. (1.84) in the basis of the final points  $x_N = \{x_N^{(j)}\}_1^M$ ,  $x'_N = \{x_N'^{(j)}\}_1^M$  of time evolution after time  $t$ , and insert identity resolutions  $I = \int \left[ \prod_{j=1}^M Dx^{(j)} \right] |x\rangle \langle x|$ ,  $I = \int \left[ \prod_{j=1}^M Dx^{(j)'} \right] |x'\rangle \langle x'|$  for the forward and backward contours:

$$\begin{aligned} \rho_S(x_N, x'_N, t) &= \int \prod_{j=1}^M Dx^{(j)} \int \prod_{j=1}^M Dx^{(j)'} \\ &\quad \langle x_N(t) | \left( \prod_{j=1}^M e^{\phi(X_a^{(j)}, X_c^{(j)})} |x\rangle \langle x'| \right) |x'_N(t)\rangle \rho_S(x, x', 0) \end{aligned} \quad (1.85)$$

We note that Eq. (1.85) has the same form as Eq. (1.65), since the entity  $\prod_{j=1}^M e^{\phi(X_a^{(j)}, X_c^{(j)})}$  straightforwardly factorizes into  $e^{\phi(X_a^{(j)}, X_c^{(j)})}$  objects for each individual  $j$ . Making use of this analogy, we follow the same steps as in Eq. (1.65)-(1.72) of Sec. 1.1.3 to obtain

$$\begin{aligned} \rho_S(x_N, x'_N, t) &= \int \prod_{j=1}^M Dx^{(j)} \int \prod_{j=1}^M Dx^{(j)'} \\ &\quad \langle x_N | \left( e^{t\mathcal{L}_S} |x\rangle \langle x'| \right) |x'_N\rangle \prod_{j=1}^M I_j(x^{(j)}, x^{(j)'}) \rho_S(x, x', 0) \end{aligned} \quad (1.86)$$

Eq. (1.86) is the path integral representation of the time-evolved reduced density matrix  $\rho_S(t)$  (now in the Schrödinger picture) which corresponds to integrating over

the contributions of all the reduced system trajectories  $x = \{x^{(j)}\}_1^M, x' = \{x^{(j)'}\}_1^M$ . Here, the interaction between the system and a bath  $j$  enters through the influence functional

$$I_j(x^{(j)}, x^{(j)'}) = e^{\phi(x^{(j)} + x^{(j)'}, x^{(j)} - x^{(j)'})} \quad (1.87)$$

We note that since the different baths  $j \in [1, M]$  are independent, the corresponding influence functionals  $I_j(x^{(j)}, x^{(j)'})$  in Eq. (1.86) are also independent. Therefore, in the presence of multiple independent baths and the system-bath interaction terms Eq. (1.76) in the Hamiltonian Eq. (1.42), the system-bath coupling effects add up extensively and do not lead to any cross terms between different baths. In Chapter 6, the additive nature of the system-bath interaction will allow us to treat the non-Markovian effects experienced by each particle  $j$  coupled to its own bath  $j$  independently, thus greatly simplifying the problem.

## 1.2 Driven dissipative coupled cavity arrays

### 1.2.1 Quantum simulation with photonic systems

Strongly correlated quantum matter is one frontier of research in condensed matter physics. Quantum many body systems with strong correlations are extremely difficult to solve using analytical approximations or numerical simulations on classical computers due to the exponentially large number of degrees of freedom [50, 51]. The experimental observation of quantum phenomena in such systems and controlling their individual components is equally challenging due to the small length, time, energy, or temperature scales involved [51]. Quantum simulation offers a promising alternative: building an artificial structure with well-controlled parameters that mimics a quantum many-body system and its model Hamiltonian [50–52]. This idea has become a reality with cold atoms in optical lattices [53, 54], trapped ions [21] and other architectures [55] where quantum optical techniques enable a fine tuning of particle arrangements and their interactions, as well as a measurement of the microscopic properties. Such quantum simulators have opened a new direction for solving a variety of problems in physics, including quantum phase transitions, high temperature superconductivity, frustrated magnetism, computing molecular energy levels, and even the high energy physics phenomena [15, 21, 55, 56].

More recently, the astonishing experimental progress in the fabrication of superconducting circuits [15], photonic crystals [57, 58] and microcavities [24, 59] has brought a surge of interest in building photonic quantum simulators where the excitations responsible for collective phenomena have a strong photon character. Since the number of photons is generally not conserved, photonic quantum simulators are inherently open systems subject to photon loss, and serve as an excellent platform for exploring nonequilibrium physics. Therefore, by creating a synthetic quantum matter based on photons we can access different physics than that typically studied in experiments with cold atoms or trapped ions [15, 53, 54, 60]. The understanding of such collective nonequilibrium physics is vital to the ongoing developments of nanoscale and mesoscale quantum technology discussed in the introduction, and is a major driving force behind the research of nonequilibrium quantum matter. From



a more fundamental perspective, many condensed matter systems equilibrate with a cold environment on short timescales, naturally preparing a many-body system near its ground state. While the equilibrium quantum matter has been studied for many decades, our understanding of the transient dissipative dynamics – the path to strongly correlated states observed in equilibrium – is far more limited. The upcoming generation of nonequilibrium quantum simulators will enable us to address this question.

One class of photonic quantum simulators is driven dissipative lattices of coupled nonlinear optical cavities, which will be our main focus in the first part of the thesis. The key idea here is using cavity quantum electrodynamics (cavity QED) to trap photons in optical cavities and making them interact with nonlinear optical elements, to generate polaritonic light-matter excitations with effective interactions between them [61–63]. Due to their optical nature, these systems experience the dissipation of photons into their surroundings, typically an external heat bath formed by a continuum of electromagnetic modes. In experiments, these photon losses are compensated by an optical pump, usually a coherent laser drive. The competition between drive and dissipation eventually brings the system to a nonequilibrium steady state rather than its ground state. The driven dissipative many body physics poses numerous questions about the interplay between coherent and dissipative dynamics, the nonequilibrium phase diagrams and engineered phases of matter, the dissipative phase transitions and universality out of equilibrium, and many others. In fact, recent theoretical research has demonstrated that the nonequilibrium states of coupled cavity systems can exhibit an even richer collective behaviour than their thermal equilibrium counterparts [44, 64–76].

### 1.2.2 From cavity QED to coupled cavity arrays

One possible building block of coupled cavity arrays is an optical cavity containing a confined electromagnetic field and a two-level atom, which interact via series of photon absorption and emission events, well approximated by dipole coupling [60, 77]. We can describe such a system by Jaynes-Cummings model (JCM) [60]:

$$H_{JC} = \omega_c a^\dagger a + \frac{\epsilon}{2} \sigma^z + g (a \sigma^+ + a^\dagger \sigma^-) \quad (1.88)$$

where  $a, a^\dagger$  are creation/annihilation operators of the cavity photons with frequency  $\omega_c$ ;  $\sigma^z, \sigma^\pm$  are Pauli operators of the two-level atom with transition frequency  $\epsilon$ ;  $g$  is the light-atom coupling strength - the rate of coherent exchange of excitations between the atom and the electromagnetic field (i.e. Rabi oscillations). The JCM Hamiltonian assumes the rotating-wave approximation, which neglects the fast-rotating, off-resonant transition terms. This approximation is valid as long as the light-matter coupling strength is  $g \ll \omega_c, \epsilon$  (i.e. we are safely away from the ultrastrong coupling regime where  $g \sim \omega_c, \epsilon$  and where the off-resonant terms play a crucial role) which will always be the case in the systems we study. The light-atom coupling leads to the hybridized atom and photon field eigenstates of JCM Eq. 1.88, often called dressed states [77]. The elementary excitations are no longer photonic and atomic excitations, but rather polariton quasiparticles. Polaritonic states in a

JCM system thus consist of an empty ground state  $|0, g\rangle$  with energy  $E_0 = 0$  (i.e. when no photons are present in the cavity and the atom is in its ground state), followed by a ladder of dressed states [60]:

$$|n+\rangle = \sin(\theta_n) |n, g\rangle + \cos(\theta_n) |n-1, e\rangle \quad (1.89)$$

$$|n-\rangle = \cos(\theta_n) |n, g\rangle - \sin(\theta_n) |n-1, e\rangle$$

with the corresponding energy levels

$$E_n^{(\pm)} = \omega_c n \pm \Omega_n \quad (1.90)$$

for a number of photons  $n$  in the cavity. The superposition coefficients are:

$$\sin(\theta_n), \cos(\theta_n) = \sqrt{\frac{1}{2} \left( 1 \pm \frac{\delta}{2\Omega_n} \right)} \quad (1.91)$$

with Rabi frequency:

$$\Omega_n = \sqrt{g^2 n + (\delta/2)^2} \quad (1.92)$$

and the atom-cavity detuning  $\delta = \epsilon - \omega_c$ .

We can form a many body lattice of quantum optical systems by taking a number of JCM systems and coupling them together via coherent photon tunnelling at rate  $J$  between adjacent cavities. The result is a coupled cavity array described by the Jaynes-Cummings-Hubbard model (JCHM) [60]:

$$H_{JCHM} = \sum_i H_{JC}^i + \sum_{\langle i,j \rangle} J \left( a_i^\dagger a_j + \text{H.c.} \right) \quad (1.93)$$

As we have already seen, coupled cavity arrays are inherently open systems. Unlike in atomic ensembles, the number of photons is not conserved as the coupling to environment/external heat bath introduces and removes photons from the system (hence the chemical potential of photon gas vanishes). In any realistic experimental setting, coupled cavity arrays will experience inevitable photon loss from cavities as well as relaxation of the two level systems due to spontaneous emission. We can incorporate the dissipation effects using the Lindblad master equation for the reduced density matrix  $\rho$  of the coupled cavity system, as introduced in Sec. 1.1.2:

$$\partial_t \rho(t) = -i [H, \rho(t)] + \sum_i \frac{\kappa}{2} \mathcal{D}[a_i] \rho(t) + \sum_i \frac{\gamma}{2} \mathcal{D}[\sigma_i^-] \rho(t) \quad (1.94)$$

with dissipation and relaxation rates  $\kappa$  and  $\gamma$  respectively. To counteract the dissipation, one can use optical drive that injects new photons into the system. For example, applying a simple laser drive will add a new term to the system Hamiltonian:  $H \rightarrow H + H_D$ , where

$$H_D = \frac{1}{2} \sum_i \left( \Omega_i e^{i\omega_D t} a_i + \text{H.c.} \right) \quad (1.95)$$

with the driving frequency  $\omega_D$  and the amplitude  $\Omega_i$  at site  $i$  of the cavity array.

### 1.2.3 Photon blockade

At first sight, the idea of studying many body physics with photons might appear somewhat surprising since photons do not interact with each other in free space. We can create effective interactions between photons by coupling them to nonlinear optical emitters, such as two-level systems in JCM cavities. The light-matter coupling leads to the formation of ‘dressed photons’ (polaritons), which experience repulsive interactions with each other, owing to their matter-like component. This effective repulsion arises due to anharmonicity of the polariton energy spectrum, i.e. optical nonlinearity – the energy cost  $U$  of adding the second photon to the cavity  $E_2^{(\pm)} - E_1^{(\pm)}$  relative to the energy cost of adding the first photon  $E_1^{(\pm)} - E_0$ :

$$U = E_2^{(\pm)} - E_1^{(\pm)} - [E_1^{(\pm)} - E_0] \quad (1.96)$$

When the energy cost  $U$  becomes much larger than the drive strength  $\Omega$  and the polariton linewidth  $\delta E$

$$U \gg \Omega, \delta E \quad (1.97)$$

the presence of a single photon in a cavity will inhibit the excitation of the second photon [78, 79]. This is the photon blockade effect, which is the key ingredient in generating strongly correlated photonic states. Creating strong optical nonlinearities on the single photon level, and using them to generate nonclassical photonic states has long been a central goal of quantum optics [80, 81]. However, it was not until the last decade that the photon blockade was truly realized in cavity QED experiments [82–84], due to the technical challenges of creating strong light-matter couplings  $g$  on a single photon level, which must be much larger than a set of characteristics, such as the cavity loss rate, or the power and the bandwidth of a laser being used to drive the system. The observation of photon blockade in cavity QED systems [82–84] has fuelled interest in using them to study many body physics. Nissen et al [64] presented a study demonstrating that photon blockade survives in large (effectively infinite) coupled cavity arrays. More specifically, they observed that photon blockade occurs at small photon hopping  $J$ , but gradually breaks down when  $J$  becomes large, which allows tuning a coupled cavity array between strongly correlated and non-interacting regimes.

### 1.2.4 Experimental realizations and circuit QED

There are various experimental setups that one could use to build systems of optical cavities, including photonic crystal devices with quantum dots [59] and micropillar structures in semiconductor microcavities [85]. However, circuit QED technology using microwave resonators with superconducting qubits stands as the most promising platform for realizing extended coupled cavity arrays with strong nonlinearities [15, 86]. Superconducting circuits offer highly tunable system parameters, and the local properties of individual sites are more accessible compared to the cold atoms in optical lattices [15]. In a circuit QED setup, each JCM cavity is a transmission line resonator capacitively coupled to a superconducting qubit on a microchip. The superconducting qubit acts as a two-level atom, whose energy levels

can be tuned by magnetic flux. Exceptionally strong light-matter couplings can be realized in circuit QED, owing to the large dipole moment of the qubit and the small mode volume of the transmission line resonator; meanwhile, the superconducting gap also helps to maintain a low dissipation [87]. One can then construct a chain of transmission line resonators connected via coupling capacitors that mediate microwave photon tunnelling between adjacent sites. In this setting, the polariton quasiparticles are simply the circuit excitations [60]. Both local and collective properties of coupled-cavity arrays are accessible via correlation functions, transmission signals and optical spectra of the emitted photons [15, 60].

The first circuit QED experiments focused on small coupled cavity systems [80]. A few examples include the demonstration of quantum-limited amplification in a Bose-Hubbard dimer [88], observation of a dissipation-induced quantum phase transition in a Jaynes-Cummings dimer [89], realization of chiral ground state currents in a cavity trimer [90], and engineering of cooling and heating processes in a Bose-Hubbard trimer [91]. More recently, circuit QED arrays have begun to enter the realm of many body physics. In a pioneering study, Fitzpatrick et al [86] have built a circuit QED chain of 72 resonators and qubits, each resonator coupled to its nearest neighbour and its local transmon qubit. They studied the transmission spectrum of this coupled cavity array by feeding microwave photons at one end, and measuring the output field at the other end to identify the resonant modes of this chain. By sweeping the drive power from low to high at a constant frequency, they observed an abrupt dissipative phase transition to a suppressed transmission state, demonstrating the potential of superconducting circuits as photonic simulators of quantum many body physics. In another recent work, Ma et al [36] have utilized superconducting circuits to build a Bose-Hubbard lattice of 8 transmon qubits interacting with microwave photons. This study has realized, for the first time, a photonic Mott insulator stabilized against losses. In particular, they have used a combination of coherent pumping and engineered dissipation to create an environment, which constantly refills the coupled cavity system with photons that order in a strongly correlated state. This work has also examined the thermalization dynamics in the chain near its steady state by observing the propagation of a hole defect in the dissipatively prepared Mott insulator phase. More generally, the recent experimental progress has shown that circuit QED technology is already capable of fitting hundreds of resonators on a single chip [15], while keeping a reasonably low disorder in resonator parameters [92]. While the experiments with coupled cavity arrays are still at their early stage, it is already clear that circuit QED technology has a bright future for realizing quantum simulators and studying many body physics far from equilibrium.

We have started our discussion with JCHM as the most intuitive way of explaining the physics of coupled cavity systems. However, we can equally use a superconducting circuit setup to realize a coupled cavity array described by the Bose-Hubbard model (BHM) [60, 80]:

$$H_{BHM} = \omega_c \sum_i a_i^\dagger a_i - J \sum_{\langle ij \rangle} \left( a_i^\dagger a_j + a_j^\dagger a_i \right) + U \sum_i a_i^\dagger a_i^\dagger a_i a_i \quad (1.98)$$

in terms of a single quasiparticle species formed by, for instance, a superposition of

resonator and qubit excitations. Here,  $a_i^\dagger, a_i$  are creation/annihilation operators of excitations at site  $i$ ;  $\omega_c$  is the local cavity mode frequency;  $J$  is the photon hopping rate between adjacent cavities. Quasiparticles interact via onsite nonlinearities  $U$ . Similarly to JCHM systems, we can include the optical pumping by adding an extra term to the BHM in Eq. (1.98)  $H \rightarrow H + H_D$  where the specific form of  $H_D$  depends on the type of driving being used (for instance, a simple coherent drive in Eq. (1.95)). As before, we can describe the driven dissipative dynamics using Lindblad master equation:

$$\partial_t \rho(t) = -i [H, \rho(t)] + \sum_i \frac{\kappa}{2} \mathcal{D}[a_i] \rho(t) \quad (1.99)$$

where the dissipation arises due to the decay of intracavity excitations at rate  $\kappa$ , caused by the photon loss from cavities.

Let us now briefly describe two examples of BHM implementation using superconducting circuits. One of the basic requirements for a circuit design is the ability to generate strong nonlinearities  $U$ . The essential ingredient of nonlinear elements in circuit QED is the Josephson junction, which behaves as a nonlinear inductor with Josephson energy  $E_J$  [80, 86]. Various superconducting circuits often use transmon qubits as their nonlinear elements: a transmon qubit consists of a Josephson junction connected in parallel with a metal capacitor with charging energy  $E_C$ . As a result, transmons can be modelled as nonlinear oscillators whose nonlinearity is conditioned by a large  $E_J/E_C$  ratio [80, 86].

Ref. [36] have realized BHM by constructing an array of transmon qubits connected to microwave resonators, with each transmon representing a single site of a 1D lattice. Here, the low-lying transmon levels behave as an anharmonic resonator  $H_0 = P_n (\omega_c a^\dagger a + U a^\dagger a^\dagger a a) P_n^\dagger$  with frequency  $\omega_c$  and nonlinearity  $U$  [36, 86]. The ladder operators  $a^\dagger, a$  create and annihilate transmon excitations, and projectors  $P_n$  truncate the transmon Hilbert space to  $n$  levels confined within transmon's potential well. Thus, transmon anharmonicity creates a nonlinear Hubbard interaction  $U$  between the circuit excitations. The excitation of the lattice sites (transmons) is achieved by driving them with microwave photons via a separate transmission line and a set of resonators connected to the transmons. The transmon excitation level then corresponds to the occupation on a given lattice site, and the leading dissipation process is caused by the transmons emitting microwave photons into an external electromagnetic bath. The neighbouring transmons are capacitively coupled to each other, producing a constant nearest-neighbour tunnelling  $J$  of microwave photons with the tunnelling rate set by the capacitance between the adjacent transmons. In this realization, the lattice (transmon) excitations are effectively described by the BHM in Eq. (1.98). Ref. [87] took a different approach and proposed a superconducting circuit setup comprising an array of coplanar waveguide resonators. The nonlinearity  $U$  in each resonator is generated by inserting a Josephson junction (or a dc-SQUID) into its central conductor, at the location of a current node of the bare resonator. Each resonator represents a lattice site, and the capacitive coupling between the resonators enables the photon tunnelling  $J$  between adjacent lattice sites. All resonators are also coupled to the input and output lines. Normally, one would expect that hybridization between the resonator and nonlinear circuit

element modes will lead to a model with two species of elementary excitations, similarly to Ref. [93]. Given a very strong coupling between resonators and their Josephson junctions (or dc-SQUIDs) in the proposal by Ref. [87], the normal mode splitting inside a resonator becomes so large that the mixing between their excitations is negligible [80, 87]. In this limit, one can effectively describe each resonator in terms of the excitations in the lower polariton mode only, leading to the Hamiltonian Eq. (1.98) for a single excitation species, and a single dissipation channel in the master equation Eq. (1.99) corresponding to the decay of the lower polaritons.

Although the Hubbard and JCM nonlinearities play a similar role in both models, they become very different for large numbers of intra-cavity excitations [67], and thus BHM Hamiltonian does not map onto JCHM Hamiltonian [67]. Nevertheless, both models often exhibit analogous phases of strongly-interacting polaritons: an inherent feature of both JCHM and BHM is the competition between the photon hopping  $J$  and the on-site repulsive interactions mediated by optical nonlinearity  $U$  [67]. The photon hopping  $J$  attempts to delocalize polaritons over the array, while the repulsive nonlinear interactions try to enforce a localization of polaritons at their sites. A dominant nonlinearity induces photon blockade in both BHM and JCHM.

### 1.2.5 Review of theoretical results: collective behaviour in coupled cavity arrays

The first theoretical studies of coupled cavity arrays have addressed the paradigmatic superfluid - Mott insulator (SF-MI) phase transition under equilibrium conditions [61–63, 94–98], which is a powerful illustration of the localization-delocalization competition between the kinetic  $J$  term and the repulsive  $U$  term. Above some critical hopping rate  $J > J_{\text{critical}}$ , the hopping dominates and polaritons are delocalized over the array, while in MI phase  $J < J_{\text{critical}}$  the repulsion dominates and polaritons are localized, inhibiting the double occupancy of any site (at commensurate filling). In a driven-dissipative system, however, the drive breaks the  $U(1)$  symmetry of either JCHM or BHM and we no longer observe the equilibrium SF-MI transition: instead there is a smooth crossover from the weak hopping regime with photon blockade to the strong hopping regime where a coherent state forms [64], [93], [99].

One fascinating manifestation of photon blockade is polariton crystallization and formation of solid phases in coupled cavity arrays. Hartmann [68] studied the steady state of a Bose-Hubbard coupled cavity array (described by Eq. (1.98)) with dissipation and coherent drive. In this setup, lasers driving adjacent cavities have a phase difference of  $\pi/2$  that induces a flow of polaritons in the system. In the regime of strong nonlinearities, the interplay between polariton flow and nonlinearity  $U$  results in a steady state where polaritons are crystallized into dimers, which flow around the array [68]. Similar results were reported for JCHM lattices [67]. Polaritons can form an even more pronounced crystalline structure in 1D and 2D lattices, where the neighbouring cavities in a Bose-Hubbard array are coupled via additional nonlinear elements [69, 70] and polaritons in adjacent cavities interact via cross-Kerr nonlinearities. Here, a sufficiently strong nonlinearity leads

to the formation of a crystalline phase: a checkerboard pattern in polariton density. As photon hopping  $J$  increases, polaritons become delocalized and the crystalline phase is replaced by a uniform uncorrelated phase. The polariton crystallization and their localization-delocalization behaviour hold the key to the quantum simulation of strongly correlated solid-state matter in photonic systems. The inclusion of cross-Kerr nonlinearities may also allow us to realize systems with longer range interactions [69],[70] in complement to the shorter range models [68].

Photon fermionization is another effect in the strongly-correlated photon regime [72]. For effectively infinite Kerr nonlinearities  $U/J \rightarrow \infty$  (the impenetrable boson limit), we can transform a bosonic many-body wavefunction into an equivalent fermionic wavefunction using the Bose-Fermi mapping [100], [101]. Polaritons then form a Tonks-Girardeau gas of fermions. Notably, the transformation preserves the total energy and momentum of the bosonic state, but the momentum distribution of the fermionic states does not correspond to the momenta of the original bosonic single-particle states [72]. Therefore, the hard-core boson interaction due to photon blockade can simulate fermionic statistics, where no two particles can occupy the same state. The ability to simulate fermionic statistics has further consequences. Bardyn and Imamoglu [71] proposed a parametric pump-like scheme (instead of the usual coherent drives), to inject paired photons into a BHM array in its impenetrable boson limit. The scheme generates a p-wave pairing of fermionized photons, which simulate Majorana-like modes in the steady state.

In the regime of strong nonlinearities  $U \gg J$ , photon blockade reduces the effective polariton Hilbert space to that of spin-1/2 particles [62], [71]. The presence/absence of a polariton in a cavity mimics the “up/down” states of a spin particle, and coupled cavity arrays then emulate spin chain Hamiltonians [62]. For instance, one can realize transverse field anisotropic XY model, transverse field Ising model [62], or even high-spin Heisenberg models [102] where photon tunnelling mediates the spin-spin coupling [60].

The driven-dissipative nature of coupled cavity arrays can lead to a range of other genuinely nonequilibrium phenomena. For instance, Rabi-Hubbard model realized using a Raman-pumping scheme [103] exhibits steady-states with ferroelectric, antiferroelectric and incommensurate orders, distinct from the equilibrium setting [75]. Here, the incommensurate order implies that the lattice periodicity and the spin correlation periodicity occur at irrational ratios. Another peculiar feature of open quantum systems is the oscillating steady states, also known as limit cycles. Even in the steady-state, various observables, such as correlation functions or magnetization, oscillate in time [75] [104], [70], [105]. The onset of a limit cycle can occur when a pair of eigenvalues (with nonzero imaginary parts) of master equation become simultaneously unstable, which triggers an oscillatory instability.

### 1.2.6 Theoretical methods

In contrast to the traditional condensed matter problems in equilibrium, quantum optical many-body systems are subject to drive and dissipation, and are governed by the Lindblad master equation. Theoretical description of the nonequilibrium physics and strong correlations in coupled cavity arrays inevitably requires new

analytical and numerical tools. The early studies of driven dissipative systems have resorted to the mean field based analysis, which ignores quantum fluctuations present in the system [64, 69, 70, 73, 106–109].

Various methods, aiming to go beyond the mean field theory, have been developed and we will discuss some examples below. One of them is the variational ansatz technique [110], which proceeds by minimizing a suitable norm of the master equation to find the approximation for the steady state density matrix. The exact variational calculation, in general, faces exponential scaling with the system size. Nonetheless, instead of requiring the exact solution, one can obtain the upper bound to the norm only, reducing the computational complexity of the problem. Although highly versatile in principle, the performance of this method is strongly dependent on the choice of the variational state ansatz and the norm, and is limited by the known trade-offs between the computability and formal suitability of the norm [110, 111]. Another method, Cluster Mean Field Theory [76], divides the system into clusters, and solves for the steady state treating interactions within a cluster exactly and those between adjacent clusters – on the mean field level. While the method treats the short-range correlations much more accurately compared to the mean field theory, its ability to capture the long-range correlations remains very limited. The accuracy can, nonetheless, be improved by using large cluster sizes attainable when Cluster Mean Field Theory is interfaced with a quasi-exact method for treating intra-cluster interactions, e.g. matrix product state or quantum trajectory simulations in 1D.

The quantum trajectory technique is a widely used stochastic approach for solving master equations in quantum optics, which has also been applied to driven dissipative many body systems [111, 112]. The central idea is to write the initial density matrix as a statistical ensemble of  $M$  pure state wavefunctions. One then propagates the individual wavefunctions in time under a non-Hermitian effective Hamiltonian modified by the dissipative terms of the Lindblad master equation. The wavefunctions evolve independently from each other, and each wavefunction traverses a path in Hilbert space over time, known as a quantum trajectory. Since we evolve the individual trajectories, it significantly reduces the memory storage requirements compared to the time evolution of the full density matrix. Observables can be calculated at different times as an average over the entire ensemble of the stochastically propagated trajectories, and  $M \sim O(10^3)$  is usually needed to ensure low statistical errors. However, in most cases, the quantum trajectory method can only simulate relatively small many-body systems of up to  $N = 20 - 30$  particles [111, 112].

Tensor networks is yet another class of computational techniques capable of simulating driven dissipative many-body systems. Matrix product states (MPS) is a one dimensional tensor network ansatz, which has recently been extended to the mixed state problems [40–44]. In particular, MPS has enabled quasi-exact simulations of both the steady states and time evolution governed by the Lindblad master equation in 1D, while fully accounting for quantum correlations. The MPS algorithms for open quantum systems fall into two main categories. The first one performs a direct time evolution of a mixed state density matrix using a Lindblad propagator [40, 43, 44], while the second category implements a global variational



search targetting the null eigenstate of either the Liouvillian  $\mathcal{L}$  [42] or a Hermitian positive semidefinite object  $\mathcal{L}^\dagger \mathcal{L}$  [41]. Importantly, MPS simulations can reach large lattice sizes of  $N = O(10^2)$  sites and even the thermodynamic limit [40–44, 68, 75, 76, 113–115]. The generality of MPS methods and their ability to simulate truly large many-body problems both make MPS a particularly appealing choice for studying one dimensional coupled cavity arrays. The extension of two-dimensional tensor networks to driven dissipative systems remains a much more challenging problem, and will be explored in detail in Chapter 4.

Other promising developments for open quantum systems with Lindblad dissipation that we would like to mention include corner-space renormalization technique [116, 117], self-consistent projection operator theory [118, 119] and Keldysh field theory [120–122]. We will present a more detailed discussion of computational methods for two-dimensional coupled cavity systems in Chapter 4.

### 1.3 Non-Markovian dynamics

In the previous section we have focused on quantum optical systems that interacted with their environment via emission and absorption of photons. The system-environment interaction was weak, and the environment itself was an unstructured continuum of electromagnetic modes, which conditioned the system dynamics to be Markovian and independent of its past. This convenient picture is no longer true for strong couplings and general structured environments. The excitations that system has induced in its environment then do not decay away immediately, and can flow back into the system in the course of its time evolution. Therefore, the information that has once entered the environment from the system is not forgotten and can return to the system to influence its dynamics at later times. This implies that time evolution of the system at a given instant depends not only on its current state, but also on the history of its past states. This type of dynamics is called non-Markovian since it cannot be described by a Markov chain anymore, and we need different modelling approaches that account for the memory effects. To picture this more clearly, one can consider the following example. If a system simply emits excitations into a structureless continuum of modes, its dynamics can be safely approximated as Markovian because the excitations are irretrievably lost and never return to the system. On the other hand, if a system periodically exchanges a single excitation with the bath, the system dynamics becomes non-Markovian. Intuitively, a shorter periodicity implies stronger memory effects.

Non-Markovian behaviour is, in fact, encountered a lot more frequently than the idealised Markovian approximation. It arises in an immense variety of open quantum systems that are a subject of intense experimental and theoretical research in various fields. One major area is the solid state quantum devices whose constituents – such as superconducting circuits [16, 123], semiconductor quantum dots [20, 124], or nanomechanical resonators [18] – are subject to dissipative effects caused by, for instance, thermal vibrations in the surrounding matrix of a solid state chip. Such interaction usually induces decoherence; on the other hand, engineered quantum noise can counteract decoherence, and even be exploited as a tool for

generating robust quantum states [125, 126]. The understanding of and the ability to control the system-environment interactions and the resulting system dynamics is thus vital to the applications of quantum computing and quantum information processing [127, 128]. However, the mechanisms that underpin dissipation are often very intricate due to the complex structure of the solid state environment in which these devices are embedded, and exhibit highly peaked spectra. They can lead to strongly non-Markovian effects in system dynamics, where the memory effects must be accounted for.

In nature, structured environments are ubiquitous in organic and biological molecules where interactions between electronic states and molecular vibrations take place. A particularly intriguing problem is the excitonic energy transport in photosynthetic systems [129–132]. When light is captured by a photosynthetic complex, it creates an electronic excitation which is then transported through a network of chlorophyll molecules to the reaction centre, where it enables the synthesis of energy-rich molecules such as ATP. The crucial part of the process is efficient excitation transfer between different quantum coherent sites. An excitation tunnelling between chlorophyll molecules interacts with a structured phonon bath of the vibrating protein scaffold (as well as the ionic and dipole fluctuations in the surrounding solvent medium) [16, 129]. Although dissipation usually leads to decoherence, it has been shown that coupling between electronic excitations and the noisy vibrational environment actually enhances the transport and even makes it robust against defects [129, 131, 133, 134]. Elucidating the mechanisms behind this noise-assisted transport is a topic of active research. Organic molecules used for light-emitting devices and solar cells provide another example of a non-Markovian system [135, 136]. The strong light-matter coupling and the interactions between electronic states and phonons lead to the formation of organic polariton quasiparticles that exist as a hybridized mixture of electronic, photonic, and phononic modes. The structured phononic environment, again arising due to vibrations of the molecular scaffold, significantly modifies the spectroscopic properties of these organic molecules and induces non-Markovian effects in the dynamics of their polaritonic states [46, 137].

Non-Markovianity is also important in modelling quantum transport phenomena. One example is the macroscopic tunnelling of flux in superconducting circuits, for example in Josephson junction devices (such as SQUID) where it is subject to Ohmic dissipation, arising, e.g. due to a resistor connected in parallel to the junction [138–140]. The relevant questions here are the effects of dissipation on the tunnelling rate, and the conditions when this dissipation destroys the coherent tunnelling in the system. Other examples include the incoherent tunnelling of bistable defects in metals and amorphous systems [141, 142], electron and proton transfer in solvent environments [143], and heat transport in molecular junctions [144].

It is clear that simulating non-Markovian dynamics presents a grand theoretical challenge since one has to handle the history of past states during the time evolution. In the first place, the underlying theory of non-Markovian systems is still in its early stages of development [145, 146]. Aside from the few problems that have exact analytical solutions (e.g. pure dephasing models) [147], a whole range of methods has been proposed [145]. Frequently employed are unitary transformations and

perturbative expansions. One example involves polaron master equations [148–150]. These techniques exploit the unitary polaron transformation that transforms the equations of motion into a more optimal basis where one can access regimes with intermediate to strong couplings. However, they produce time-local master equations and their validity is generally restricted to specific parameter regimes. Another example takes the form of diagrammatic perturbative expansions that can be used as a basis of real-time diagrammatic Monte Carlo approaches such as the Inchworm Monte Carlo algorithm [151–153].

The Hierarchical Equations of Motion technique is a prominent non-perturbative method that decomposes the exact non-Markovian equations of motion into a set of linear equations of motion that can be solved numerically [154]. Such hierarchical decomposition is advantageous as it allows one to compute the reduced density matrix of the system while including all orders of the system-environment couplings, and it is not constrained by approximations used to derive master equations. This makes the approach well-suited for simulating strong coupling regimes. It also offers a systematic way of truncating the hierarchy of equations under certain conditions, and high performance parallel software packages already exist [155]. The hierarchical expansion method, however, requires specific assumptions about bath density of states and is severely limited in scope to specific cases: for instance, it is known to work well at higher temperatures and for Drude-Lorentz or Debye spectral densities but faces difficulties in most other scenarios [153, 155].

Some other non-perturbative approaches proceed by incorporating a part of the environment within the Hilbert space of the system [45, 46, 156, 157]. One of them is the Reaction Coordinate Mapping technique that includes the collective coordinate of the environment into the system Hamiltonian [157]. Once the resonant modes of the environment have been transferred to the system, the spectrum of the remaining environment is unstructured and Markovian. Hence, one has reduced the problem to solving a Markovian master equation. This technique performs well when environment has very few resonant modes, and notably allows one to derive an analytical form of master equation for Drude-Lorentz density of states. However, its computational cost scales exponentially with the number of resonant modes, which greatly limits the applicability. A promising alternative strategy has been proposed by [45, 46, 158]. It uses the orthogonal polynomial transformation to map the Hamiltonian of a single impurity coupled to a bath onto a 1D chain with the nearest-neighbour interactions [159, 160]. The subsequent studies [45, 46, 158] have extended this approach to multipartite open quantum systems with multiple environments, by using tree tensor network states [161] to represent a wavefunction comprising the electronic states of the system and a large number of vibrational modes of the environments. One then evolves the wavefunction using the time-dependent variational principle [162]. This method offers a dramatic improvement of the idea behind the reaction coordinate approach and enables an efficient treatment of the system-environment interactions. On the other hand, it assumes specifically a vibrational bath and relies on the ability of a large but finite number of modes to approximate the full environment. Since capturing the environment already requires a large tensor network, the method is also difficult to apply to many body systems with a reasonably large number of molecules or lattice sites.

Yet another non-perturbative method simulates non-Markovian dynamics by propagating an augmented density tensor [47, 163, 164]. In essence this means augmenting the Hilbert space by recording the history of past states of the system. Unlike in Markovian dynamics, quantum states at different points of time can be highly correlated and therefore they are not separable. Instead, the time-evolved system is represented by an object known as the augmented density tensor that contains information about the system states at different instances during the time evolution up to some memory cutoff time at a sufficiently distant point in the past. This memory cutoff is set by the environment correlation time. The numerical algorithm derives from the Feynman-Vernon influence functional formalism [47] described in Sec. 1.1.3 and is called a Quasi-adiabatic propagator path integral method (QUAPI). As one might expect, the size of the augmented density tensor scales exponentially with the environment memory time and quickly becomes computationally unmanageable.

A bigger picture emerges from this overview: while powerful non-Markovian techniques exist, most of them are restricted to isolated special cases of application. Many of these techniques assume specific types of environment and specific parameter regimes, or suffer from a prohibitive scaling of their computational cost and memory requirements. Clearly missing is a more general framework that would enable us to study the general principles that underpin open quantum systems interacting with complex environments. One method that deserves a special mention here is QUAPI. It does not rely on any particularly restrictive assumptions, other than those already discussed in Sec. 1.1.3 while introducing the influence functional formalism – i.e. it is not restricted to specific parameter regimes and is basically applicable to baths with arbitrary spectral densities. The broad applicability of QUAPI is a significant advantage over many other numerical techniques discussed here. In Chapters 5 and 6 of this thesis, we will show how QUAPI can be reformulated as a tensor network that one may compress using standard matrix product state techniques, thereby reducing the scaling from exponential to low-order polynomial.

### 1.3.1 The spin-boson model

In this subsection we will introduce the spin-boson model (SBM), which is a paradigmatic model in the theoretical study of non-Markovian open quantum systems [139, 165]. It describes an N-level system interacting with a bosonic bath of harmonic modes:

$$H = \Omega S_x + \epsilon S_z + S_z \sum_k \left( g_k a_k + g_k^* a_k^\dagger \right) + \sum_k \omega_k a_k^\dagger a_k \quad (1.100)$$

where  $S^{x,z}$  are spin operators representing the N-level system,  $\Omega$  is the coherent tunnelling amplitude between the system eigenstates with energy splitting  $\epsilon$ ,  $\omega_k$  is the frequency and  $a_k^\dagger, a_k$  are the creation/annihilation operators of the  $k$ 'th bath mode, which couples to the system with strength  $g_k$ . The bosonic bath is fully characterized by the spectral density

$$J(\omega) = \sum_k |g_k|^2 \delta(\omega - \omega_k) \quad (1.101)$$

We have already met this definition of bath density of states in Eq. (1.60) of Sec. 1.1.3 when deriving the bath autocorrelation function Eq. (1.62). The specific form of Eq. (1.101) depends on the details of system-bath coupling. SBM is often a good description of quantum impurity problems. For example, one frequently deals with a nanoscale quantum system embedded in a crystalline lattice, which behaves as an impurity and couples to some phonon modes of the lattice much more strongly than others. This interaction shapes the spectral density  $J(\omega)$  of the bath such that it is strongly peaked at the frequencies of these modes. One can also interpret this as a response of the bath to the dynamical perturbation by the system. While the structure of  $J(\omega)$  can be highly complex, it is often possible to find a simplified phenomenological form that captures the relevant physics. For large macroscopic baths with a continuum of modes, a widely used form that describes various types of the system-bath interaction and the low-energy behaviour of the bath spectrum is

$$J(\omega) = 2\alpha\omega^\nu\omega_c^{1-\nu}e^{-\omega/\omega_c} \quad (1.102)$$

where  $\alpha$  is the system-bath coupling strength, and  $\omega_c$  is the cutoff frequency that sets the maximum energy scale in the system as well as the timescale  $\tau_B \sim 1/\omega_c$  for the decay of bath correlations. The exponential factor parameterized by  $\omega_c$  provides a soft cutoff for high energy modes to ensure that  $J(\omega)$  does not diverge at high frequencies. The parameter  $\nu$  sets the weight of contribution from low-energy modes to the system-bath interaction, and divides the behaviour of Eq. (1.102) into three regimes. The  $\nu = 1$  case is the Ohmic dissipation where the bath has a linear spectrum  $J(\omega) \sim \omega$ . In classical systems, the Ohmic dissipation occurs when the damping is linear in the first derivative of the oscillating quantity, e.g. when the drag force is proportional to the velocity of mechanical oscillator, or the resistance term is proportional to the electrical current in a circuit. The  $\nu < 1$  and  $\nu > 1$  cases correspond to Subohmic and Superohmic regimes respectively.

To gain some insight into SBM physics, let us consider a simple example of a particle tunnelling between two quantum wells, assuming an initial state localised in one well – a scenario captured by spin-1/2 SBM coupled to an Ohmic bath. Let us imagine for a moment that there is no interaction with the environment. In this idealised setting, the particle undergoes coherent oscillations between the lowest energy levels of the two wells. In a more realistic setting, the particle will be in contact with a bath that consists of a large number of other particles vibrating as harmonic oscillators. The interaction with the surrounding vibrational modes will now exert a damping force on the particle (for instance, via collisions) as it tries to tunnel from one well to another: it will experience an incoherent dissipation during the tunnelling process. If the interaction becomes too strong, the damping effect of these vibrations will prevent the particle from tunnelling and it will become localized in one of the wells. This phenomenon is called the localization phase transition: the particle goes from a delocalized state between the two wells to a localized state in one of them as the dissipation increases. It is a basic example of a dissipative phase transition, and an example of how interaction with environment can fundamentally change the behaviour of the system.

Although the SBM Hamiltonian Eq. (1.100) appears to be deceptively simple, it finds applications in a vast range of physical problems involving dissipation, and has

been a subject of research for decades [139]. SBM has been used to model various systems ranging from exciton-phonon coupling in organic molecules [131, 132] or dynamics of coupled quantum dots [19], to magnetic flux transport in superconducting circuits [123] or relaxation of dilute impurities in solid state materials [166–168]. One reason behind its success is that SBM can accurately represent various phenomena that involve the relaxation of a quantum system coupled to a bath, and many superficially unrelated systems can be mapped to the form of system-environment interaction in Eq. (1.100) [169]. Solving the Hamiltonian Eq. (1.100) also poses a serious computational challenge owing to the large Hilbert space of the environment – it thus provides a testbed for new numerical methods. We will make use of SBM as our reference system in Chapter 5, and the principles introduced here will underpin much of our work on modelling non-Markovian dynamics in Chapters 5 and 6.

# Chapter 2

## Tensor networks

In this chapter, we will describe tensor network techniques that form the basis of the research work in this thesis. Sec. 2.1 will introduce the reader to the fundamentals: the diagrammatic language of tensor networks, as well as the concepts of entanglement and the area law. In the following Sec. 2.2 we discuss a highly successful class of one-dimensional tensor networks: matrix product states (MPS) and the extension of the MPS algorithms to open quantum systems. Finally, Sec. 2.3 presents a more challenging topic of two-dimensional tensor networks, namely the projected entangled pair states (PEPS).

### 2.1 Fundamentals

#### 2.1.1 Tensor diagrams

As their name suggests, tensor networks are made of a large number of connected tensors on which we perform various mathematical operations. Before discussing any further details we will introduce the language of tensor network diagrams. As we will soon discover, tensor calculations lead to extremely cumbersome mathematical expressions that involve a large number of coefficients and sums over multiple indices. Instead we use a graphical representation of tensor networks which allows us to perform complex mathematical calculations diagrammatically and to visualize sophisticated computational algorithms, or even the structure of entanglement in the system. Tensor network diagrams thus play a role similar to that of Feynman diagrams in quantum field theory.

A tensor is a multidimensional array of complex numbers and the number of array indices is called a tensor rank. We will represent a tensor by an object such as a circle, a square or a triangle, and the tensor indices – by legs projecting from it. Fig. 2.1(a-d) shows a few examples: rank-0 tensor  $V$  is a scalar and has no legs; rank-1 tensor  $A_i$  is a vector with one index, rank-2 tensor  $B_{ij}$  is a matrix with two indices, rank-3 tensor  $C_{ijk}$  has three indices, and so on. Fig. 2.1(e-g) illustrates some simple calculations in this diagrammatic representation: matrix multiplication  $C_{ik} = A_{ij}B_{jk}$ , matrix multiplication followed by trace  $v = \text{Tr}(A_{ij}B_{jk}) = A_{ij}B_{ji}$ , and contraction of rank-2 and rank-3 tensors  $C_{ijl} = A_{ijk}B_{kl}$ . By analogy to Einstein summation convention, the connected legs correspond to indices shared by

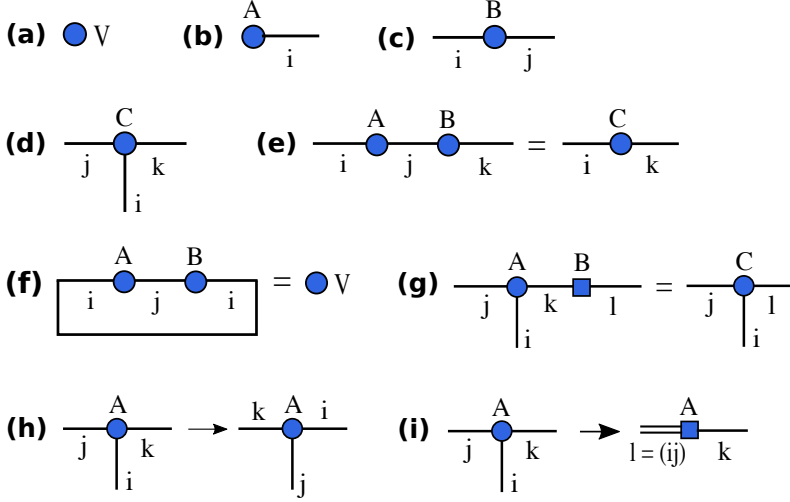


Figure 2.1: Tensor network diagrams. (a) Scalar  $V$ ; (b) Vector  $A_i$ ; (c) Matrix  $B_{ij}$ ; (d) Rank-3 tensor  $C_{ijk}$ ; (e) Matrix multiplication  $C_{ik} = A_{ij}B_{jk}$ ; (f) Trace  $v = \text{Tr}(A_{ij}B_{jk})$ ; (g) Tensor contraction  $C_{ijl} = A_{ijk}B_{kl}$ ; (h) Tensor transposition  $A_{ijk} \rightarrow A_{jki}$ ; (i) Merging multiple tensor indices into one  $A_{ijk} \rightarrow A_{(ij),k} = A_{lk}$ .

two tensors that we sum over, while the open legs are indices belonging to only one tensor and are not being summed over. As seen in Fig. 2.1(e-g), tensor contraction produces a new tensor where only the open indices are left uncontracted. Another common tensor operation is the permutation of indices (a higher dimensional analogue of matrix transposition)  $A_{ijk} \rightarrow A_{jki}$  displayed in Fig. 2.1(h), which corresponds merely to relabelling the legs in a diagram. We can also reshape our tensor by combining some of its indices together which also leads to a reduction of the tensor rank:  $A_{ijk} \rightarrow A_{(ij),k} = A_{lk}$ . In the diagrammatic language this means merging the corresponding legs into one, see Fig. 2.1(i). A familiar example here is that of reshaping a matrix into a vector.

A situation that happens often in tensor network calculations is that there are multiple ways of carrying out the same tensor contraction. In general, a contraction involving a number of tensors is always done pairwise: at each step we contract only two tensors at a time. Let us consider the network in Fig. 2.2 where each tensor index has a dimension  $D$ : performing the pairwise contraction steps in order (a) and order (b) yields  $O(D^4)$  and  $O(D^5)$  computational cost scaling respectively. In more sophisticated networks such as Fig. 2.2(c,d), different orders of contraction could yield far more contrasting cost scalings. Fig. 2.2(c,d) illustrates a contraction of two rows of tensors. If each row consists of  $N$  tensors, the contraction (c) scales exponentially as  $O(D^N)$ . Meanwhile, the contraction (d) can be broken down into smaller steps shown in (a) each costing  $O(D^4)$  – and so the overall contraction has a relatively cheap scaling  $O(ND^4)$ . Finding the most efficient order of contractions could thus affect dramatically the practical applicability of an algorithm. Choosing the ‘right’ order could enable us to simulate more complex systems within computational time that is orders of magnitude shorter, while choosing a ‘wrong’ order could render the simulation impossible.

Let us now discuss how one can express a quantum many-body state in the



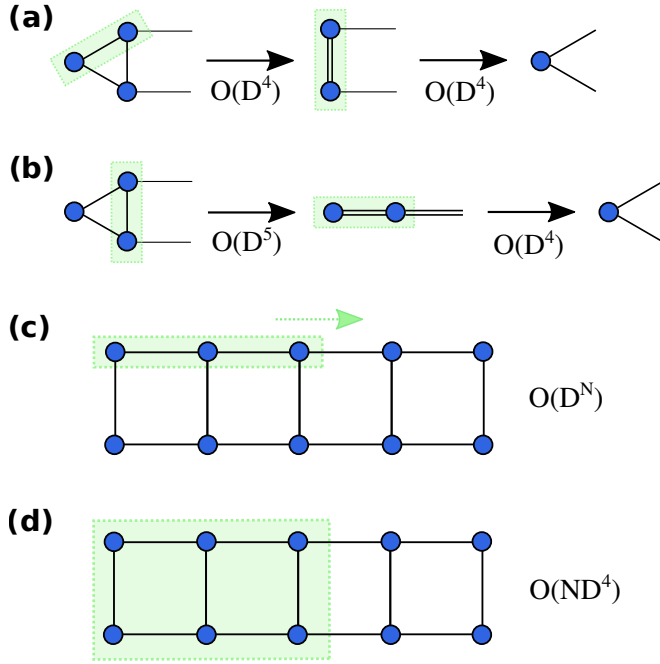


Figure 2.2: Different orders of tensor contraction. The computational cost of contracting the same three tensors in order (a) scales as  $O(D^4)$ , while in order (b) it scales as  $O(D^5)$ . The cost of contracting two rows with  $N$  tensors using order (c) scales exponentially with  $N$ :  $O(D^N)$ , while in order (d) the cost is polynomial:  $O(ND^4)$ .

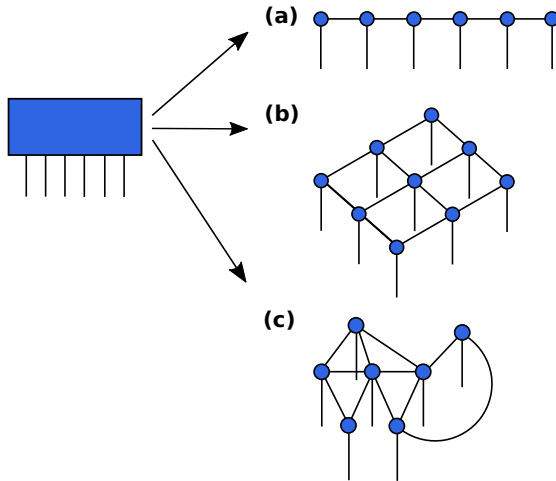


Figure 2.3: The decomposition of a high-rank tensor into a network of low-rank tensors: (a) A 1D tensor network, known as a matrix product state (MPS); (b) A 2D tensor network, known as a projected entangled pair state (PEPS); (c) An arbitrary tensor network.

language of tensor networks. More specifically, consider a generic many-body wavefunction for a system with  $N$  particles where a particle  $n$  has  $d_n$  physical states:

$$|\Psi\rangle = \sum_{k_1, k_2, \dots, k_N} \Psi_{k_1, k_2, \dots, k_N} |k_1, k_2, \dots, k_N\rangle \quad (2.1)$$

For instance, a two-level system will have a Hilbert space with  $d_n = 2$  local basis states, a three-level system will have  $d_n = 3$  local basis states, and so on. The index  $k_n$  runs over all basis states  $1, \dots, d_n$  of a particle  $n$ . A spin-1/2 particle, for example, may have the spin ‘up’ and ‘down’ states as its basis, while a spin-1 particle may have the ‘up’, ‘down’, and ‘zero’ states in its local Hilbert space. The wavefunction coefficient  $\Psi_{k_1, k_2, \dots, k_N}$  contains the full Hilbert space of the many-body system: the number of parameters it needs to store then scales exponentially with the system size  $N$ . For example, if the local Hilbert space dimension  $d_n = d$  for all particles  $n$ , the size of  $\Psi_{k_1, k_2, \dots, k_N}$  scales as  $O(d^N)$ . To illustrate these exponential memory requirements of  $\Psi_{k_1, k_2, \dots, k_N}$ , consider a system with  $N = 1000$  spin-1/2 particles: the total dimension of  $\Psi_{k_1, k_2, \dots, k_N}$  will be  $\sim 2^{1000} \sim 10^{301}$  elements whereas an array of 1 GB can store  $\sim 10^7$  complex numbers. Moreover, if we assume that computation requires only one operation per complex value, and work on a 1 GHz processor, the computation times will be on the order of  $O(10^{292})$  seconds, which is an astronomical scale even compared to  $O(10^{17})$  seconds, the current estimate for the age of the Universe. The consequence of such exponential scaling is that any calculations quickly become impossible for increasing system sizes  $N$ . This problem is commonly known as ‘the curse of dimensionality’.

One can imagine the wavefunction coefficient  $\Psi_{k_1, k_2, \dots, k_N}$  as a rank- $N$  tensor. The main idea behind tensor networks is to decompose the exponentially large tensor  $\Psi_{k_1, k_2, \dots, k_N}$  into a network of smaller rank tensors that is computationally manageable. Tensor network algorithms provide the means of finding such a compressed form of the wavefunction, essentially by discarding the irrelevant parts of its Hilbert space. Tensor networks that result from such decompositions can take different forms shown in Fig. 2.3, depending on the physical system we are studying. A one-dimensional lattice system is often represented by a chain of tensors in Fig. 2.3(a) where each tensor corresponds a spatial lattice site. Tensor networks of this form are known as matrix product states (MPS). Fig. 2.3(b) shows a two-dimensional lattice system represented by a grid of tensors where each tensor, again, represents a lattice site. Such two-dimensional networks are known as projected entangled pair states (PEPS). The Fig. 2.3(c) illustrates a tensor network with an arbitrary structure. We will discuss the specific types of tensor networks in a lot more detail later in this chapter.

### 2.1.2 Entanglement and the area law

So far we have deliberately ignored the principal question: why does the tensor network representation work? The answer lies in the structure of entanglement in quantum many-body states, which we examine below. To understand the properties of entanglement, let us partition our many-body lattice system into a subregion  $A$  and subregion  $B$  as in Fig. 2.4. Mathematically, this is done by Schmidt decompo-

sition (or, equivalently, the singular value decomposition) of the pure state of the full system  $A + B$ :

$$|\Psi\rangle = \sum_{\alpha} \Lambda_{\alpha} |\alpha\rangle_A \otimes |\alpha\rangle_B \quad (2.2)$$

where  $|\alpha\rangle_{A,B}$  are the orthonormal Schmidt bases of subregions  $A$  and  $B$  respectively, and  $\Lambda_{\alpha} \geq 0$  are their corresponding probability amplitudes; for a normalized state  $\sum_{\alpha} \Lambda_{\alpha}^2 = 1$ . We find the reduced density matrix of subregion  $A$  by tracing out the degrees of freedom of  $B$ :

$$\rho_A = \text{Tr}_B (|\Psi\rangle \langle\Psi|) = \sum_{\alpha=1}^D \Lambda_{\alpha}^2 |\alpha\rangle_A \langle\alpha|_A \quad (2.3)$$

which is a mixed-state density matrix defined using the basis of subregion  $A$ . The basis states  $|\alpha\rangle_A$  of  $A$  are the eigenvectors of  $\rho_A$ , the probabilistic weights  $\Lambda_{\alpha}^2$  are its eigenvalues, and we suppose there are  $D$  eigenvalues in total. We can measure the amount of bipartite entanglement between the subregions  $A$  and  $B$  of the pure state  $|\Psi\rangle$  using the von Neumann entanglement entropy:

$$S = -\text{Tr} (\rho_A \log \rho_A) = -\sum_{\alpha=1}^D \Lambda_{\alpha}^2 \log \Lambda_{\alpha}^2 \quad (2.4)$$

This measure is equivalent to counting the number of entangled bits or particles between  $A$  and  $B$  – in other words, the von Neumann entropy quantifies the level of difficulty of simulating a given quantum state on a classical computer. If the subregions  $A$  and  $B$  are completely unentangled, then only one of the Schmidt coefficients is nonzero:  $\Lambda_{\alpha=1} = 1$  for  $\alpha = 1$  and  $\Lambda_{\alpha>1} = 0$  for the rest. In such case, the full system wavefunction Eq. (2.2) is a product state  $|\Psi\rangle = |1\rangle_A \otimes |1\rangle_B$ , and the entanglement entropy Eq. (2.4) is zero. Once  $A$  and  $B$  become entangled, more than one of  $\Lambda_{\alpha}$  coefficients is nonzero:  $|\Psi\rangle$  can no longer be decomposed as a product state, and the entanglement entropy Eq. (2.4) becomes greater than zero  $S > 0$ . A flat entanglement spectrum with all Schmidt coefficients  $\Lambda_{\alpha} = 1/\sqrt{D} \ \forall \alpha$  corresponds to a maximally entangled state – in this case, the von Neumann entropy Eq. (2.4) assumes its largest possible value for a given  $D$ . It is worth noting that the largest possible  $D$  is limited by the smaller Hilbert space dimension of the two subsystems  $A$  and  $B$ . As a result, the bipartition that results in at least one of  $A$  or  $B$  having a small Hilbert space, will yield a small von Neumann entropy even if the entanglement spectrum is flat. This means that a maximally entangled state has a maximum amount of entanglement for a given bipartition of the system. A useful educational example is the GHZ state [39]  $|\Psi\rangle = \frac{1}{\sqrt{2}} (|0\rangle^{\otimes N} + |1\rangle^{\otimes N})$  for a  $1D$  system of  $N$  spin-1/2 particles, where  $|1\rangle$  and  $|0\rangle$  are the spin ‘up’ and ‘down’ states. If we partition a one-dimensional GHZ lattice into a subsystem  $A$  containing a single site at the edge of the lattice and a subsystem  $B$  containing all the remaining sites, we will obtain a maximally entangled state with a flat entanglement spectrum. Yet, this bipartition of a GHZ lattice requires as few as  $D = 2$  Schmidt coefficients due to the small Hilbert space dimension of  $A$ , thus resulting in a small von Neumann entropy. An important question to us in this chapter is the scaling of entanglement

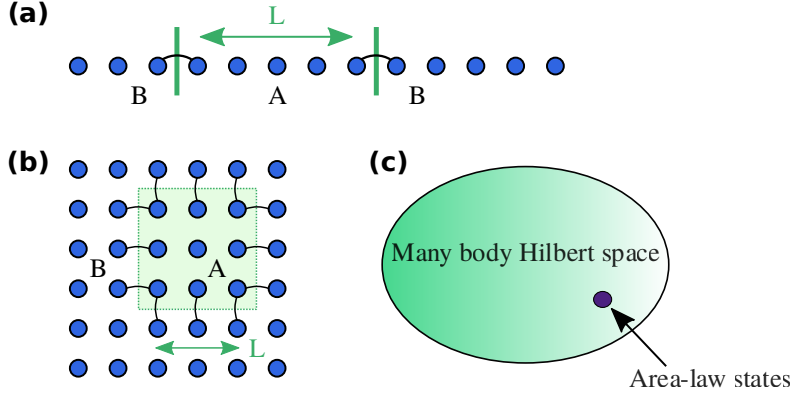


Figure 2.4: The area law in (a) 1D and (b) 2D. Entanglement entropy between subsystems  $A$  and  $B$  scales with the size of the boundary. The black lines indicate local interactions between  $A$  and  $B$  across the boundary, and  $L$  is the size of subregion  $A$ . (c) In many systems, the physical states of interest obey the area law and reside in a tiny corner of the entire Hilbert space.

entropy with the size  $V_A$  of subregion  $A$ . A ‘typical’ quantum state drawn at random from the Hilbert space of the system will have probabilistic weights  $\Lambda_\alpha^2 \approx \frac{1}{2^{V_A}}$ , i.e. it will be a nearly-maximally entangled state. In this case, the entanglement entropy Eq. (2.4) will scale as the volume of the subregion  $A$ :  $S \sim V_A$ . We can then see that the number of Schmidt values scales as  $D \sim e^{V_A}$ , which simply implies that the Hilbert space size of the system scales exponentially with its size: the ‘curse of dimensionality’ problem we encountered at the end of last subsection.

Fortunately, this is not the end of the story. A lot of the many-body systems that arise in various fields of research have local Hamiltonians. The locality usually means that, for example, a Hamiltonian of a lattice system consists of the nearest-neighbour or the next-nearest-neighbour couplings only. The assumption of locality is indeed physically intuitive. For instance, the interactions between electrons in a strongly correlated material, the couplings between magnetic moments, the tunnelling rates between optical cavities in a coupled cavity system or between atoms in an optical lattice all decay with distance: as a result, the correlations for low-energy states of these systems vanish at long distances. This is captured by a vast variety of models such as the fermionic Hubbard model, the Bose-Hubbard model, or the Heisenberg model, to name a few well-known examples, that contain only the local interactions. Such a local Hamiltonian can be decomposed in terms of local few-body Hamiltonians  $H_n$ :

$$H = \sum_{n \in A+B} H_n \quad (2.5)$$

and it will have only  $O(V_A + V_B)$  degrees of freedom, in contrast to the total number of degrees of freedom  $O(e^{V_{A(B)}})$  needed to describe subregion  $A$  ( $B$ ). In Fig. 2.4(a,b) we can see how this locality of a Hamiltonian translates into the entanglement of a quantum state. In a system with local interactions, only interactions across the boundary of  $A$  and  $B$  between e.g. the nearest neighbour or next-nearest-neighbour particles contribute to entanglement entropy Eq. (2.4), simply because the more

distant particles do not interact. The amount of entanglement then scales with the area  $W_A$  of the boundary of  $A$ :  $S = O(W_A)$ . This implies  $S = O(L^{d-1})$  scaling for a  $d$ -dimensional subregion  $A$  with volume  $V_A = L^d$ , as illustrated in Fig. 2.4(a,b), which is commonly known as the area law. Although a rigorous proof of the area law has only been presented for one dimensional systems, there exists a lot of numerical evidence that it is also true in higher dimensions [170–172]. As a consequence, there is a small subset of all quantum states – including the low-energy states and the ground state of a local Hamiltonian – that obey the area law scaling instead of the usual volume scaling [173]. These low-entanglement states are the states relevant to most physical problems, and they live in a tiny corner of the exponentially large Hilbert space, as illustrated in Fig. 2.4(c). Therefore, we need an efficient way to target the physical corner of the Hilbert space, which can be done with resources that have a polynomial scaling with system size. This is exactly the idea at the heart of tensor network algorithms: parametrize a quantum state by a set of connected tensors and optimize them while discarding the irrelevant states of the Hilbert space, until the target state is found. We have assumed so far that our local Hamiltonian is gapped, i.e. there is a finite energy gap separating the ground state and the first excited state in the thermodynamic limit. The spatial correlation functions then decay exponentially with distance due to the short range of interactions, on the lengthscale specified by the correlation length  $\xi$ . In gapless models, however, the correlation length diverges  $\xi \rightarrow \infty$ , and the correlations instead decay by a power law. This violates the area law and normally leads to logarithmic corrections in the scaling  $S = O(L^{d-1}) \log(L)$ . Nonetheless, this growth is still much weaker than the one seen in the volume scaling, and efficient tensor network algorithms have been developed for simulating such Hamiltonians [161, 174, 175].

One outstanding question is the practical implementation of the above ideas to obtain a compressed representation of quantum states. The key step is truncating the Schmidt decomposition of a quantum state  $|\Psi\rangle$  to  $\chi \leq D$  largest Schmidt values

$$|\tilde{\Psi}\rangle = \sum_{\alpha=1}^{\chi} \Lambda_{\alpha} |\alpha\rangle_A \otimes |\alpha\rangle_B \quad (2.6)$$

such that the distance  $\Delta$  between the exact state  $|\Psi\rangle$  and its truncated approximation  $|\tilde{\Psi}\rangle$

$$\Delta = || |\Psi\rangle - |\tilde{\Psi}\rangle ||^2 \ll \epsilon \quad (2.7)$$

is smaller than some threshold value  $\epsilon$ . As we have seen above, a ‘typical’ state with volume scaling will have Schmidt values  $\Lambda_{\alpha}^2 \approx \frac{1}{2^{V_A}}$ . Therefore, the Schmidt values of all  $D \sim e^{V_A}$  states will have approximately equal contributions, and efficient truncation will not be possible. On the other hand, quantum states that obey the area law (or only violate it weakly) will have a decaying Schmidt spectrum, with only a limited number of Schmidt values that contribute significantly. The sparse Schmidt basis of  $|\Psi\rangle$  allows us to discard a large number of negligible, near-zero Schmidt values, keeping only a small number  $\chi$  of the largest ones. As a result, we only retain the relevant part of the huge Hilbert space to obtain a compressed representation  $|\tilde{\Psi}\rangle$  of the original state  $|\Psi\rangle$ .

In practice, we usually perform either a tensor decomposition followed by truncation, or a variational optimization of tensors that minimizes the distance  $\Delta$  between

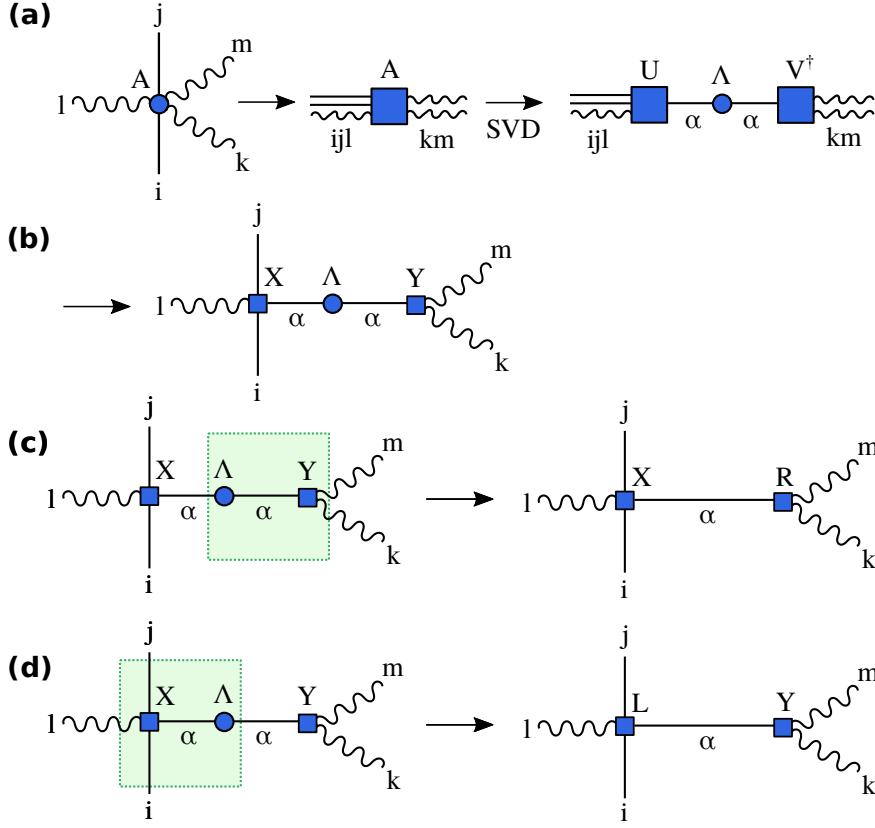


Figure 2.5: The generalization of SVD to tensors. (a) To perform tensor decomposition of  $A_{ijklm}$ , we reshape it into a matrix  $A_{(ijl),(km)}$ , and decompose it using the matrix SVD in Eq. (2.8). (b) Reshaping  $U_{(ijl),\alpha} \rightarrow X_{ij\alpha l}$  and  $V^\dagger_{\alpha,(km)} \rightarrow Y_{k\alpha m}$  yields a tensor decomposition  $A_{ijklm} \approx X_{ij\alpha l} \Lambda_{\alpha\alpha} Y_{k\alpha m}$ . (c) The left decomposition that absorbs the diagonal matrix  $\Lambda$  into  $Y$ . (d) The right decomposition that absorbs  $\Lambda$  into  $X$ .

the original state and the one compressed to  $\chi$  Schmidt values. We will briefly introduce the concept of tensor decomposition here. At its core is the singular value decomposition (SVD), which is a generalization of eigendecomposition to rectangular matrices:

$$\theta = U \Lambda V^\dagger \quad (2.8)$$

where  $\theta$  is a  $m \times n$  matrix,  $U$  is a  $m \times k$  matrix whose columns are the orthonormal singular vectors of  $\theta$  such that  $U^\dagger U = I$ ,  $V^\dagger$  is a  $k \times n$  matrix whose rows are the orthonormal singular vectors of  $\theta$  such that  $V^\dagger V = I$ , and  $\Lambda$  is a diagonal  $k \times k$  matrix that contains the singular values of  $\theta$ . The total number of singular values is  $k = \text{MIN}(m, n)$ . SVD is mathematically equivalent to the Schmidt decomposition discussed above. In the spirit of Eq. (2.6) we truncate the number of singular values (or Schmidt values) by keeping only  $k'$  largest ones, which reduces the matrix dimensions to  $m \times k'$  for  $U$ ,  $k' \times n$  for  $V^\dagger$ , and  $k' \times k'$  for  $\Lambda$ . SVD can be further generalized to tensors. To give an example, consider a tensor  $A_{ijklm}$  in Fig. 2.5 that we wish to decompose in such way that its indices are split into two sets,  $i, j, l$  and  $k, m$ . As shown in Fig. 2.5, we merge its legs  $i, j, l \rightarrow (ijl)$  and  $k, m \rightarrow (km)$  such that  $A_{ijklm} \rightarrow A_{(ijl),(km)}$  is now a matrix which we decom-

pose using SVD in Eq. (2.8)  $A_{(ijl),(km)} = U_{(ijl),\alpha} \Lambda_{\alpha,\alpha} V_{\alpha,(km)}^\dagger$ , optionally truncating the number of singular values to yield truncated matrices  $\tilde{U}_{(ijl),\alpha} \tilde{\Lambda}_{\alpha,\alpha} \tilde{V}_{\alpha,(km)}^\dagger$ . We finally reshape them back into  $\tilde{U}_{(ijl),\alpha} \rightarrow X_{ij\alpha}$  and  $\tilde{V}_{\alpha,(km)}^\dagger \rightarrow Y_{k\alpha m}$ . This yields a tensor decomposition  $A_{ijklm} \approx X_{ij\alpha} \Lambda_{\alpha\alpha} Y_{k\alpha m}$  where we have truncated the index  $\alpha$  to discard the negligible singular values. Depending on the specific problem at hand, one can instead obtain a decomposition of  $A$  into two tensors by contracting the diagonal matrix  $\Lambda$  into either  $X$  or  $Y$ . This gives respectively the left-decomposition  $A_{ijklm} \approx X_{ij\alpha} R_{k\alpha m}$  with  $R_{k\alpha m} = \Lambda_{\alpha\alpha} Y_{k\alpha m}$ , or the right-decomposition  $A_{ijklm} \approx L_{ij\alpha} Y_{k\alpha m}$  with  $L_{k\alpha m} = X_{ij\alpha} \Lambda_{\alpha\alpha}$ . Our final tensors have a compressed size of  $\chi$  for index  $\alpha$ , which allows us to keep tensor dimensions under control and exploit the sparse Hilbert space of the quantum state. The last statement brings a crucial point to our attention: the area-law scaling of entanglement is a vital prerequisite for the applicability of tensor networks. For general quantum states that do not obey the area law (e.g. in systems with arbitrarily long range interactions) we will not be able to perform truncation efficiently and still end up with tensors whose dimensions scale exponentially with the system size.

## 2.2 Matrix product states

Matrix product states (MPS) are the simplest, the most famous and the most developed type of tensor networks [38, 39]. An MPS is essentially a one-dimensional array of tensors, where each tensor represents a single site of a many-body system. MPS form the basis of some very powerful algorithms for simulating quantum many-body systems in 1D, in particular the Density Matrix Renormalization Group (DMRG) [176, 177], the Time-Evolving Block Decimation (TEBD) [178–181], and their various extensions [162, 182]. The long list of their applications includes calculations of ground states [176, 177] and low-energy excited states [183, 184], many-body quantum dynamics and spectral properties [185–189], and finite temperature simulations [190, 191]. In addition, MPS techniques have proven successful in simulating two-dimensional solid state systems [192, 193], molecular systems [194, 195], sampling problems in classical statistical mechanics [196]. MPS have also found applications in machine learning [197].

Let us consider a one-dimensional quantum many-body system with  $N$  sites described by wavefunction Eq. (2.1). Our goal is to decompose the rank- $N$  state tensor  $\Psi_{k_1, k_2, \dots, k_N}$  into a product of rank-3 tensors. Formally, this can be done by performing successive tensor SVD decompositions introduced in the last section, while sweeping across  $\Psi_{k_1, k_2, \dots, k_N}$ , as shown in Fig. 2.6(b). The result of this procedure is an MPS:

$$|\Psi_{k_1, k_2, \dots, k_N}\rangle = \sum_{k_1, k_2, \dots, k_N} A_{\alpha_1}^{[1]k_1} A_{\alpha_1, \alpha_2}^{[2]k_2} A_{\alpha_2, \alpha_3}^{[3]k_3} \dots A_{\alpha_{N-2}, \alpha_{N-1}}^{[N-1]k_{N-1}} A_{\alpha_{N-1}}^{[N]k_N} |k_1, k_2, \dots, k_N\rangle \quad (2.9)$$

where each tensor  $A_{\alpha_{n-1}, \alpha_n}^{[n]k_n}$  has three legs and represents site  $n$  of the many-body system. The vertical leg is the physical index  $k_n = 1, \dots, d_n$  corresponding to the local Hilbert space of site  $n$ , with local dimension  $d_n$ . Meanwhile, the horizontal

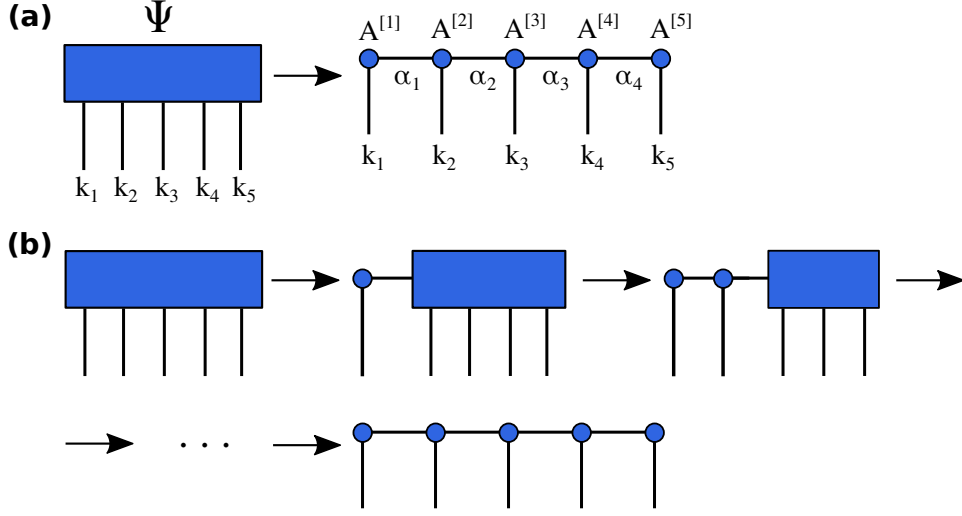


Figure 2.6: (a) A matrix product state (MPS) with  $N$  sites emerges as a 1D tensor decomposition of a rank- $N$  quantum state tensor  $\Psi_{k_1, k_2, \dots, k_N}$ . Each MPS site is a rank-3 tensor  $A^{[n]k_n}_{\alpha_{n-1}, \alpha_n}$ , with physical index  $k_n$  and bond indices  $\alpha_{n-1}, \alpha_n$ . (b) Formally, one can obtain MPS by performing successive SVDs of  $\Psi_{k_1, k_2, \dots, k_N}$ .

legs  $\alpha_{n-1}, \alpha_n$  connect the neighbouring sites together: these are virtual bond indices that have emerged from the decomposition of  $\Psi_{k_1, k_2, \dots, k_N}$ . The bond indices represent entanglement between different sites of the many-body system, and have the maximum allowed dimension of  $\chi$  imposed during SVD. If our system is not entangled, then all bond indices are singletons of size  $\chi = 1$  and Eq. (2.9) is a simple product state. Note that indices at the ends of the chain run over a single value  $\alpha_0, \alpha_N = 1$  since the sites  $n = 1$  and  $n = N$  have no connections to their left and right respectively. The bond dimension  $\chi$  is the parameter that controls the precision of MPS representation. One can show that the entanglement entropy for any subsystem of an MPS network has the upper bound of  $S \sim \log(\chi)$  [198]. As a result, MPS fulfill the area law in 1D yielding an efficient parameterization for targetting the low-energy states of one-dimensional lattice systems [199, 200]. For  $\chi = 1$ , MPS becomes an uncorrelated product state, which corresponds to a mean field ansatz. With an exponentially large  $\chi$  one could, in principle, represent any state in the Hilbert space beyond the area law domain. One limitation is that MPS with a finite  $\chi$  only supports exponentially decaying correlation functions. Therefore, it cannot target gapless systems and critical quantum wavefunctions where the correlation length diverges, since they violate the area law and carry more entanglement than MPS is able to support. In practical applications, the quality of MPS results for gapless models will vary from excellent to moderate depending on the extent to which the area law is violated [39]. There also exist other families of tensor networks designed to capture the quantum critical states, such as the Tree Tensor Network States and MERA [161, 174].

The MPS representation Eq. (2.9) of a state  $|\Psi_{k_1, k_2, \dots, k_N}\rangle$  is not unique and has a gauge freedom on every bond index [38]. One can transform MPS tensors by inserting  $X^{-1}X = I$  on any bond connecting two tensors. One can use this gauge



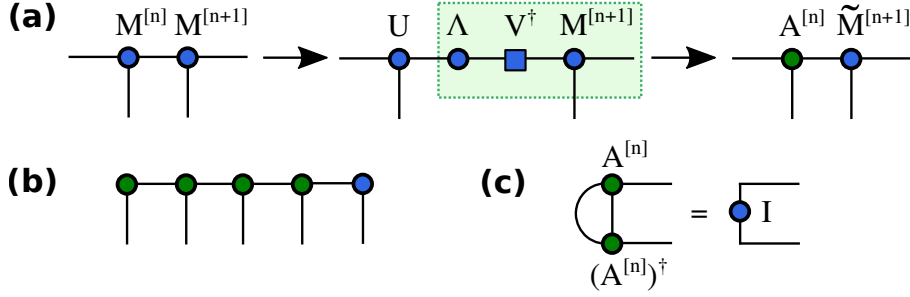


Figure 2.7: (a) We can transform a given MPS bond connecting sites  $n, n + 1$  into the left-canonical form by computing the SVD of tensor  $M^{[n]}$ , and subsequently absorbing  $\Lambda$  and  $V^\dagger$  into the tensor  $M^{[n+1]}$  on the right, which leaves a left-unitary matrix  $U$  on the site  $n$ . Sweeping across MPS from left to right while repeating the operation (a) transforms the MPS into the left-canonical form (b) with the orthonormality centre at  $n_C = N$ , where the green tensors  $A^{[n]}$  satisfy the orthonormality condition (c) due to  $U^\dagger U = I$ .

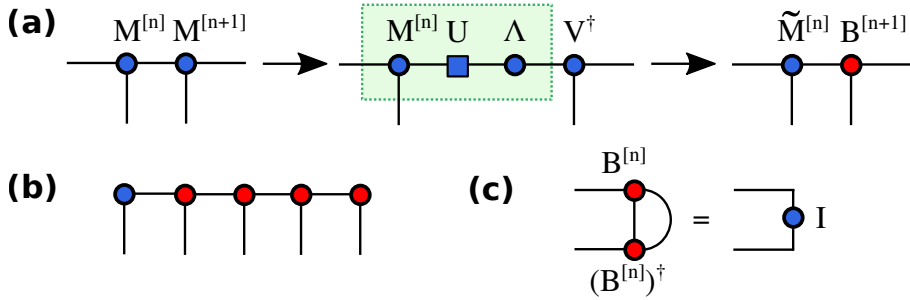


Figure 2.8: (a) We can transform a given MPS bond connecting sites  $n, n + 1$  into the right-canonical form by computing the SVD of tensor  $M^{[n+1]}$ , and subsequently absorbing  $U$  and  $\Lambda$  into the tensor  $M^{[n]}$  on the left, which leaves a right-unitary matrix  $V^\dagger$  on the site  $n$ . Sweeping across MPS from right to left while repeating the operation (a) transforms the MPS into the right-canonical form (b) with the orthonormality centre at  $n_C = 0$  where the red tensors  $A^{[n]}$  satisfy the orthonormality condition (c) due to  $V^\dagger V = I$ .

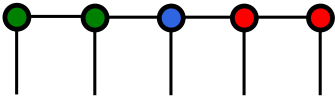


Figure 2.9: MPS in the mixed canonical form, with an arbitrary orthonormality centre at site  $n_C$ . The green tensors at sites  $n < n_C$  obey the left orthonormality condition Fig. 2.7(c) while the red tensors at sites  $n > n_C$  obey the right orthonormality condition Fig. 2.8(c).

freedom to define a convenient canonical form of our MPS. For instance, MPS can be transformed into a left-canonical form by performing an exact SVD (i.e. without truncation) on every bond of MPS, see Fig. 2.7(a,b). Since  $U$  is a unitary matrix with  $U^\dagger U = I$ , every transformed tensor  $\tilde{A}^{[n]}$  now has the orthonormality property in Fig. 2.7(c). Similarly, one can bring MPS into a right-canonical form as shown in Fig. 2.8(a,b) so that it satisfies the orthonormality condition in Fig. 2.8(c). We can also define the mixed-canonical form in Fig. 2.9 by transforming all tensors on the left and the right of a given site  $n$  into the left-canonical and the right-canonical form respectively. The site  $n$  is then called the orthonormality centre of our MPS. MPS canonical forms have various advantages. Imposing a canonical form fixes the gauge of MPS tensors, which both enables the optimal bond truncation and improves the numerical stability of MPS algorithms [38, 39]. As we will see below, MPS inner products in the mixed canonical form can be evaluated by only contracting tensors around the orthonormality centre instead of contracting the entire MPS. This becomes advantageous for computing expectation values, and for algorithms like DMRG that involve iterative sweeping across the MPS.

We will now demonstrate how to do some simple calculations with MPS. The Fig. 2.10(a) shows a diagrammatic representation of the inner product  $\langle \phi | \Psi \rangle$ . We can perform the calculation starting from one end of the chain and repeating the pattern in Fig. 2.10(b) until we reach the other end of the chain. The final result of the contraction is then a scalar value  $\langle \phi | \Psi \rangle$ . Similarly, Fig. 2.10(c) shows the expectation value  $\langle \Psi | O^{(n)} | \Psi \rangle$  of an operator  $O$ . It may be calculated by first multiplying the operator  $O$  with tensor  $A^{[n]}$ , and subsequently contracting the inner product  $\langle \Psi | O^{(n)} | \Psi \rangle$  in the same way as we have already done in Fig. 2.10(b). For demonstration purposes, this time we will follow a more efficient approach by transforming  $|\Psi\rangle$  into the mixed-canonical form around site  $n$ . As Fig. 2.10(c) shows, we can then exploit the orthonormality conditions in Fig. 2.7(c), Fig. 2.8(c). This allows us to calculate the expectation value by only contracting the tensors around the orthonormality centre, instead of computing overlap for the entire MPS.

Another important aspect of MPS concerns the boundary conditions. The MPS we have considered so far had a finite size  $N$  with open boundary conditions (OBC) and singleton bonds at both ends of the chain. We can also define a finite-size MPS with periodic boundary conditions (PBC): in such a case, the tensors  $A^{[1]}$  and  $A^{[N]}$  are connected by an additional bond to reflect the periodicity of the lattice, as shown in Fig. 2.11. It is also possible to construct an infinite MPS (iMPS) with  $N \rightarrow \infty$ , OBC, and translational invariance, and work directly in the thermodynamic limit. This can be done by choosing a unit cell that contains  $M$  sites: our MPS will then consist of these  $M$  tensors repeated periodically along the 1D lattice, as in Fig. 2.11(c) with  $M = 2$ . At first glance iMPS appears to be of no practical use, since computing observables would require contracting an infinite number of tensors. The way forward here is to exploit the translational invariance of iMPS. Since all unit cells are identical, we first define a transfer matrix  $T$  as shown in Fig. 2.12(b) for a one-site unit cell. The inner product  $\langle \Psi | \Psi \rangle$  will consist of such transfer matrices repeated along the chain ad infinitum. Transfer matrix  $T$  has the

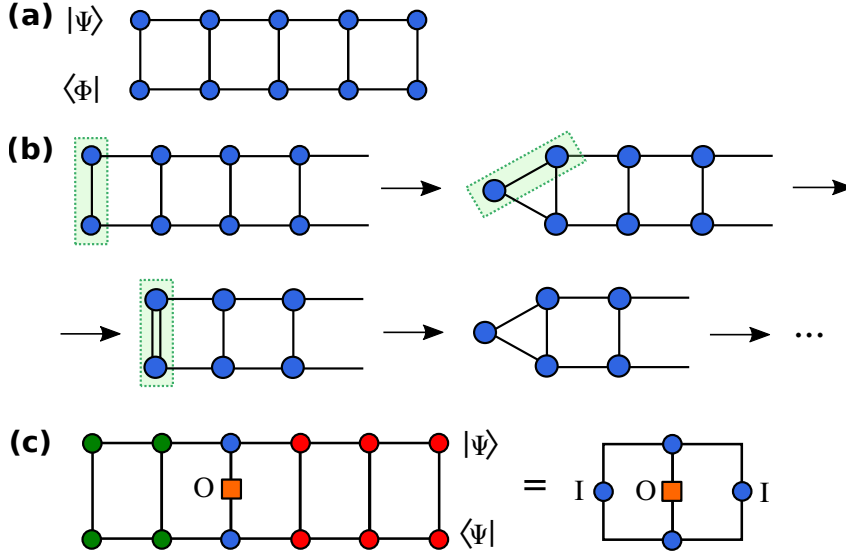


Figure 2.10: (a) The inner product of two MPS  $\langle\phi|\Psi\rangle$ ; (b) A single step of MPS-MPS contraction; (c) The expectation value  $\langle\Psi|O^{(n)}|\Psi\rangle$ . The calculation is substantially simplified if one uses the mixed-canonical form around the site  $n$ , as the sequences of green and red tensors reduce to identity matrices on the left and on the right of the operator  $O^{(n)}$ .

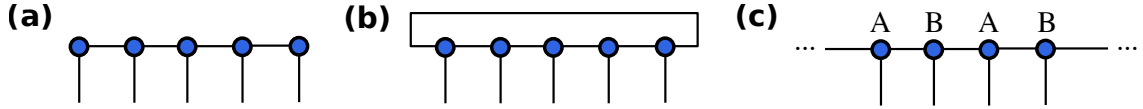


Figure 2.11: MPS with (a) open boundary conditions (OBC), (b) periodic boundary conditions (PBC), and (c) infinite boundary conditions with a periodic unit cell containing  $M = 2$  sites  $A$  and  $B$ .

eigendecomposition

$$T = \sum_k \lambda_k |R_k\rangle \langle L_k| \quad (2.10)$$

where  $\lambda_k$  is the  $k$ 'th eigenvalue while  $|R_k\rangle$  and  $\langle L_k|$  are the corresponding left and right eigenvectors. In the limit  $N \rightarrow \infty$ , only the contribution from the dominant eigenvalue  $\lambda_1$  and the corresponding eigenvectors  $|R_1\rangle$  and  $\langle L_1|$  survives

$$\lim_{N \rightarrow \infty} T^N = \lim_{N \rightarrow \infty} \sum_k \left( \frac{\lambda_k}{\lambda_1} \right)^N |R_k\rangle \langle L_k| \approx |R_1\rangle \langle L_1| \quad (2.11)$$

where we have normalized  $T$  such that its largest eigenvalue is 1; Eq. (2.11) is illustrated diagrammatically in Fig. 2.12(d). We can subdivide  $\langle\Psi|\Psi\rangle$  into the left and right semi-infinite chains that are bounded by  $\langle v_L|$  and  $|v_R\rangle$  vectors infinitely far away. These semi-infinite chains can be represented by the left dominant eigenvector  $\lim_{N \rightarrow \infty} \langle v_L| T^N \approx \langle L_1|$  and the right dominant eigenvector  $\lim_{N \rightarrow \infty} T^N |v_R\rangle \approx |R_1|$  of  $T$  respectively. This gives  $\langle\Psi|\Psi\rangle = \langle L_1|T|R_1\rangle = 1$ , i.e. iMPS is normalized as long as the periodic transfer matrix  $T$  is normalized to have the largest eigenvalue

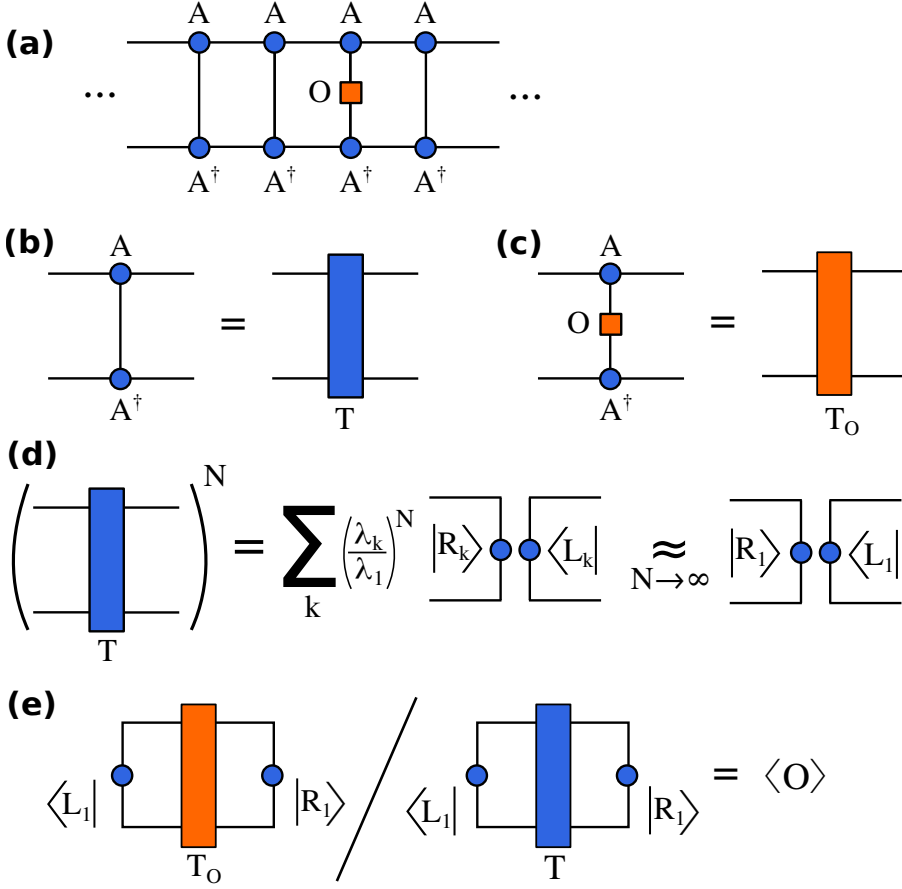


Figure 2.12: (a) Expectation value  $\langle O \rangle$  in the iMPS representation with a  $M = 1$  unit cell containing site  $A$ . (b) Transfer matrix  $T$  corresponding to a unit cell of the inner product in (a). (c) Transfer matrix  $T_O$  of a unit cell containing the operator  $O$ . (d) Diagrammatic representation of Eq. (2.11). (e) Diagrammatic representation of Eq. (2.12): the expectation value (a) expressed in terms of the transfer matrices from (b,c), and the left and right dominant eigenvectors  $\langle L_1|, |R_1\rangle$  of transfer matrix  $T$ .

equal to 1. The Fig. 2.12(e) shows a diagrammatic calculation of a generic observable

$$\langle O \rangle = \langle \Psi | O | \Psi \rangle = \frac{\langle L_1 | T_O | R_1 \rangle}{\langle L_1 | T | R_1 \rangle} \quad (2.12)$$

where  $T_O$  is a transfer matrix with operator  $O$  inserted, shown in Fig. 2.12(c). We have therefore reduced the infinite MPS-MPS contraction, required to compute expectation values, to the problem of contracting a finite MPS-MPS network bounded by the dominant eigenvectors of  $T$ .

### 2.2.1 Matrix product operators

We have seen that a quantum many-body state  $|\Psi\rangle$  can be decomposed as an MPS, a one-dimensional chain of rank-3 tensors  $\tilde{A}^{[n]}$ . Along the same lines, we can

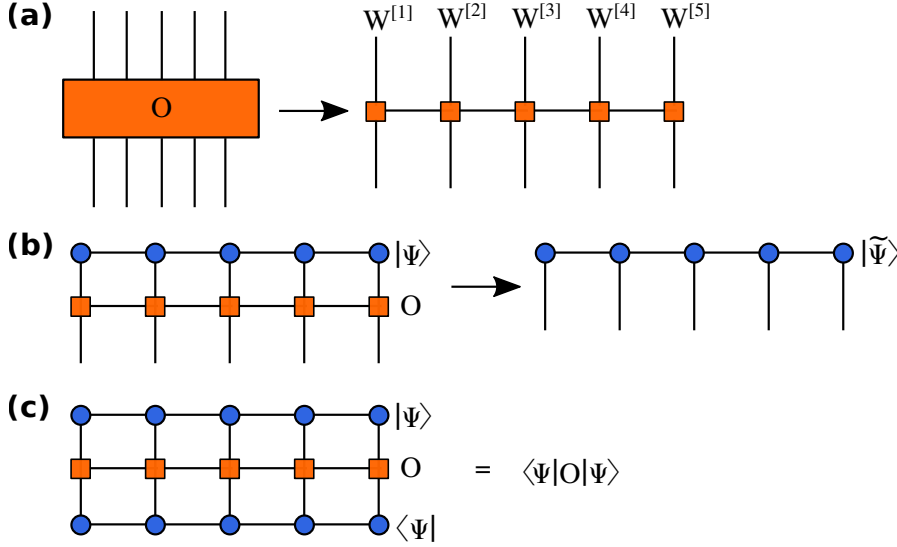


Figure 2.13: (a) A matrix product operator (MPO) with  $N$  sites in Eq. (2.14) is a 1D tensor decomposition of a rank- $N$  many body operator  $O$  in Eq. (2.13) into rank-4 tensors  $\{W^{[n]}\}$ . (b) Applying MPO  $O$  to MPS  $|\Psi\rangle$  yields a transformed MPS  $|\tilde{\Psi}\rangle = O|\Psi\rangle$ . (c) MPS-MPO-MPS inner product  $\langle\Psi|O|\Psi\rangle$ .

decompose a general many body operator

$$O = \sum_{k_1, k_2, \dots, k_N} \sum_{q_1, q_2, \dots, q_N} w_{k_1, k_2, \dots, k_N}^{q_1, q_2, \dots, q_N} |k_1, k_2, \dots, k_N\rangle \langle q_1, q_2, \dots, q_N| \quad (2.13)$$

into a one-dimensional chain of rank-4 tensors, known as a matrix product operator (MPO):

$$O = \sum_{k_1, \dots, k_N} \sum_{q_1, \dots, q_N} W_{\alpha_1}^{[1]k_1 q_1} W_{\alpha_1, \alpha_2}^{[2]k_2 q_2} \dots W_{\alpha_{N-1}}^{[N]k_N q_N} |k_1, \dots, k_N\rangle \langle q_1, \dots, q_N| \quad (2.14)$$

where each tensor  $W_{\alpha_{n-1}, \alpha_n}^{[n]k_n q_n}$  has four legs – with two physical indices  $q_n = 1, \dots, d_n$  and  $k_n = 1, \dots, d_n$  instead of just one, that represent an operator action on site  $n$  of a many-body system. Like MPS, it also has two bond indices  $\alpha_{n-1}, \alpha_n$ . The MPO bonds represent interactions between sites and the bond dimension  $\sigma$  of an MPO can be related to the number of intersite coupling terms in the operator  $O$ . The Fig. 2.13(a) shows an MPO in its diagrammatic representation.

In real calculations, we often use MPOs to represent many-body Hamiltonians, propagators, or other operator objects involving many-body interactions. By applying MPO to MPS, we can compute, for instance, the action  $H|\Psi\rangle$  of a Hamiltonian  $H$  on a wavefunction  $|\Psi\rangle$  as shown in Fig. 2.13(b). Similarly to local observables in the last section, we can calculate expectation values of MPOs such as the energy  $E(\Psi) = \langle\Psi|H|\Psi\rangle$  of the eigenstate  $|\Psi\rangle$  of  $H$ , which amounts to contracting the MPS-MPO-MPS network shown in Fig. 2.13(c). We will meet MPS-MPO contractions at various points in this thesis.

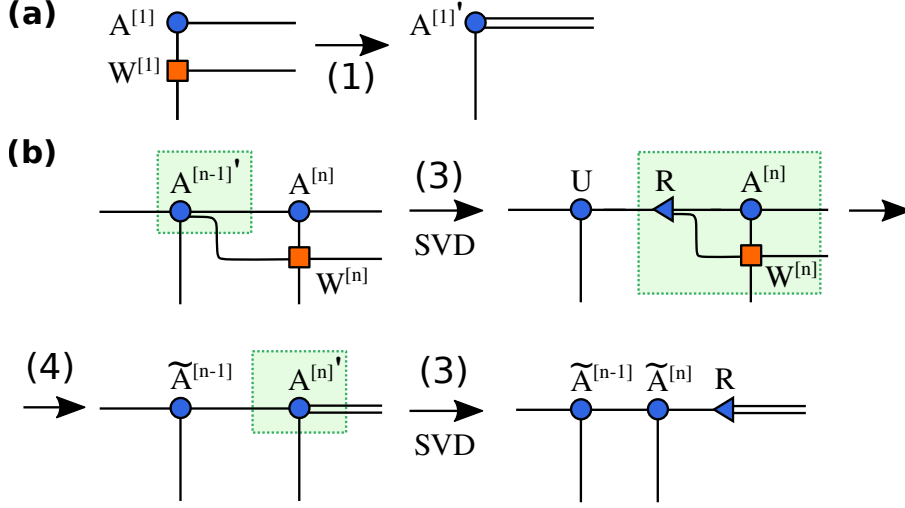


Figure 2.14: MPS-MPO multiplication using the zip-up algorithm. (a) Step (1) to initiate the zipping process at site  $n = 1$ ; (b) Steps (3 – 4) to update a given MPS bond ( $n - 1$ ,  $n$ ).

### 2.2.2 MPS-MPO multiplication

MPS-MPO multiplication is a common task in tensor network calculations. Yet it comes with its own subtleties. An important problem that arises is the fact that multiplication by an MPO destroys the canonical form of MPS [201]. The lack of fixed gauge can lead to numerical stability problems if we perform repeated MPS-MPO multiplications. Without a canonical form, MPS truncation is also very often suboptimal, making higher bond dimensions necessary to maintain the same level of accuracy [38]. Therefore, a proper MPS-MPO multiplication algorithm must implement a scheme that restores the canonical form. Another issue is related to efficiency. To make the discussion more specific, suppose we are trying to multiply MPS with physical dimension  $d$  at all sites and the bond dimension of at most  $\chi$ , by an MPO with the same physical dimension and the bond dimension  $\sigma$  for all bonds. A naive MPS-MPO multiplication would contract all MPS and MPO tensors first, and subsequently truncate all MPS bonds using SVD. This is, however, highly inefficient as it carries the computational cost of  $O(N\chi^3\sigma^3d)$  for the SVDs. An efficient multiplication needs an approach that multiplies and truncates tensors on the fly to ensure optimal computational cost. The method of our choice is the zip-up algorithm proposed by Stoudenmire and White [201], which has a scaling of  $O(N\chi^3\sigma d^2 + N\chi^2\sigma^2 d^2)$ . Outlined below are the main steps of the zip-up algorithm:

1. Initiate the zipping process: multiply the first site  $n = 1$  of MPS  $A^{[1]}$  with the first site of MPO  $W^{[1]}$  as shown in Fig. 2.14(a). The result is a new tensor  $A^{[1]}'$  with the right bond dimension increased to  $\chi\sigma$ . Shift to the next site  $n = 1 \rightarrow n = 2$ .
2. For a general site  $n$ , perform the following steps shown diagrammatically in Fig. 2.14(b):

3. Decompose  $A^{[n-1]}'$  tensor at the preceding site into  $U$  and  $R = \Lambda V^\dagger$  tensors using SVD and truncating the bond dimension. Update the preceding MPS site with a new truncated tensor  $\tilde{A}^{[n-1]} = U$ .
4. Contract  $R$ , MPO site  $W^{[n]}$  and MPS site  $A^{[n]}$  to give a new tensor  $A^{[n]}'$  with the right bond dimension increased to  $\chi\sigma$ . Shift to the next site  $n \rightarrow n + 1$ .
5. Repeat steps (2-4) sweeping along the MPS-MPO network from left to right until we reach the end. By the time we reach the end, the zip-up process has transformed all MPS tensors  $\tilde{A}^{[n]}$  (except  $\tilde{A}^{[N]}$ , the centre of orthonormality) into the left-canonical form.
6. Sweep backwards from right to left, performing SVD and truncation on MPS tensors, and transforming them into the right canonical form as shown in Fig. 2.8(a). The backward sweep ensures that MPS tensors are truncated optimally.
7. Once the backward sweep reaches the first site  $n = 1$ , the MPS has been fully updated, and all tensors  $\tilde{A}^{[n]}$  (except  $\tilde{A}^{[1]}$ , the centre of orthonormality) are now in the right-canonical form.

We emphasize that on the forward left-to-right sweep it is important to perform truncation using a fixed precision  $\lambda_c$  instead of fixed bond dimension  $\chi$ , i.e. one should truncate by discarding singular values below some small fixed cutoff value  $\lambda_c$ . This is due to the fact that any SVD truncation in the zip-up algorithm optimizes local tensors instead of optimizing MPS globally which is achieved by gradient-driven variational algorithms [38]. The purpose of using a fixed precision  $\lambda_c$  is to compensate for a loss of accuracy due to this locality, which helps us to avoid discarding important information. Once we reach the right edge of the chain, all MPS tensors are already in the left-canonical form. Hence, SVD is optimal on the backward right-to-left sweep and one is free to truncate either using a fixed precision  $\lambda_c$  or a fixed bond dimension  $\chi$ .

### 2.2.3 TEBD algorithm

Among the standard MPS methods, particularly relevant to our work is the Time Evolving Block Decimation (TEBD) algorithm. TEBD and its infinite system variant iTEBD (i.e. infinite Time Evolving Block Decimation) were proposed by Vidal [178–181] and have become established as a simple yet efficient and versatile technique for simulating time evolution of quantum states. It also has a straightforward extension to the dissipative dynamics of open quantum systems [40], which is a part of our motivation for choosing this algorithm. In this thesis, we will often work with lattice systems in the thermodynamic limit  $N \rightarrow \infty$  making use of iMPS introduced earlier in this section. Therefore, in this section we focus specifically on iTEBD. The algorithm starts with some initial state  $|\Psi(0)\rangle$  written as an iMPS, and evolves it for some time  $t$  under Hamiltonian  $H$ :

$$|\Psi(t)\rangle = U(t) |\Psi(0)\rangle \quad (2.15)$$

with time evolution operator  $U(t) = e^{-iHt}$ . We will mainly be interested in systems with the nearest-neighbour interactions only (e.g. coupled cavity lattices with tunnelling between adjacent cavities). In such models the most convenient way to construct the tensor network form of propagator  $U(t)$  is by decomposing it into two-body propagators, each evolving a single bond. Let us first split our Hamiltonian

$$H = H_E + H_O \quad (2.16)$$

into terms  $H_E = \sum_{j \text{ even}} H_{j,j+1}$  and  $H_O = \sum_{j \text{ odd}} H_{j,j+1}$  acting on the even and odd bonds of the lattice respectively. The next step is to discretize the time  $t = N\delta t$  using a number of timesteps  $N$  of size  $\delta t$ :

$$U(t) = [U(\delta t)]^N \quad (2.17)$$

Since  $H_E$  and  $H_O$  do not commute with each other, we perform Trotter decomposition of  $U(\delta t)$

$$U(\delta t) = e^{-i(H_E+H_O)\delta t} = e^{-iH_E\delta t} e^{-iH_O\delta t} + O(\delta t^2) \quad (2.18)$$

which approximates the exponential of  $H_E + H_O$  by the product of  $H_E$  and  $H_O$  exponentials. In the limit  $\delta t \rightarrow 0$  the above splitting becomes exact; in practice, we typically use a small timestep  $\delta t$  such that the error  $O(\delta t^2)$  is sufficiently small. The equation (2.18) corresponds to the first order Trotter decomposition, which carries an error of  $O(\delta t^2)$ . We note that arguments presented here can be straightforwardly adapted to higher order Trotter decompositions. For instance, in our numerical simulations we employ the second order splitting  $U(\delta t) = e^{-iH_E\delta t/2} e^{-iH_O\delta t} e^{-iH_E\delta t/2} + O(\delta t^3)$ , with a reduced error of  $O(\delta t^3)$ . However, for ease of explanation we use the first order decomposition in our description of iTEBD here. Using Eq. (2.18) we can express our propagator entirely in terms of two-body gates:

$$U(\delta t) = \prod_{j \text{ even}} e^{-iH_{j,j+1}\delta t} \prod_{j \text{ odd}} e^{-iH_{j,j+1}\delta t} \quad (2.19)$$

The standard iTEBD algorithm uses a slightly different form of iMPS than the one introduced in the last section. In Figs. 2.7, 2.8 we absorbed the diagonal  $\Lambda$  matrices produced by SVDs into their adjacent  $A^{[n]}$  MPS tensors. Instead of absorbing  $\Lambda$ 's, iTEBD keeps them uncontracted. Let us denote the MPS tensor at site  $n$  by  $\Gamma^{[n]}$ , and the diagonal matrix  $\Lambda$  at the bond connecting sites  $n$  and  $n+1$  by  $\Lambda^{[n]}$ . The  $\Lambda^{[n]}$  matrices contain Schmidt values of their respective bonds, and are normalized such that  $\sum_{\alpha} [\Lambda_{\alpha}^{[n]}]^2 = 1$ . This alternative representation of iMPS is known as Vidal form: Fig. 2.15 shows Vidal form of iMPS with two-site translational invariance. For simplicity, it would be most convenient to consider an iMPS that has a one-site unit cell. However, Trotter decomposition Eq. (2.19) modifies the translational invariance from one-site to two-site – thus we will be obliged to use a two-site unit cell in our algorithm instead.

We now have all the ingredients needed for iTEBD algorithm, which we outline below step by step.



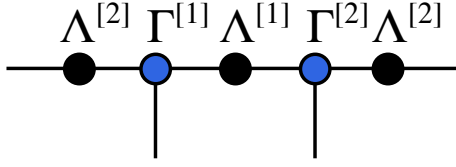


Figure 2.15: An iMPS with a two-site unit cell in Vidal form.  $\Gamma^{[n]}$  represents site  $n$  of the unit lattice, and the diagonal matrix  $\Lambda^{[n]}$  contains the singular value spectrum of bond  $(n, n + 1)$ .

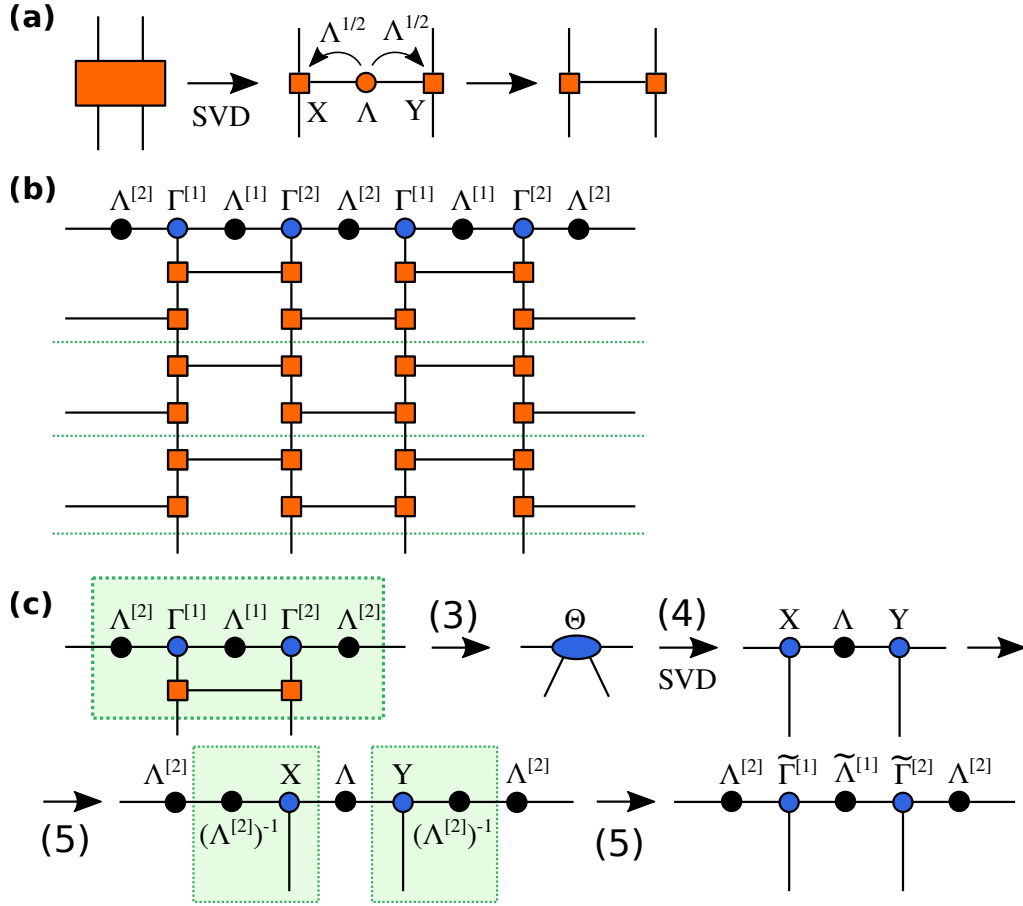


Figure 2.16: (a) A two-body propagator  $e^{-iH_{j,j+1}\delta t}$  decomposed into a two-site MPO using SVD. The diagonal  $\Lambda$  matrix emerging from SVD is absorbed symmetrically into both MPO sites  $X$  and  $Y$ . (b) iTEBD time evolution using the Trotter decomposition Eq. (2.19) into a series of two-body MPO propagators. The green lines separate adjacent timesteps. (c) The steps (3-5) to update a single iMPS bond using a two-body MPO propagator.

1. Start with some initial state  $|\Psi(0)\rangle$  represented as iMPS in Vidal form with tensors  $\Gamma^{[1,2]}$  and  $\Lambda^{[1,2]}$ , and local Hilbert space dimension  $d$  at each site. We usually initialize iMPS as a random-number state or a product state with bond dimension  $\chi = 1$ .
2. Apply two-body propagator  $e^{-iH_{j,j+1}\delta t}$  to the even bonds of iMPS as in Fig. 2.16(b). To update iMPS tensors, we take the following steps to update each  $(1, 2)$  bond, as shown in Fig. 2.16(c):
3. Contract the propagator  $e^{-iH_{j,j+1}\delta t}$  with  $\Gamma^{[1,2]}$  and  $\Lambda^{[1,2]}$  tensors around the  $j, j+1$  bond into a single  $\theta$  tensor.
4. Decompose  $\theta$  tensor into  $X$ ,  $Y$ , and  $\Lambda$  tensors using SVD. After update, the size of  $j, j+1$  bond has increased from  $\chi$  to  $d\chi$ . In general, successive multiplications with two-body propagators will cause the amount of information in iMPS grow exponentially. Therefore, we must truncate iMPS by retaining  $\chi$  largest singular values to keep the size of iMPS tensors under control. As long as the discarded singular values are small, iMPS will continue to be an accurate representation of the actual quantum state even after truncation.
5. Update iMPS with truncated  $X$ ,  $Y$ , and  $\Lambda$  tensors by setting  $\tilde{\Gamma}^{[1]} = X$ ,  $\tilde{\Gamma}^{[2]} = Y$ , and  $\tilde{\Lambda}^{[1]} = \Lambda$ . To restore  $\Lambda^{[2]}$  on the external bonds, we divide  $\tilde{\Gamma}^{[1,2]}$  by  $\Lambda^{[2]}$ . This procedure brings iMPS back to its original Vidal form, with updated tensors  $\tilde{\Gamma}^{[1,2]}$ ,  $\tilde{\Lambda}^{[1]}$  for each  $(1, 2)$  bond on the lattice.
6. Apply two-body propagator  $e^{-iH_{j,j+1}\delta t}$  to the odd bonds of iMPS as in Fig. 2.16(b). Repeat steps (3-5) to update each  $(2, 1)$  bond.
7. iMPS has now been propagated forward by a single timestep  $\delta t$ . Repeat steps (2-6) to evolve iMPS for a desired number of timesteps  $N$ .

The iTEBD algorithm described so far simulates the real time evolution of a quantum state. However, it can easily be repurposed to perform imaginary time evolution for ground state calculations [38, 39]. This amounts to replacing real time with imaginary time  $it \rightarrow \tau$  in all propagators Eq. (2.15), (2.18), (2.19), while all other steps of the algorithm remain the same as outlined above. For  $\tau \rightarrow \infty$ , imaginary time evolution yields the ground state of a Hamiltonian  $H$ :

$$|\Psi_{GS}\rangle = \lim_{\tau \rightarrow \infty} \frac{e^{-H\tau} |\Psi(0)\rangle}{\|e^{-H\tau} |\Psi(0)\rangle\|} \quad (2.20)$$

In practice, we evolve the state for  $N$  imaginary timesteps  $\delta\tau$  until convergence is achieved with respect to the spectrum of singular values in  $\Lambda^{[1,2]}$  and/or the relevant observables of the system. A common practice that helps to improve the convergence accuracy of imaginary time evolution is to start with a large timestep  $\delta\tau \sim 10^{-1}$  and then gradually decrease the timestep size during the simulation to reduce the effects of Trotter error. The large initial timestep helps us to avoid a possibility of getting stuck in a local minimum, as well as to speed up the simulation. The smallest  $\delta\tau$  needed to achieve convergence is strongly problem dependent. We repeat the whole simulation for increasing values of iMPS bond dimension  $\chi$  until we see a satisfactory convergence with respect to  $\chi$ .

### 2.2.4 Liouvillian time evolution

Originally, MPS techniques were developed for calculations based on quantum many-body wavefunctions and so far we have discussed them in that context. The dynamics in standard time-dependent MPS simulations – for instance, the TEBD algorithm described in Sec. 2.2.3 – are thus generated by the Schrödinger equation

$$i\partial_t |\Psi(t)\rangle = H |\Psi(t)\rangle \quad (2.21)$$

More recently, MPS have started gaining momentum as a framework for simulating the dissipative mixed-state dynamics of density matrices, governed by Liouvillian superoperators. Here we discuss how one can apply the MPS methods presented so far to the reduced density matrices of open quantum many-body systems. More specifically, let us consider a driven dissipative quantum lattice system in 1D with  $N$  sites. We assume that the system is described by a nearest-neighbour Hamiltonian  $H$  and is weakly coupled to a Markovian bath by dissipation. The dynamics of its reduced density matrix  $\rho(t)$  is governed by the Lindblad master equation from Sec. 1.1.2:

$$\partial_t \rho = \mathcal{L}[\rho(t)] = -i[H, \rho(t)] + \sum_{\mu, n} \left( L_{\mu, n} \rho(t) L_{\mu, n}^\dagger - \frac{1}{2} \rho(t) L_{\mu, n}^\dagger L_{\mu, n} - \frac{1}{2} L_{\mu, n}^\dagger L_{\mu, n} \rho(t) \right) \quad (2.22)$$

where  $\mathcal{L}$  is the Liouvillian superoperator and  $L_{\mu, n}$  is a Lindblad jump operator  $L_\mu$  acting on a lattice site  $n$ . We suppose that each lattice site  $n$  has a local Hilbert space  $\mathcal{H}^{[n]} \cong \mathcal{C}_d$  with dimension  $d$ , and the whole lattice system 'lives' in the Hilbert space  $\mathcal{H} \cong \mathcal{C}_d^{\otimes N}$ , the  $N$ -fold tensor product of local Hilbert spaces  $\mathcal{C}_d$ .

Zwolak and Vidal [40] proposed a method for mapping Lindblad master equations onto a vectorized space using Choi isomorphism, which has enabled them to extend MPS time evolution to mixed states. Here we follow their approach to show how solving Eq. (2.22) can be transformed into an MPS problem. Let us first define a vector space  $\mathcal{K}^{[n]} \cong \mathcal{M}(\mathcal{H}^{[n]}) \cong \mathcal{C}_{d^2}$  of  $d \times d$  complex matrices for each site  $n$ . Here  $\mathcal{M}(\mathcal{H})$  denotes a set of linear mappings on the Hilbert space  $\mathcal{H}$  of the system. We then represent a  $d \times d$  density matrix  $\rho$  as a superket state vector  $|\rho\rangle_\#$  of size  $d^2$  that 'lives' in  $\mathcal{K}$  space

$$\rho \in \mathcal{M}(\mathcal{H}) \rightarrow |\rho\rangle_\# \in \mathcal{K} \quad (2.23)$$

and a generic superoperator  $\mathcal{Q}$  as a linear map  $\mathcal{M}(\mathcal{K})$  that acts on superkets 'living' in  $\mathcal{K}$

$$\mathcal{Q} \in \mathcal{M}(\mathcal{M}(\mathcal{H})) \rightarrow \mathcal{Q}_\# \in \mathcal{M}(\mathcal{K}) \quad (2.24)$$

We then define the action of  $\mathcal{Q}_\#$  on  $|\rho\rangle_\#$

$$|\mathcal{Q}[\rho]\rangle = \mathcal{Q}_\# |\rho\rangle_\# \quad (2.25)$$

Here, the subscript  $\#$  indicates the vectorized representation in the space of superkets. The above mapping essentially corresponds to reshaping a matrix into a vector, e.g. by stacking its columns (or joining its rows) together. We can therefore imagine this as writing a many body density matrix  $\rho$  as an MPO and subsequently reshaping it into an MPS by combining both of its physical indices into one at

each site, as illustrated in Fig. 2.17. An important question remains whether the arguments about truncation of Schmidt basis of pure quantum states introduced in Sec. 2.1.2 actually apply to the superkets of mixed states. To answer this question, let us take a quantum many body lattice described by a mixed state density matrix and divide it into subregions  $A$  and  $B$ . Given a superoperator  $Q$  in this bipartite Hilbert space  $\mathcal{H}^{[A]} \otimes \mathcal{H}^{[B]}$  and an orthonormal basis set  $\{|\beta\rangle_{\#}\} \in \mathcal{K}^{[B]} \cong \mathcal{M}(\mathcal{H}^{[B]})$ , we can define a partial trace over subregion  $B$

$$\text{Tr}_{\#B}(Q_{\#}) = \sum_{\beta} \langle \beta | Q_{\#} | \beta \rangle_{\#} \quad (2.26)$$

By analogy to the reduced density matrices in Sec. 2.1.2, we introduce reduced superoperators  $Q_{\#}^{[A,B]}$  acting on subregions  $A, B$

$$Q_{\#}^{[A]} = \text{Tr}_{\#B}(|\rho\rangle_{\#\#}\langle\rho|) = \sum_{\alpha=1}^D \lambda_{\alpha}^2 |\alpha_A\rangle_{\#\#}\langle\alpha_A| \in \mathcal{M}(\mathcal{K}^{[A]}) \quad (2.27)$$

and

$$Q_{\#}^{[B]} = \text{Tr}_{\#A}(|\rho\rangle_{\#\#}\langle\rho|) = \sum_{\alpha=1}^D \lambda_{\alpha}^2 |\alpha_B\rangle_{\#\#}\langle\alpha_B| \in \mathcal{M}(\mathcal{K}^{[B]}) \quad (2.28)$$

where the orthonormal basis sets  $\{|\alpha_{A,B}\rangle_{\#}\}$  of  $A, B$  are the eigenvectors of  $Q_{\#}^{[A,B]}$ ,  $\Lambda_{\alpha}^2$  are the corresponding eigenvalues, and there are  $D$  eigenvalues in total. Having defined the orthonormal basis of  $A, B$ , we can now generalize the Schmidt decomposition Eq. (2.2) to superkets 'living' in  $C_{d^2}^{\otimes N}$  space:

$$|\rho\rangle_{\#} = \sum_{\alpha=1}^D \lambda_{\alpha} |\alpha_A\rangle_{\#} \otimes |\alpha_B\rangle_{\#} \quad (2.29)$$

with  $\sum_{\alpha} \Lambda_{\alpha}^2 = 1$  for a normalized state. Similarly to Sec. 2.1.2, the rank  $D$  of the reduced superoperators  $Q_{\#}^{[A,B]}$  describes the amount of bipartite entanglement between  $A$  and  $B$ . It can be truncated to a smaller rank  $\chi \leq D$  to find a compressed representation of  $|\rho\rangle_{\#}$ , thus generalizing the pure state equation Eq. (2.6) to mixed states. The actual rank  $\chi$  will depend on the amount of correlations between the partitions  $A$  and  $B$ . While the pure-state MPS calculations truncate the space  $\mathcal{H}^{[A]}$  of the reduced density matrix  $\rho_A$ , the mixed-state calculations truncate the space  $\mathcal{K}^{[A]} \cong \mathcal{M}(\mathcal{H}^{[A]})$  of the reduced superoperator  $Q_{\#}^{[A]}$ .

Our next step is to find a mixed state propagator defined as a linear map  $\mathcal{M}(\mathcal{K})$  that acts on superkets in  $\mathcal{K}$  space. To this end, we use the tensor product property

$$|X\rho Y\rangle_{\#} = X \otimes Y^T |\rho\rangle_{\#} \quad (2.30)$$

to map the superoperator master equation Eq. (2.22) onto a vectorized master equation

$$\partial_t |\rho(t)\rangle_{\#} = \mathcal{L}_{\#} |\rho(t)\rangle_{\#} \quad (2.31)$$

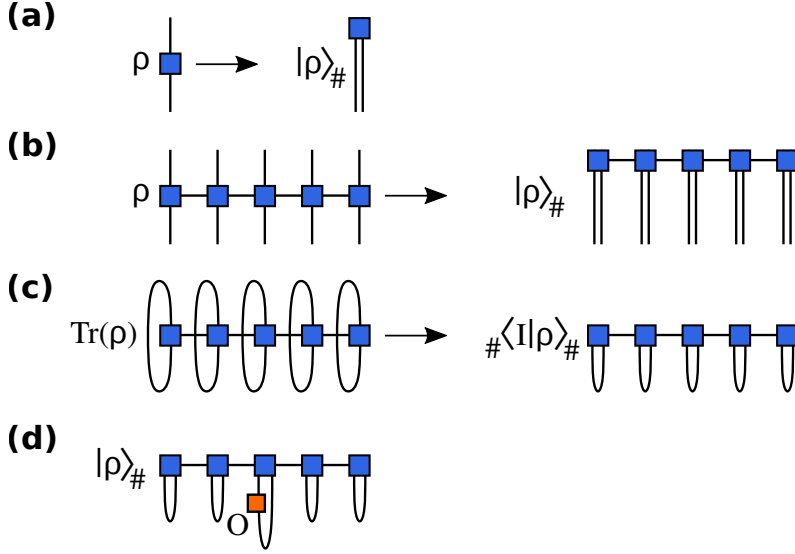


Figure 2.17: (a) Density matrix  $\rho$  can be vectorized by merging its indices together to give the vectorized density matrix  $|\rho\rangle_\#$ . (b) Likewise, an MPO representing a many body density operator  $\rho$  can be vectorized by merging its local indices together at each site, to give a vectorized density matrix MPS  $|\rho\rangle_\#$ . (c) Computing the trace of vectorized density matrix MPS  $|\rho\rangle_\#$ . (d) Computing an expectation value  $\langle O \rangle = \text{Tr}(O\rho)$  with  $|\rho\rangle_\#$  MPS.

where the vectorized Liouvillian is

$$\mathcal{L}_\# = -i (H \otimes I - I \otimes H^T) + \sum_{\mu,n} \left( L_{\mu,n} \otimes L_{\mu,n}^* - \frac{1}{2} I \otimes (L_{\mu,n}^\dagger L_{\mu,n})^T - \frac{1}{2} L_{\mu,n}^\dagger L_{\mu,n} \otimes I \right) \quad (2.32)$$

We can then define the overlap for general  $d \times d$  matrices  $A, B$ :

$$\# \langle A | B \rangle_\# = \frac{1}{d} \text{Tr} (A^\dagger B) \quad (2.33)$$

and the expectation value of a general  $d \times d$  operator  $O$ :

$$\langle O \rangle = \frac{\text{Tr}(O\rho)}{\text{Tr}(\rho)} = \frac{\# \langle O | \rho \rangle_\#}{\# \langle I | \rho \rangle_\#} = \frac{\# \langle I | O \otimes I | \rho \rangle_\#}{\# \langle I | \rho \rangle_\#} \quad (2.34)$$

where we have introduced the trace map  $|I\rangle_\#$ :

$$I = \sum_{k_1, \dots, k_N} |k_1, \dots, k_N\rangle \langle k_1, \dots, k_N| \rightarrow |I\rangle_\# = \sum_{k_1, \dots, k_N} |k_1, \dots, k_N\rangle \otimes |k_1, \dots, k_N\rangle \quad (2.35)$$

The vectorized master equation Eq. (2.31) generates time evolution of  $|\rho(t)\rangle_\#$

$$|\rho(t)\rangle_\# = e^{t\mathcal{L}_\#} |\rho(0)\rangle_\# \quad (2.36)$$

analogous to imaginary time evolution Eq. (2.20). In this form, finding the steady state  $|\rho_{SS}\rangle_\#$  of Eq. (2.31) requires solving the equation:

$$\mathcal{L}_\# |\rho_{SS}\rangle_\# = 0 \quad (2.37)$$

which essentially means targetting the null eigenstate of  $\mathcal{L}_\#$ . The problems of targetting the ground state of a Hamiltonian and the zero eigenstate of a Liouvillian share important similarities and differences. In both cases we target the zero eigenstate by using propagation to  $t \rightarrow \infty$ . On the other hand, the first problem concerns the space of real eigenvalues of a Hermitian operator using imaginary time evolution, while the second problem deals with the space of complex eigenvalues of a non-Hermitian Liouvillian using real time evolution. Nonetheless, in both problems one may represent the desired eigenstate as an MPS, and the propagator as an MPO or a set of two-body gates – and implement a reduced density operator or a reduced superoperator space truncation to keep the MPS bond dimensions from growing indefinitely during the propagation. All the ideas presented in this section suggest that we can recycle MPS time evolution algorithms, such as TEBD introduced in Sec. 2.2.3, to simulate the dissipative real-time evolution Eq. (2.36) of a reduced density matrix  $|\rho(t)\rangle_\#$  in a superket form. Propagating for a sufficiently long time  $t \rightarrow \infty$  will then target the zero eigenstate of  $\mathcal{L}_\#$ , which corresponds to the steady state Eq. (2.37):

$$|\rho_{ss}\rangle_\# = \lim_{t \rightarrow \infty} \frac{e^{t\mathcal{L}_\#} |\rho(0)\rangle_\#}{\langle I | e^{t\mathcal{L}_\#} |\rho(0)\rangle_\#} \quad (2.38)$$

Throughout this thesis, we will make an extensive use of the ideas described here, which will form the basis for tensor network simulations of open quantum systems in the following chapters. For brevity of notation, we will drop the  $\#$  subscripts of vectorized superoperators and superkets.

## 2.3 Projected entangled pair states

Projected entangled pair states (PEPS) are another important class of tensor network states that we will meet in this thesis. PEPS is a natural generalization of MPS to two and higher dimensional systems [39]. Here we focus on the 2D case only. The basic idea behind PEPS is to parameterize the quantum state tensor  $\Psi_{k_1, k_2, \dots, k_N}$  by a two-dimensional array of interconnected rank-5 tensors, as shown diagrammatically in Fig. 2.18(a), in order to overcome the exponential scaling problem. Each individual tensor represents a single site of the quantum many-body system, with one vertical leg corresponding to the local Hilbert space of dimension  $d$ , and four horizontal legs corresponding to the bonds between different lattice sites. We denote the bond dimension of PEPS by  $D$ , which limits the amount of entanglement that can be captured by PEPS. While PEPS depicted in Fig. 2.18(a) represents a square lattice, it can be defined for any lattice geometry such as triangular, kagome, honeycomb, and others. It is straightforward to show that the entanglement entropy for any sublattice of size  $L$  within a PEPS has the upper bound of  $S \sim L \log(D)$  [39]. Therefore, PEPS satisfy the area law in 2D and are well-suited for targetting the low-energy sector of a Hamiltonian with local interactions. Of course, we can represent any state in the many-body Hilbert space using PEPS with an exponentially large  $D$ . One notable feature of PEPS is that it supports algebraically decaying correlations. Hence, in principle, it is capable of simulating gapless Hamiltonians and critical quantum states [202]. Contrary to MPS, PEPS does not have a known

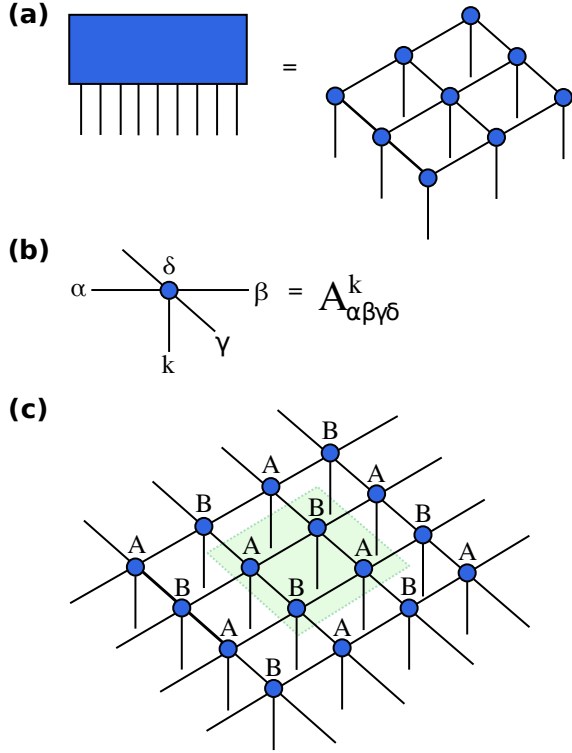


Figure 2.18: (a) A projected entangled pair state (PEPS) with  $N$  sites is a 2D tensor decomposition of a rank- $N$  quantum state tensor  $\Psi_{k_1, k_2, \dots, k_N}$ . (b) A PEPS site is a rank-5 tensor  $A^k_{\alpha\beta\gamma\delta}$ , with physical index  $k$  and bond indices  $\alpha, \beta, \gamma, \delta$ . (c) The infinite PEPS (iPEPS) representation with a two-site unit cell made of tensors  $A$  and  $B$ .

canonical form, in a sense that it is impossible to define orthonormal basis for all bond indices simultaneously [39]. This stems from the fact that one cannot split the network into left and right pieces by cutting a single bond as we did for MPS with OBC, and so it is not possible to perform the Schmidt decomposition into the left and right parts. Finding a suitable way to fix the gauge of PEPS tensors is, in fact, one of the unsolved technical issues in the field [203, 204].

The emergence of PEPS has led to many important algorithms for simulating two-dimensional quantum lattice systems [39]. This includes the PEPS [205] and iPEPS [206] algorithms for ground states, tensor renormalization group and related methods [207–209], variational PEPS algorithms for ground states [210, 211] and their extensions to excited states [212] using the tangent-space methods. PEPS has proven competitive in simulating the ground states of various spin and fermionic models: frustrated magnetic systems [213–216],  $SU(N)$  Heisenberg models [217–219], fermionic t-J and Hubbard models [220–223], and high-temperature superconductivity [224]. Although PEPS has seen many promising developments, it remains full of unsolved technical challenges and has yet to achieve the same standard as MPS already has in 1D.

In Chapter 4 we will tackle the problem of extending PEPS to open quantum systems, focusing on infinite lattices with the nearest-neighbour interactions. One can simulate these systems using the infinite PEPS (iPEPS) ansatz [206] and work-

ing directly in the thermodynamic limit where the boundary and finite size effects are eliminated. Just like iMPS in one dimension, we can construct an iPEPS by choosing a unit cell and representing its sites with tensors. The physical problems of our interest will have a square lattice geometry, in particular the two-site unit cell shown in Fig. 2.18(c). Therefore, we will need only two tensors  $A$  and  $B$  to define iPEPS. We now introduce the iPEPS algorithm that performs imaginary time evolution to find the ground states of infinite lattice models in  $2D$ . It consists of two main ingredients: the imaginary time propagation of iPEPS and the calculation of the environment needed to extract observables. Chapter 4 will focus on extending this algorithm to nonequilibrium steady states of Lindblad master equation.

### 2.3.1 Corner transfer matrix method

For the iPEPS representation to be of practical use, we must be able to extract expectation values from it. Here we face a challenging problem: calculating  $\langle \Psi | O | \Psi \rangle$  requires us to compute the iPEPS-iPEPS inner product in Fig. 2.19(a), which in turn appears to require contraction of a tensor network that is infinite in all directions. In fact, a similar problem occurs even for finite PEPS. Unlike MPS where we could evaluate overlaps exactly at a polynomial cost, the exact contraction of two PEPS is an exponentially hard problem that scales as  $O(e^L)$  with PEPS size  $L$  [39]. Fortunately, there exist various computational algorithms that can perform this contraction approximately with high precision. For infinite systems, these methods typically proceed by computing the approximate environment of an iPEPS unit cell, see Fig. 2.19. This effective environment consists of a small set of tensors that represent the infinite tensor network surrounding the unit cell. Possibly the most successful technique for computing iPEPS environments is the corner transfer matrix (CTM) method [225–227], which will be the method of our choice. Other contraction schemes include the boundary iMPS method [206] and a whole family of tensor renormalization approaches [207–209]. However, most of them have various technical disadvantages compared to CTM such as a lack of efficiency, or the difficulties that arise when computing long-range spatial correlation functions [39]. In this section we will explain the details of the CTM algorithm.

Fig. 2.19(a) shows the contraction of two iPEPS, which produces an infinite 2D network made of reduced tensors  $a$  – except at the site where the operator is applied, leading to a different reduced tensor  $a_O$ . Each reduced tensor  $a$  results from the contraction of  $[M^A]^\dagger$  and  $M^A$  iPEPS tensors by their physical indices, as shown in Fig. 2.19(b). Supposing the bond indices of  $M^A$  had dimension  $D$ , the reduced tensors  $a$  now have bonds of dimension  $D^2$ . For simplicity of exposition, we will start by considering a one-site unit cell. However, as we have seen in Sec. 2.2.3, methods based on Trotter decomposition into even and odd bonds modify the translational invariance from one-site to two-site. Therefore, in practice we always use the two-site version of the CTM algorithm, which we explain later in the text. Let us now subdivide this network into a  $1 \times 1$  unit cell made of  $a$  tensors, and its environment that contains the remaining infinite tensor network in which the unit cell is embedded. The key idea is to represent the environment by a set of four corner matrices  $\{C_{1,2,3,4}\}$ , and four transfer tensors  $\{T_{1,2,3,4}\}$  as in Fig. 2.19(c)



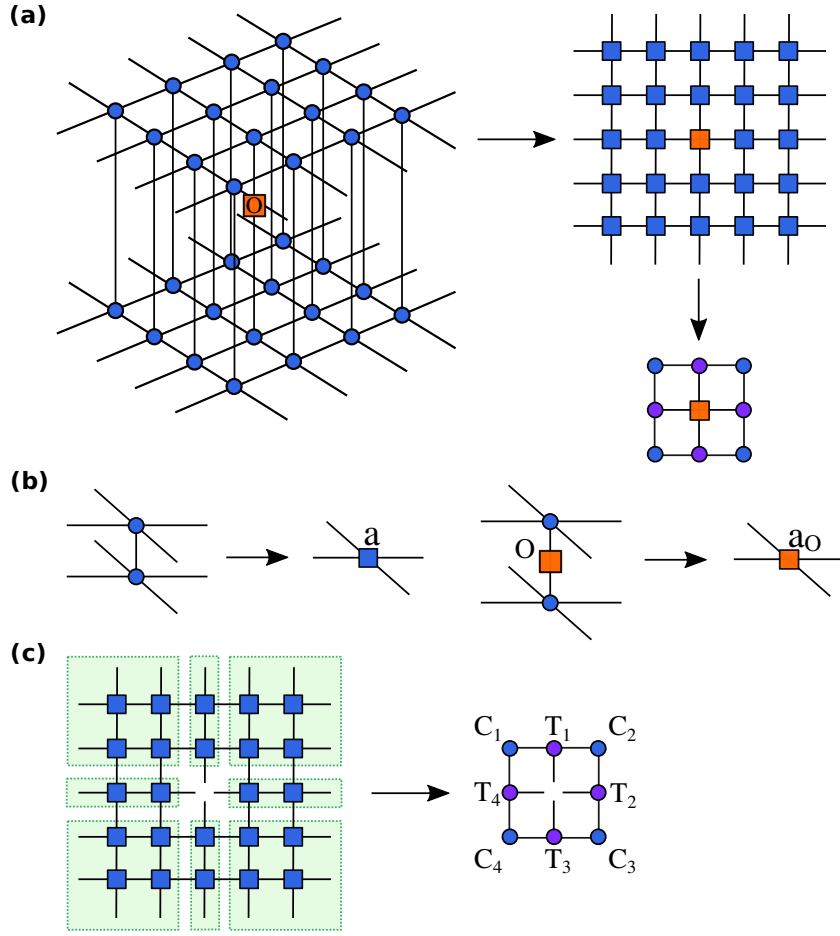


Figure 2.19: (a) Computing an expectation value  $\langle \Psi | O | \Psi \rangle$  with iPEPS. The contraction of two iPEPS leads to an infinite 2D network made of reduced tensors. (b) Reduced tensors of the iPEPS-iPEPS network. (c) The infinite environment of an iPEPS site represented by eight CTM tensors.

– these tensors are connected by new virtual bond indices of size  $\chi$ . Similarly to the bond dimension of MPS and PEPS, the environmental bond dimension  $\chi$  is the parameter that controls the accuracy of the CTM approximation of environment. The goal of CTM algorithm is to obtain the environmental tensors by performing a series of coarse graining moves:

1. Initialize the CTM tensors, e.g. using a random-number initialization, or a mean field environment with  $\chi = 1$ .
2. Perform four coarse graining moves in the left, right, up, and down directions. The left move involves the following steps, illustrated graphically in Fig. 2.20(a):
3. Insertion: insert an extra column into the CTM network that contains the unit cell tensor  $a$ , and the transfer tensors  $T_{1,3}$ .

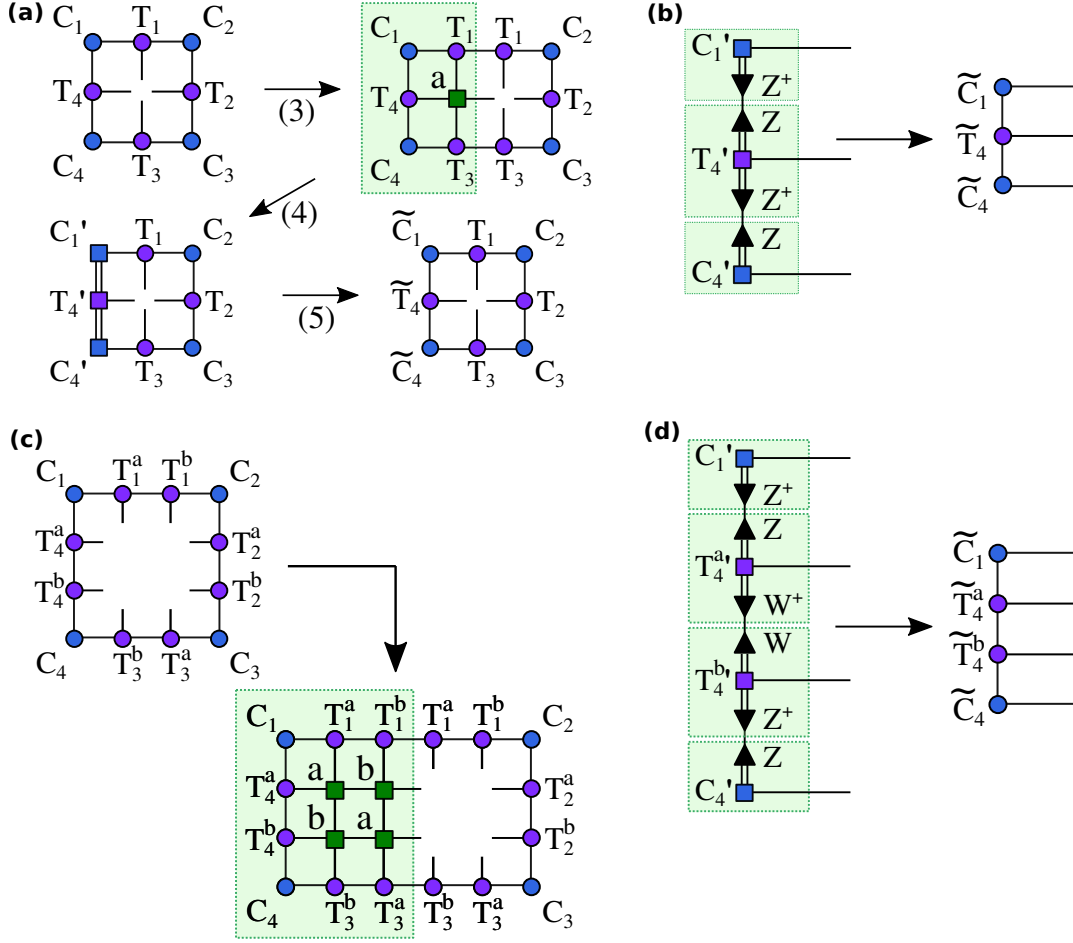


Figure 2.20: (a) The main steps (3-5) of the left move of the CTM algorithm for a one-site unit cell containing tensor  $a$ . (b) The renormalization step (5) is done by inserting isometries  $ZZ^+ = I$  into the left edge of CTM network. (c) The insertion step of the left move of the CTM algorithm for a two-site unit cell containing tensors  $a, b$ . (d) The renormalization step for a two-site unit cell is done by inserting two types of isometries,  $ZZ^+ = I$  and  $WW^+ = I$ .

4. Absorption: absorb the new column into the left side of the CTM environment by contracting their respective tensors. This increases the environmental bond dimension by  $\chi \rightarrow D^2\chi$ : to prevent the bonds from growing indefinitely we must implement an appropriate truncation scheme.
5. Renormalization: truncate the environmental tensors by inserting appropriate isometries  $ZZ^+ = I$  that reduce the bond dimensions  $D^2\chi \rightarrow \chi$  by projecting onto a relevant subspace, as shown in Fig. 2.20(b).
6. Repeat steps (2-5) to let the CTM environment grow in all four directions until it converges. Convergence is typically achieved when the eigenspectrum of each corner matrix  $\{C_{1,2,3,4}\}$  reaches the fixed point.

The CTM algorithm for a two-site unit cell, containing two  $a$  and  $b$  tensors, follows the same steps as the one-site algorithm outlined above. The environment

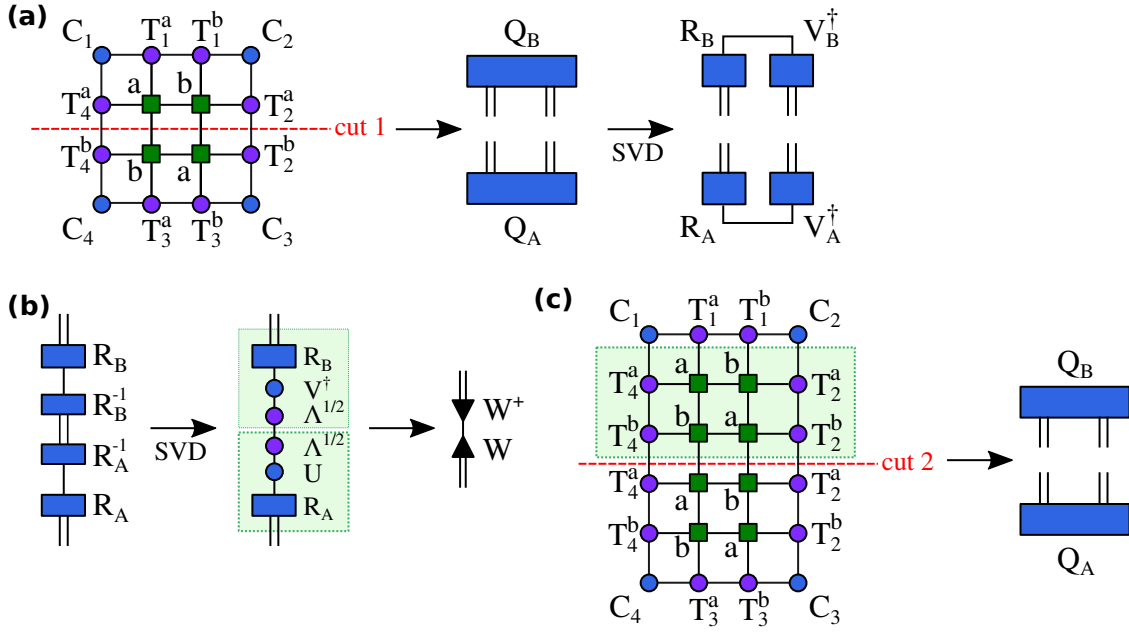


Figure 2.21: (a,b) The steps to compute  $W, W^+$  isometries for the bonds split by the 'cut-1'. (c) To compute  $Z, Z^+$  isometries for the bonds split by the 'cut-2', we perform a translationally-invariant shift by inserting two extra rows of tensors in the green box, and repeat the steps in (a).

is now specified by a set of four corner matrices  $\{C_{1,2,3,4}\}$ , and eight transfer tensors  $\{T_{1,2,3,4}^a, T_{1,2,3,4}^b\}$ . The main difference is that in the 'Insertion' step we now insert two new columns instead of just one, as shown in Fig. 2.20(c). There are now two 'Absorption' and 'Renormalization' steps in the algorithm: the absorption of each column is followed by renormalization to reduce the bond dimension  $D^2\chi \rightarrow \chi$ . The two-site algorithm also needs two types of isometries  $ZZ^+ = I$  and  $WW^+ = I$  in the 'Renormalize' step, to obtain renormalized transfer tensors  $\tilde{T}_4^{a,b}$  and corner tensors  $\tilde{C}_{1,4}$  in Fig. 2.20(d).

Clearly, the crucial step of CTM algorithm is calculating the isometries. Several different methods exist, for instance the ones described in Refs. [220, 225, 228], which we have implemented and tested in the process of developing our iPEPS code. The prescription we have found to work best was the one in Ref. [228], which achieved a smoother convergence and a more efficient representation of the environment than its predecessors. Fig. 2.21 illustrates graphically the calculation of  $Z, W$  isometries to be used in the 'Renormalize' step of the left move. In Fig. 2.21(a,b) we compute  $W, W^+$  isometries to be inserted into the bonds split by the 'cut-1'. In the first stage in Fig. 2.21(a), we contract the lower and upper parts of the network, producing the tensors  $Q_A$  and  $Q_B$  respectively. In the second stage, also in Fig. 2.21(a), we decompose  $Q_A$  and  $Q_B$  using an exact SVD to obtain the  $R_{A,B}$  and  $V_{A,B}^\dagger$  tensors. In the third stage in Fig. 2.21(b), we form the product  $I = R_A [R_A^{-1} R_B^{-1}] R_B$ , and decompose  $[R_A^{-1} R_B^{-1}] = U \Lambda V^\dagger$  using SVD, this time truncating to the  $\chi$  dominant singular values. The  $R_{A,B}$  matrices and the SVD matrices are then combined in the symmetrized fashion  $I \approx [R_A U \Lambda^{1/2}] [\Lambda^{1/2} V^\dagger R_B] = W W^+$  to construct the

isometries  $W = [R_A U \Lambda^{1/2}]$  and  $W^+ = [\Lambda^{1/2} V^\dagger R_B]$ . To obtain the  $Z, Z^+$  isometries for the bonds split by the 'cut-2', we perform a translationally-invariant shift by inserting two extra rows of tensors in the green box, as shown in Fig. 2.21(c). Contracting the lower and upper parts of the network then gives tensors  $Q_{A,B}$  for the cut-2. We can now compute  $Z, Z^+$  repeating exactly the same steps as for the  $W, W^+$  before. Once all isometries  $Z, Z^+$  and  $W, W^+$  are available, one can finally use them to carry out the renormalization in Fig. 2.20(d).

The CTM algorithm described above has a computational complexity of  $O(\chi^3 D^6 + \chi^2 D^8)$ . The reader may question if the renormalization scheme above is truly the optimal way of performing truncation. An important fact here is that, unlike MPS, PEPS does not have a well defined canonical form, and so there is no clear way of constraining the gauge freedom of PEPS tensors. As a consequence, there is no obvious optimal truncation procedure for CTM. The existing CTM renormalization schemes such as the one described here thus mainly rely on intuition and empirical evidence [228]. Once we have found a converged CTM environment, it can be used to compute various observables, as shown in Fig. 2.19(a) for a one-site unit cell.

### 2.3.2 iPEPS algorithm: simple update

We next introduce two different imaginary time update schemes for iPEPS with the nearest-neighbour interactions. The first one is the Simple Update (SU), which follows essentially the same main steps as the imaginary time iTEBD algorithm in Sec. 2.2.3 to compute the ground state given by Eq. (2.20). However, there are a few important differences due to the higher dimensionality that we will discuss here. First, in two dimensions we perform Trotter decomposition by splitting our Hamiltonian into four terms  $H_U, H_D, H_R$  and  $H_L$  (instead of just two in 1D), describing respectively the 'U' (up), 'D' (down), 'R' (right), and 'L' (left) bonds of the lattice, as shown in Fig. 2.22:

$$H = H_U + H_D + H_R + H_L \quad (2.39)$$

The first order Trotter decomposition of the time evolution operator  $U(\delta\tau) = e^{-H\delta\tau}$  then reads:

$$U(\delta\tau) = e^{-\delta\tau H_U} e^{-\delta\tau H_R} e^{-\delta\tau H_D} e^{-\delta\tau H_L} + O(\delta\tau^2) \quad (2.40)$$

where  $\delta\tau$  is the imaginary timestep. Similarly to iTEBD in one dimension, in SU we represent iPEPS using Vidal form. An iPEPS with a two-site unit cell is fully specified by two  $\Gamma^{[A,B]}$  site tensors and four  $\Lambda^{[U,R,D,L]}$  diagonal matrices that store the singular values of iPEPS bonds, as seen in Fig. 2.22. We label the local Hilbert space dimension by  $d$ , and the bond dimension by  $D$ .

Another difference lies in the update procedure itself. For a more specific example, let us consider the tensor update of an 'U' bond. Fig. 2.23 shows diagrammatically the following steps of SU which replace the steps (3-5) of the one dimensional iTEBD algorithm in Sec. 2.2.3:

1. Absorb  $\Lambda^{[R,D,L]}$  tensors on the external bonds into  $\Gamma^{[A,B]}$  to obtain  $Q^{[A,B]}$ .

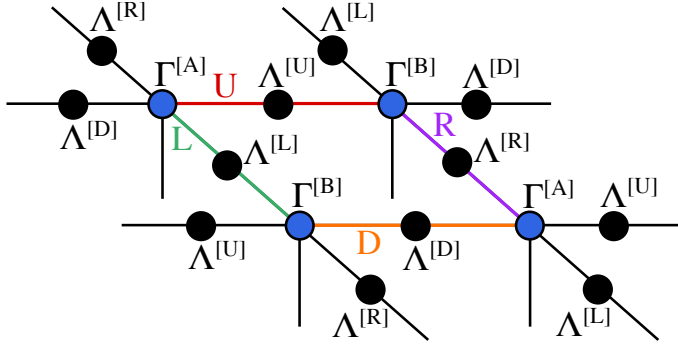


Figure 2.22: The iPEPS time evolution using Eq. (2.40) involves propagating four different bonds ‘U’, ‘D’, ‘R’, and ‘L’, indicated by different colours. The SU algorithm uses Vidal form with  $\Gamma^{[A,B]}$  site tensors and  $\Lambda^{[U,R,D,L]}$  diagonal bond matrices to represent iPEPS with a two-site unit cell.

2. Decompose each of  $Q^{[A,B]}$  into subtensors  $v_{A,B}$  and  $X_A, Y_B$  using an exact SVD or QR/LQ decompositions. The original rank-5 tensors  $\Gamma^{[A,B]}$  had the dimensionality of  $d \times D \times D \times D \times D$  giving rise to a large computational cost  $O(d^3 D^9)$  of the update procedure. However, an update performed using the new rank-3 subtensors has a substantially reduced cost of  $O(d^6 D^3)$  since the dimensions of  $v_{A,B}$  are considerably smaller and equal to  $d \times dD \times D$  and  $d \times D \times dD$  respectively.
3. Contract the two-body propagator  $e^{-\delta\tau H_U}$  with  $v_{A,B}$  and  $\Lambda^{[U]}$  to form  $\theta$  tensor.
4. Decompose  $\theta$  tensor into  $\tilde{v}_{A,B}$  and  $\tilde{\Lambda}^{[U]}$  tensors using SVD. To prevent the bond dimension of our tensors from growing indefinitely, we must truncate  $\tilde{v}_{A,B}$  and  $\tilde{\Lambda}^{[U]}$  by retaining  $D$  largest singular values and discarding the rest.
5. Recover the updated rank-5 tensors  $\tilde{Q}^{[A,B]}$  by contracting the rank-3 subtensors  $\tilde{v}_{A,B}$  with  $X_A, Y_B$  respectively.
6. To restore  $\Lambda^{[R,D,L]}$  on the external bonds, we divide each of  $Q^{[A,B]}$  by  $\Lambda^{[R]}$ ,  $\Lambda^D$ , and  $\Lambda^{[L]}$ . This procedure brings iPEPS back to its original Vidal form, with updated tensors  $\tilde{\Gamma}^{[A,B]}$  and  $\tilde{\Lambda}^{[U]}$  for each ‘U’ bond on the lattice.

All other steps than the ones discussed above remain exactly the same as in the one dimensional TEBD algorithm. As before, to find the ground state we propagate iPEPS for  $N$  imaginary timesteps  $\delta\tau$  until convergence is achieved with respect to the spectrum of singular values in  $\Lambda^{[U,R,D,L]}$ .

The SU algorithm is both simple and very efficient, with computational cost  $O(D^3 d^6)$  of the time evolution. The bottleneck of an SU iPEPS simulation is the CTM calculation of the environment, scaling as  $O(\chi^3 D^6 + \chi^2 D^8)$ . Fortunately, it only has to be done once, to extract observables after the ground state has converged. However, SU is suboptimal since it employs local truncations without taking into account the full environment of a unit cell. For MPS updates, this issue can be resolved relatively easily by transforming the tensor network into a canonical form, which orthonormalizes other bonds surrounding the bond being truncated.

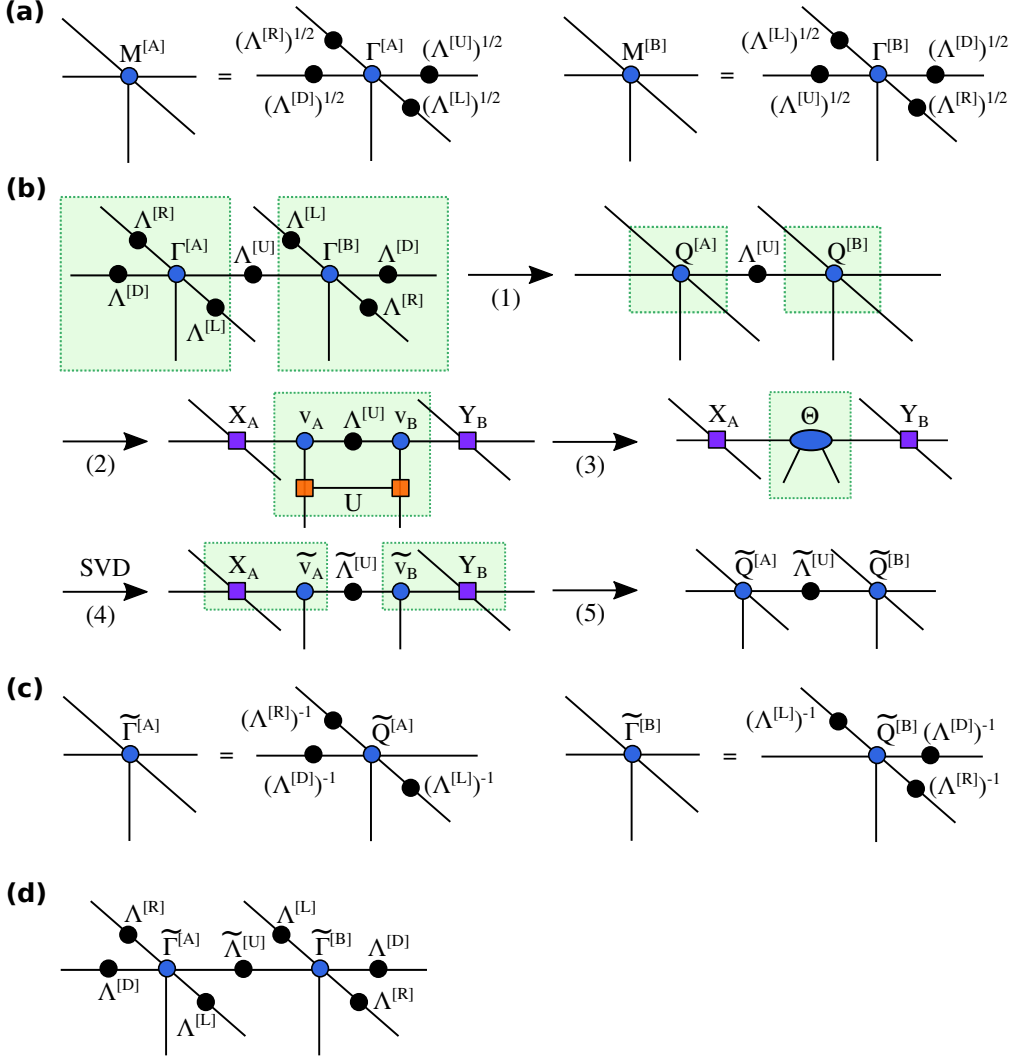


Figure 2.23: (a) Relation between iPEPS in the standard form in Fig. 2.18 in terms of  $M^{[A,B]}$  tensors, and iPEPS in Vidal form in terms of  $\Gamma^{[A,B]}$  and  $\Lambda^{[U,R,D,L]}$  tensors in Fig. 2.22. (b) Steps (1-5) of SU for 'U' bond of iPEPS. (c) Step (6) of SU for 'U' bond. (d) iPEPS with  $\tilde{\Gamma}^{[A,B]}$  and  $\tilde{\Lambda}^{[U]}$  updated for each 'U' bond in the lattice.

Due to the aforementioned non-existence of the PEPS canonical form, this solution is not possible in 2D, and SU will always introduce systematic errors due to its local nature. To achieve an optimal truncation, one must use a variational update scheme that computes the full environment at every step. This procedure, known as the Full Update (FU), is considerably more expensive and bears the computational cost of  $O(N\chi^3D^6 + N\chi^2D^8)$  where  $N$  is the number of steps of the imaginary time evolution. In practice, SU has been applied extensively to various models and yields highly accurate results for systems with large gaps and sufficiently short correlation lengths [221]. Due to its simplicity and efficiency, it allows shorter computation times and significantly higher bond dimensions than FU, and thus remains popular in the PEPS community. However, it is far less accurate near quantum critical points when correlation lengths become long, and in these cases FU should be used

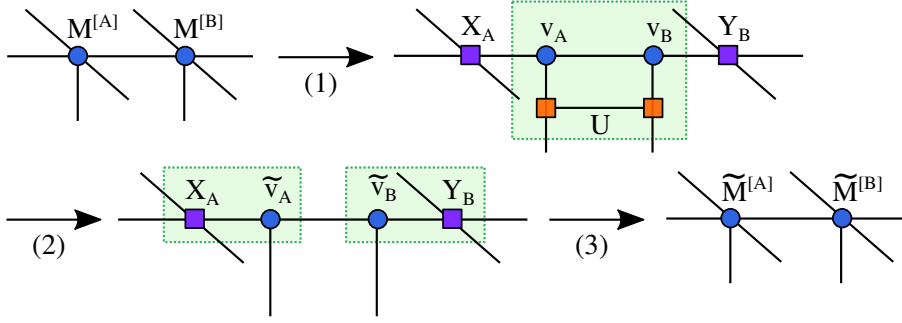


Figure 2.24: The steps of FU update for ‘U’ bond of iPEPS expressed in terms of  $M^{[A,B]}$  tensors. (1) Decompose each of  $M^{[A,B]}$  into subtensors  $v_{A,B}$  and  $X_A, Y_B$  using an exact SVD or QR/LQ decompositions. (2) Update  $v_{A,B}$  subtensors using the two-body propagator  $e^{-\delta\tau H_U}$ , to find new subtensors  $\tilde{v}_{A,B}$ . (3) Recover the updated  $M^{[A,B]}$  tensors by contracting the new subtensors  $\tilde{v}_{A,B}$  with  $X_A, Y_B$  respectively.

instead.

### 2.3.3 iPEPS algorithm: full update

The Full Update (FU) algorithm is a more accurate approach for updating iPEPS that takes into account the full environment of a unit cell. The basic steps of the FU procedure are shown in Fig. 2.24 – they remain essentially the same as in the SU algorithm outlined in the last section. Instead of Vidal form, FU uses the regular iPEPS representation, as in Fig. 2.18, that does not have  $\Lambda$  tensors on the bonds.

The main difference between the two algorithms occurs in the step (2) of FU compared to the step (4) of SU. While SU updates iPEPS tensors by simply truncating the spectrum of singular values, FU performs a two-site variational optimization instead. Applying a two-body propagator  $e^{-\delta\tau H_i}$  ( $i \in \{U, R, D, L\}$ ) to  $v_{A,B}$  without any truncation yields the exact updated subtensors  $v_{A,B}'$ . The goal of FU is to find the optimal subtensors  $\tilde{v}_{A,B}$  approximated by a fixed bond dimension  $D$ . To this end, we minimize the distance  $F(\tilde{v}_A, \tilde{v}_B, v_A', v_B')$  between the state  $|\Psi(\tilde{v}_A, \tilde{v}_B)\rangle$  with the approximate subtensors, and the state  $|\Psi(v_A', v_B')\rangle$  with the exact subtensors:

$$\begin{aligned}
 F(\tilde{v}_A, \tilde{v}_B, v_A', v_B') &= || |\Psi(\tilde{v}_A, \tilde{v}_B)\rangle - |\Psi(v_A', v_B')\rangle ||^2 \\
 &= \langle \Psi(\tilde{v}_A, \tilde{v}_B) | \Psi(\tilde{v}_A, \tilde{v}_B) \rangle + \langle \Psi(v_A', v_B') | \Psi(v_A', v_B') \rangle \\
 &\quad - \langle \Psi(v_A', v_B') | \Psi(\tilde{v}_A, \tilde{v}_B) \rangle - \langle \Psi(\tilde{v}_A, \tilde{v}_B) | \Psi(v_A', v_B') \rangle
 \end{aligned} \tag{2.41}$$

The first step of FU is to compute the environment of the bond being updated by utilizing the CTM algorithm and obtain the diagrammatic representation in Fig. 2.25 that consists of six environmental tensors  $E_{1,2,3,4,5,6}$ . Since we are optimizing the subtensors  $\tilde{v}_{A,B}$  rather than the original iPEPS tensors  $M^{[A,B]}$ , the full environment of the bond is given by the  $E$  tensor in Fig. 2.25 and we can write the distance Eq. (2.41) diagrammatically as Fig. 2.26(a). Since  $F(\tilde{v}_A, \tilde{v}_B, v_A', v_B')$  is a quadratic function of  $\tilde{v}_{A,B}$ , we can minimize it using the Alternating Least-Squares (ALS) technique. Let us first minimize  $F(\tilde{v}_A, \tilde{v}_B, v_A', v_B')$  with respect to  $\tilde{v}_A$  while

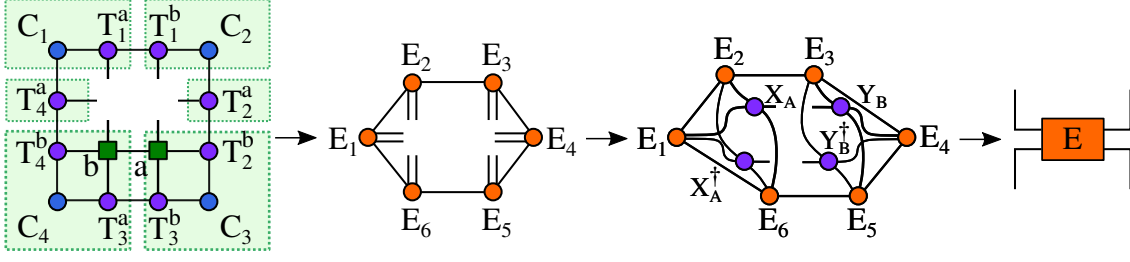


Figure 2.25: Computing the iPEPS environment of the ‘U’ bond. We first contract the CTM tensors and the lower bond with tensors  $b$ ,  $a$  (corresponding to the ‘D’ bond of iPEPS in Fig. 2.22), into a six-site representation of the environment consisting of tensors  $E_{1,2,3,4,5,6}$ . Combining  $E_{1,2,3,4,5,6}$  with  $X_A$ ,  $Y_B$  sub-tensors then yields a single  $E$  tensor describing the environment of the two sub-tensors  $v_{A,B}$  of interest.

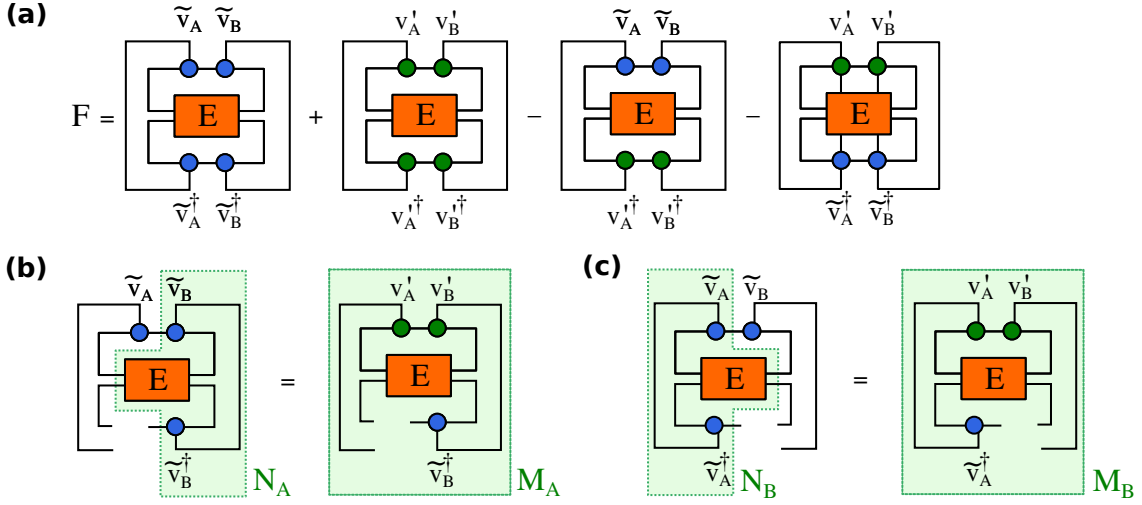


Figure 2.26: (a) Diagrammatic representation of the distance  $F$  in Eq. (2.41). (b) Diagrammatic representation of the linear equation Eq. (2.43) with matrix  $\mathcal{N}_A$  and vectors  $\mathcal{M}_A$ ,  $\tilde{v}_A$ . (c) Diagrammatic representation of the linear equation Eq. (2.45) with matrix  $\mathcal{N}_B$  and vectors  $\mathcal{M}_B$ ,  $\tilde{v}_B$ . The matrices  $\mathcal{N}_{A,B}$  and vectors  $\mathcal{M}_{A,B}$ ,  $\tilde{v}_{A,B}$  have composite three-leg indices.

holding  $\tilde{v}_B$  fixed

$$\frac{\partial F(\tilde{v}_A, \tilde{v}_B, v_A', v_B')}{\partial [\tilde{v}_A]^\dagger} = 0 \quad (2.42)$$

illustrated graphically in Fig. 2.26(b). Treating  $\tilde{v}_A$  as a vector with combined triple index, Eq. (2.42) can be written as a matrix-vector equation

$$\mathcal{N}_A \tilde{v}_A - \mathcal{M}_A = 0 \quad (2.43)$$

with matrix  $\mathcal{N}_A$  and vector  $\mathcal{M}_A$  defined in Fig. 2.26(b). Therefore, we have just reduced the problem of minimizing the sum of iPEPS-iPEPS overlaps in Eq. (2.41) with respect to  $\tilde{v}_A$  to a simple linear algebra problem Eq. (2.43) that one can easily solve for  $\tilde{v}_A$  using standard linear algebra packages. The solution  $\tilde{v}_A$  is then used to update all structures in Fig. 2.26(a) before the next minimization takes place.



Following the same steps, we minimize  $F(\tilde{v}_A, \tilde{v}_B, v_{A'}, v_{B'})$  with respect to  $\tilde{v}_B$  while holding  $\tilde{v}_A$  fixed:

$$\frac{\partial F(\tilde{v}_A, \tilde{v}_B, v_{A'}, v_{B'})}{\partial [\tilde{v}_B]^\dagger} = 0 \quad (2.44)$$

shown in Fig. 2.26(c). Again, it can be written as a matrix-vector equation

$$\mathcal{N}_B \tilde{v}_B - \mathcal{M}_B = 0 \quad (2.45)$$

which we solve for  $\tilde{v}_B$  and update all structures in the equation Fig. 2.26(a). This alternating minimization process is iterated until we observe that the subtensors  $\tilde{v}_{A,B}$  have converged, which completes the step (2) in Fig. 2.24. Often an effective approach is to combine the best of both update schemes: compute the ground state iPEPS using imaginary time evolution with the Simple Update, and then use it as a starting point for imaginary time evolution with the Full Update.



## Part II

# Driven dissipative coupled cavity arrays



# Chapter 3

## Fluorescence spectrum and thermalization in 1D

### 3.1 Introduction

Nonlinear coupled cavity arrays provide a promising platform for studying the nonequilibrium physics in driven dissipative many body systems [15, 60, 80]. Owing to recent experimental progress in the fabrication of superconducting circuits, circuit QED networks made of superconducting qubits and microwave resonators provide powerful means for realizing extended coupled cavity arrays with strong optical nonlinearities [15, 36, 86]. In circuit QED, polariton quasiparticles are simply the circuit excitations [60]. Both local and collective properties of coupled cavity arrays are then accessible via correlation functions, transmission signals and optical spectra of the emitted photons [15, 60].

The first circuit QED experiments focused on small coupled cavity systems, such as cavity dimers and trimers [80]. Nonetheless, more recent experiments are already entering the territory of many-body physics. Fitzpatrick et al [86] have built a circuit QED chain of 72 resonators and qubits, each resonator coupled to its nearest neighbour and its local transmon qubit. They studied the transmission spectrum of this coupled cavity system, observing a dissipative phase transition to a suppressed transmission state while sweeping the driving power from low to high at a constant frequency. In another recent work, Ma et al [36] have utilized superconducting circuits to build a Bose-Hubbard lattice of 8 transmon qubits interacting with microwave photons, and have realized a photonic Mott insulator stabilized against losses. This work has also examined the thermalization dynamics in the chain near its steady state by observing the propagation of a hole defect in the dissipatively prepared Mott insulator phase.

In this chapter, we explore a novel area relevant to the experimental probes of driven dissipative lattice systems: the multi-time correlation functions and fluorescence spectra. Most theoretical work to date has focused exclusively on the static observables, such as order parameters and equal-time spatial correlation functions, and on utilizing them to characterize steady state phase diagrams [44, 65, 67–70, 72, 73, 76, 229].

On the other hand, previous work has hardly considered dynamical observables,

such as frequency-resolved spectra and two-time correlations. In a system with a coherent optical drive, static observables correspond to observing the elastically scattered light. A driven nonlinear system, however, will involve inelastic scattering processes and thus emit radiation at frequencies other than the drive frequency. Dynamical correlation functions correspond to measuring such incoherent fluorescence. To understand the nature of this fluorescence, let us look at the photon emission process more closely. Due to the strong light-matter coupling, photons and optical emitters in a coupled cavity system form polaritons that are created or destroyed when photons enter or leave a cavity. Emission of a photon from a cavity destroys a polariton in a coupled cavity array. Yet, the energy and momentum conservation laws ensure that the energy and momentum of this photon are directly related to those of the destroyed polariton. In other words, polaritons in our setting possess a momentum  $\mathbf{k}$  aligned with one axis of a 1D coupled cavity array. Once photons escape, they propagate in the free 3D space satisfying the dispersion relation  $E(\mathbf{k}) = c|\mathbf{k}|$  in three dimensions – but, at the same time, the momentum  $\mathbf{k}$  of a photon retains the same magnitude and remains aligned in the same way as it was inside the 1D coupled cavity system. Measuring the fluorescence of such escaping photons reflects the energy and momentum of the polaritons inside the coupled cavity array, and contains the fingerprints of their scattering processes. Therefore, incoherently scattered light from coupled cavity lattice systems carries a wealth of important information about their underlying many body physics: the normal modes and their occupations, coherence times, scattering phenomena that are particularly relevant to nonlinear optics, exotic nonequilibrium phenomena such as limit cycles and time crystals, and many others. The second order two-time correlations also allow us to measure photon statistics – the bunching or antibunching of photons [230, 231].

In the context of experiments with microwave resonators and superconducting qubits [15, 36, 86], one can access these properties by measuring fluorescence spectra. A relevant example here is Ref. [232], who demonstrated the utility of the fluorescence spectrum and second order two-time correlations for characterizing photon blockade and effective photon-photon interactions in a single-cavity circuit QED setup. More specifically, they observed the appearance of the Mollow triplet in the resonance fluorescence spectrum of the system, and a strong photon antibunching in the second order two-time correlation function as the key signatures of photon blockade. It is also possible to obtain momentum-resolved fluorescence spectra of extended coupled-cavity lattice systems by observing the interference of light emitted from different cavities. The interference measurements allow a site-resolved spectroscopy of the coupled cavity lattice, and we can subsequently obtain the momentum-resolved spectrum by taking a Fourier transform. One can connect such measurements with observables extracted using solid state probes, for example, angle resolved photon emission, spectroscopic scanning tunneling microscopy, or neutron scattering, since they measure the excitation and fluctuation spectra of correlated states. More generally speaking, one usually obtains the information about many body physics in various types of interacting light-matter systems from spectroscopic measurements of the light emitted, absorbed or transmitted through the system, making theoretical calculations of spectra an important tool for pre-

dicting the properties of these systems.

However, the calculations of spectra and dynamics have largely been missing in the studies of quantum optical many body lattice systems. In this chapter, we will present a numerically exact algorithm based on MPS techniques for calculating two-time correlations in the thermodynamic limit. We will then utilize it to compute two-time correlation functions of a driven dissipative infinite lattice system in 1D, and use them to simulate the energy and momentum resolved fluorescence spectra. The focal point of this chapter will be to demonstrate how we can extract the information about the nature of the nonequilibrium steady state (NESS) of a coupled cavity array by measuring its emission spectrum. In particular, we will use fluorescence to study the quasi-thermalization occurring in the NESS, and show that blue-detuned pumping stabilizes a state with a negative effective temperature. Finally, we will compare our numerical results to analytical spin-wave theory in the limit of low density of excitations.

## 3.2 Calculating two-time correlations in the thermodynamic limit

Let us first discuss the problem of calculating two-time correlations in open quantum many-body lattice systems in 1D. Our primary goal is going beyond the mean field theories or low-order expansions, and developing a numerically exact method that fully accounts for quantum fluctuations and offers a systematic way to control the errors so that we can avoid making uncontrolled approximations. Also, we are looking for a method that can access the thermodynamic limit, and thus allow us to study truly large many body systems. The MPS techniques satisfy both of these criteria: various one-dimensional tensor network algorithms such as iTEBD or iDMRG enable us to simulate infinite size systems. In particular, iTEBD can perform the time evolution directly in the thermodynamic limit, and has readily been extended to density matrices of open quantum systems [40–44].

The reader may question if the thermodynamic limit is indeed relevant to our understanding and the present day experiments with coupled cavity arrays. From the conceptual perspective, one motivation is the difficulty in distinguishing the phenomena that arise due to the genuine many-body physics of the bulk, from the phenomena introduced by the boundary and the finite size effects in our numerical simulations [233]. In the infinite lattice simulations, these effects are completely eliminated, offering an easier way to gain insight into the many-body physics compared to the simulations of large but finite size systems. In many problems, one is also interested in the phenomena with long range correlations, such as the critical behaviour where correlation lengths diverge as  $\xi \rightarrow \infty$ . To capture the physics accurately in such situations, one needs appropriate simulation methods that work directly in the thermodynamic limit.

On the purely experimental side, it is important to note that the circuit QED realizations of coupled cavity arrays are rapidly moving towards larger scales. While the first experiments were restricted to cavity dimers and trimers [88–91], a coupled cavity array with 72 sites has already been built [86], and setups comprising

hundreds of resonators and qubits are now within the reach of current technology [15]. Overall, building quantum simulators for large scale quantum matter out of equilibrium is the ultimate goal of the field [15, 60, 80, 86]. This provides a major impetus both for large scale circuit QED networks and for numerical methods in the thermodynamic limit, which will be increasingly more relevant as the experimental realizations grow in size.

A simple recipe for computing a two-time correlation function  $\langle O_2^{(j)}(t)O_1^{(i)}(0) \rangle$  for a system in the nonequilibrium steady state (NESS) would be as follows. We first precompute NESS using iTEBD algorithm, which finds a translationally invariant infinite MPS representing the NESS density matrix  $\rho_{ss}$  for a Liouvillian  $\mathcal{L}$ , such that  $\mathcal{L}\rho_{ss} = 0$ . Next, we can use the quantum regression theorem to find a two-time correlator of a Markovian system [1]

$$\langle O_2^{(j)}(t)O_1^{(i)}(0) \rangle = \frac{\text{Tr} [O_2^{(j)} e^{t\mathcal{L}} O_1^{(i)} \rho_{ss}]}{\text{Tr} [e^{t\mathcal{L}} \rho_{ss}]}. \quad (3.1)$$

where  $O_{1,2}$  are local operators that act on lattice sites  $i, j$  respectively. Starting in NESS  $\rho_{ss}$ , we apply the first operator  $O_1^{(i)}$  at time  $\tau = 0$  and lattice site  $i$ . We then evolve the new state until a later time  $\tau = t$  under Liouvillian propagator  $e^{t\mathcal{L}}$ . At time  $\tau = t$ , we apply the second operator  $O_2^{(j)}$ , which acts on lattice site  $j$ , and compute the trace. This procedure gives a general two-time, two-point correlator  $\langle O_2^{(j)}(t)O_1^{(i)}(0) \rangle$ . Unfortunately, applying a local operator  $O_1^{(i)}$  at  $\tau = 0$  introduces a local perturbation at site  $i$  of the system and breaks its translational symmetry so that it can no longer be represented by an infinite MPS. A direct time evolution is thus incompatible with the infinite TEBD algorithm. A naive solution would be to resort to a finite-size extrapolation: i.e. to time evolve a finite MPS using TEBD for increasingly larger lattice sizes until convergence with respect to the size is achieved. While this approach may prove to be sufficient for some problems, it has serious conceptual issues. In particular, it will be prone to boundary and finite-size effects: the finite lattice size would restrict the extent of correlations in both space and time, as excitations will be reflected back from the boundaries, and the simulation will be no longer valid at later times [233]. Such simulation would also incur an additional computational cost that scales linearly with the system size which will be inefficient for large lattices needed to approximate the thermodynamic limit, in comparison to only two sites required for the simplest unit cell in iTEBD. Nevertheless, such a finite-size approach has recently been used to calculate aging dynamics in the XXZ model [234]. Fortunately, it is possible to eliminate the finite size issues entirely. To achieve this, we build on a method proposed by Bañuls et al [235] for the unitary real-time evolution of wavefunctions of isolated quantum systems. This method is based on transfer MPOs, and enables the calculation of two-time correlations in an infinite lattice directly, without using a finite-size extrapolation. In our work, we extend this method to the non-unitary Liouvillian time evolution for density matrices of open quantum systems. We describe the transfer MPO algorithm below, along with some of its technical details.

The main idea behind the transfer MPO algorithm is to avoid explicit stepwise time evolution of MPS. Instead of evolving MPS in time step by step, we con-



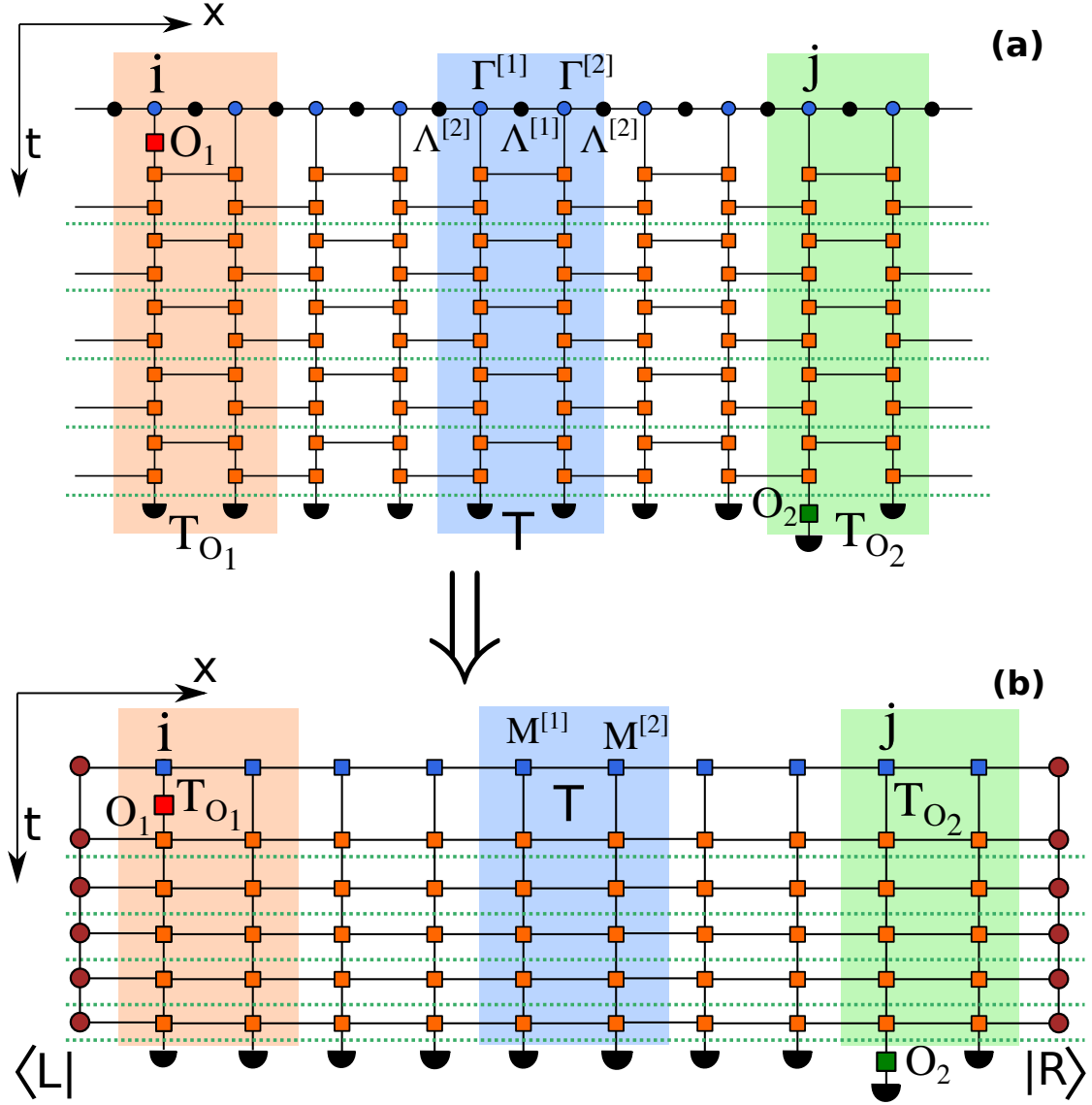


Figure 3.1: (a) Tensor network representation of Eq. (3.1). We perform time evolution of the vectorized density matrix  $|\rho\rangle_{\text{ss}}$  iMPS in Vidal form (blue and black circles are  $\Gamma$  and  $\Lambda$  tensors respectively) using iTEBD with two-body propagators (orange squares). At the initial time  $\tau = 0$  operator  $O_1$  (red square) acts on site  $i$ , and at the final time  $\tau = t$  operator  $O_2$  (green square) acts on site  $j$ . At  $\tau = t$  we take the trace by applying vectorized identity matrices (black semicircles) at each site. The green dotted lines separate adjacent timesteps. (b) Tensor network corresponding to Eq. (3.4), where the time evolution network in (a) is expressed in terms of transfer MPOs  $T$  (blue box),  $T_{O_1}$  (red box), and  $T_{O_2}$  (green box) as well as the left and right boundary MPS  $\langle L|$  and  $|R\rangle$  (brown circles). To obtain the MPO-MPS structure in (b), we have combined the two-body propagators within the same timestep into a single MPO, as illustrated in Fig. 3.2(a). We have also absorbed  $\Lambda$  tensors symmetrically into  $\Gamma$  tensors, as shown in Fig. 3.2(b). The vertical  $t$  and the horizontal  $x$  axes in both figures are the temporal and spatial axes respectively.

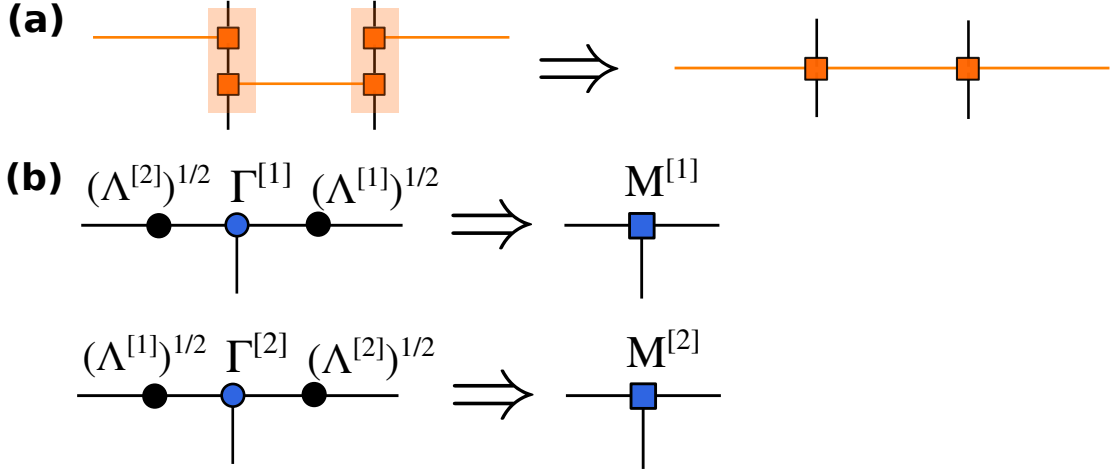


Figure 3.2: (a) Combining two-body propagators within the same timestep into a single MPO. (b) Absorbing  $\Lambda$  tensors symmetrically into  $\Gamma$  tensors gives iMPS with  $M^{[1,2]}$  tensors.

construct a two-dimensional network representing the entire time evolution, displayed in Fig. 3.1(a). For simplicity of explanation, the time evolution in Fig. 3.1(a) uses the first order Trotter splitting. The arguments presented in this section are easily extendable to the higher order Trotter decompositions, and all of our numerical results use the second order Trotter decomposition. We start from the initial infinite MPS of the vectorized NESS density matrix  $|\rho_{ss}\rangle$ , and apply the first operator  $O_1^{(i)}(0)$  at the initial time  $t = 0$ . Then, for every time evolution step we insert a propagator represented as an MPO in Fig. 3.2(a). After repeating this for the required number of timesteps, we apply the second operator  $O_2^{(j)}(t)$  at the final time  $t$ . Taking the trace at the final time removes the dangling physical dimension at each site of the last MPO propagator. We obtain a two-dimensional network that corresponds to an exact (unnormalized) two-time, two-point correlator  $\langle O_2^{(j)}(t) O_1^{(i)}(0) \rangle$ , since no truncation has taken place yet. If we did not apply any operators and did not take the trace after the last time step, this network would instead represent an exact time-evolved MPS.

The resulting network is infinite along the spatial axis but finite along the time axis. We exploit the translational symmetry, and define a transfer MPO  $T$  along the time axis in Fig. 3.1(a,b). This transfer MPO contains the time evolution of a single unit cell of the lattice. In the case of models with one-site translational invariance, iMPS will have a one-site unit cell. However, as explained earlier in Sec. 2.2.3, the pairwise propagation using two-body gates of the iTEBD algorithm modifies the translational symmetry from one-site to two-site, and one must work with a two-site unit cell instead. In our case, the transfer MPO is therefore a composite double-layer MPO that consists of two MPOs defined along the time axis, since it contains the time evolution of a two-site unit cell, as seen in Fig. 3.1. More generally, one may consider a transfer MPO for an arbitrary  $m$ -site unit cell, which will consist of  $m$  MPOs along the time axis. All transfer MPOs are identical and repeated ad

infinitem across the lattice, except at the sites where the operators are applied, and so the unnormalized correlator can be expressed as:

$$\langle O_2^{(j)}(t) O_1^{(i)}(0) \rangle \propto \lim_{N \rightarrow \infty} T^N T_{O_1} T^{|i-j|-1} T_{O_2} T^N, \quad (3.2)$$

where  $T$  is the transfer MPO of the evolved density matrix, and  $T_{O_{1,2}}$  are transfer MPOs with operators  $O_{1,2}$  applied at the initial and final times at lattice sites  $i, j$ , as shown in Fig. 3.1. As a result, our network contains a semi-infinite chain of transfer MPOs  $T$  to the left of  $T_{O_1}$  and to the right of  $T_{O_2}$ . From linear algebra, we can write down the eigendecomposition of a transfer MPO  $T = \sum_k \lambda_k |R_k\rangle \langle L_k|$ , where  $\lambda_k$  is the  $k$ 'th eigenvalue and  $|R_k\rangle$  and  $\langle L_k|$  are the corresponding right and left eigenvectors of  $T$ . If  $T$  is repeated an infinite number of times, one has  $\lim_{N \rightarrow \infty} T^N = \lim_{N \rightarrow \infty} \sum_k \lambda_k^N |R_k\rangle \langle L_k| = \lim_{N \rightarrow \infty} \lambda^N |R\rangle \langle L|$  where  $\lambda$  is the largest eigenvalue of  $T$  while  $|R\rangle$  and  $\langle L|$  are the corresponding dominant eigenvectors. Plugging this into Eq. (3.2) we obtain

$$\text{Tr} \left[ O_2^{(j)} e^{t\mathcal{L}} O_1^{(i)} \rho_{ss} \right] = \lim_{N \rightarrow \infty} \lambda^{2N} \langle L | T_{O_1} T^{|i-j|-1} T_{O_2} | R \rangle \quad (3.3)$$

which simply means that we may effectively replace the semi-infinite lattices to the left of  $T_{O_1}$  and to the right of  $T_{O_2}$  by  $|R\rangle$  and  $\langle L|$  respectively. By setting both operators to identity  $O_{1,2} = I$ , we obtain a network that equals the trace of a time-evolved density matrix  $\text{Tr} \rho(t) = \text{Tr} [e^{t\mathcal{L}} \rho_{ss}] = \lim_{N \rightarrow \infty} \lambda^{2N} \langle L | T^{|i-j|+1} | R \rangle = \lim_{N \rightarrow \infty} \lambda^{2N+|i-j|+1}$ . The normalized two-point two-time correlator is then given by:

$$\langle O_2^{(j)}(t) O_1^{(i)}(0) \rangle = \frac{\text{Tr} \left[ O_2^{(j)} e^{t\mathcal{L}} O_1^{(i)} \rho_{ss} \right]}{\text{Tr} [\rho(t)]} = \frac{\langle L | T_{O_1} T^{|i-j|-1} T_{O_2} | R \rangle}{\lambda^{|i-j|+1}}, \quad (3.4)$$

In practice, we compute an MPS approximation of the eigenvectors  $|R\rangle, \langle L|$  using the MPS-MPO power method. We start with an initial guess for our MPS defined along the time axis, and multiply it by  $T$  expressed as an MPO along the time axis a sufficient number of times until it converges. We perform the right-multiplication to compute  $|R\rangle$ , and left-multiplication to compute  $\langle L|$ . An efficient MPS-MPO multiplication requires extra care, and we have implemented the zip-up algorithm described in Chapter 2, which multiplies and truncates MPS on the fly. The truncation of the MPS bonds is done along the time axis, i.e. in the space of the  $|R\rangle, \langle L|$  eigenvectors rather than the actual density matrix MPS. Once we have calculated  $|R\rangle$  and  $\langle L|$ , the resulting network in Fig. 3.1(b) is finite along both space and time axes, and is given by a series of MPOs sandwiched between the two boundary MPSs. It can thus be contracted straightforwardly and efficiently using MPO-MPS and MPS-MPS multiplication algorithms [38, 201] described in Chapter 2, to give the desired two-time, two-point correlator Eq. (3.4).

The transfer MPO method thus provides powerful means to compute general two-time, two-point correlation functions in infinite lattice systems, and is straightforward to extend to higher order correlators (which would simply mean inserting more operators in the time evolution network). It also allows us to simulate time

evolution in the thermodynamic limit even in the presence of local perturbations or impurities, since it avoids the explicit breaking of the translational symmetry. Once we have found two-time correlation functions, spectra can be easily computed by performing a Fourier transform.

We also briefly discuss the shortcomings of transfer MPO approach. The most important one is that for the method to be successful, the transfer MPO must have a non-degenerate largest eigenvalue and eigenvectors that can be approximated by MPS of a sufficiently small bond dimension. It will, however, fail if the largest eigenvalue is degenerate, and more advanced methods such as Arnoldi iteration will be needed to compute the full set of degenerate dominant eigenvectors, and use a sum of networks to represent the time evolution, where each term in the sum comes from a different pair of the left and right eigenvectors. Another disadvantage is that the method requires storing MPS eigenvectors that will have as many sites as there are timesteps in time evolution, which can be very memory-consuming. We note that other promising methods have been proposed for computing dynamical correlations with MPS in the thermodynamic limit, based on infinite boundary conditions [233], or tangent space MPS methods [162, 182, 236]. While these methods have potential advantages over the transfer MPO approach, it remains unclear how they could be extended to Liouvillian time evolution of density matrices, which is a possible direction for future research. A major advantage of the transfer MPO algorithm is its versatility. It does not rely on any assumptions about the physical nature of the system and does not require any specific (e.g. Hermitian) form of the propagators. Hence, one can, in principle, extend it to any problem that can be simulated with MPS techniques, as we have demonstrated for open quantum systems in this section.

### 3.3 Thermalization and the fluctuation dissipation theorem

We next turn to a specific physical problem, where we will use two-time correlations to investigate thermalization in systems driven far from equilibrium. Generally speaking, thermalization is the relaxation process of a system to a thermal equilibrium state that is described by Boltzmann statistics and has a well-defined temperature. The broad question we would like to ask here is: if a system is driven out of equilibrium, under what conditions will it thermalize? This question has been studied in a variety of physical contexts: for instance, the models of mode populations in photon [34, 237] and polariton condensates [238–240], and the emergence of a low-energy effective temperature in the Keldysh field theory of driven atom-photon systems [109, 121, 122, 125, 241–243]. One can also connect the nonequilibrium steady state behaviour in a driven dissipative system to the occurrence of a prethermalized phase after a sudden quench in an isolated system [244–246]. The prethermalized phase emerges when a system relaxes from a far from equilibrium initial state to a metastable quasi-stationary state on a short timescale, long before reaching the true thermal equilibrium state. One characteristic feature of prethermalization is the establishment of the approximate equilibrium

equation of state and of the kinetic temperature. As a result, prethermalized observables approximately assume their thermal values while particle statistics still deviates very strongly from the equilibrium Bose-Einstein or Fermi-Dirac distribution [247]. Both in a prethermalized isolated system and in a NESS of a driven dissipative system, there is a flow of energy between different degrees of freedom that underlies the thermal or non-thermal behaviour of these systems. While it is known that isolated systems can return to a thermal state, it is considerably more difficult to determine if an open system has established an effectively thermal state – because of the external drive, it cannot equilibrate with its surroundings in the first place.

Indeed, an attempt to define the effective temperature in a nonequilibrium setting like ours may seem surprising. However, effective thermalization processes play an important role in various experimental realizations of nonequilibrium systems. A prominent example is the Bose-Einstein condensation of exciton polaritons in semiconductor microcavities [24, 239]. Such microcavities are driven dissipative systems and inevitably operate out of equilibrium. Although full thermalization with the surroundings cannot be established, the polariton-polariton scattering events produce an effectively thermalized polariton gas. To form a Bose-Einstein condensate, the effective quasi-equilibrium temperature of the polariton gas must be below the condensation threshold. Hence, the effective temperature is a decisive factor in the condensation process. In fact, one can obtain this effective temperature from the occupations of polaritonic states that, in turn, can be extracted from the far-field fluorescence data. A related example is the Bose-Einstein condensation of photons in a dye-filled optical microcavity with pumping and photon loss [34]. Here, the photon gas achieves a number-conserving thermalization via repeated absorption and re-emission events by the dye molecules, thereby thermalizing to the temperature of the dye solution. Yet another example is provided by cavity optomechanics [248], where a nanomechanical oscillator is coupled to an optical field. Here, the cooling and heating of the oscillator are of great interest and one typically defines an effective temperature to model these effects.

While we normally speak of positive temperatures, negative effective temperatures also become possible in nonequilibrium systems. The negative effective temperature states are associated with an inverted Boltzmann statistics, when the higher energy states are more occupied than the lower energy ones. Counterintuitively, states with a negative effective temperature behave as if they are ‘hotter’ than any positive temperature state. A standard example of such behaviour arises in laser physics, where negative effective temperatures are used to model the population inversion [249]. A more recent example is Ref [250] who have realised negative temperature states for spin degrees of freedom in ultracold atom experiments. In another study, Ref. [251] have prepared a negative temperature state for motional degrees of freedom. Starting with a gas of repulsively interacting cold atoms in an optical lattice described by the Bose-Hubbard model, they have created an ensemble with attractive interactions between atoms, characterized by a negative temperature.

Evidently, there is a whole range of nonequilibrium systems where the emergence of an effectively thermal state plays a key part in determining the physics of the

system. Moreover, such an effective temperature is an experimentally measurable quantity. For instance, in the case of photonic and polaritonic systems, one can extract it by measuring the fluorescence spectrum of the system [24].

Formally, a quantum system in a thermalized state is described by a density matrix that takes the Gibbs form:  $\rho = \exp(-H_{\text{eff}}/T_{\text{eff}})$  with some effective Hamiltonian  $H_{\text{eff}}$  and the effective temperature  $T_{\text{eff}}$ . Mathematically, however, *any* density matrix can be written in the Gibbs form. The criterion only becomes physically meaningful if one has a method to determine  $H_{\text{eff}}$  independently. Such a method is provided by the fluctuation dissipation theorem  $S_{O,O^\dagger}(\omega) = F(\omega) \chi''_{O,O^\dagger}(\omega)$ , which relates the fluctuation spectrum  $S_{O,O^\dagger}(\omega)$  and the response function of the system  $\chi''_{O,O^\dagger}(\omega)$  [1, 243] via the distribution function  $F(\omega)$ . Below we describe these quantities in more detail. The  $S_{O,O^\dagger}(\omega)$  and  $\chi''_{O,O^\dagger}(\omega)$  spectra measure the occupations and the density of states in the system, for an operator  $\hat{O}$  that corresponds to a certain degree of freedom of the system. They are both Fourier transforms of two-time correlation functions

$$\tilde{S}_{O,O^\dagger}(t) = \frac{1}{2} \left\langle \{ \hat{O}(t), \hat{O}^\dagger(0) \} \right\rangle, \quad (3.5)$$

$$\tilde{\chi}_{O,O^\dagger}(t) = i\theta(t) \left\langle [ \hat{O}(t), \hat{O}^\dagger(0) ] \right\rangle, \quad (3.6)$$

which we may evaluate using the quantum regression theorem, Eq. (3.1) introduced in the previous section. The distribution function  $F(\omega)$  measures particle statistics. In an equilibrium system, it depends only on whether  $\hat{O}$  obeys fermionic or bosonic (anti-)commutation relations. When a bosonic system is in thermal equilibrium, the distribution function is:  $F(\omega) \equiv 2n_B(\omega) + 1 = \coth((\omega - \mu)/2T)$ . where  $n_B(\omega) = \frac{1}{1+e^{(\omega-\mu)/T}}$  is the occupation number for Bose-Einstein statistics,  $T$  is the temperature of the system in units such that  $k_B = 1$ , and  $\mu$  is the chemical potential. For low energy modes with  $\omega \rightarrow 0$ , the distribution function takes the form  $F(\omega) \sim 2T/\omega$ , which gives us a simple way to extract the effective temperature when the fluctuation dissipation theorem is obeyed. Since coupled cavity arrays are inherently bosonic systems whose physics is dominated by photons interacting with optical emitters, we will focus on the bosonic case for the remainder of this work. In a driven dissipative system that operates far from thermal equilibrium,  $F(\omega)$  can take a more general form – the deviation of  $F(\omega)$  from the thermal form above is an indicator of nonequilibrium behaviour. However, a number of studies have demonstrated in other contexts [109, 121, 122, 125, 241–243, 252] that low energy modes often display an effectively thermal behaviour in driven systems coupled to a Markovian bath. In such cases, the distribution function is given by

$$F(\omega) \sim 2T_{\text{eff}}/\omega \quad (3.7)$$

for low energy modes with  $\omega \rightarrow 0$ , analogous to the one discussed above in the thermal equilibrium setting. This means that one can use the fluctuation dissipation theorem to identify a low energy effective temperature  $T_{\text{eff}}$  for low energy modes:

$$T_{\text{eff}} = \lim_{\omega \rightarrow 0} \frac{\omega S_{O,O^\dagger}(\omega)}{2 \chi''_{O,O^\dagger}(\omega)} \quad (3.8)$$

More generally, we can use it to extract the form of  $F(\omega)$  which will indicate thermal or non-thermal behaviour of the system. Studying thermalization then reduces to computing the two-time correlators Eq. (3.5), (3.6), which we can do by utilizing the transfer MPO algorithm introduced in the previous section.

### 3.4 The Driven Dissipative XY Model

To study fluorescence spectra and thermalization, we will focus on a coupled cavity array described by the transverse field anisotropic XY model. A driven dissipative realization of this model has been proposed by [71], and the steady state properties studied by [42, 44] using matrix product state approaches. In this section we describe the derivation of this model, starting from a model of a coupled cavity array in the photon blockade regime, with a two-photon pump that creates pairs of photons on adjacent sites (see Fig. 3.3), following Refs. [44, 71].

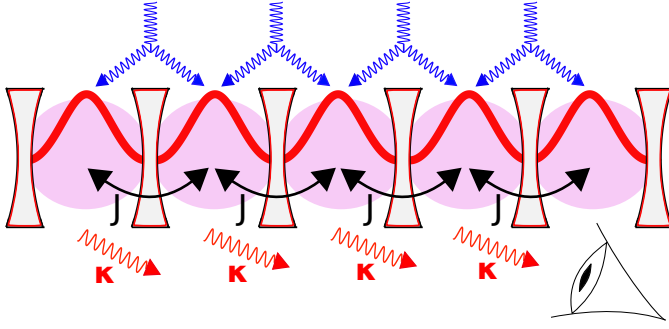


Figure 3.3: Coupled cavity array with hopping  $J$ , photon loss  $\kappa$  and two-photon pumping (blue line). When strong nonlinearity (purple shading) in each cavity leads to photon blockade, this yields the transverse field anisotropic XY model [71].

We consider a 1D lattice of optical or microwave cavities supporting photon modes  $b_j$  with tunneling amplitude  $J$  between adjacent cavities, and an on-site optical nonlinearity  $U$  which induces effective photon-photon interactions in each cavity  $j$ . Such a coupled cavity array is thus described by the Bose-Hubbard Hamiltonian:

$$H = \sum_j \left[ \omega_c b_j^\dagger b_j + U b_j^\dagger b_j^\dagger b_j b_j - J \left( b_j^\dagger b_{j+1} + \text{H.c.} \right) \right].$$

Possible experimental realizations of Bose-Hubbard lattices using circuit QED have been discussed in Sec. 1.2. Our model also includes a two-photon drive  $\Omega \cos(2\omega_P t)$  near the two-photon resonance  $\omega_P \approx \omega_c$ . We work in the limit of strong optical nonlinearities with a perfect photon blockade, which restricts the occupations to at most one photon in each cavity. Therefore, the two-photon drive is only resonant with creation of photon pairs on adjacent cavities. The above considerations allow us to replace each cavity mode with a spin-1/2, equivalent to replacing the bosonic

operators by Pauli matrices:  $b_j \rightarrow \sigma_j^-$ . Our model Hamiltonian then becomes:

$$H_0 = \sum_j \frac{\omega_c}{2} \sigma_j^z - J \sum_j [\sigma_j^+ \sigma_{j+1}^- + \text{H.c.}] - \Omega \sum_j [\sigma_j^+ \sigma_{j+1}^+ e^{-2i\omega_p t} + \text{H.c.}] . \quad (3.9)$$

where  $\sigma_j^{x,y,z}$ ,  $\sigma_j^\pm$  are Pauli spin operators for each cavity  $j$ . Defining the dimensionless parameters  $g = (\omega_p - \omega_c)/2J$ ,  $\Delta = \Omega/J$ , we can transform  $H_0$  to a rotating frame (at pump frequency  $\omega_p$ ) to gauge away the explicit time dependence and write:

$$H = -J \sum_j \left[ g \sigma_j^z + \frac{1+\Delta}{2} \sigma_j^x \sigma_{j+1}^x + \frac{1-\Delta}{2} \sigma_j^y \sigma_{j+1}^y \right] . \quad (3.10)$$

The Hamiltonian  $H$  of a coupled cavity array thus takes the form of the XY model where  $g$  acts as a transverse magnetic field that depends on the pump-cavity detuning, and  $\Delta$  is the anisotropy of spin-spin interactions given by the ratio of pump strength and photon hopping  $J$ . In the remainder of this chapter we will set  $J = 1$  and use units of  $J$  for all of our quantities. The  $\Delta = 0$  limit corresponds to the isotropic XY model (an empty coupled cavity array without any photons) and the  $\Delta = 1$  limit – to the transverse field Ising model.

As discussed in Chapter 1, any realistic coupled cavity system will experience photon loss at rate  $\kappa$  into an external bath of electromagnetic radiation modes. In systems operating at optical frequencies, the characteristic energy scales are much larger than the energy scale set by the temperature of the environment,  $k_B T$ . Hence, one can safely consider a zero temperature bath at  $T = 0$ , which corresponds to dissipation into empty radiation modes. In the spin language, the dissipation process flips spins from the ‘up’ state to the ‘down’ state. Our effective spin system is then described by the Lindblad master equation:

$$\partial_t \rho = \mathcal{L}\{\rho\} = -i[H, \rho] + \frac{\kappa}{2} \sum_j (2\sigma_j^- \rho \sigma_j^+ - \sigma_j^+ \sigma_j^- \rho - \rho \sigma_j^+ \sigma_j^-) . \quad (3.11)$$

A non-driven system would eventually equilibrate with the bath and relax to an empty (thermal) state  $\rho$ . However, we have derived our Hamiltonian in a frame rotating at the pump frequency. As a consequence, the time-dependence induced by the drive breaks the detailed balance and leads to a nonequilibrium steady state (NESS) instead.

### 3.5 Correlations in the nonequilibrium steady state

Before we proceed to calculating the dynamical correlations, let us first briefly discuss the NESS of the driven dissipative anisotropic XY model in the Ising limit ( $\Delta = 1$ ). The spatial correlations in the NESS of this model have previously been studied by [42, 44] for a finite size 1D lattice with  $N = 40$  and  $N = 15$  sites respectively. Here instead we compute the NESS of an infinite 1D lattice using iTEBD algorithm, since we are interested in the thermodynamic limit  $N \rightarrow \infty$ .



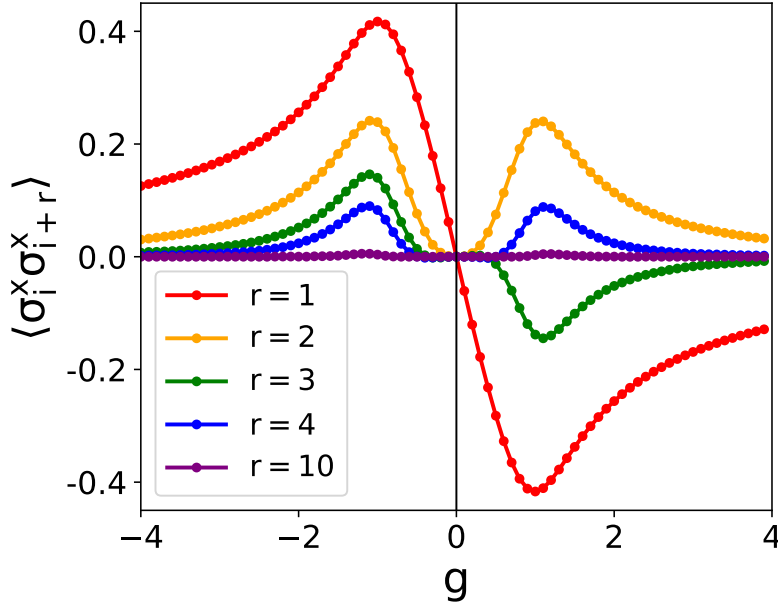


Figure 3.4: The spatial spin-spin correlations in an infinite 1D lattice as a function of the transverse field  $g$  for different separations  $r$ . Energies given in units of  $J$ . Other parameters used:  $\kappa = 0.5$ .

The Fig. 3.4 displays  $\langle \sigma_{i+r}^x \sigma_i^x \rangle$  spatial spin-spin correlations as a function of the transverse field  $g$  for different separations  $r$ , which agree very well with the  $N = 40$  results presented by Ref. [44].

As shown by Ref. [44], the presence of dissipation destroys the critical behaviour observed in the ground state of the transverse field Ising model in 1D: the correlation lengths remain finite and no phase transition occurs at  $|g| = 1$ . However, many features of spatial correlations are similar to those of the equilibrium Ising model [44]. For  $g < 0$ , the NESS exhibits short-range ferromagnetic (FM) spatial order that can be related to the ground state of this model. On the other hand, for  $g > 0$  the correlations become short-range antiferromagnetic (AFM). Therefore, for  $g > 0$ , the spatial order in NESS corresponds to the maximum-energy state of the transverse field Ising model, stabilized by the dissipation. At large  $|g|$  the spins become uncorrelated: for  $g < 0$  this implies a paramagnetic NESS, while for  $g > 0$  the dissipation leads to an antiparamagnetic NESS with spins aligned against the transverse field as it always tries to bring the spins to a state pointing along the  $-z$  direction, regardless of the sign of  $g$ . An interesting property of this model is that there exists a duality, which allows us to relate the form of correlations at  $g > 0$  and  $g < 0$ . As originally discussed in [44], this duality states that the transformation  $g \mapsto -g$  is equivalent to the combination of the inversion  $H \mapsto -H$  and the spin rotation by  $\pi$  around the  $z$  axis on every other lattice site. It follows that reversing the sign of  $g$  corresponds to flipping the sign of all the energies of the system as well as the sign of spatial correlations between odd and even spins. Therefore, if NESS has nearest-neighbour FM correlations for  $g < 0$  associated with the ground state

of  $H$ , a switch to AFM order will occur for  $g > 0$  and the highest energy state of  $H$  will be favoured due to the sign reversal of energies. In the following parts of this chapter we will only show the results for the positive transverse field  $g > 0$ , since the correlations for  $g < 0$  follow straightforwardly from the duality above. We refer an interested reader to [253] for a more general discussion of such dualities.

### 3.6 Fluorescence spectrum and the low energy effective temperature

We next compute two-time correlations and fluorescence spectra of a coupled cavity array described by the driven dissipative anisotropic XY model. In order to eliminate the boundary and finite-size effects, we perform our calculations for a translationally invariant 1D lattice in the thermodynamic limit using the transfer MPO approach. In this section we focus on the on-site correlations ( $i = j$  in Eq. (3.1)), whereas the intersite correlations will be discussed later in Section 3.8.

Figure 3.5 presents the fluctuation spectrum and the susceptibility, which are the Fourier transforms of the correlators defined in Eq. (3.5), (3.6), for  $\hat{O}_1 = \hat{O}_2 = \hat{O} \in \{\sigma^x, \sigma^z\}$  operators and different values of transverse field  $g$ . The figure shows both the Ising limit ( $\Delta = 1$ , left and middle columns), as well as the results at small  $\Delta$  corresponding to a low excitation density (right column). In the latter regime, it is also possible to obtain analytical results using spin-wave theory that we will discuss later in this section. The panels (a–c) display the fluctuation spectrum  $S(\omega)$ , which measures the occupation numbers of normal modes with different energies  $\omega$ . The panels (d–f) show the susceptibility  $\chi''(\omega)$ , which measures the density of states. We note in passing that, although  $S(\omega)$  for  $\sigma^x$  and  $g = 0, 1$  is highly peaked at  $\omega = 0$ , it always remains finite since the driven dissipative XY model does not undergo a phase transition. In Section 3.8 we will see how the form of both the fluctuation spectrum and the density of states can be explained using the momentum-resolved correlations. In this section we are particularly interested in the inverse distribution function  $F(\omega)^{-1} = \chi''_{O,O^\dagger}(\omega) / S_{O,O^\dagger}(\omega)$  displayed in the bottom row of Fig. 3.5 for  $\hat{O} = \sigma^x, \sigma^z$ . It is evident from Fig. 3.5(g,h,i) that  $F(\omega)^{-1}$  is linear at low frequencies  $\omega \rightarrow 0$ . As discussed in Section 3.3, this linearity implies that the low energy modes have effectively thermalized and the distribution function takes the form Eq. (3.7) for  $\omega \rightarrow 0$ . As a consequence, a low energy effective temperature emerges in this model, and is given by Eq. (3.8). For higher energy modes, however,  $F(\omega)^{-1}$  deviates considerably from the thermal form. For instance, the inverse distribution function of a completely thermalized system would approach the asymptotic limit of  $|F(\omega)|^{-1} = 1$  at high frequencies [1, 2]. This limit corresponds to a minimum fluctuation-dissipation ratio as the eigenspectrum of physical operators  $\hat{O}$  is positive. In our coupled cavity system operating far from equilibrium, we observe instead that  $|F(\omega)|^{-1}$  always falls below 1 at high energies, indicating larger fluctuations than one would observe in a genuinely thermal state. Nevertheless, the results in Fig. 3.5(g,h,i) appear to suggest that  $|F(\omega)|^{-1}$  becomes more similar to a thermal form at larger  $g$ .

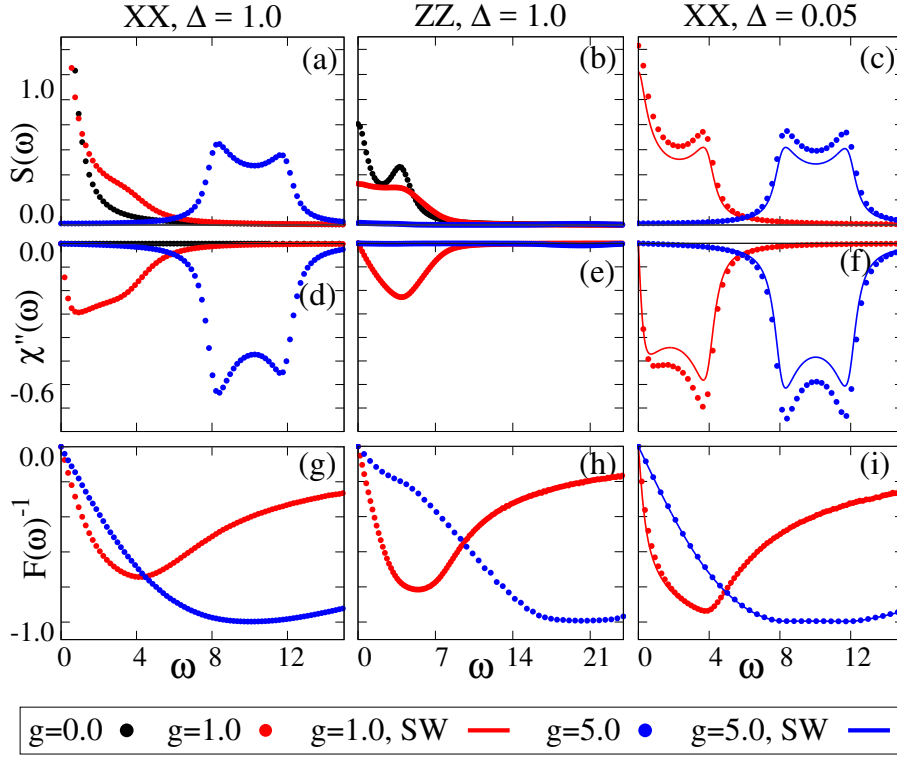


Figure 3.5: Spectrum of fluctuations  $S(\omega)$ , imaginary part of response function  $\chi''(\omega)$ , and inverse distribution function  $F(\omega)^{-1}$ . Left two columns: Ising limit  $\Delta = 1$ , Right column shows  $\Delta = 0.05$  where spin-wave theory (solid lines) matches well. Energies given in units of  $J$ . Other parameters used:  $\kappa = 0.5$ .

The right column of Fig. 3.5 compares the transfer MPO results (points) with analytic results derived from spin-wave theory [254], which is valid in the limit of low density of excitations  $\Delta \rightarrow 0$ . Spin-wave theory and transfer MPO numerics show a good qualitative agreement at  $\Delta = 0.05$  for both the fluctuation spectrum  $S(\omega)$  and the susceptibility  $\chi''(\omega)$  of  $\sigma^x$  excitations. Meanwhile, the spectra for  $\sigma^z$  trivially vanish in the linearized spin-wave theory, and so are not shown here. The agreement for inverse distribution  $F(\omega)^{-1}$  is even better than for spectra  $S(\omega)$ ,  $\chi''(\omega)$  individually, showing a quantitatively exact match between the analytical and numerical results. It is worth noting that, despite being a linear theory, spin-wave theory is able to capture the crucial features such as the low energy effective temperature, the thermal-like flat region with  $|F(\omega)| \simeq 1$  observed at intermediate frequencies and its breakdown at higher frequencies. We will discuss the details of spin-wave calculations in Section 3.7, and show how the effective temperature and other features emerge in spin-wave theory.

We can calculate the low energy effective temperature using Eq. (3.8). Hence, the NESS density matrix  $\rho$  of our system formally takes the Gibbs-like form for low energy modes. Intuitively, one may expect a system to have a positive  $T_{\text{eff}}$  and favour the lowest energy order. A remarkable observation is that our inverse distribution function instead has a negative slope at low energies. From Eq. (3.8), this implies a negative  $T_{\text{eff}} < 0$ , which leads to inverted Boltzmann statistics, and

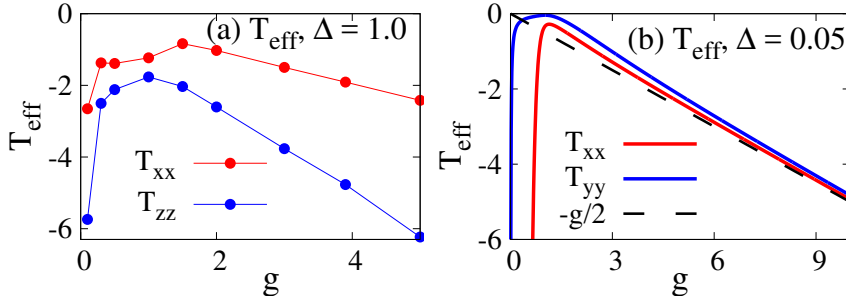


Figure 3.6: The effective temperature  $T_{\text{eff}}$  as a function of transverse field  $g$ . (a) MPS results for  $\sigma^{x,z}$  fluctuations and the transverse-field Ising limit ( $\Delta = 1.0$ ); (b) Spin wave results for  $\sigma^{x,y}$  fluctuations at  $\Delta = 0.05$ . Energies given in units of  $J$ . Other parameters used:  $\kappa = 0.5$ .

makes the system favour NESS with the maximum energy order for  $g > 0$ . This is consistent with the spatial correlations in Section 3.5 indicating that the NESS is a high energy AFM state for  $g > 0$ . The appearance of  $T_{\text{eff}} < 0$  is in fact inevitable in this model as we will see below. First, we recall the duality discussed in Section 3.5, which states that changing the sign of  $g$  reverses the sign of all the energies  $\omega \rightarrow -\omega$  and the sign of correlations between spins at odd and even lattice sites. In addition to this duality, the fluctuation spectrum has an even parity  $S(-\omega) = S(\omega)$  whereas the susceptibility has an odd parity  $\chi''(-\omega) = -\chi''(\omega)$ . This implies that the distribution function also has an odd parity:  $F(-\omega) = -F(\omega)$ . Therefore, it follows that reversing the sign of  $g$  yields the sign change of  $F(-\omega)$  and the effective temperature  $T_{\text{eff}}$ . We observe that  $g < 0$  gives a positive  $T_{\text{eff}}$  and favours the ground state order, while  $g > 0$  corresponds to a negative  $T_{\text{eff}}$  that stabilizes the maximum energy order. A more intuitive picture of the different behaviour at  $g < 0$  and  $g > 0$  comes from the fact that  $g$  is proportional to the pump-cavity detuning. The  $g < 0$  corresponds to a red-detuned pump and the cooling of the system to a NESS with the lowest energy order. Meanwhile,  $g > 0$  corresponds to a blue-detuned driving, which typically induces heating and the buildup of energy. Instead of a high positive  $T_{\text{eff}}$ , in our model it leads to a NESS with a negative  $T_{\text{eff}}$ . Finally, we note that at  $g = 0$  the susceptibility  $\chi''(\omega)$  vanishes and thus  $T_{\text{eff}}$  diverges.

We can explicitly extract the low energy effective temperature  $T_{\text{eff}}$  from transfer MPO results by fitting a thermal form  $F(\omega) \simeq A \coth(b\omega)$  at low frequencies  $\omega \leq 1.0$ , and plotting  $T_{\text{eff}} \equiv A/2b$ . Fig. 3.6(a) shows the effective temperatures  $T_{\text{eff}}$  of  $\sigma^x$  and  $\sigma^z$  fluctuations as a function of the transverse field  $g$ . We have previously discussed that the deviation from the thermal form of  $F(\omega)$  in Fig. 3.5(g,h,i) is an obvious signature of nonequilibrium behaviour. Another important distinction from a thermalized system is that both the distribution function  $F(\omega)$  and the low energy effective temperature are different for different system operators. This is clearly seen in Fig. 3.6(a) where the 'thermometers' of  $\sigma^{x,z}$  fluctuations measure different temperatures, indicating that there is a lack of equilibration between different degrees of freedom in the system. Similarly, Fig. 3.6(b) displays  $T_{\text{eff}}$  at a low excitation density ( $\Delta = 0.05$ ) for  $\sigma^x$  and  $\sigma^y$  fluctuations, calculated

using the spin-wave theory – as we have seen above,  $\sigma^z$  correlation functions vanish in the spin-wave theory. We observe that while  $T_{\text{eff}}$  of  $\sigma^{x,y}$  is different in general, for  $\Delta \rightarrow 0$ ,  $g \rightarrow \infty$  the  $\sigma^{x,y}$  excitations equilibrate with each other to establish the same effective temperature,  $T_{\text{eff}} \approx -g/2 \left(1 + O\left(\frac{1 \pm \Delta}{g}\right)\right)$  since the higher order terms  $O\left(\frac{1 \pm \Delta}{g}\right)$  are suppressed by the factor of  $1/g$ . We will show in Section 3.7 that this arises due to the fact that the effective temperature  $T_{\text{eff},k}$  of modes with different momentum  $k$  becomes independent of  $k$  in this limit.

To study quasi-thermalization of the  $\sigma^x$  and  $\sigma^z$  excitations in a coupled cavity array, we have computed spectra of the  $XX$  and  $ZZ$  correlators in Fig. 3.5. Before moving forward, let us briefly discuss how these spectra could be measured in practice. First, we recall that we have derived our model in Sec. 3.4 by taking a hardcore-boson limit of the underlying Bose-Hubbard model where bosonic quasiparticles are expressed in terms of the spin-1/2 operators:  $b_j \rightarrow \sigma_j^-$ . When a photon leaves a cavity, it destroys a spin-1/2 quasiparticle excitation in the coupled cavity array. As we have seen earlier in this chapter, the energy and momentum of this photon are directly related to those of the destroyed quasiparticle due to the energy and momentum conservation. Therefore, measuring the correlation functions of the emitted photons directly corresponds to the quasiparticle correlations in the coupled cavity array.

The  $XX$  correlators of the form  $\langle \sigma^x(\tau) \sigma^x(0) \rangle$  and  $YY$  correlators of the form  $\langle \sigma^y(\tau) \sigma^y(0) \rangle$  are two-field correlators, because  $\sigma^x(\tau) = \sigma^+(\tau) + \sigma^-(\tau)$  and  $\sigma^y(\tau) = (\sigma^+(\tau) - \sigma^-(\tau)) / i$ . In a quantum optics experiment operating at optical frequencies, one can measure such correlators using a setup based on the homodyne or heterodyne detection [255]. One example is a Mach-Zender type interferometer with a variable delay  $\tau$  in one of its branches [256]. The photocurrent detectors count the number of photons in the output branches of the interferometer. The photocurrent difference then gives the information about the desired two-field correlator. On the other hand,  $ZZ$  correlators are expressed in terms of four-field correlators  $\langle \sigma^z(\tau) \sigma^z(0) \rangle = \langle \sigma^+(\tau) \sigma^-(\tau) \sigma^+(0) \sigma^-(0) \rangle - \langle \sigma^-(\tau) \sigma^+(\tau) \sigma^+(0) \sigma^-(0) \rangle + \langle \sigma^-(\tau) \sigma^+(\tau) \sigma^-(0) \sigma^+(0) \rangle - \langle \sigma^+(\tau) \sigma^-(\tau) \sigma^-(0) \sigma^+(0) \rangle$ . To obtain these four-field correlators, one needs a phase sensitive two-photon measurement such as a Hanbury Brown and Twiss type interferometer with a variable delay  $\tau$  introduced after one of the two photodetectors [256]. We can extract a four-field correlation function by measuring cross-correlations between the photocurrents of the two detectors [256].

To perform similar measurements at microwave frequencies, typical in circuit QED experiments, Ref. [256] have developed a quadrature amplitude detection system. This system is based on a modified variant of a Hanbury Brown and Twiss interferometer that uses linear field quadrature detectors, rather than photon intensity detectors. In this scheme, a propagating photon field is transmitted through a 50/50 beam splitter. Subsequently, one performs a heterodyne measurement to extract both quadrature amplitudes of the output field in each branch of the interferometer using IQ mixer detectors. The observer can then reconstruct any correlation function, including the two-field and four-field correlators, from the instantaneous values of the measured quadrature amplitudes. The four-field correlators, for example, are extracted by measuring the cross-correlation of the signals in each

branch. A convenient feature of the scheme is that combining the quadrature measurements also allows reordering the operators in a correlation function [232, 256]. Finally, recording the correlations as a function of time straightforwardly allows a calculation of the emission spectrum by taking a Fourier transform of the relevant correlator.

## 3.7 Spin-wave calculations

In this section we present the details of spin-wave calculations [254] that we have used in the previous section to describe the behaviour of the driven dissipative anisotropic XY model at low excitation numbers. More specifically, the low excitation regime arises in the limit of small  $\Delta$  or the limit of large  $|g|$ . The spin wave theory was used earlier by Ref. [44] to compute the static correlation functions at small  $\Delta$ . In our work, we extend this approach to dynamical correlations and spectra. The basic idea is that for a zero pumping (i.e.  $\Delta = 0$ ) or a very large pump-cavity detuning (i.e.  $g \rightarrow -\infty$ ), the NESS of our model corresponds to an empty state. For a small  $\Delta$ , or a large but finite  $g$ , one can then use the spin-wave approximation, which ignores the constraint on double occupancy of a lattice site, and so is only valid for a low density of excitations. In this regime of small excitation numbers, we can revert from spin-1/2 operators (hardcore bosons) to bosonic fields:  $\sigma_j^- \rightarrow b_j$ , hence recovering the characteristics of a weakly interacting bosonic model.

### 3.7.1 Calculating correlation functions

#### Spin-wave approximation and equations of motion

We first follow the steps described in Ref. [44] to derive the Hamiltonian in terms of bosonic system operators  $b_k$  and  $b_{-k}^\dagger$ . Transforming master equation Eq. (3.11) with Hamiltonian Eq. (3.10) to the momentum basis  $b_k = \sum_j e^{ikj} b_j / \sqrt{N}$  we obtain:

$$\partial_t \rho = -i \sum_k [h_k, \rho] + \frac{\kappa}{2} \sum_k \left( 2\hat{b}_k \rho b_k^\dagger - b_k^\dagger b_k \rho - \rho b_k^\dagger b_k \right), \quad (3.12)$$

where

$$h_k = - \begin{pmatrix} b_k^\dagger & b_{-k} \end{pmatrix} \begin{pmatrix} g + \cos(k) & \Delta \cos(k) \\ \Delta \cos(k) & g + \cos(k) \end{pmatrix} \begin{pmatrix} b_k \\ b_{-k}^\dagger \end{pmatrix}, \quad (3.13)$$

Since  $\Delta$  corresponds to the driving strength and  $\max(\kappa, g, J = 1)$  sets the cost of creating new excitations in the system, the low excitation regime arises when  $\Delta \ll \max(\kappa, g, 1)$ . To derive correlation functions, however, we will not solve the above master equation directly. Instead, we consider the equivalent Heisenberg-Langevin equations for the system operators coupled to a Markovian bath, which will yield a linear order expansion in bosonic operators  $b_k$  [257]. The equations of motion for  $b_k$  and  $b_{-k}^\dagger$  can be written in a matrix form:

$$\partial_t f(t) = M f(t) + v(t), \quad (3.14)$$

with the vectors:

$$f(t) = \begin{pmatrix} b_k(t) \\ b_{-k}^\dagger(t) \end{pmatrix}, \quad v(t) = \sqrt{2\kappa} \begin{pmatrix} b_k^{\text{in}}(t) \\ b_{-k}^{\dagger\text{in}}(t) \end{pmatrix}, \quad (3.15)$$

and the matrix:

$$M = \begin{pmatrix} -\kappa + 2i(g + \cos(k)) & 2i\Delta \cos(k) \\ -2i\Delta \cos(k) & -\kappa - 2i(g + \cos(k)) \end{pmatrix}. \quad (3.16)$$

Here, coupling to a Markovian bath introduces the input noise term  $b_k^{\text{in}}(t)$ . Since we consider a zero temperature bath, there is only vacuum quantum noise, and the only nonzero correlator is  $\langle b_k^{\text{in}}(t) b_{k'}^{\dagger\text{in}}(t') \rangle = \delta_{k,k'} \delta(t - t')$ .

The solution of Eq. (3.14) is:

$$f(t) = e^{Mt} f(0) + \int_0^t dt' e^{M(t-t')} v(t').$$

In the long-time limit  $t \rightarrow \infty$  we find the expressions for system operators:

$$\begin{aligned} b_k(t) &= \sqrt{2\kappa} \int_0^t dt' \left[ G_1(t-t') b_k^{\text{in}}(t') + G_2(t-t') b_{-k}^{\dagger\text{in}}(t') \right], \\ b_{-k}^\dagger(t) &= \sqrt{2\kappa} \int_0^t dt' \left[ G_1^*(t-t') b_{-k}^{\dagger\text{in}}(t') + G_2^*(t-t') b_k^{\text{in}}(t') \right]. \end{aligned} \quad (3.17)$$

where the propagators  $G_{1,2}(\tau)$  are matrix elements of  $e^{Mt}$  given by:

$$G_1(\tau) = e^{-\kappa\tau} \left[ \cos(\xi_k \tau) + i\epsilon_k \frac{\sin(\xi_k \tau)}{\xi_k} \right], \quad (3.18)$$

$$G_2(\tau) = i\eta_k e^{-\kappa\tau} \frac{\sin(\xi_k \tau)}{\xi_k}, \quad (3.19)$$

with dispersions  $\epsilon_k = 2(g + \cos(k))$ ,  $\eta_k = 2\Delta \cos(k)$ , and  $\xi_k = \sqrt{\epsilon_k^2 - \eta_k^2}$ .

### Correlations and effective temperatures for $\hat{\sigma}_x$

After deriving the system operators, we now proceed to calculate the frequency-resolved spectra for  $XX$  correlations. Since  $\sigma_j^x \rightarrow b_j + b_j^\dagger$  in the spin-wave limit, we can express the on-site  $XX$  two-time correlator as:

$$\tilde{C}^{xx}(\tau) = \langle \sigma^x(0) \sigma^x(\tau) \rangle = \langle b^\dagger(0) b^\dagger(\tau) \rangle + \langle b(0) b(\tau) \rangle + \langle b^\dagger(0) b(\tau) \rangle + \langle b(0) b^\dagger(\tau) \rangle, \quad (3.20)$$

where the correlations are given by a Fourier transform from momentum space to real space:

$$\langle b^\dagger(0) b(\tau) \rangle = \int_{-\pi}^{\pi} dk e^{ikl} \left\langle b_k^\dagger(0) b_k(\tau) \right\rangle \Big|_{l=0},$$

and similar expressions for other correlators. We then substitute in the solutions for operators Eq. (3.17), and evaluate the time integrals at unequal times,  $t + \tau$  and  $t$ . This gives a two-time correlator:

$$\tilde{C}^{xx}(\tau) = \frac{e^{-\kappa\tau}}{2\pi} \int_{-\pi}^{\pi} dk \left[ \cos(\xi_k \tau) + i(\eta_k - \epsilon_k) \frac{\sin(\xi_k \tau)}{\xi_k} + \frac{\eta_k(\eta_k - \epsilon_k)}{\xi_k^2 + \kappa^2} \left( \cos(\xi_k \tau) + \kappa \frac{\sin(\xi_k \tau)}{\xi_k} \right) \right]. \quad (3.21)$$

The quantities of interest are the fluctuation spectrum  $S(\omega)$  and susceptibility  $\chi''(\omega)$  given by the Fourier transforms of  $\tilde{S}(\tau) = \frac{1}{2}(\tilde{C}(\tau)^* + \tilde{C}(\tau))$  and  $\tilde{\chi}(\tau) = i\Theta(\tau)(\tilde{C}(\tau)^* - \tilde{C}(\tau))$  respectively. Plugging in Eq. (3.21) and taking a Fourier transform with respect to  $\tau$ , we obtain  $XX$  spectra:

$$S_{xx}(\omega) = \frac{\kappa}{\pi} \int_{-\pi}^{\pi} dk \frac{P_k + \omega^2 + 2\eta_k(\eta_k - \epsilon_k)}{Q_k(\omega)}, \quad (3.22)$$

$$\chi''_{xx}(\omega) = \frac{2\kappa\omega}{\pi} \int_{-\pi}^{\pi} dk \frac{\eta_k - \epsilon_k}{Q_k^{-1}(\omega)}, \quad (3.23)$$

where we have introduced auxiliary functions  $P_k = \xi_k^2 + \kappa^2$ , and  $Q_k(\omega) = (P_k - \omega^2)^2 + (2\omega\kappa)^2$ .

One can then substitute  $e^{ik} \rightarrow z$ , and the integrals in Eqs. (3.22), (3.23) become contour integrals around a unit circle  $C$  with  $|z| = 1$ . The values of Eqs. (3.22), (3.23) are then determined by the residues of poles  $z = Z$  located inside  $C$  (i.e. with  $|Z| < 1$ ). Both Eq. (3.22) and Eq. (3.23) have the same set of eight poles given by:

$$Z = \theta_{s_1, s_2} \pm \sqrt{\theta_{s_1, s_2}^2 - 1},$$

$$\theta_{s_1, s_2} = \frac{-g + s_1 \sqrt{g^2 \Delta^2 - \frac{1-\Delta^2}{4} [\kappa^2 - \omega^2 + s_2 2i\omega\kappa]}}{1 - \Delta^2},$$

with  $s_1 = \pm 1$ ,  $s_2 = \pm 1$ . Evaluating the contour integrals gives the fluctuation spectrum:

$$S_{xx}(\omega) = 2\kappa \sum_{|Z_n| < 1} Z_n \alpha_n, \quad (3.24)$$

where

$$\alpha_n = \frac{[(1 - \Delta)Z_n^2 + 2gZ_n + (1 - \Delta)]^2 + (\omega^2 + \kappa^2)Z_n^2}{(1 - \Delta^2)^2 \prod_{m=1, m \neq n}^8 (Z_n - Z_m)}.$$

Similarly the susceptibility is given by:

$$\chi''_{xx}(\omega) = -4\kappa\omega \sum_{|Z_n| < 1} Z_n^2 \beta_n, \quad (3.25)$$

where

$$\beta_n = \frac{(1 - \Delta)Z_n^2 + 2gZ_n + (1 - \Delta)}{(1 - \Delta^2)^2 \prod_{m=1, m \neq n}^8 (Z_n - Z_m)}.$$



In both expressions, the sum runs over poles  $Z_n$  inside the unit circle  $C$  with  $|Z_n| < 1$ . From Eq. (3.24) and Eq. (3.25) it is straightforward to derive the distribution function  $F_{xx}(\omega)$  of fluctuation-dissipation theorem:

$$F_{xx}(\omega) = \frac{S_{xx}(\omega)}{\chi''_{xx}(\omega)} = -\frac{1}{2\omega} \frac{\sum_{|Z_n|<1} Z_n \alpha_n}{\sum_{|Z_n|<1} Z_n^2 \beta_n}. \quad (3.26)$$

It is evident that in the low frequency limit  $\omega \rightarrow 0$ , the distribution  $F_{xx}(\omega)$  is dominated by the  $1/\omega$  divergence. The effective thermalization of NESS thus already emerges in spin-wave theory, leading to an effective temperature  $T_{\text{eff}}$ :

$$T_{\text{eff},xx} = -\frac{1}{4} \frac{\sum_{|Z_n|<1} Z_n \alpha_n}{\sum_{|Z_n|<1} Z_n^2 \beta_n} \Big|_{\omega=0}. \quad (3.27)$$

### Correlations and effective temperatures for $\hat{\sigma}_y$

Similarly to the previous subsection, we can calculate the fluctuation spectrum and susceptibility for  $YY$  excitations in the spin wave limit where  $\sigma_j^y \rightarrow -i(b_j - b_j^\dagger)$ . By following the same steps as for  $XX$  correlators, we obtain the  $YY$  spectra:

$$S_{yy}(\omega) = \frac{\kappa}{\pi} \int_{-\pi}^{\pi} dk Q_k^{-1}(\omega) [P_k + \omega^2 + 2\eta_k(\eta_k + \epsilon_k)], \quad (3.28)$$

$$\chi''_{yy}(\omega) = \frac{2\kappa\omega}{\pi} \int_{-\pi}^{\pi} dk Q_k^{-1}(\omega)(\eta_k + \epsilon_k). \quad (3.29)$$

The  $YY$  spectra (3.28), (3.29) only differ from  $XX$  spectra (3.22), (3.23) by  $(\eta_k - \epsilon_k) \rightarrow (\eta_k + \epsilon_k)$ . Consequently, the  $YY$  contour integrals have the same poles as the  $XX$  ones, but with different residues and thus different weights.

Continuing along the same steps as for  $XX$  correlators, we find the  $YY$  fluctuation spectrum:

$$S_{yy}(\omega) = 2\kappa \sum_{|Z_n|<1} Z_n \gamma_n, \quad (3.30)$$

where

$$\gamma_n = \frac{[(1 + \Delta)Z_n^2 + 2gZ_n + (1 + \Delta)]^2 + (\omega^2 + \kappa^2)Z_n^2}{(1 - \Delta^2)^2 \prod_{m=1, m \neq n}^8 (Z_n - Z_m)}.$$

The  $YY$  susceptibility is given by:

$$\chi''_{yy}(\omega) = -4\kappa\omega \sum_{|Z_n|<1} Z_n^2 \delta_n, \quad (3.31)$$

where

$$\delta_n = \frac{(1 + \Delta)Z_n^2 + 2gZ_n + (1 + \Delta)}{(1 - \Delta^2)^2 \prod_{m=1, m \neq n}^8 (Z_n - Z_m)}.$$

and the poles  $Z_n$  are the same as in  $XX$  spectra. One can then straightforwardly derive the distribution function  $F_{yy}(\omega)$ :

$$F_{yy}(\omega) = \frac{S_{yy}(\omega)}{\chi''_{yy}(\omega)} = -\frac{1}{2\omega} \frac{\sum_{|Z_n|<1} Z_n \gamma_n}{\sum_{|Z_n|<1} Z_n^2 \delta_n}. \quad (3.32)$$

and the effective temperature  $T_{\text{eff}}$ :

$$T_{\text{eff},yy} = -\frac{1}{4} \frac{\sum_{|Z_n|<1} Z_n \gamma_n}{\sum_{|Z_n|<1} Z_n^2 \delta_n} \Big|_{\omega=0}. \quad (3.33)$$

### Vanishing correlations for $\sigma_z$

The spin wave approximation has enabled us to derive analytical expressions for the  $XX$  and  $YY$  correlators. However, the same small excitation approximation cannot be used to find the  $ZZ$  correlators. This becomes apparent if we express the  $ZZ$  correlator in the spin-wave limit, using  $\sigma_j^z = b_j^\dagger b_j - b_j b_j^\dagger$ :

$$\begin{aligned} \tilde{C}^{zz}(\tau) = \langle \sigma^z(0) \sigma^z(\tau) \rangle &= \langle b^\dagger(0) b(0) b^\dagger(\tau) b(\tau) \rangle - \langle b(0) b^\dagger(0) b^\dagger(\tau) b(\tau) \rangle \\ &+ \langle b(0) b^\dagger(0) b(\tau) b^\dagger(\tau) \rangle - \langle b^\dagger(0) b(0) b(\tau) b^\dagger(\tau) \rangle. \end{aligned} \quad (3.34)$$

Since the problem involves non-interacting bosons, the NESS is Gaussian and we can expand the four-field correlators using Wick's theorem, which leads to  $\tilde{C}^{zz}(\tau) = 0$ . Therefore, at this order of approximation all  $ZZ$  correlators and spectra are trivially zero. Such outcome is not surprising, since spin wave theory is a linear expansion whereas the  $\sigma^z$  correlators are quartic.

### 3.7.2 Temperature of individual bosonic modes

Building on the spin wave theory introduced above, we now discuss the emergence of a low energy effective temperature under this linear approximation by considering the contribution of individual bosonic modes. From Eqs. (3.22), (3.23) we define the momentum-resolved fluctuation spectrum and susceptibility:

$$S_{xx}(\omega, k) = \frac{\kappa}{\pi} Q_k^{-1}(\omega) [P_k + \omega^2 + 2\eta_k(\eta_k - \epsilon_k)]. \quad (3.35)$$

$$\chi''_{xx}(\omega, k) = \frac{2\kappa\omega}{\pi} Q_k^{-1}(\omega)(\eta_k - \epsilon_k). \quad (3.36)$$

The distribution function of an individual bosonic  $k$ -mode is then given by

$$F_{xx}(\omega, k) = \frac{S_{xx}(\omega, k)}{\chi''_{xx}(\omega, k)} = \frac{\xi_k^2 + \omega^2 + \kappa^2 + 2\eta_k(\eta_k - \epsilon_k)}{2\omega(\eta_k - \epsilon_k)}. \quad (3.37)$$

which can be written in the form:

$$F_{xx}(\omega, k) = \frac{2T_{\text{eff},xx,k} + \lambda_{xx,k}\omega^2}{\omega}, \quad (3.38)$$

where  $\lambda_{xx,k} = [2(\eta_k - \epsilon_k)]^{-1}$ , and the low energy effective temperature of an individual bosonic mode  $k$  in the  $\omega \rightarrow 0$  limit is:

$$T_{\text{eff},xx,k} = \frac{\kappa^2 + (\eta_k - \epsilon_k)^2}{4(\eta_k - \epsilon_k)}, \quad (3.39)$$

where we have used the definition of  $\xi_k^2 = \epsilon_k^2 - \eta_k^2$ . From the definition Eq. (3.37), we see that the distribution function  $F(\omega)$  in Fig. 3.5(g,h,i) can be expressed as

a weighted average over momentum-resolved distributions  $F(\omega, k)$  of individual bosonic modes  $k$ :

$$F(\omega) = \frac{\int_{-\pi}^{\pi} dk F(\omega, k) \chi''(\omega, k)}{\int_{-\pi}^{\pi} dk \chi''(\omega, k)}. \quad (3.40)$$

Here, the weight coefficients correspond to the  $k$ -resolved density of states  $\chi''(\omega, k)$ . The above results show that spin wave theory predicts the appearance of a low energy effective temperature for each individual  $k$  mode, in spite of being a linear theory. In fact, this follows directly from the form Eq. (3.38). We have also seen in the previous section that spin wave results predict the thermal-like flat region  $F(\omega) \simeq 1$  at intermediate frequencies and its breakdown at high frequencies, in agreement with transfer MPO numerics. However, the momentum-resolved inverse distribution  $F_{xx}(\omega, k)^{-1}$  does not exhibit this flat region with  $|F_{xx}(\omega, k)|^{-1} \simeq 1$ . Instead,  $|F_{xx}(\omega, k)|^{-1}$  has a peak at  $\omega = \omega_{xx,k}^* \equiv \sqrt{2T_{\text{eff},xx,k}/\lambda_{xx,k}} = \sqrt{\kappa^2 + (\eta_k - \epsilon_k)^2}$  with height

$$|F_{xx}(\omega_{xx,k}^*, k)|^{-1} = \frac{1}{\sqrt{8T_{\text{eff},xx,k}\lambda_{xx,k}}} = \sqrt{\frac{(\eta_k - \epsilon_k)^2}{\kappa^2 + (\eta_k - \epsilon_k)^2}}.$$

which always satisfies a required condition that  $|F_{xx}(\omega, k)|^{-1} \leq 1$ , and tends to 1 for a weak dissipation  $\kappa \ll |\eta_k - \epsilon_k|$ . Nevertheless, the  $F(\omega)$  distribution is given by the weighted average Eq. (3.40), which integrates over all peaks; the combination of peaks with different frequencies residing in the range  $\sqrt{\kappa^2 + 4[g - (1 - \Delta)]^2} < \omega_{xx,k}^* < \sqrt{\kappa^2 + 4[g - (1 + \Delta)]^2}$  gives a flattened inverse distribution  $|F(\omega)|^{-1} \simeq 1$  at intermediate  $\omega$ . From the range of peak frequencies above, we can also see that the  $|F(\omega)|^{-1} \simeq 1$  region shifts to higher frequencies as  $g$  increases, which is consistent with Fig. 3.5(g,h,i). At high frequencies, we can see from Eq. (3.38) that  $F(\omega) \propto \omega$ . This leads to an inevitable breakdown of  $|F(\omega)|^{-1} \simeq 1$  – thus the non-thermal behaviour of high energy modes is also encoded in spin wave theory.

As mentioned earlier, we can find analogous results for the  $YY$  distribution function and the effective temperature simply by replacing  $(\eta_k - \epsilon_k) \rightarrow (\eta_k + \epsilon_k)$  in the  $XX$  results above. This replacement means that  $T_{\text{eff},yy,k}$  is conditioned to be different from  $T_{\text{eff},xx,k}$  in general; the same statement also applies to the distribution functions of occupied modes  $F_{yy}(\omega, k)$  and  $F_{xx}(\omega, k)$ . In the limit of large transverse fields  $g$ , however, the effective temperature in Eq. (3.39) becomes  $T_{\text{eff},xx,k} \approx -g/2 \left(1 + O\left(\frac{1-\Delta}{g}\right)\right)$ ,  $T_{\text{eff},yy,k} \approx -g/2 \left(1 + O\left(\frac{1+\Delta}{g}\right)\right)$ , i.e. independent of momentum  $k$  and of the operator being measured if one considers the leading order behaviour. Here, the  $-g/2$  term constitutes the leading order behaviour, while the higher order terms  $O\left(\frac{1\pm\Delta}{g}\right)$  are suppressed by the factor of  $1/g$ . Since this result is independent of  $k$ , the momentum-integrated effective temperature in Eq. (3.40) also approaches the same asymptotic value:

$$T_{\text{eff}} \approx -\frac{g}{2} \left(1 + O\left(\frac{1 \pm \Delta}{g}\right)\right). \quad (3.41)$$

As a consequence, the effective temperatures of  $\sigma^{x,y}$  excitations both approach the same value at large  $g$ , as we have seen in Fig. 3.6 in the previous section.

### 3.7.3 Fluctuation dissipation relation in linear theories

As we have discussed above, it is remarkable that the spin-wave results predict a low energy quasi-thermal distribution with a non-zero effective temperature for  $XX$  and  $YY$  excitations. This result is particularly intriguing in the light of research such as Ref. [258] suggesting that correlators computed using the quantum regression theorem fail to predict a thermal spectrum, yielding a flat (i.e. frequency independent) distribution  $F(\omega)$ . Here we discuss briefly why this is not the case in our model. In particular, we have seen above that the distribution function depends on the mode considered. We will first show that if we considered the correlations  $\tilde{C}_{bb^\dagger}(\tau) = \langle b(0)b^\dagger(\tau) \rangle$  of the creation and annihilation operators  $b, b^\dagger$  instead of the  $\sigma^{x,y}$  operators, the resulting distribution  $F_{bb^\dagger}(\omega)$  would be flat. Subsequently we will discuss why the  $XX$  and  $YY$  distribution functions are not flat, and address the differences between our model and the one considered by Ref. [258].

Let us consider a quantum harmonic oscillator (with frequency  $\Omega$ , and field operators  $b, b^\dagger$ ) interacting with a bath of radiation modes (with frequency  $\omega_k$ , and field operators  $B_k^\dagger, B_k$  for each mode) via coupling strength  $g_k$  is described by the Hamiltonian

$$H = \Omega b^\dagger b + \sum_k \omega_k B_k^\dagger B_k + \sum_k \left[ g_k b B_k^\dagger + \text{H.c.} \right]. \quad (3.42)$$

Here  $g_k$  is the system-bath coupling strength. Using the standard input-output formalism [257] in the Markovian limit we derive Heisenberg-Langevin equation of motion

$$\partial_t b(t) = -i\Omega b(t) - \kappa b(t) + \sqrt{2\kappa} b^{\text{in}}(t), \quad (3.43)$$

where the input noise operator  $b^{\text{in}}(t)$  is introduced by coupling to a Markovian bath. For a zero-temperature bath there is only vacuum noise and the only non-zero correlator is  $\langle b^{\text{in}}(t)b^{\text{in}}(t') \rangle = \delta(t - t')$ . Next, one can obtain the steady-state solution (at  $t \rightarrow \infty$ ):

$$b(t) = \sqrt{2\kappa} \int_{-\infty}^t dt' e^{-i\Omega(t-t') - \kappa(t-t')} b^{\text{in}}(t'). \quad (3.44)$$

The only non-vanishing two-time correlator then is

$$\langle b(0)b^\dagger(\tau) \rangle = e^{-\kappa|\tau| + i\Omega\tau}. \quad (3.45)$$

Taking a Fourier transform of the symmetrized correlator  $\tilde{S}_{bb^\dagger}(\tau) = \frac{1}{2} \langle \{b(0), b^\dagger(\tau)\} \rangle = e^{-\kappa|\tau| + i\Omega\tau}$  and response function  $\tilde{\chi}_{bb^\dagger}(\tau) = i\theta(\tau) \langle [b(0), b^\dagger(\tau)] \rangle = i\theta(\tau) e^{-\kappa|\tau| + i\Omega\tau}$  gives the fluctuation spectrum and susceptibility:

$$S_{bb^\dagger}(\omega) = \chi''_{bb^\dagger}(\omega) = \frac{2\kappa}{(\omega - \Omega)^2 + \kappa^2}. \quad (3.46)$$

Subsequently, one obtains a flat distribution spectrum for  $b, b^\dagger$  modes, in contrast to the quasi-thermal distribution of the  $XX$  and  $YY$  modes in Eqs. (3.26), (3.32):

$$F_{bb^\dagger}(\omega) = \frac{S_{bb^\dagger}(\omega)}{\chi''_{bb^\dagger}(\omega)} = 1. \quad (3.47)$$

However, there are two key differences between the derivation above and the spin-wave equations earlier in this section. The first one is the presence of anomalous terms proportional to  $\Delta$  in the Hamiltonian Eq. (3.13), which leads to the cross coupling of  $b$  to both  $b^{\text{in}}$  and  $b^{\dagger\text{in}}$  in Eq. (3.17) – in contrast to Eq. (3.44). The second difference arises due to the fact that we have considered the  $XX$  and  $YY$  correlators in our spin-wave calculations, instead of  $\tilde{C}_{bb^\dagger}(\tau)$ . As a consequence, the fluctuation and response functions contain sums and differences of correlators  $\langle b(0)b^\dagger(\tau) \rangle$  and  $\langle b^\dagger(0)b(\tau) \rangle$ : the combinations of single-mode correlators yield the frequency dependent spectra and distribution in Eqs. (3.35–3.37). Such an outcome contradicts the argument by Ford and O’Connell [258] that results computed using the quantum regression theorem can never give a thermal spectrum. The problem in Ref. [258] is similar to ours since it deals with the  $XX$  correlations and involves anomalous terms (which appear due to the fact that no rotating-wave approximation is made in the system-bath coupling). However, the important difference is that the calculation in Ref. [258] proceeds by assuming an Ohmic rather than Markovian bath. Thus, the statement made by Ford and O’Connell [258] cannot be generalized to any physical setting, and its validity is subject to the underlying assumptions about the dissipation and system-bath interactions.

### 3.8 Momentum-resolved fluorescence spectrum

In Section 3.6 we have considered two-time correlations  $C(t)$  evaluated at equal positions. This corresponds to recording light emitted from a single cavity, and gives energy-resolved fluorescence spectrum  $P(\omega)$  that is implicitly integrated over momentum since  $P(\omega) = \int_{-\infty}^{\infty} dt e^{i\omega t} C(t) = \int_{-\infty}^{\infty} dk p(\omega, k)$  where  $p(\omega, k)$  is a momentum-resolved spectrum. We can extract more information about the structure of correlations, such as energy-momentum dispersion relations, by considering momentum-resolved spectra. To achieve this, we will compute two-time correlators at non-equal sites  $i, j$ , and perform a double Fourier transform with respect to separation in both time  $t$  and space  $|i - j|$ . One can obtain such momentum-resolved fluorescence spectra experimentally, for example, by measuring the interference of light emitted from different cavities.

Fig. 3.7 displays the fluctuation spectra  $S(\omega, k)$  for  $\hat{O} = \sigma^x, \sigma^z$  operators, and two values of  $g = 1.0, 5.0$ , in the Ising limit  $\Delta = 1$ . As before, we only consider the results for  $g > 0$ , since the  $g < 0$  spectra can be found from the duality discussed in Sec. 3.5. We will show that the features appearing in  $S(\omega, k)$  can be described in terms of dispersion relations derived from the Jordan-Wigner solution of the transverse field Ising model. For details of the Jordan-Wigner method we refer the reader to [259].

Let us start at large positive transverse field  $g = 5.0$  where the spin-spin correlations are weak (see Fig. 3.4). Here, the NESS is a maximum energy state with spins pointing in the  $-\hat{z}$  direction against the magnetic field, as already mentioned in Sec. 3.5. The  $\sigma^x$  operator corresponds to single particle excitations that flip a single spin. Hence, its spectrum obeys the single particle dispersion relation

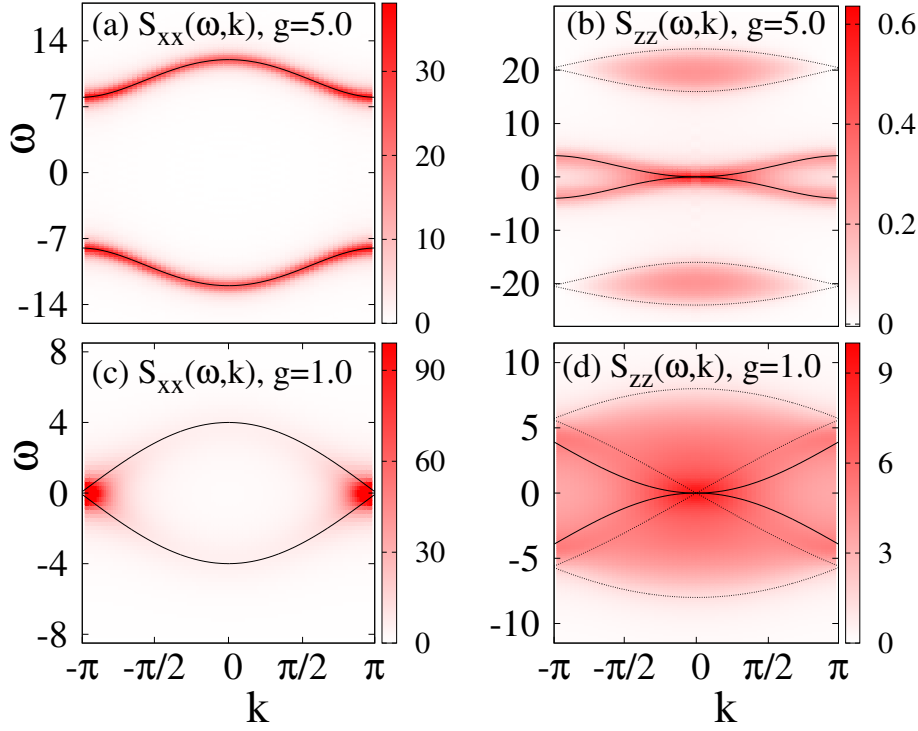


Figure 3.7:  $S(\omega, k)$  momentum-resolved fluctuation spectrum for excitations of: (a)  $\sigma^x$  at  $g = 5.0$ ; (b)  $\sigma^z$  at  $g=5.0$ ; (c)  $\sigma^x$  at  $g = 1.0$ ; (d)  $\sigma^z$  at  $g = 1.0$ . Energies given in units of  $J$ . Other parameters used:  $\kappa = 0.5$ .

$\omega(k) = \epsilon(k)$  with

$$\epsilon(k) \equiv 2J\sqrt{1 + g^2 + 2g \cos(k)} \quad (3.48)$$

for the *de*-excitations of the *maximum* energy state. It is shown as a black line in Fig. 3.7(a). Meanwhile, the  $\sigma^z$  operator corresponds to two-particle excitations, which come in two varieties. The first kind is a continuum of two-particle states with  $\omega = \epsilon(k_1) + \epsilon(k_2)$ ,  $k = k_1 + k_2$ . These states are located within the boundary specified by  $\epsilon_{\min}(k) < \omega(k) < \epsilon_{\max}(k)$ , with the dispersion relation  $\epsilon_{\max/\min}(k) = 4J\sqrt{1 + g^2 \pm 2g \cos(k/2)}$ , which is indicated in Fig. 3.7(b) by the dotted black lines. The second kind of excitations corresponds to scattering the particles from one state with momentum  $q$  to another with momentum  $q + k$ . Such excitations carry the energy  $\omega(k) = \Delta\epsilon(q, k) \equiv \epsilon(q + k) - \epsilon(q)$  where the dominant contribution comes from  $q = 0$ , since it corresponds to the state of maximum energy  $\epsilon(k)$ , which is maximally occupied for a negative temperature NESS. The scattering energy  $\Delta\epsilon(0, k)$  is shown in Fig. 3.7(b) by the black solid line, which indeed matches the dominant scattering band. Importantly, we can now straightforwardly explain the structure of the spectral functions in Fig. 3.5(a,d). The peaks in the fluctuation spectra in Fig. 3.5(a,d), integrated with respect to momentum  $k$ , simply arise due to the turning points in the momentum-resolved spectra in Fig. 3.7(a,b) – which, in turn, lead to van Hove singularities at the band edges.

When we tune the transverse field to  $g = 1.0$ , the NESS shows strong AFM correlations between the spins, as seen in Fig. 3.4. The fluctuation spectra retain

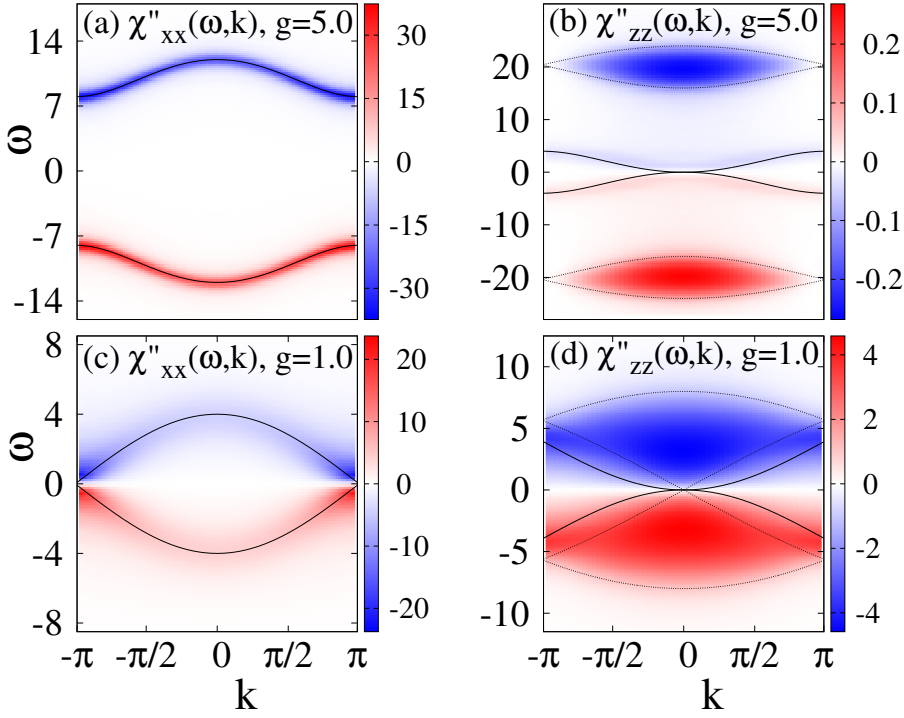


Figure 3.8:  $\chi''(\omega, k)$  momentum-resolved susceptibility for excitations of: (a)  $\sigma^x$  at  $g = 5.0$ ; (b)  $\sigma^z$  at  $g=5.0$ ; (c)  $\sigma^x$  at  $g = 1.0$ ; (d)  $\sigma^z$  at  $g = 1.0$ . Energies given in units of  $J$ . Other parameters used:  $\kappa = 0.5$ .

their basic features, but become distorted due to the spin-spin interactions. The  $\sigma^x$  spectrum is displayed in Fig. 3.7(c) and Fig. 3.5(a,d), where the  $k = \pm\pi$  modes become highly populated, giving rise to the dominant peaks at  $k = \pm\pi$ , near  $\omega = 0$ . The  $\sigma^z$  spectrum is shown in Fig. 3.7(d) and Fig. 3.5(b,e) where the scattering band is swallowed by the two-particle continuum. In both cases (i.e.  $\sigma^{x,z}$ ), the black lines correspond to the same dispersion relations as before. One may note that the dispersion relations match the fluctuation spectrum less accurately at  $g = 1.0$  than they did at  $g = 5.0$ . To understand this discrepancy, we recall that the ground state of transverse field Ising model enters the FM phase when  $|g| < 1$ , and the gap closes at  $g = 1.0$ . In contrast, the NESS of our system involves no phase transition – and is already in the AFM phase at  $g = 1.0$  where it also reaches the peak of the AFM spin-spin correlations. Therefore, it is not surprising to find a lower quality match between the ground state Jordan-Wigner results and the spectra at  $g = 1.0$ . If we keep decreasing the transverse field  $g \rightarrow 0$ , the modes near  $\omega = 0$  become even more prominent, as can be seen in Fig. 3.5(a–f).

For completeness, we also include the momentum-resolved susceptibility  $\chi''(\omega, k)$  in Fig. 3.8. It exhibits very similar features as  $S(\omega, k)$  since in an effectively thermal NESS the two quantities are straightforwardly related by the fluctuation dissipation theorem. The black lines here indicate the same dispersion relations as discussed above.





# Chapter 4

## Computing steady states in 2D

### 4.1 Introduction

Solving the Lindblad master equation for many body systems is, no doubt, a very demanding task. Not only we face the ‘curse of dimensionality’ problem, familiar from Chapter 2 but also the fact that a single wavefunction is insufficient to represent an open quantum system. Instead, the fundamental object here is a mixed-state density matrix whose dimensions scale quadratically with the Hilbert space dimension, and that is subject to physical constraints such as positivity and hermiticity. Numerical algorithms must also account for the fact that the generator of reduced system dynamics is a non-Hermitian Liouvillian superoperator, rather than the more familiar Hamiltonian; the majority of computational many body techniques in existence indeed rely on the mathematical properties of a Hamiltonian.

Unsurprisingly, many of the earlier research efforts concerning coupled cavity arrays and other driven dissipative many body problems have resorted to mean field based calculations [64, 69, 70, 73, 106–109]. In 1D, the extension of MPS to open quantum systems has paved the way for quasi-exact numerical calculations that fully account for quantum fluctuations. Importantly, MPS simulations can obtain both the dissipative dynamics and the nonequilibrium steady states (NESS) for reasonably large lattice sizes, reaching  $N = O(10^2)$  sites and even the thermodynamic limit [40–44, 68, 75, 76, 113–115].

However, studying driven dissipative lattices beyond 1D remains difficult, and efficient numerical methods for solving the many-body Lindblad master equation in two and higher dimensions are scarce. As a consequence, our knowledge about the interplay between many body interactions and dissipative effects in these systems is still very limited. The nonequilibrium states of coupled cavity arrays in 1D are known to exhibit rich collective behaviour [44, 64–76], and we could access a much broader range of nonequilibrium systems in 2D if suitable numerical methods were available.

So far, most experimental realizations of coupled cavity arrays using superconducting circuits have been one-dimensional. Nonetheless, the circuit QED technology is perfectly suitable for building two-dimensional coupled cavity arrays with various lattice geometries, using similar approaches for generating strong optical nonlinearities as in 1D [15]. An encouraging progress has been shown by Ref. [260],

who devised a network of coplanar waveguide resonators and used it to realize two dimensional tight-binding kagome lattices in a curved hyperbolic space. As such, their work has shown the potential of two-dimensional coupled cavity arrays to create a novel class of synthetic quantum materials in a non-Euclidean space, impossible in the usual solid state systems. The design in Ref. [260] did not yet include any nonlinear elements, and thus involved no onsite interactions between photons. However, interacting nonlinear setups are relatively straightforward to create by incorporating qubits or kinetic inductance materials in each resonator, and can be expected to appear in the near future. Another exciting direction for two-dimensional coupled cavity arrays is to explore the geometrical effects arising in topological materials [261–263] or in the presence of frustration [264] in a nonequilibrium setting – as well as their applicability in novel quantum devices that inevitably operate under dissipative conditions. In contrast to 1D arrays, 2D geometry would allow us to induce phase-dependent tunnelling terms and create artificial magnetic fields. Proposals already exist for building two-dimensional circuit QED arrays to realize photonic fractional quantum Hall-like models and engineered topological order [261–263].

One more area is investigating the symmetry-breaking quantum phase transitions that are not possible in dissipative 1D models, but could occur in 2D [44, 76]. The central question here is identifying the nonequilibrium phase transitions in 2D, and their critical properties. Especially convenient for this purpose are the effective spin models, that can uncover the essential features of critical behaviour in synthetic nonequilibrium materials without having to deal with the excessive and complex details of actual experimental setups. Various spin models, for instance the transverse field Ising or XYZ models, can be tailored using circuit QED quantum simulators and other coupled cavity structures [265–267]. While truly large-scale experiments with nonlinear two-dimensional circuit QED arrays remain to be realized, there are other dissipative systems that can be utilized to study nonequilibrium phase transitions in 2D.

One particularly promising experimental platform that we describe here is Rydberg atoms [268]. In typical experiments, these atoms are excited by coherent driving from the ground state to a highly-excited metastable state [268–270]. The high principal quantum number of the excited Rydberg state produces strong dipole-dipole interactions between atoms, and the radiative decay of this Rydberg state is the dominant dissipative channel. Hence, the Rydberg gases provide a convenient platform to study driven dissipative systems with strong correlations. The physics of such Rydberg atom systems can be expressed in the spin-1/2 language: the spin ‘up’ state represents the excited Rydberg state and the ‘down’ state corresponds to the ground state [73, 271]. One can then use a driven dissipative Rydberg gas to create spin-1/2 Hamiltonians with Lindblad dissipation [73, 271], for example the dissipative transverse field Ising, Heisenberg, or XYZ models [73].

It is clear that experiments with circuit QED arrays and Rydberg atoms open many exciting avenues for studying two-dimensional materials and phase transitions out of equilibrium. Our main goal in this chapter is the development of an accurate and reliable numerical scheme that can predict the steady state behaviour of these systems. In the first instance, we will focus on simulating the basic spin-1/2 models,

with an aim of studying the phase diagrams of driven dissipative quantum materials and the properties of their critical behaviour.

Several approaches have been developed in attempt to compute NESS in 2D beyond the mean field theory, and we briefly discuss the most promising ones here. In Cluster Mean Field Theory [76], a system in the thermodynamic limit is divided into clusters: interactions between lattice sites within a cluster are treated exactly while those between adjacent clusters are treated on the mean field level. The method thus captures short range correlations, but is severely limited by the small cluster sizes currently accessible. Corner Space Renormalization method [116, 117] is based on real-space renormalization. It finds the steady state density matrix by using an iterative procedure that solves master equation in a corner of the Hilbert space. At each iteration, the corner space states are selected by using the eigenvectors of the density matrices of two smaller lattices, and then merging those lattices together in real space while keeping the  $M$  most probable pairs of states. Both of these methods struggle to capture full 2D correlations present in the system. The applicability of Corner Space Renormalization method to large  $N \times N$  lattices, with  $N$  greater than several sites, also remains questionable.

The neural network state ansatz has gained momentum in recent years as a novel computational technique for quantum many body systems [272]. It has also been applied to calculate NESS of driven dissipative lattices in 2D governed by Lindblad master equation [273, 274]. The basic idea behind this approach is to represent the density matrix of the system by a Restricted Boltzmann Machine neural network, and optimize it using the Variational Monte Carlo algorithm. Despite their great potential, the neural network simulations presented so far have only been able to access very small dissipative lattices with  $3 \times 3$  or  $4 \times 4$  sites.

While MPS techniques have been successfully adapted to driven dissipative lattices in 1D, tensor network algorithms are less developed in 2D. One possible approach, devised in the context of strongly correlated matter in equilibrium, is to extend MPS ansatz to 2D systems and perform DMRG calculations as in 1D. One can apply DMRG to a two-dimensional  $L_x \times L_y$  lattice directly by imposing cylindrical boundary conditions and mapping it onto a one-dimensional MPS arranged in a snake-like pattern that visits all sites of this 2D lattice [192]. The key drawback of 2D DMRG is the exponential scaling of its computational cost  $O(e^{L_y})$  with the lattice width  $L_y$ . This scaling stems from the 1D to 2D mapping, which produces MPS with pseudo-long-range interactions violating the area law, even when only the nearest neighbour couplings are present in the Hamiltonian. Such a DMRG-like approach has been adapted to open quantum systems, to compute NESS of the dissipative XY model with longitudinal and transverse fields, and NESS of the dissipative transverse field Ising model, reaching lattice sizes of  $L_x = 12$  and  $L_y = 4$  [275].

In this chapter, we will pursue an alternative strategy. The extension of TEBD and iTEBD algorithms to Liouvillian propagation using the superoperator renormalization group described in Sec. 2.2.4 has proven to be a powerful tool for calculating NESS of various driven dissipative models in 1D [40, 43, 44, 68, 75, 76, 113–115]. Motivated by the success of MPS simulations of Lindblad master equation in 1D, we utilize the same superoperator renormalization group to extend the iPEPS

ansatz introduced in Sec. 2.3 to mixed-state density matrices. In our context, the 2D version of iTEBD algorithm, known as the Simple Update iPEPS algorithm introduced in Sec. 2.3.2, appears to be the simplest and the most promising route forward. Since PEPS is fully compliant with the area law, it does not suffer from exponential scaling limitations of the 2D MPS approach described above. The iPEPS algorithm also works directly in the thermodynamic limit and so is capable of finding NESS of truly large lattice systems. We will refer to this approach as the iPEPO algorithm, since it deals with a vectorized infinite Projected Entangled Pair Operator (iPEPO) expressed as an iPEPS, as we will see in the next section.

Kshetrimayum et al [276] have recently demonstrated that the iPEPO algorithm can simulate open quantum systems on infinite 2D lattices, and used it to calculate NESS of the dissipative XYZ and transverse field Ising models. Here, we present our study concerning the applications of iPEPO algorithm to driven dissipative systems in 2D. In contradiction to Kshetrimayum et al [276], we find that the algorithm only converges in some parameter regimes while in others it fails to find a converged NESS at all. We begin the chapter by describing our implementation of the iPEPO algorithm in Sec. 4.2. In Sec. 4.3, we proceed to benchmark our method by computing the ground states of the transverse field Ising model and the hardcore Bose-Hubbard model in 2D. In Sec. 4.4 we apply the iPEPO algorithm to calculate NESS of the dissipative XYZ model in 2D, and analyse its convergence behaviour. Finally, Sec. 4.5 briefly discusses alternative tensor network approaches for computing NESS in 2D.

## 4.2 Implementation of iPEPO algorithm

Extending the Simple Update (SU) iPEPS algorithm from ground states of Hamiltonians to nonequilibrium steady states of Lindblad superoperators is remarkably straightforward. The main idea is to utilize the superoperator renormalization group [40] introduced in Sec. 2.2.4 for vectorized many body density matrices. In Sec. 2.2.4 and Fig. 2.17 we have expressed a mixed-state density operator  $\rho$  of a 1D lattice as an MPO, and applied vectorization by reshaping it into a superket MPS  $|\rho\rangle_{\sharp}$ . Likewise, we have recast superoperators as linear maps and represented them by MPOs that act on superket MPSs. By using the vectorization described in Sec. 2.2.4, one may equally represent the density matrix  $\rho$  of a 2D many body system as a Projected Entangled Pair Operator (PEPO) – a generalization of MPO in 2D. Subsequently, we can reshape it into a PEPS  $|\rho\rangle_{\sharp}$  by combining both of its physical indices into one at each site, as illustrated in Fig. 4.1(a). For an infinite 2D lattice, the vectorized density matrix  $|\rho\rangle_{\sharp}$  is then described by an iPEPS. The problem of computing NESS thus becomes equivalent to the problem of finding the ground states of Hamiltonians using the iPEPS algorithm, except the imaginary time Hamiltonian propagation is now replaced by the real time Liouvillian propagation. Therefore, at least in principle, we can apply the SU iPEPS algorithm described in Sec. 2.3.2 to compute NESS of the Lindblad master equation for an infinite 2D lattice with dissipation. To distinguish between iPEPS used to represent wavefunctions and vectorized density operators, we will refer to this approach as

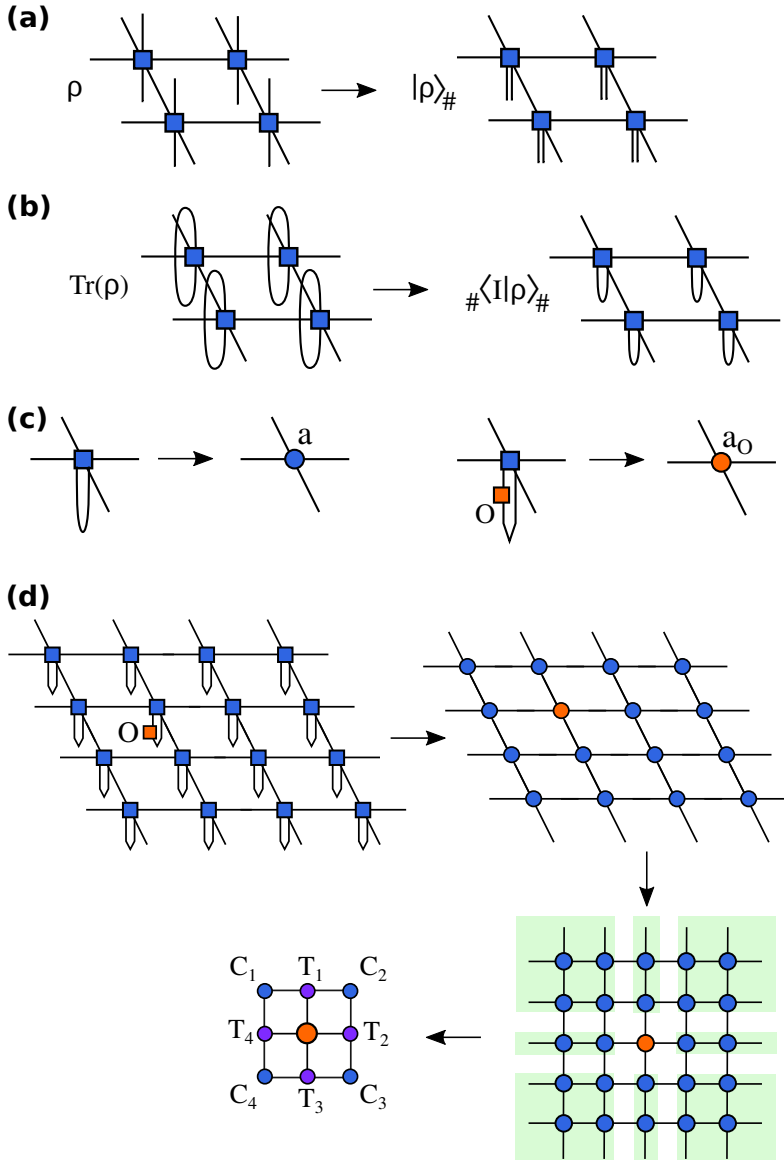


Figure 4.1: (a) PEPO representing a many body density operator  $\rho$  can be vectorized by merging its local indices together at each site, to give PEPS representing a vectorized density matrix  $|\rho\rangle_{\#}$ . (b) Computing the trace of a vectorized density matrix represented as PEPS  $|\rho\rangle_{\#}$ . (c) Reduced tensors of the iPEPS network representing  $|\rho\rangle_{\#}$ , analogous to Fig. 2.19(b). (d) Calculation of an expectation value  $\langle O \rangle = \text{Tr}(O\rho)$  for  $|\rho\rangle_{\#}$  iPEPS using the reduced tensors from (c) and the CTM effective environment of iPEPS unit cell, by analogy to Fig. 2.19(c).

the iPEPO algorithm, since it essentially deals with a vectorized iPEPO expressed as an iPEPS. All the main steps of the iPEPO algorithm for NESS remain exactly the same as in Sec. 2.3.2, except for two differences that we discuss below.

The first obvious difference is the propagator. The imaginary time two-body propagators  $U_{\alpha}(\delta\tau) = e^{-\delta\tau H_{\alpha}}$  with Hamiltonian  $H_{\alpha}$  for a bond  $\alpha \in \{U, R, D, L\}$  are replaced by the real time two-body propagators  $U_{\alpha}(\delta t) = e^{-\delta t \mathcal{L}_{\alpha}}$ , where  $\mathcal{L}_{\alpha}$  is the two-body Liouvillian for a bond  $\alpha \in \{U, R, D, L\}$  and  $t$  is the real time.

The second difference relates to the fact that we now extract observables from a density matrix rather than a wavefunction, i.e. observables are calculated using  $\langle O \rangle = \text{Tr}(O\rho)$ , instead of  $\langle O \rangle = \langle \Psi|O|\Psi \rangle$ . Similarly, the correct normalization of a density matrix is  $\text{Tr}(\rho) = 1$  as shown in Fig. 4.1(b), in contrast to the normalization of a wavefunction  $\langle \Psi|\Psi \rangle = 1$ . To extract observables from a density matrix iPEPS, one first needs to compute the environment of a unit cell formed by reduced tensors of the iPEPS network. The reduced tensors of the density matrix iPEPS are defined by tracing out every local index as shown in Fig. 4.1(c), instead of computing inner products, which was the case for wavefunction iPEPS in Fig. 2.19. We subsequently apply the CTM method from Sec. 2.3.1 to calculate the effective environment of this unit cell, and obtain observables as illustrated graphically in Fig. 4.1(d).

One potential issue that we have not touched upon yet is the diffusion of entanglement in the course of real time evolution of an out-of-equilibrium state. The unitary time evolution creates correlated quasiparticle excitations that propagate across the lattice. After evolving the state for time  $t$ , the lattice sites within a separation  $d = ct$  will become entangled, where  $c$  is a constant determined by the propagation speed of excitations in the system [38]. The buildup of entanglement is described by the Lieb-Robinson theorem [38], which implies that the entanglement will grow (at worst) linearly in time:  $S(t) \leq S(0) + ct$ , and the bond dimension required to maintain an accurate representation of the quantum state will grow (at worst) exponentially in time:  $D = O(e^t)$ . As a consequence, we can only simulate nonequilibrium unitary time evolution efficiently for short times. This poses a fundamental obstacle in isolated quantum systems after a quench [38, 277]. The same issue remains relevant to the non-unitary Liouvillian propagation as it inevitably involves a contribution from the Hamiltonian component in Eq. (2.22), and the bond dimension may become intractable well before we reach the fixed point. For zero dissipation, Liouvillian propagation reduces to unitary time evolution with an unbounded growth of  $D$ . On the other hand, the Lindblad dissipation that we consider in this thesis (e.g. photon loss) removes excitations from the system and tries to destroy the entanglement – a purely dissipative evolution will then result in an unentangled steady state with  $D = 1$ . In general, Liouvillian time evolution is determined by the competition between Hamiltonian and dissipative dynamics and eventually brings the system to its steady state, which will have finite entanglement and a finite bond dimension  $D$  due to the dissipation. This implies an upper limit that the dissipation imposes on the growth of entanglement: the initial growth must either saturate or decay to a fixed value after reaching its peak. As long as the dissipation is sufficiently strong relative to the rate of entanglement growth, we may be able to simulate time evolution efficiently for long times. MPS simulations in recent years [40–44, 68, 75, 76, 113–115] constitute a numerical evidence that this is indeed the case for many systems in 1D, and one may reasonably expect an analogous behaviour in 2D.

So far, we have only discussed the implementation of SU scheme for NESS calculations, but have not mentioned the possibility of implementing the Full Update (FU) version of the iPEPO algorithm. In contrast to a two-body Hamiltonian used in the ground state iPEPS calculations, a two-body Liouvillian is a non-Hermitian object. To perform the two-site variational minimization in Sec. 2.3.3 it is thus

necessary to find a reliable non-Hermitian algorithm that could substitute the Alternating Least-Squares scheme used in the standard FU. An alternative strategy could be to abandon the idea of time evolution altogether, and solve a global variational search problem targetting the null eigenstate  $|\rho\rangle$  of either Liouvillian  $\mathcal{L}$  or Hermitian positive semidefinite object  $\mathcal{L}^\dagger \mathcal{L}$  – both of these approaches have been applied with success in MPS calculations [41, 42]. It is evident in any case that the problem of extending the variational update algorithms to NESS calculations in 2D lies on a far less familiar ground compared to the SU iPEPO time evolution, and requires a substantial departure from the existing ground state algorithms, which is well beyond the scope of this thesis. Therefore, in this work we concentrate on the SU iPEPO algorithm, leaving the variational techniques for future endeavours to explore.

We have implemented our iPEPO code in Fortran, including the CTM algorithm, the functionality required for computing local observables and two-point correlators, the SU procedure for both NESS and ground state calculations, as well as the FU procedure for ground state calculations (for benchmarking purposes only).

### 4.3 Benchmarking with ground state calculations

Due to the close analogy between the iPEPS and iPEPO algorithms, both of them share the same codebase except for the two minor differences discussed above. This overlap allows us to benchmark our implementation of iPEPO against the known numerical results from ground state calculations. We apply our iPEPO machinery to compute the ground states of two models: the transverse field Ising model, and the hardcore Bose-Hubbard model.

Our first test problem is the transverse field Ising model on an infinite square lattice. It is a paradigmatic model of quantum phase transitions and quantum magnetism, with a spin-1/2 particle at each site of the lattice:

$$H = -J \sum_{\langle i,j \rangle} \sigma_i^z \sigma_j^z - g \sum_i \sigma_i^x \quad (4.1)$$

where  $\sigma_i^{x,z}$  are Pauli matrices at site  $i$ ,  $J$  is the nearest-neighbour coupling between spins, and  $g$  is the transverse magnetic field along the  $x$  axis. This Hamiltonian is invariant under transformation  $\sigma_i^z \rightarrow -\sigma_i^z$ , known as the  $Z_2$  symmetry. Its ground state  $|\Psi_{\text{GS}}\rangle$  exhibits a second order phase transition between the paramagnetic phase, and the ferromagnetic phase with spontaneous alignment of spins along the  $z$  axis, breaking the  $Z_2$  symmetry. The longitudinal magnetization  $M_z = \langle \Psi_{\text{GS}} | \sigma^z | \Psi_{\text{GS}} \rangle$  is therefore the order parameter of this model. It acquires a nonzero value in the ferromagnetic phase at small  $g/J$ , and is zero in the paramagnetic phase at large  $g/J$ . We will work in units of  $J = 1$  throughout this section.

Refs. [206, 225, 278] have employed the iPEPS algorithm to study the 2D transverse field Ising model in the thermodynamic limit. Here, we compute the ground state of Eq. (4.1) using the SU and FU versions of the algorithm. Fig. 4.2(a) shows

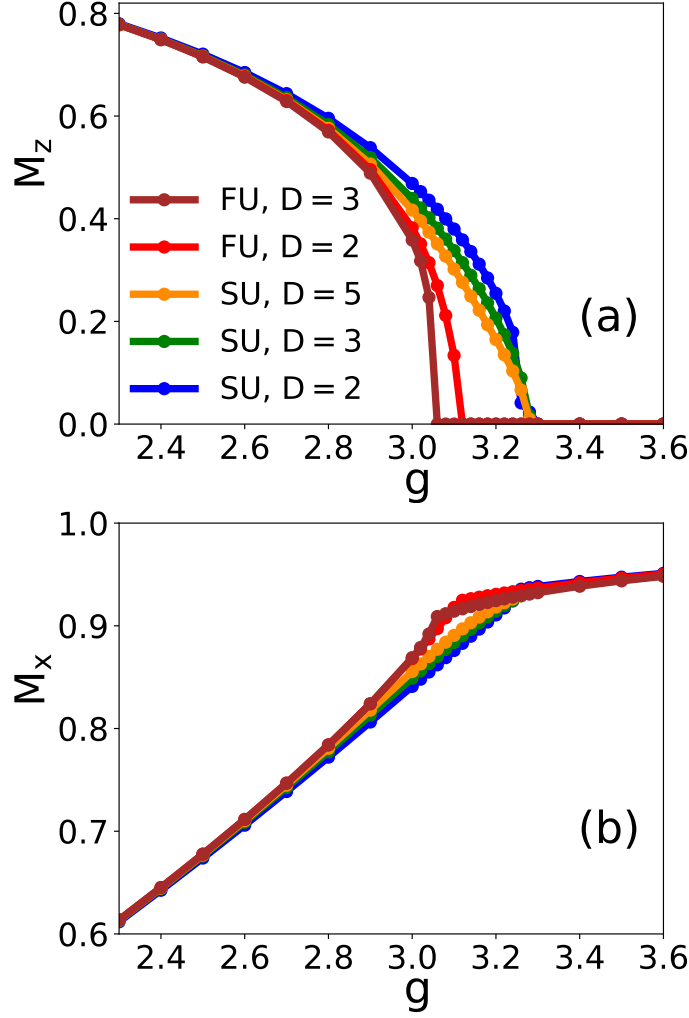


Figure 4.2: Ground state results for the transverse field Ising model. (a) The longitudinal magnetization  $M_z$  and (b) the transverse magnetization  $M_x$  as a function of transverse field  $g$  in the vicinity of phase transition, computed for different iPEPS bond dimensions  $D$  using both SU and FU. Energies given in units of  $J$ .

the longitudinal magnetization  $M_z$  as a function of transverse field  $g$  in the vicinity of phase transition, for different values of iPEPS bond dimension  $D$ . Our implementation of iPEPS reproduces accurately both the SU and FU results of Ref. [278]. As expected, the SU and FU calculations match well far from the critical point where the correlations are local, and the results converge fast with increasing values of  $D$ . However, near the critical point FU becomes considerably more accurate than SU. Here, SU is only qualitatively correct – it has difficulty in describing faithfully the correct physics due to the diverging correlation length in the system, and a much higher value of  $D$  is needed to achieve the same level of accuracy as FU with  $D = 2, 3$ . As seen from Fig. 4.2(a), the FU calculation with  $D = 3$  predicts the critical point around  $g \approx 3.05$ , in good agreement with previous iPEPS results in Refs. [206, 225, 278] and with Quantum Monte Carlo results in Ref. [279]. While SU also captures the phase transition, it overestimates the location of the criti-



cal point at  $g = 3.28$  instead. Fig. 4.2(b) displays the transverse magnetization  $M_x = \langle \Psi_{\text{GS}} | \sigma^x | \Psi_{\text{GS}} \rangle$  plotted against  $g$ . As before, our iPEPS calculations match accurately the results by Refs. [206, 225, 278], and the distinction in performance of SU and FU, as well as for different values of  $D$ , becomes visible near the critical point. Our mixed-state iPEPO algorithm relies on the SU scheme specifically, and so it is the SU iPEPS algorithm that is most directly relevant to us. Nevertheless, there is a great overlap in the code underlying the SU and FU schemes, and the FU iPEPS serves as an especially demanding test for the CTM calculations that need to be done thousands of times, in numerically challenging parameter regimes requiring high CTM bond dimensions.

We next benchmark our iPEPO code by computing the ground state  $|\Psi_{\text{GS}}\rangle$  of the Bose-Hubbard model (BHM) in 2D, on an infinite square lattice. The BHM provides a simplified description of interacting bosonic gas in a lattice potential. We consider the hardcore BHM where the occupations are restricted to 0 or 1 bosons on each lattice site:

$$H = -J \sum_{\langle i,j \rangle} (a_i^\dagger a_j + \text{H.c.}) - \mu \sum_i a_i^\dagger a_i \quad (4.2)$$

Here,  $a_i^\dagger, a_i$  are hardcore bosonic creation and annihilation operators at site  $i$ , satisfying the commutation relation  $[a_i^\dagger, a_j] = (1 - 2a_i^\dagger a_i) \delta_{ij}$ .  $J$  is the hopping rate between adjacent sites, and  $\mu$  is the onsite chemical potential. The Hamiltonian Eq. (4.2) has the  $U(1)$  symmetry, i.e. is invariant under transformation  $a_j \rightarrow a_j e^{i\phi} a_j^\dagger a_j$ ,  $\phi \in [0, 2\pi]$ . The ground state of this model has two phases. When the hopping  $J$  term dominates, the model is in the superfluid phase with bosons delocalized over the lattice. This phase is characterized by a nonzero fraction of bosons in the zero-momentum mode  $k = 0$ , forming a condensate and thus breaking the  $U(1)$  symmetry. When the onsite  $\mu$ -term dominates, bosons become localized at their lattice sites, and the system becomes a Mott insulator. The model Eq. (4.2) undergoes a second order phase transition between the superfluid and the Mott insulator phases at the critical value of  $\mu/J$ . As before, we choose to work in units of  $J = 1$  for the remainder of our discussion.

The 2D hardcore BHM has been studied using iPEPS techniques by, for example, Refs. [278, 280, 281] and thus provides a convenient test case for our iPEPS code. Fig. 4.3 shows the number density of bosons  $n = \langle \Psi_{\text{GS}} | a^\dagger a | \Psi_{\text{GS}} \rangle$  and the condensate fraction  $n_0 = |\langle \Psi_{\text{GS}} | a | \Psi_{\text{GS}} \rangle|^2$  as a function of chemical potential  $\mu$ , for different bond dimensions  $D$  of iPEPS. Again, our iPEPS calculations reproduce accurately the ground state results of Refs. [278, 280, 281]. When  $\mu$  is large and negative, the lattice is completely empty with  $n = 0$ ; likewise, when  $\mu$  is large and positive, the lattice is completely full with  $n = 1$ . Both of these cases correspond to the Mott insulator phase, where adding or removing bosons incurs a large energy cost. For  $-4 < \mu < 4$ , the number density  $n$  takes values in the range  $n \in (0, 1)$ . The energy gap vanishes and the system is in the broken symmetry superfluid phase with a finite condensate fraction  $n_0$ .

As already mentioned, it is the SU iPEPS scheme that we are particularly interested in benchmarking. Therefore, this time we have performed our calculations

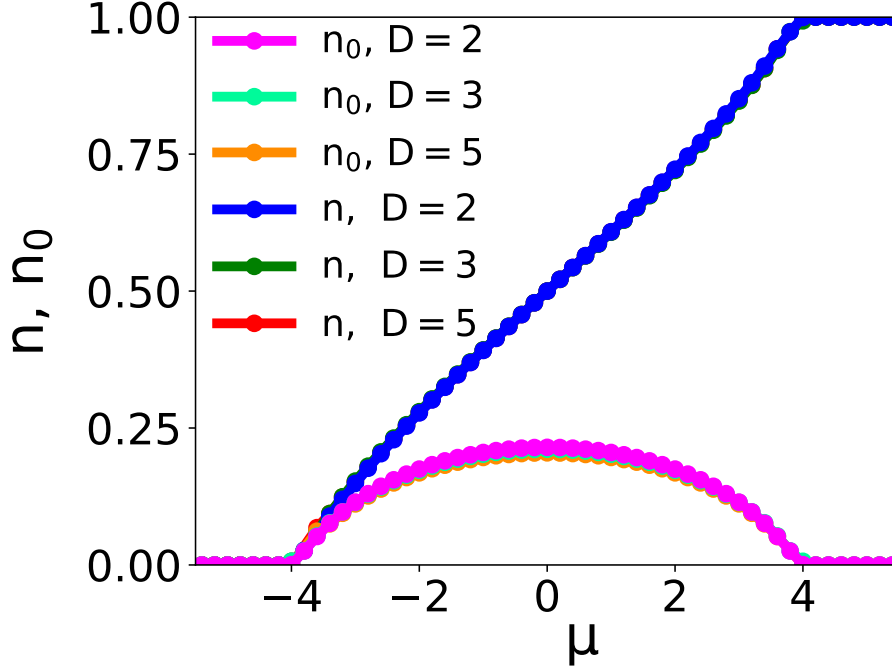


Figure 4.3: Ground state results for the hardcore Bose-Hubbard model. The number density of bosons  $n$  per lattice site and the condensate fraction  $n_0$  on a single lattice site as a function of chemical potential  $\mu$ , computed for different iPEPS bond dimensions  $D$  using SU. Energies given in units of  $J$ .

using SU only as it already captures the relevant physics described above with a sufficient accuracy for our purposes, and the results are already well converged at low  $D$ .

## 4.4 Steady states of the dissipative XYZ model

Having tested our iPEPO implementation with ground state calculations, we now use it to study NESS of the dissipative spin-1/2 XYZ model on an infinite square lattice. The XYZ Hamiltonian is given by

$$H = \sum_{\langle i,j \rangle} (J_x \sigma_i^x \sigma_j^x + J_y \sigma_i^y \sigma_j^y + J_z \sigma_i^z \sigma_j^z) \quad (4.3)$$

where  $\sigma_j^{x,y,z}$  are Pauli matrices at lattice site  $j$ , and  $J_{x,y,z}$  are spin-spin coupling constants. This model has a rich phase diagram, and can be realized using a driven array of coupled nonlinear cavities [282] or a gas of Rydberg atoms [73]. Similarly to the effective spin-1/2 coupled cavity systems discussed in Chapter 3, it will experience photon loss into a  $T = 0$  electromagnetic bath, flipping spins from the ‘up’ state to the ‘down’ state at rate  $\kappa$ . The dissipative dynamics of such coupled cavity arrays is governed by the Lindblad master equation:

$$\partial_t \rho = \mathcal{L}\{\rho\} = -i[H, \rho] + \frac{\kappa}{2} \sum_j (2\sigma_j^- \rho \sigma_j^+ - \sigma_j^+ \sigma_j^- \rho - \rho \sigma_j^+ \sigma_j^-). \quad (4.4)$$

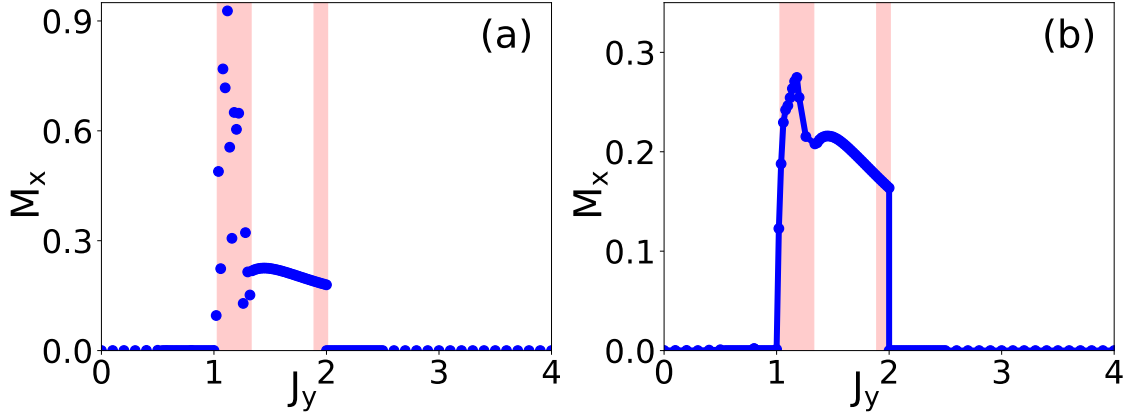


Figure 4.4: The magnetization order parameter  $M_x$  of the dissipative XYZ model as a function of coupling strength  $J_y$ , for  $J_x = 0.5$ ,  $J_z = 1$  and  $D = 4$ . Energies given in units of  $\kappa = 1$ . The red highlighted areas indicate parameter regimes where the iPEPO algorithm fails to converge. (a) Results computed using timesteps  $\delta t = 10^{-1}, 10^{-2}$ . (b) Dummy results calculated using a large timestep  $\delta t = 10^{-1}$  to demonstrate that the results of Ref. [276] may be approximately reproduced if one deliberately stops the simulation early, after at most  $N = 1000$  steps.

where  $\rho$  is the reduced density matrix of the system,  $\mathcal{L}$  is Liouvillian superoperator and  $\sigma_j^\pm$  are Pauli raising/lowering operators at site  $j$ .

The dissipative XYZ model has recently been investigated by Kshetrimayum et al [276], using the iPEPO algorithm introduced in the previous section to compute the NESS phase diagram. This makes it a natural starting point for us to compare our iPEPO calculations against the results of Ref. [276] before studying other, less familiar problems. To this end, we compute NESS of the dissipative XYZ model for the same parameters considered by Ref. [276]. In our calculations, we start the time evolution using an appropriate timestep  $\delta t$  and then gradually decrease  $\delta t$  during the simulation to reduce the effects of Trotter error. This numerical practice is widely employed to improve the convergence accuracy of non-unitary time evolution with iPEPS or iMPS. As a criterion for convergence of iPEPO during time evolution, we require that the spectrum of singular values contained in each diagonal bond matrix  $\Lambda \in \{\Lambda^{[U,D,R,L]}\}$  in Fig. 2.22 stops changing with respect to the number of timesteps, within some accuracy  $\epsilon$ . More specifically, we take the largest difference between singular values in diagonal matrices  $\Lambda_n$  and  $\Lambda_{n-1}$ , at timesteps  $n$  and  $n-1$  respectively, rescaled by the largest singular value  $|\Lambda_n|_{\max}$  and by timestep size  $\delta t$ :

$$\epsilon_\Lambda = \frac{|\Lambda_n - \Lambda_{n-1}|_{\max}}{\delta t |\Lambda_n|_{\max}} \quad (4.5)$$

and require that  $\epsilon_\Lambda < \epsilon$  for each  $\Lambda \in \{\Lambda^{[U,D,R,L]}\}$ .

Fig. 4.4(a) shows magnetization  $M_x = \frac{1}{2}(|\langle \sigma_{i=A}^x \rangle| + |\langle \sigma_{i=B}^x \rangle|)$  averaged over the two sites  $i = A, B$  of iPEPO unit cell in Fig. 2.22, as a function of coupling strength  $J_y$  for  $J_x = 0.5$  and  $J_z = 1$ , in units of  $\kappa = 1$ , and using iPEPO bond dimension  $D = 4$ . Surprisingly, we find that iPEPO algorithm only converges for

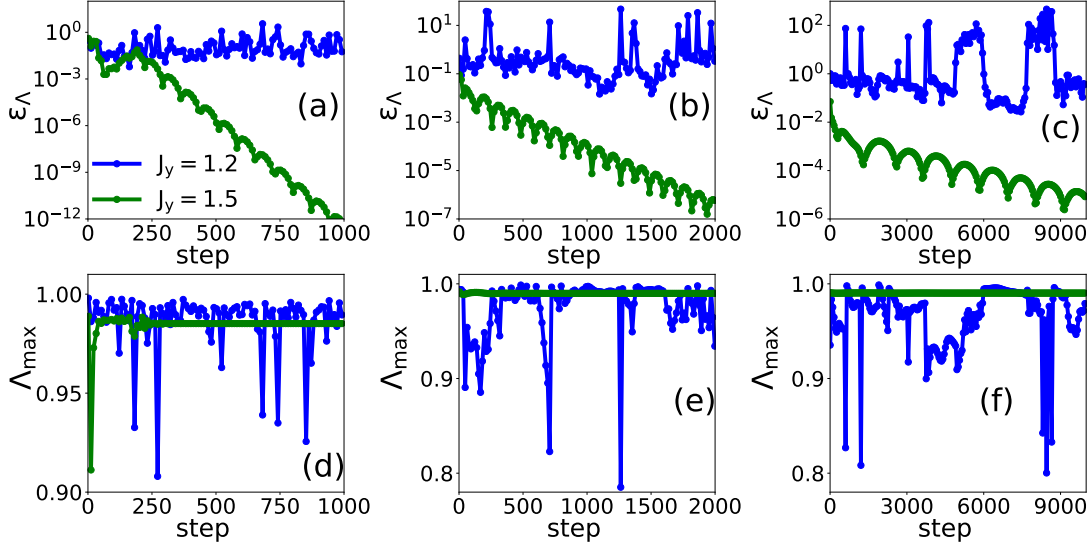


Figure 4.5: The evolution of  $\epsilon_\Lambda$  at a non-converging point  $J_y = 1.2$  and a converging point  $J_y = 1.5$  of the parameter space, using timesteps (a)  $\delta t = 10^{-1}$ , (b)  $\delta t = 10^{-2}$ , (c)  $\delta t = 10^{-3}$ . Time evolution of the largest singular value  $\Lambda_{\max}$  at  $J_y = 1.2, 1.5$ , using timesteps (d)  $\delta t = 10^{-1}$ , (e)  $\delta t = 10^{-2}$ , (f)  $\delta t = 10^{-3}$ . All other parameters are the same as in Fig. 4.4. Energies given in units of  $\kappa = 1$ .

some values of  $J_y$ , while in the red highlighted areas it fails to converge – contrary to the account by Kshetrimayum et al [276]. Our converged results agree reasonably well with Ref. [276], whereas the unconverged NESS lead to spurious values of  $M_x$ , starkly different from Ref. [276]. Following the prescription by Ref. [276], we have used the first order Trotter decomposition with timestep sizes  $\delta t = 10^{-1}, 10^{-2}$ . However, decreasing  $\delta t$  further did not improve convergence. We also find that by using a large timestep size  $\delta t = 10^{-1}$  in the problematic parameter regimes, and deliberately stopping the simulation in its early phase – i.e. after a small number of steps  $N = 1000$  before truncation errors accumulate – one can reproduce a phase diagram Fig. 4.4(b) similar to the one presented by Kshetrimayum et al [276]. However, since these ‘dummy’ results were extracted from an unconverged iPEPO, they by no means correspond to the actual NESS. They also inevitably contain significant Trotter errors due to the large timestep size. We emphasize that the non-convergent behaviour we observe occurs specifically in the SU time evolution of iPEPO, which, in our implementation of the SU scheme, is completely unaffected by the CTM calculations or contractions needed to compute observables.

These observations raise an important question about the validity of iPEPO algorithm as a tool for calculating NESS of open quantum systems. In particular, we have encountered similar convergence issues in other parameter regimes of the dissipative XYZ model, as well as other systems such as the dissipative transverse field Ising model in 2D. To keep the discussion concise, however, we will restrict our attention to the dissipative XYZ model. Our main goal in this section is to understand the behaviour of iPEPO algorithm by analysing its convergence properties.

In Figs. 4.5(a-c) we plot our convergence metric  $\epsilon_\Lambda$  defined in Eq. (4.5) against the number of steps during the simulation, for timestep sizes  $\delta t = 10^{-1}, 10^{-2}, 10^{-3}$

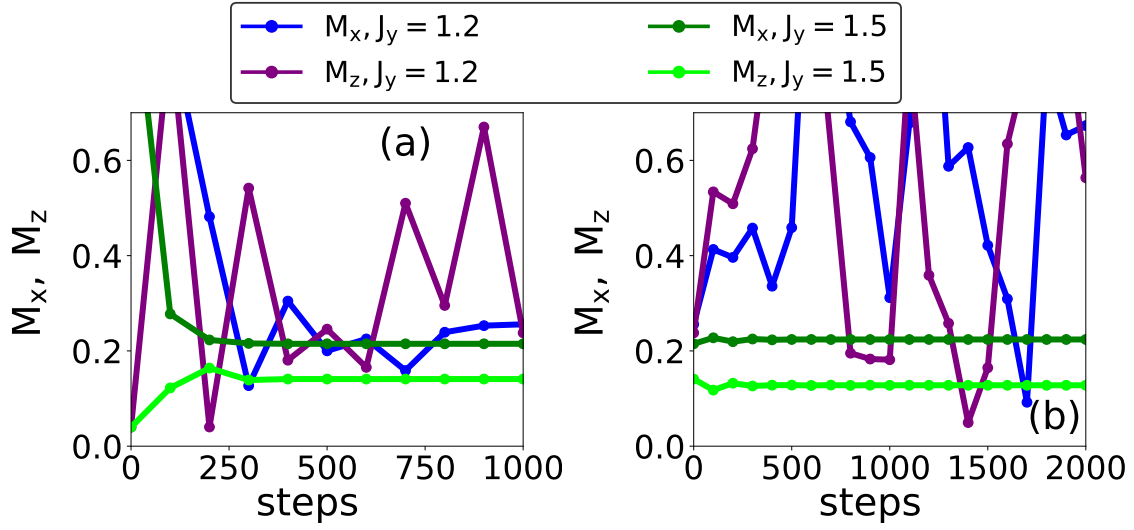


Figure 4.6: Time evolution of the magnetizations  $M_{x,z}$  at  $J_y = 1.2$  and  $J_y = 1.5$ , using timesteps (a)  $\delta t = 10^{-1}$ , (b)  $\delta t = 10^{-2}$ . All other parameters are the same as in Fig. 4.4. Energies given in units of  $\kappa = 1$ .

respectively. We show the time evolution of  $\epsilon_\Lambda$  at a characteristic point  $J_y = 1.2$  of the parameter regime where iPEPO fails to converge (blue line), and an example point of the parameter space  $J_y = 1.5$  where iPEPO converges successfully (green line). We saw that the time evolution at other values of  $J_y$  where iPEPO failed to converge was very similar to the one observed at  $J_y = 1.2$ , while the dynamics at other values of  $J_y$  where iPEPO converged was similar to the dynamics at  $J_y = 1.5$ . Since all four  $\Lambda$  matrices evolved in a similar fashion in all of our simulations, we show the results for  $\Lambda^{[U]}$  matrix only, as an example. At  $J_y = 1.5$ , we observe clearly that  $\epsilon_\Lambda$  quickly decreases to very low values below  $\epsilon = 10^{-4}$ , indicating a fast convergence of the singular value spectrum  $\Lambda$  of iPEPO. However, at  $J_y = 1.2$  iPEPO does not show any tendency to converge at all, and  $\epsilon_\Lambda$  undergoes very noisy oscillations during the entire time evolution for all timestep sizes. To illustrate the connection between  $\epsilon_\Lambda$  and the singular values  $\Lambda$  themselves more explicitly, we also display time evolution of the largest singular value  $\Lambda_{\max}$  in Figs. 4.5(d-f), for  $\delta t = 10^{-1}, 10^{-2}, 10^{-3}$  respectively. Here,  $\Lambda_{\max}$  reaches its fixed point very fast when  $J_y = 1.5$ , but continues to oscillate randomly at all times when  $J_y = 1.2$ . The dynamical patterns in the evolution of  $\Lambda$ 's translate into a similar convergent and non-convergent behaviour of intermediate observables in Figs. 4.6(a,b), shown for  $\delta t = 10^{-1}, 10^{-2}$  respectively. Fig. 4.6 displays time evolution of the magnetizations  $M_{x,z} = \frac{1}{2}(|\langle \sigma_{i=A}^{x,z} \rangle| + |\langle \sigma_{i=B}^{x,z} \rangle|)$  averaged over the two sites  $i = A, B$  of iPEPO unit cell at  $J_y = 1.2, 1.5$ . Both observables quickly relax to their steady state values for  $J_y = 1.5$ , and never even come close to the fixed point for  $J_y = 1.2$ .

We further demonstrate that the non-convergent behaviour of iPEPO does not improve with different initial conditions or simulation protocols. Figures 4.7(a-c) show that the evolution of  $\epsilon_\Lambda$  at  $J_y = 1.2$  remains non-convergent for various initial states, with timesteps  $\delta t = 10^{-1}, 10^{-2}, 10^{-3}$  respectively. A few examples of initial conditions used in our simulations that are displayed in Fig. 4.7 include a random

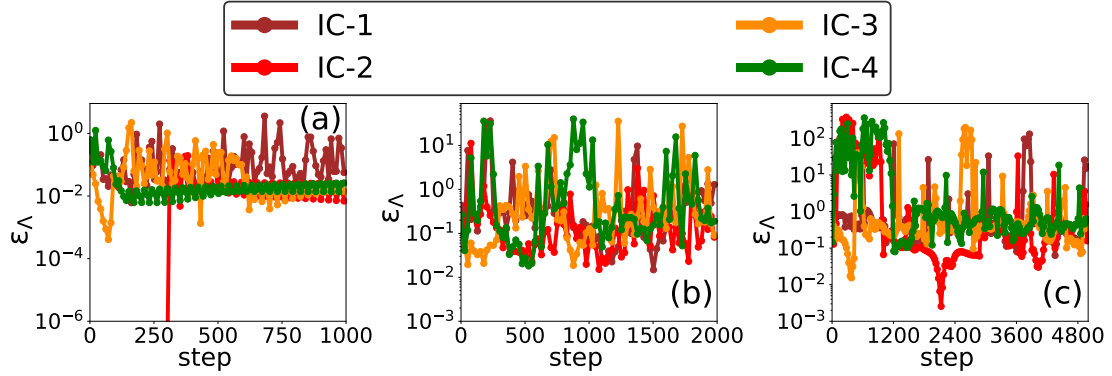


Figure 4.7: The evolution of  $\epsilon_\Lambda$  at  $J_y = 1.2$  using different initial conditions (IC): a random number state (“IC-1”, brown line), an empty state with all spins pointing ‘down’ (“IC-2”, red line), a full state with all spins pointing ‘up’ (“IC-3”, orange line), and a state where each spin has components  $\langle \sigma^x \rangle = 1$ ,  $\langle \sigma^y \rangle = 1$ ,  $\langle \sigma^z \rangle = -1$  (“IC-4”, green line), for timesteps (a)  $\delta t = 10^{-1}$ , (b)  $\delta t = 10^{-2}$ , (c)  $\delta t = 10^{-3}$ . All other parameters are the same as in Fig. 4.4. Energies given in units of  $\kappa = 1$ .

number state (brown line), an empty state with all spins pointing ‘down’ (red line), a full state with all spins pointing ‘up’ (orange line), and a state where each spin has components  $\langle \sigma^x \rangle = 1$ ,  $\langle \sigma^y \rangle = 1$ ,  $\langle \sigma^z \rangle = -1$  (green line). Other initial conditions that we have tested (not shown here) produced a similar behaviour as in Fig. 4.7.

Another possible way to approach steady states in the problematic parameter regimes is by using an adiabatic parameter sweep. We first calculate NESS for some value of  $J_y$  where iPEPO converges easily, and then perform an adiabatic sweep by changing  $J_y$  in small steps from the “easy” value to the desired “difficult” value, obtaining a converged NESS at each intermediate  $J_y$ , and using it as initial state for the next simulation with a slightly different value of  $J_y$ . This strategy often helps to bypass highly entangled intermediate states where a very high  $D$  may be needed to ensure a stable and accurate numerical simulation, and allows one to obtain high quality results in otherwise inaccessible parameter regimes. In our case, we first compute a converged NESS at  $J_y = 1.4$ , and gradually reduce  $J_y$  in steps of  $\Delta J_y = 0.01$  to  $J_y = 1.2$ . For each value of  $J_y$ , we perform time evolution using timesteps  $\delta t = 10^{-2}, 10^{-3}$ . Figs. 4.8(a,b) display the evolution of  $\epsilon_\Lambda$  for selected values of  $J_y$  during the adiabatic sweep, with timesteps  $\delta t = 10^{-2}, 10^{-3}$  respectively. We observe that iPEPO converges until  $J_y = 1.33$ , but simply decrementing  $J_y$  by a tiny step of 0.01 beyond that point immediately leads to non-convergent behaviour for  $J_y \leq 1.32$ . Smaller timesteps  $\delta t$  and smaller sweeping steps  $\Delta J_y$  have led to the same conclusion. The iPEPO algorithm thus becomes unstable as soon as we enter the highlighted areas of Fig. 4.4, even using a very slow adiabatic change of  $J_y$ .

Yet another strategy is to compute NESS in a strong dissipation regime (i.e. at large  $\kappa$ ) where it can be approximated by an unentangled product state, and apply a similar adiabatic sweep to lower  $\kappa$  gradually and calculate steady states in regimes with weak dissipation. We first compute NESS for  $\kappa = 8$ , and slowly reduce  $\kappa$  in steps of  $\Delta \kappa = 0.1$  down to  $\kappa = 1$  used in Fig. 4.4. For each value of  $\kappa$ , we perform time evolution using timesteps  $\delta t = 10^{-2}, 10^{-3}$ . Figs. 4.9(a,b) show the

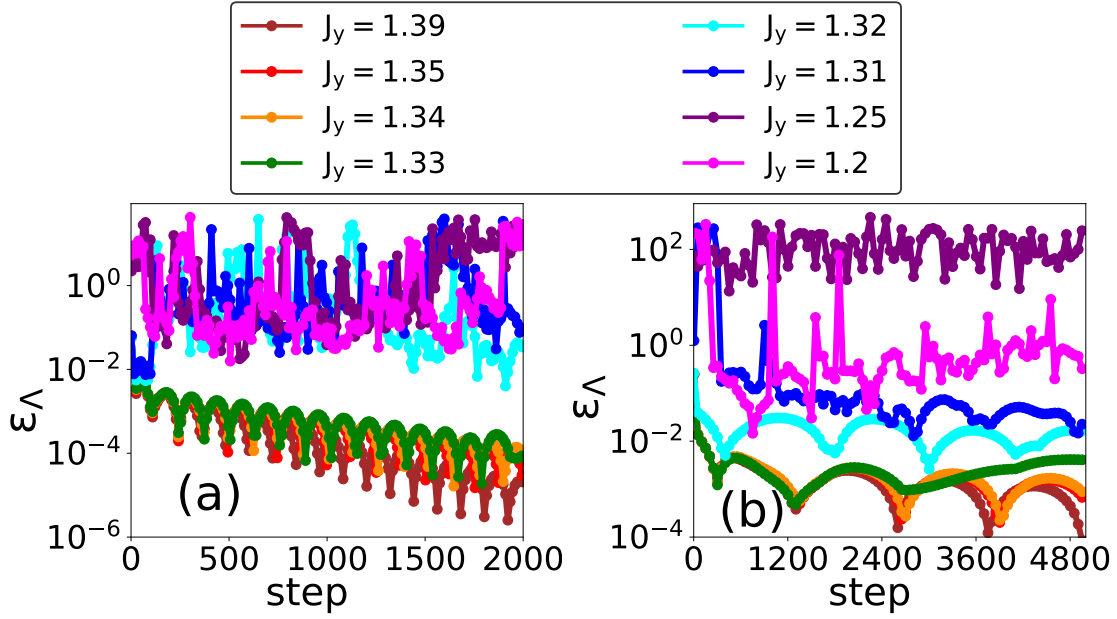


Figure 4.8: The evolution of  $\epsilon_\Lambda$  at selected values of  $J_y$  during the adiabatic parameter sweep from a converging parameter regime with  $J_y = 1.4$  to a non-converging parameter regime with  $J_y = 1.2$  in steps of  $\Delta J_y = 0.01$  and using timesteps (a)  $\delta t = 10^{-2}$ , (b)  $\delta t = 10^{-3}$ . All other parameters are the same as in Fig. 4.4. Energies given in units of  $\kappa = 1$ .

time evolution of  $\epsilon_\Lambda$  at  $J_y = 1.2$  for selected values of  $\kappa$  during the adiabatic sweep, with timesteps  $\delta t = 10^{-2}, 10^{-3}$  respectively. Similarly to the  $J_y$  sweep, we find that iPEPO converges for large  $\kappa$  until the critical value of  $\kappa = 5.2$ , beyond which a clearly non-convergent behaviour begins to dominate. We thus reach a similar conclusion that even an adiabatic sweep in  $\kappa$  fails to approach the low dissipation regimes, such as the one in Fig. 4.4. As seen in Fig. 4.9, the iPEPO algorithm becomes easily prone to instability once the dissipation is sufficiently weak and the many-body correlations are no longer insignificant.

We have also investigated the behaviour for a range of iPEPO bond dimensions  $D$ . Figs. 4.10(a-c) display time evolution of  $\epsilon_\Lambda$  at  $J_y = 1.2$  for timesteps  $\delta t = 10^{-1}, 10^{-2}, 10^{-3}$  respectively. Each panel shows simulations performed using different bond dimensions  $3 \leq D \leq 6$ . Our results indicate that the iPEPO algorithm remains strongly non-convergent for all values of  $D$  shown in the figure. Meanwhile, Figs. 4.10(d-f) display the evolution of  $\epsilon_\Lambda$  at  $J_y = 1.5$ , again for  $\delta t = 10^{-1}, 10^{-2}, 10^{-3}$  respectively. Notably, while iPEPO converges for smaller bond dimensions  $D = 3, 4$ , it becomes unstable when  $D$  is increased to 5 or 6, even at  $J_y = 1.5$ . In Fig. 4.11 we repeat the simulation at  $J_y = 1.2$  for larger bond dimensions  $10 \leq D \leq 15$ . Remarkably, we observe that the algorithmic behaviour changes when we increase the bond dimension to  $D = 12$ , and iPEPO converges for  $\delta t = 10^{-2}, 10^{-3}$ . However, increasing the bond dimension further to  $D = 14, 15$  leads to non-convergent behaviour again. We note that our CTM calculations for bond dimensions of  $D \geq 15$  already exceed the storage memory limit on a 128 GB of RAM machine. Hence, it quickly becomes very difficult to extract accurate



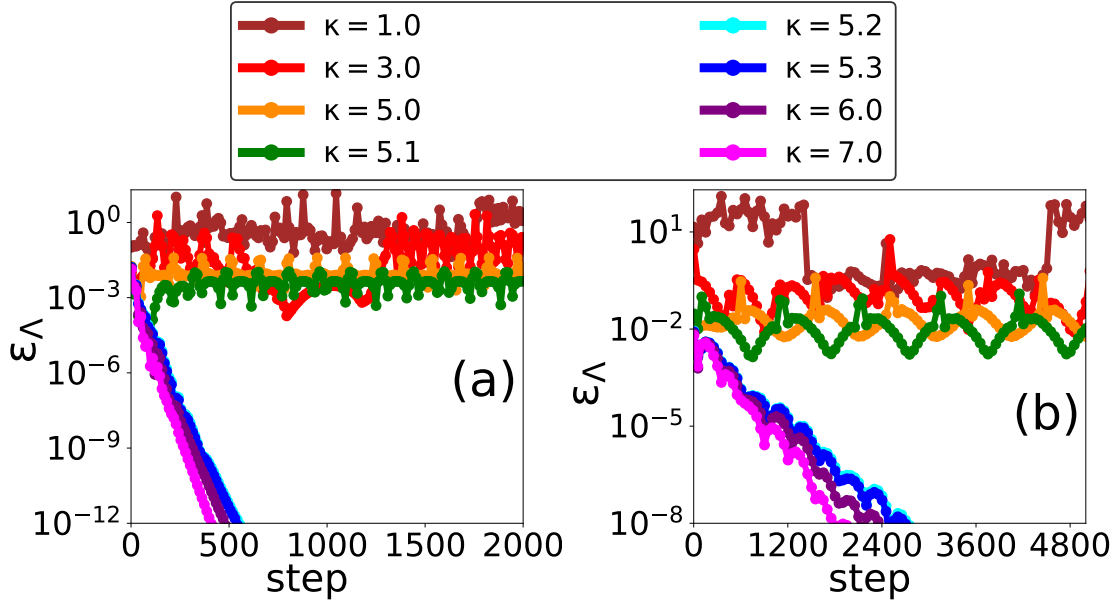


Figure 4.9: The evolution of  $\epsilon_\Lambda$  at selected values of  $\kappa$  during the adiabatic parameter sweep from a strong dissipation regime with  $\kappa = 8$  to a weak dissipation regime with  $\kappa = 1$  in steps of  $\Delta\kappa = 0.1$  and using timesteps (a)  $\delta t = 10^{-2}$ , (b)  $\delta t = 10^{-3}$ . All other parameters are the same as in Fig. 4.4. Energies given in units of  $\kappa = 1$ .

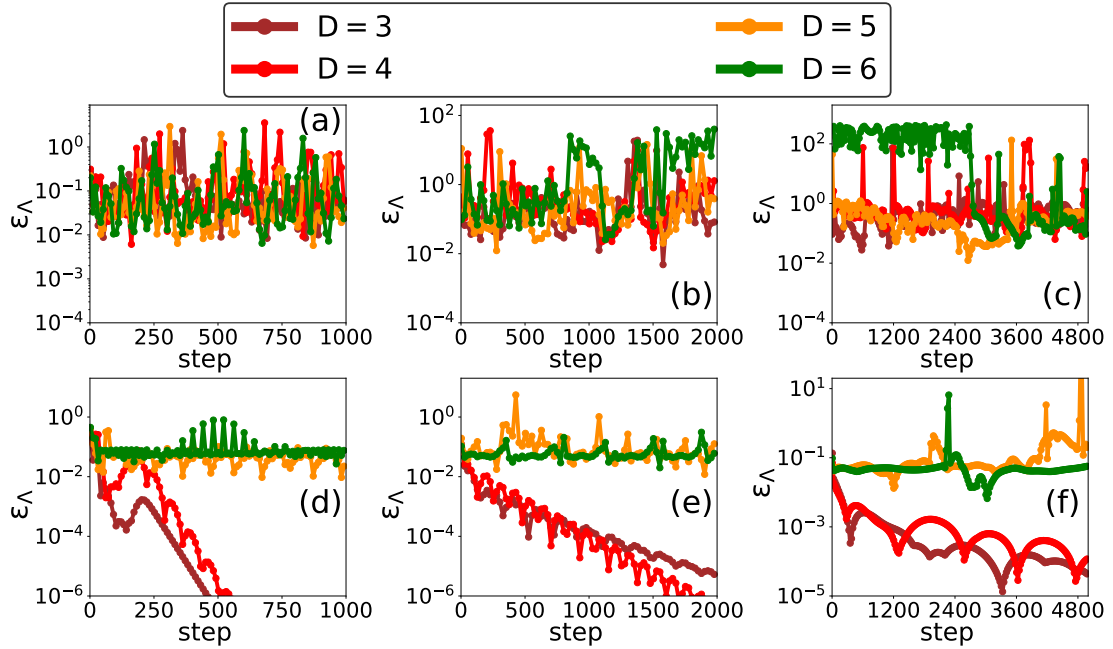


Figure 4.10: The evolution of  $\epsilon_\Lambda$  at a non-converging point  $J_y = 1.2$  of the parameter space for different iPEPO bond dimensions  $D = 3$  (brown line),  $D = 4$  (red line),  $D = 5$  (orange line) and  $D = 6$  (green line), using timesteps (a)  $\delta t = 10^{-1}$ , (b)  $\delta t = 10^{-2}$ , (c)  $\delta t = 10^{-3}$ . We have repeated the same simulation at a converging point  $J_y = 1.5$  of the parameter space, using timesteps (d)  $\delta t = 10^{-1}$ , (e)  $\delta t = 10^{-2}$ , (f)  $\delta t = 10^{-3}$ . All other parameters are the same as in Fig. 4.4. Energies given in units of  $\kappa = 1$ .



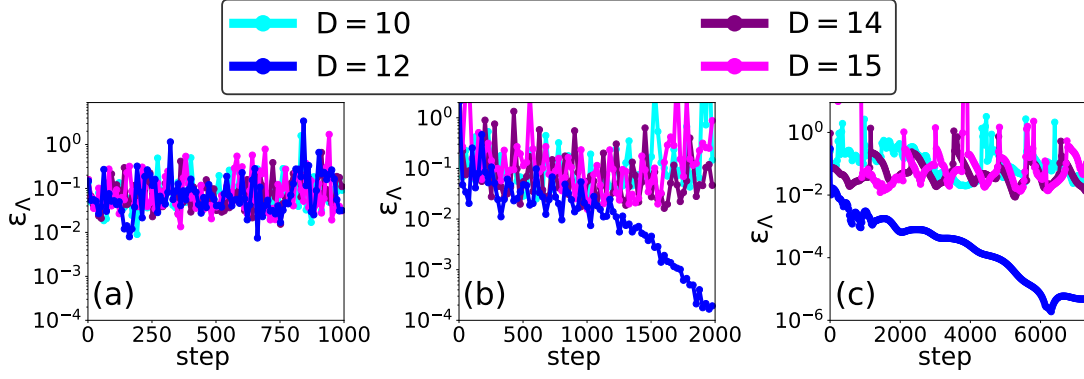


Figure 4.11: The evolution of  $\epsilon_\Lambda$  at a non-converging point  $J_y = 1.2$  of the parameter space for larger iPEPO bond dimensions  $D = 10$  (light blue line),  $D = 12$  (blue line),  $D = 14$  (purple line) and  $D = 15$  (pink line), using timesteps (a)  $\delta t = 10^{-1}$ , (b)  $\delta t = 10^{-2}$ , (c)  $\delta t = 10^{-3}$ . All other parameters are the same as in Fig. 4.4. Energies given in units of  $\kappa = 1$ .

expectation values at large  $D$  and validate that iPEPO yields physical observables – thus rendering the iPEPO algorithm of no practical use for  $D \geq 15$  with our computational resources.

## 4.5 Conclusions

The findings of the last section lead us to conclude that the iPEPO algorithm in its present form is unstable, converging only in some parameter regimes while failing to find a converged steady state in others. It is thus not suitable for applications to driven dissipative systems, except in the parameter regimes with a very strong Lindblad dissipation that tries to bring the system to a trivial steady state.

The iPEPO algorithm continued to exhibit non-convergent behaviour for the range of bond dimensions  $D$  that we could access, and increasing  $D$  has even led to a new instability in some cases that were convergent for smaller  $D$ . One possible cause of the instability could be related to the dissipative real-time evolution of iPEPO visiting highly-entangled intermediate states before relaxing to NESS – one then needs a sufficiently large  $D$  to represent these intermediate states accurately and ensure a stable convergence. An improved stability at  $D = 12$  may suggest that the iPEPO algorithm would become more robust if we could access even larger  $D$  than discussed in this chapter. However, it remains unclear if this problem is tractable at all, with computational resources available at present. Unlike the iTEBD algorithm in 1D, the SU iPEPS algorithm in 2D thus cannot be straightforwardly extended to Liouvillian propagation. We discuss below some alternative strategies for calculating NESS in 2D that could be explored in future research.

One potential issue in the iPEPO algorithm is the fact that it does not preserve the positivity and hermiticity of the reduced density matrix. Implementing a scheme that satisfies these conditions could help us constrain the iPEPO time evolution to explore the space of physical states. A similar approach was proposed by Ref. [43], using locally purified MPOs for time evolution of 1D systems. This approach,

however, can be computationally far more expensive due to the large additional tensor dimensions introduced in the locally purified form of the density matrix, which may be difficult to treat efficiently in 2D. A related study [283] has also shown that an efficient and locally positive semidefinite description of mixed states does not exist, and one can only find approximations for it. An important consequence is that the bond dimension of the locally purified representation may be considerably larger than that of the vectorized representation used in the superoperator renormalization group in Sec. 2.2.4. Overall, the question of ensuring positivity in tensor network simulations of mixed states remains a challenging problem in both 1D and 2D.

We have already mentioned the possibilities of adapting FU iPEPS algorithm to the Lindblad time evolution of mixed states, or implementing a global variational search algorithm that targets the null eigenstate  $|\rho\rangle$  of either Liouvillian  $\mathcal{L}$  or a Hermitian positive semidefinite object  $\mathcal{L}^\dagger\mathcal{L}$ . Solving the variational problem with  $\mathcal{L}^\dagger\mathcal{L}$  is particularly appealing since it allows reusing the standard and robust Hermitian optimization algorithms. However, even when  $\mathcal{L} = \sum_l \mathcal{L}_{l,l+1}$  contains only the nearest-neighbour terms, taking the product  $\mathcal{L}^\dagger\mathcal{L} = \sum_{l,r} \mathcal{L}_{l,l+1}^\dagger \mathcal{L}_{l+r,l+r+1}$  will inevitably introduce highly nonlocal cross terms. While the problem is still manageable in 1D [41], the effective nonlocal couplings may easily lead to iPEPS bond dimensions unfeasibly large for a 2D tensor network. Therefore, it becomes necessary to truncate the range  $r$  of these nonlocal terms, which has been shown to be effective for at least some models in 1D [284]. Another way forward is solving the variational search problem with  $\mathcal{L}$ , which will require appropriate non-Hermitian optimization algorithms. In any case, the variational optimization approaches will require computationally expensive tensor contractions involving both the iPEPS representing  $|\rho\rangle$  and the iPEPO representing either  $\mathcal{L}$  or  $\mathcal{L}^\dagger\mathcal{L}$ . This is particularly true for  $\mathcal{L}^\dagger\mathcal{L}$ : if  $\mathcal{L}$  can be expressed as an iPEPO with bond dimension  $D_W$ , then  $\mathcal{L}^\dagger\mathcal{L}$  iPEPO will need a squared bond dimension  $D_W^2$ , resulting in extremely costly contractions.

Nonetheless, Refs. [210, 211] have recently proposed two novel variational iPEPS techniques for ground state calculations in 2D: one of them optimizes iPEPS tensors using tangent space methods, and the other one – by solving the generalized eigenvalue problem. Notably, both approaches utilize a systematic summation of Hamiltonian contributions coming from individual terms in the Hamiltonian, thus circumventing the need of constructing a full Hamiltonian iPEPO. Adapting these algorithms to either  $\mathcal{L}$  or  $\mathcal{L}^\dagger\mathcal{L}$  could dramatically reduce the computational costs that limit the practical use of variational iPEPS methods. The global variational optimization could also offer a potentially much more robust way of finding the NESS of  $\mathcal{L}$  than one could hope to achieve with the standard iPEPS algorithm relying on two-body updates.

Although the above ideas are beyond the scope of this thesis, we hope that they could be explored in future work.

## **Part III**

### **Non-Markovian dynamics**



# Chapter 5

## Time-evolving matrix product operators

### 5.1 Introduction

Strong couplings and structured environments give rise to non-Markovian open system dynamics by allowing a backflow of information from the environment to the system. There are an immense variety of open quantum systems of fundamental and technological interest that exhibit non-Markovian quantum dynamics.

Various solid state quantum devices and their constituents – such as superconducting circuits [16, 123], semiconductor quantum dots [20, 124], or nanomechanical resonators [18] – experience dissipation, for example, due to thermal vibrations in their solid state environments that often display complex, highly structured spectra. While such system-environment interaction usually induces decoherence, engineered quantum noise can also counteract decoherence or even help us generate robust quantum states [125, 126]. Therefore, our ability to understand and control the non-Markovian dissipation is vital to the applications of quantum computing and quantum information processing [127, 128]. Understanding how baths with vibrational spectra affect the excitation transport in organic molecules is another active area of research. A prominent example here is the noise-assisted transport in photosynthetic complexes [129–132], where the coupling between electronic excitations and the noisy vibrational environment can enhance the coherent excitation transfer. Non-Markovian dissipation also underpins quantum transport phenomena in other systems, including the macroscopic tunnelling of flux in superconducting circuits [138–140], incoherent tunnelling of bistable defects in metals and amorphous systems [141, 142], electron and proton transfer in solvent environments [143], and heat transport in molecular junctions [144].

Yet, as we have already seen in Section 1.3, theoretical description of non-Markovian systems remains challenging as most existing tools are either restricted to isolated cases of application or face a prohibitive scaling in computational resources. In this chapter, we propose a general, efficient and numerically exact computational algorithm for simulating non-Markovian dynamics. Our new method builds on the Quasi-adiabatic propagator path integral (QUAPI) algorithm introduced by Makri and Makarov [163], [164]. It is based on the discretization of the

Feynman-Vernon influence functional, formulated as time evolution of an object called the augmented density tensor (ADT) that records the history of past states of the system to capture the non-Markovian memory effects of the environment. In principle, QUAPI is applicable to environments with arbitrary spectral densities and is not limited to any specific parameter regimes – this generality makes it a fertile ground for building more efficient computational schemes. The main shortcoming of QUAPI is the exponential scaling of the memory storage requirements with the bath correlation time. Here we show how one can decompose the ADT and its propagators as a tensor network and apply standard MPS/MPO techniques described in Chapter 2 to improve the scaling from exponential to low-order polynomial. We call this technique the time-evolving matrix product operator (TEMPO) algorithm. The dramatic reduction of scaling of CPU time and memory with bath memory time in TEMPO enables efficient simulations of non-Markovian dynamics in various physical scenarios far beyond the reach of other numerical methods.

In this work, our applications of TEMPO will primarily focus on the paradigmatic spin-boson model (SBM), introduced in Sec. 1.3.1. Despite its deceptive simplicity, SBM can accurately represent relaxation phenomena in a wide range of quantum systems, including exciton-phonon coupling in organic molecules [131, 132], dynamics of coupled quantum dots [19], magnetic flux transport in superconducting circuits [123], and relaxation of dilute impurities in solid state materials [166–168].

Unsurprisingly, much effort has recently been invested into the understanding of the fundamental properties and dynamics of SBM [285]. For example, Ref. [123] have designed a quantum simulation with superconducting circuits and transmission line resonators to probe SBM experimentally, in a well-controlled environment. However, numerical simulations of SBM dynamics and phase diagram remain challenging, especially in the strong-coupling regime. With this motivation in mind, we will first apply TEMPO to study the bath-induced localization phase transition of the Ohmic SBM. The second problem that we will investigate with TEMPO is excitation transfer between two spatially separated two-level systems in a common environment. This type of process occurs in a multitude of physical situations, such as the experiments with coupled quantum dots [286–291]. Here, the vibrational environment leads to the phonon-assisted transport of excitons between two or more semiconductor quantum dots, which is a key process in these systems [292]. A similar excitation transfer takes place in waveguide-QED systems, and is responsible for cooperative effects between qubits strongly coupled to a continuum of waveguide modes [293]. This interaction can generate long-range entanglement between the qubits, and provides a basis for scalable quantum networking architectures. As we will see later, the large separation regime of this problem is currently not accessible to any existing methods and largely remains an uncharted territory.

We expect that TEMPO will enable accurate simulations of such energy transfer processes and – in a longer term perspective – will greatly advance our understanding about solid state environments of quantum dots or qubits, and excitation transport in organic molecules. We begin the chapter by introducing QUAPI in Sec. 5.2, followed by the discussion of TEMPO in Sec. 5.3 where we reformulate ADT propagation as a tensor network. We next benchmark TEMPO in Sec. 5.4 by comparing it to other known results and methods: the exact analytical solution

of the independent boson model, QUAPI simulation of the spin-boson model coupled to an Ohmic bath, and Reaction Coordinate Mapping of the spin-boson model interacting with a Drude-Lorentz bath. To demonstrate the efficiency and robustness of TEMPO, we will apply it to study two different problems in Sec. 5.5. The first problem is finding the critical point of the localization phase transition of the Ohmic spin-boson model. The second one is simulating the environment-mediated excitation transfer between two spins coupled to the same bath.

In this chapter, we present work that was performed in collaboration with Aidan Strathearn and Peter Kirton. The TEMPO code was developed by Dainius Kilda, Aidan Strathearn and Peter Kirton. The simulations in Sec. 5.4 were performed by Dainius Kilda. The simulations and analysis in Sec. 5.5 were performed by Aidan Strathearn and Peter Kirton. The text and interpretation presented here is my own original work.

## 5.2 Quasi-adiabatic propagator path integrals

In Section 1.1.3 we have introduced the Feynman path integral representation of non-Markovian dynamics of an open quantum system, with bath degrees of freedom integrated out. In particular, we have obtained the result Eq. (1.71) for the reduced density matrix of the system where the effects of system-bath interaction are described by the influence functional that acts only on the reduced system trajectories. The formal result Eq. (1.71), however, has no known analytical solution and is of little practical use. Here we derive the discretized form of the Feynman influence functional that is amenable to a numerical treatment. We will then describe the Quasi-adiabatic propagator path integral (QUAPI) numerical scheme proposed by Makri and Makarov [163], [164]. In their approach, the discretized version of Eq. (1.71) is reformulated as an iterative propagation of an object called the augmented density tensor (ADT). Our derivation here follows similar steps and uses the same set of assumptions introduced in Section 1.1.3. We consider the class of models specified by Eqs. (1.42)-(1.44); we also assume a separable initial condition Eq. (1.10) with the bath initially in the thermal state  $\rho_B(0)$  given by Eq. (1.11). Let us start with Liouvillian propagation Eq. (1.12) of the reduced system density matrix  $\rho(t)$  (the subscript “S” is dropped for brevity in this chapter):

$$\rho(t) = \text{Tr}_B (e^{t\mathcal{L}} \rho(0) \rho_B(0)) \quad (5.1)$$

where  $\mathcal{L} = \mathcal{L}_S + \mathcal{L}_B$  is the Liouvillian of the total system  $S+B$ , while  $\mathcal{L}_S = -i[H_S, \bullet]$  generates dynamics of the bare system, and  $\mathcal{L}_B = -i[H_B, \bullet]$  includes the bath Hamiltonian and the system-bath interaction. It is also possible to incorporate additional Markovian dissipation in the reduced system at no computational cost, for instance  $\mathcal{L}_S \rightarrow \mathcal{L}_S = -i[H_S, \bullet] + \gamma\mathcal{D}[L]$  where  $\mathcal{D}[L]$  is Lindblad dissipator with jump operator  $L$  and dissipation rate  $\gamma$  [294]. In contrast to the continuum representation in Section 1.1.3, here we express the time evolution in a discrete basis spanned by the system states  $|i_n\rangle, |i'_n\rangle$  corresponding to the  $n$ 'th timestep of the forward and backward time evolution respectively. Without losing generality, we choose to work in the basis where the system operator  $X$  is diagonal – i.e. the basis

states  $|i_n\rangle, |i'_n\rangle$  are the eigenstates of  $X$ . This means that the system coordinates are measured by the eigenvalues of  $X$ :  $x_{i_n} = \langle i_n|X|i_n\rangle$  and  $x_{i'_n} = \langle i'_n|X|i'_n\rangle$  at each discrete timestep  $n$  of propagation. We express Eq. (5.1) in terms of the endpoints of time evolution  $i_0, i'_0$  and  $i_N, i'_N$  at times  $\tau = 0$  and  $\tau = t$  respectively:

$$\rho_{i_N, i'_N}(t) = \text{Tr}_B \sum_{i_0, i'_0} \langle i_N | \left( e^{t\mathcal{L}} |i_0\rangle \langle i'_0| \right) |i'_N\rangle \rho_{i_0, i'_0}(0) \rho_B(0) \quad (5.2)$$

with indices running from 1 to  $d$ , the Hilbert space dimension. For convenience, we will work in the vectorized Liouville space introduced in Section 2.2.4, where a  $d \times d$  density operator is represented by a vector with  $d^2$  elements, and a superoperator acting on  $d \times d$  operators is represented by a  $d^2 \times d^2$  matrix. The  $|i\rangle, |i'\rangle$  basis in the Hilbert space thus maps to the  $|j\rangle$  basis in the Liouville space  $|i\rangle \langle i'| \rightarrow |ii'\rangle \rightarrow |j\rangle$  by virtue of Choi isomorphism, as in Sec. 2.2.4. Therefore, the density operator becomes  $\rho_{i, i'}(t) \rightarrow \rho_{ii'}(t) \rightarrow \rho_j(t)$ , where  $\rho_j(t) = \langle j|\rho(t)\rangle_\#$  and  $|\rho(t)\rangle_\#$  is the vectorized density operator. The Liouvillian superoperator becomes  $\langle i| \left( e^{t\mathcal{L}} |l\rangle \langle l'| \right) |i'\rangle \rightarrow \langle ii'|e^{t\mathcal{L}_\#}|ll'\rangle \rightarrow \langle j|e^{t\mathcal{L}_\#}|k\rangle$ , where  $\mathcal{L}_\#$  is the vectorized Liouvillian. The equation Eq. (5.2) then transforms into its equivalent Liouville space form

$$\rho_{j_N}(t) = \text{Tr}_B \sum_{j_0} \langle j_N | e^{t\mathcal{L}_\#} |j_0\rangle \rho_{j_0}(0) |\rho_B(0)\rangle_\# \quad (5.3)$$

with a discrete basis given by  $|j_n\rangle$  at  $n$ 'th timestep; all indices  $j_n$  thus run from 1 to  $d^2$ . For brevity of notation, we will drop the  $\#$  subscripts of vectorized superoperators and superkets, and simply denote the vectorized Liouvillian  $\mathcal{L}_\#$  by  $\mathcal{L}$  for the rest of the chapter.

We now discretize the time evolution by subdividing  $e^{t\mathcal{L}} = [e^{\delta t\mathcal{L}}]^N$  into  $N$  short time propagators with a small timestep  $\delta t$ . By inserting identity resolution  $I = \sum_{j_n} |j_n\rangle \langle j_n|$  between each  $e^{\delta t\mathcal{L}}$ , we can express the time evolution in Eq. (5.3) as a path sum over the system states  $|j_n\rangle$ :

$$\langle j_N | e^{t\mathcal{L}} |j_0\rangle = \sum_{j_1, \dots, j_{N-1}} \prod_{n=1}^N \langle j_n | e^{\delta t\mathcal{L}} |j_{n-1}\rangle \quad (5.4)$$

If the timestep  $\delta t$  is sufficiently small, one can use a Trotter decomposition to separate the system and bath propagation:

$$e^{\delta t\mathcal{L}} = e^{\delta t\mathcal{L}_B} e^{\delta t\mathcal{L}_S} + O(\delta t^2) \quad (5.5)$$

The above splitting is the first order Trotter decomposition which carries an error of  $O(\delta t^2)$ . We note that all the arguments presented in this section are straightforward to extend to the higher order Trotter decompositions, and all the numerical results in Chapters 5 and 6 use the second order Trotter decomposition, with an error of  $O(\delta t^3)$ . However, for ease of explanation, we use the first order decomposition Eq. (5.5) in our derivations here. Using Eq. (5.5) we can express  $\langle j_n | e^{\delta t\mathcal{L}} |j_{n-1}\rangle$  in



Eq. (5.4) as

$$\begin{aligned} \langle j_n | e^{\delta t \mathcal{L}} | j_{n-1} \rangle &\approx \langle j_n | e^{\delta t \mathcal{L}_B} e^{\delta t \mathcal{L}_S} | j_{n-1} \rangle \\ &= e^{\delta t \mathcal{L}_B(j_n)} \langle j_n | e^{\delta t \mathcal{L}_S} | j_{n-1} \rangle = e^{\delta t \mathcal{L}_B(j_n)} [e^{\delta t \mathcal{L}_S}]_{j_n, j_{n-1}} \end{aligned} \quad (5.6)$$

Substituting the Liouvillian overlaps Eq. (5.6) and Eq. (5.4) back into Eq. (5.3) gives

$$\rho_{j_N}(t) = \text{Tr}_B \sum_{j_0, \dots, j_{N-1}} \prod_{n=1}^N e^{\delta t \mathcal{L}_B(j_n)} [e^{\delta t \mathcal{L}_S}]_{j_n, j_{n-1}} \rho_{j_0}(0) |\rho_B(0)\rangle \quad (5.7)$$

After integrating out the bath degrees of freedom, and some simple rearrangements we obtain the path sum representation of the reduced density matrix  $\rho_{j_N}(t)$ :

$$\rho_{j_N}(t) = \sum_{j_0, \dots, j_{N-1}} \prod_{n=1}^N [e^{\delta t \mathcal{L}_S}]_{j_n, j_{n-1}} I(j_1, \dots, j_N) \rho_{j_0}(0) \quad (5.8)$$

where

$$I(j_1, \dots, j_N) = \text{Tr}_B \left( \prod_{n=1}^N e^{\delta t \mathcal{L}_B(j_n)} |\rho_B(0)\rangle \right) \quad (5.9)$$

is the influence functional that contains the system-bath coupling effects. The Eq. (5.8) is the discrete version of the path integral representation Eq. (1.71) in Section 1.1.3, and the Eq. (5.9) becomes equal to the influence functional Eq. (1.72) in the continuum limit. Instead of tackling Eq. (5.9) directly, the easiest way to simplify Eq. (5.9) is to discretize its continuum limit Eq. (1.72) with the influence phase given by Eq. (1.68). To this end, we discretize the system operator  $X(t) = \sum_{n=1}^N x_{j_n} \theta(t_n - t) \theta(t - t_{n-1}) |j_n\rangle$  in terms of its eigenbasis  $|j_n\rangle$  in the Liouvillian space, with discrete time  $t_n = n\delta t$ . We substitute this expression into Eqs. (1.68), (1.72); after some algebra we find the discretized influence functional

$$I(j_1, \dots, j_N) = \prod_{n=1}^N \prod_{k=0}^{n-1} I_k(j_n, j_{n-k}) \quad (5.10)$$

decomposed into influence functions

$$I_k(j, j') = \exp(\phi_k(j, j')) \quad (5.11)$$

where the influence phase is

$$\phi_k(j, j') = x_j^- (\text{Re}[\eta_k] x_{j'}^- + i \text{Im}[\eta_k] x_{j'}^+) \quad (5.12)$$

Since  $|j\rangle$  is the diagonal basis of  $X$ , the  $x_j^\pm$  simply correspond to the  $d^2$  possible sums and differences involving two eigenvalues of  $X$ . The Makri coefficients  $\eta_k$  describe the non-Markovian correlations in the reduced system between timesteps  $n$  and  $n'$ , i.e. extending across  $k = n - n'$  timesteps of time evolution:

$$\eta_{n-n'} = \begin{cases} \int_{t_{n-1}}^{t_n} dt' \int_{t_{n'-1}}^{t_{n'}} dt'' C(t' - t'') & n \neq n' \\ \int_{t_{n-1}}^{t_n} dt' \int_{t_{n-1}}^{t'} dt'' C(t' - t'') & n = n' \end{cases} \quad (5.13)$$

The  $C(t)$  here is the bath autocorrelation function Eq. (1.62) derived in Section 1.1.3, and contains information about the non-Markovian memory effects. For convenience, we absorb the free system evolution into the influence function  $I_1(j_n, j_{n-1})$ :

$$[e^{\delta t \mathcal{L}_S}]_{j_n, j_{n-1}} I_1(j_n, j_{n-1}) \rightarrow I_1(j_n, j_{n-1}) \quad (5.14)$$

for  $n > 1$ . We now substitute Eq. (5.10) into Eq. (5.8) to arrive at the final result:

$$\rho_{j_N}(t_N) = \sum_{j_1, \dots, j_{N-1}} \prod_{n=1}^N \prod_{k=0}^{n-1} I_k(j_n, j_{n-k}) \sum_{j_0} [e^{\delta t \mathcal{L}_S}]^{j_1, j_0} \rho_{j_0}(0) \quad (5.15)$$

with the redefined influence functions

$$I_k(j, j') = \begin{cases} e^{\phi_k(j, j')} & k \neq 1 \\ [e^{\delta t \mathcal{L}_S}]_{j, j'} e^{\phi_1(j, j')} & k = 1 \end{cases} \quad (5.16)$$

Each influence function  $I_k(j, j')$  is a time-nonlocal entity that connects the time evolution of the amplitude of state  $j$  to the amplitude of state  $j'$ , a number  $k$  of timesteps ago. The influence phase  $\phi_k(j, j')$  is given by Eq. (5.12) with Makri coefficients Eq. (5.13) as before. To evaluate the path sum Eq. (5.15), we will show how it can be reformulated as an iterative propagation algorithm.

One may interpret the remaining summand of Eq. (5.15) as the components of a rank- $N$  tensor

$$A^{j_N, j_{N-1}, \dots, j_1} = \prod_{n=1}^N \prod_{k=0}^{n-1} I_k(j_n, j_{n-k}) \sum_{j_0} [e^{\delta t \mathcal{L}_S}]^{j_1, j_0} \rho_{j_0}(0). \quad (5.17)$$

This object is known as the augmented density tensor (ADT), originally introduced by Makri and Makarov in [163], [164]. It is a generalization of the density matrix  $\rho_{j_N}(t)$  of the most recent timestep  $n = N$ , to a tensor  $A^{j_N, j_{N-1}, \dots, j_1}$  that stores the history of past states of the reduced system from timesteps  $n = 1, \dots, N$ , and thus lives in an augmented Hilbert (or, equivalently, Liouville) space of size  $d^{2N}$ . Each index  $j_n$  of the ADT refers to the Liouville space at timestep  $n$  and runs from 1 to  $d^2$ . In other words, the ADT contains information about the amplitudes of each trajectory that the reduced system could have traversed in its Hilbert (or Liouville) space over the previous  $n$  timesteps. As such, ADT is capable of fully describing all the non-Markovian memory effects during time evolution. It also shares many properties with a standard density matrix, including the unit trace and the hermiticity [295]. We will now see how one can build this ADT at timestep  $n = N$ , starting from the initial density matrix  $\rho_{j_0}(0)$ . Let us gather the influence functions corresponding to a given timestep  $n > 1$  into a propagator

$$B_{i_{n-1}, \dots, i_1}^{j_n, j_{n-1}, \dots, j_1} = \left[ \prod_{k=1}^{n-1} \delta_{i_{n-k}}^{j_{n-k}} \right] \left[ \prod_{k=0}^{n-1} I_k(j_n, j_{n-k}) \right] \quad (5.18)$$

that evolves ADT from timestep  $n - 1$  to timestep  $n$ . Meanwhile, for the first timestep  $n = 1$  we have:

$$B^{j_1, j_0} = I_0(j_1, j_1) [e^{\delta t \mathcal{L}_S}]^{j_1, j_0} \quad (5.19)$$

The expression Eq. (5.15) can now be computed by performing successive tensor contractions. The first step transforms  $\rho_{j_0}(0)$  into the initial rank-1 ADT:

$$A^{j_1} = B^{j_1, j_0} \rho_{j_0}(0) \quad (5.20)$$

The second propagation step is the tensor contraction

$$A^{j_2, j_1} = B_{i_1}^{j_2, j_1} A^{i_1} \quad (5.21)$$

which produces a rank-2 ADT. It represents the system state at present  $n = 2$  (spanned by index  $j_2$ ), and one timestep ago in the past  $n = 1$  (spanned by index  $j_1$ ). The third step produces a rank-3 ADT

$$A^{j_3, j_2, j_1} = B_{i_2, i_1}^{j_3, j_2, j_1} A^{i_2, i_1} \quad (5.22)$$

representing the system state at present  $n = 3$ , as well as one and two timesteps ago in the past at  $n = 2$  and  $n = 1$  respectively. The  $n$ 'th step of this tensor contraction process then reads

$$A^{j_n, j_{n-1}, \dots, j_1} = B_{i_{n-1}, \dots, i_1}^{j_n, j_{n-1}, \dots, j_1} A^{i_{n-1}, \dots, i_1} \quad (5.23)$$

Numerically, each individual step of the propagation can be performed as a matrix-vector multiplication in an augmented Liouville space. To recover the physical density matrix from ADT at any step  $n$  of time evolution, one needs to sum over all the indices corresponding to the past states  $j_{n-1}, \dots, j_1$ , keeping only the most recent index  $j_n$ :

$$\rho_{j_n}(t_n) = \sum_{j_1, \dots, j_{n-1}} A^{j_n, j_{n-1}, \dots, j_1} \quad (5.24)$$

After computing the final density matrix Eq. (5.24), one can use it to extract observables as usual. The iterative tensor propagation algorithm summarized above enables us to compute a time evolved reduced density matrix Eq. (5.15), and is known as Quasi-adiabatic propagator path integral (QUAPI). It is clear that the rank of ADT increases by 1 with each timestep to record the lengthening history of system states, and its size thus grows exponentially as  $O(d^{2N})$ . The remedy proposed by Makri and Makarov [163], [164] is the finite memory approximation. For a continuum of harmonic bath modes, the memory kernel Eq. (1.62) decays away on a timescale set by the bath correlation time. As a consequence, Makri coefficients  $\eta_{k=n-n'}$  in Eq. (5.13) vanish if two timesteps  $n$  and  $n'$  are sufficiently far apart. We can thus introduce a finite memory approximation by setting  $\eta_k = 0$  for  $k > K$ , where the memory cutoff in timesteps is defined by  $K = \tau_c / \delta t$ . The  $\tau_c$  is the memory cutoff time, which should be at least as long as the bath correlation time. This implies that bath influence functions in Eq. (5.18) are set to  $I_k(j_n, j_{n-k}) = \delta_{j_n, j_{n-k}}^{j_n}$  for  $k > K$ . Therefore, finite memory approximation modifies the propagation as follows. For  $n \leq K$  time evolution remains the same, and the  $n$ 'th step of propagation is still given by Eq. (5.23) with propagator Eq. (5.18). Once we have evolved past the cutoff point  $n > K$ , the  $n$ 'th propagation step is instead given by

$$A^{j_n, j_{n-1}, \dots, j_{n-K+1}} = B_{i_{n-1}, \dots, i_{n-K+1}, i_{n-K}}^{j_n, j_{n-1}, \dots, j_{n-K+1}} A^{i_{n-1}, \dots, i_{n-K+1}, i_{n-K}} \quad (5.25)$$

with propagator

$$B_{i_{n-1}, \dots, i_{n-K+1}, i_{n-K}}^{j_n, j_{n-1}, \dots, j_{n-K+1}} = \left[ \prod_{k=1}^K \delta_{i_{n-k}}^{j_{n-k}} \right] \left[ \prod_{k=0}^K I_k(j_n, j_{n-k}) \right] \quad (5.26)$$

where  $K < N$ , the total number of timesteps. At each step Eq. (5.25) we grow ADT by one index  $j_n$  which is the latest in time, and also remove one index  $i_{n-K}$  which is the earliest in time. This means discarding the information in the ADT for times longer than  $\tau_c = K\delta t$  in the past as we propagate forward in time. The rank of the ADT then stays constant and equal to  $K$  for all  $n \geq K$ . To make the finite memory approximation effective, we aim to maximize the memory cutoff time  $\tau_c$  so that it captures all the relevant non-Markovian correlations. We can extend  $\tau_c$  by performing QUAPI simulations with increasing  $K$  until it has no further effect on the results. Meanwhile, one also needs to adjust the timestep  $\delta t$  making it as small as possible to eliminate the Trotter error, but large enough to reach long memory times  $\tau_c$ . In practice, we tune both parameters until convergence of the results is observed with respect to both of them. Even with the finite memory approximation implemented, the computational cost and the memory storage requirements of QUAPI still scale exponentially with the memory cutoff  $O(d^{2K})$ . In particular, simulations are typically restricted to  $K < 20$ , limiting QUAPI to systems with short bath correlation times.

### 5.3 Time-evolving matrix product operators

To overcome the exponential scaling barrier in QUAPI, we propose an algorithm representing the ADT propagation as a tensor network that can be efficiently contracted using MPS/MPO techniques. The reader may notice that the exponential scaling problem concerning a rank- $K$  ADT is analogous to the ‘curse of dimensionality’ problem familiar from quantum many body calculations where one deals with an exponentially large rank- $N$  quantum state tensor needed to describe a system with  $N$  particles. One powerful solution introduced in Chapter 2 is a tensor network decomposition of the rank- $N$  tensor into  $N$  low-rank tensors whose dimensions are bounded by the area law. At its heart, this approach exploits the inherent locality of interactions present in various many body Hamiltonians. Here we build on the insight that one can use MPS to represent high-rank tensors efficiently when correlations in the system are constrained to be local. Formally, one can decompose any rank- $K$  ADT into an MPS with  $K$  tensors of rank-3 in the same way as we did in Chapter 2 – i.e. by performing SVD sweep across the ADT while truncating the spectrum of singular values on each bond with some cutoff precision  $\lambda_c$ . The result of such decomposition is displayed graphically in Fig. 5.2(a). Mathematically, the resulting object is given by

$$A^{j_n, j_{n-1}, \dots, j_1} = [a_0]_{\alpha_1}^{j_n} \left( \prod_{k=1}^{n-2} [a_k]_{\alpha_{k+1}}^{\alpha_k, j_{n-k}} \right) [a_{n-1}]^{\alpha_{n-1}, j_1} \quad (5.27)$$

with site tensors  $a_k$  and their local indices  $j_{n-k} = 1..d^2$  representing a time instant  $k$  timesteps before the current timestep  $n$ , while  $\alpha_k$  are the bond indices resulting

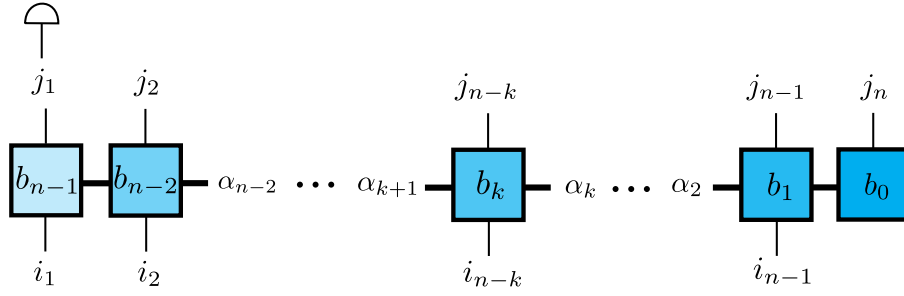


Figure 5.1: Diagrammatic representation of the MPO propagator in Eqs. (5.28)-(5.31). At timestep  $n = K + 1$ , we sum over the local index  $j_1$  earliest in time to impose the finite memory cutoff. The summation is equivalent to a contraction with a  $d^2$ -dimensional vector whose all elements are equal to one (shown as a semicircle) over the leg  $j_1$ . This figure was reproduced with permission from Ref. [296].

from the SVD. Rather than describing a many body state with strong correlations in space, the MPS in Eq. (5.27) encodes the non-Markovian memory effects in time. As we have seen in previous section, bath correlations decay to zero if a bath consists of a continuum of modes. If this decay is approximately exponential, one may expect that the effective non-Markovian ‘interactions’ between different points in time are sufficiently short-ranged. Given the locality of correlations, one could also anticipate that the ADT will only explore a tiny fraction of the Hilbert space available. In such cases, it may be possible to represent the ADT by an MPS of the form Eq. (5.27) with a sufficiently small bond dimension and the memory storage requirements that scale polynomially with the number of sites.

The central idea of this chapter is that the iterative propagation of ADT can be expressed as a tensor network with at most  $N(N + 1)/2$  tensors of at most rank-4, where  $N$  is the total number of timesteps. We exploit the product structure of Eq. (5.18), which allows us to write the ADT propagator at timestep  $n > 1$  as an MPO with  $n$  sites:

$$B_{i_{n-1}, \dots, i_1}^{j_n, j_{n-1}, \dots, j_1} = [b_0]_{\alpha_1}^{j_n} \left( \prod_{k=1}^{n-2} [b_k]_{\alpha_{k+1}, i_{n-k}}^{\alpha_k, j_{n-k}} \right) [b_{n-1}]_{i_1}^{\alpha_{n-1}, j_1} \quad (5.28)$$

where each site tensor  $b_k$  corresponds to an instant  $k$  timesteps ago from the present, and  $j_n, i_{n-1}, \dots, j_1$  and  $i_n, i_{n-1}, \dots, i_1$  are the local physical indices. Each local index runs from 1 to  $d^2$  and represents the local Liouville space of a given instant in time – by analogy to the local physical space of a given lattice site in the many body MPO calculations. Meanwhile,  $\alpha_1, \alpha_2, \dots, \alpha_{n-1}$  are internal bond indices representing the non-Markovian ‘interactions’ between different points in time. Each bond index  $\alpha_{n-k}$  has a size of  $d^2$ . We have defined the bulk sites of the MPO as rank-4 tensors

$$[b_k]_{\alpha', i}^{\alpha, j} = \delta_{\alpha'}^{\alpha} \delta_i^j I_k(\alpha, j), \quad (5.29)$$

and the end sites as the rank-2 tensor

$$[b_0]_{\alpha'}^j = \delta_{\alpha'}^i [b_0]_{\alpha', i}^{\alpha, j} = \delta_{\alpha'}^j I_0(j, j), \quad (5.30)$$

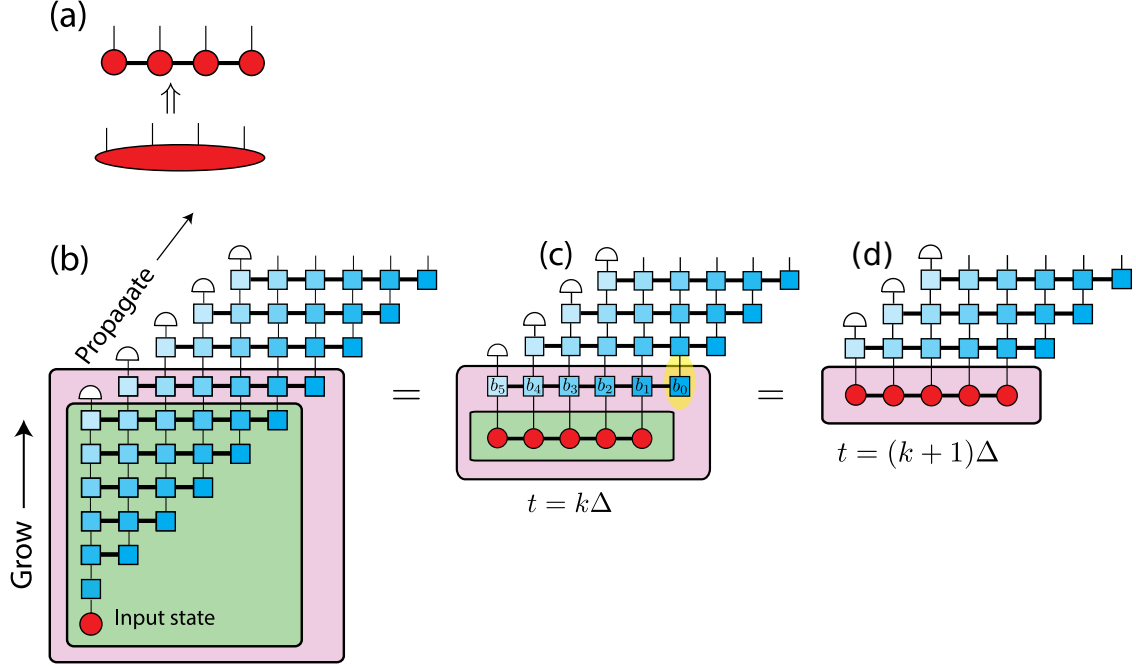


Figure 5.2: Diagrammatic representation of the TEMPO algorithm. (a) The tensor decomposition of ADT into MPS in Eq. (5.27). (b) The complete tensor network representing non-Markovian time evolution that augments the initial density operator (red circle) into an ADT with  $K$  legs shown in (c). Both ‘grow’ and ‘propagate’ phases of the algorithm are shown. (d) To evolve by a single step, we multiply MPS representing the ADT by the next MPO propagator. This figure was reproduced and modified with permission from Ref. [296].

and the rank-3 tensor

$$[b_{n-1}]_i^{\alpha,j} = \sum_{\alpha'} [b_{n-1}]_{\alpha',i}^{\alpha,j} = \delta_i^j I_{n-1}(\alpha, j). \quad (5.31)$$

Meanwhile, the propagator Eq. (5.19) at timestep  $n = 1$  is given by a one-site MPO:

$$B^{j_1, j_0} = I_0(j_1, j_1) [e^{\delta t \mathcal{L}_S}]^{j_1, j_0} \quad \text{for } n = 1 \quad (5.32)$$

One may easily verify that substituting Eqs. (5.29)-(5.31) into Eq. (5.28) recovers the same ADT propagator Eq. (5.18). The diagrammatic representation of the MPO propagator Eq. (5.28) is shown in Fig. 5.1. Although the MPO Eq. (5.28) already has a small bond dimension  $d^2$  of the internal indices, it is still possible to compress it further. We make use of the fact that there is always a degeneracy in the  $d^2$  differences  $x^-$  between the eigenvalues of the system operator  $X$  in Eq. (5.12), i.e.  $d$  of these differences are zero even if the eigenspectrum of  $X$  is nondegenerate. Hence, we can reduce the bond dimension from  $d^2$  to  $d^2 - d + 1$  by retaining only the unique values of  $x^-$ . Further reductions are possible if the spectrum of  $X$  also has degenerate eigenvalues.

With the propagator written as an MPO, the ADT time evolution in Eqs. (5.20)-(5.23) becomes equivalent to the tensor network illustrated diagrammatically in

Fig. 5.2(b-d). We contract this network by successive MPS-MPO multiplications to obtain a time evolved ADT written in an MPS form Eq. (5.27). The contraction algorithm consists of two phases, ‘grow’ and ‘propagate’. In the ‘grow’ phase, we start with an initial vectorized density matrix, which is grown into a two-site MPS after the steps Eq. (5.20), Eq. (5.21), and a three-site MPS after Eq. (5.22) as shown in Fig. 5.2(b). In general, we apply Eq. (5.23) to evolve our MPS in Eq. (5.27) by one timestep, which is accomplished by MPS-MPO multiplication. It can be done efficiently using the zip-up algorithm of Stoudenmire and White [201] that we have already introduced in Chapter 2, and applied in Chapter 3. This algorithm first sweeps across the MPS in one direction while multiplying each MPS site by a corresponding MPO site and truncating MPS bonds on the fly with an SVD. We perform truncations using a fixed precision  $\lambda_c$ , i.e. by discarding singular values whose ratio to the largest singular value is smaller than some fixed cutoff  $\lambda_c$ . Once the first sweep has reached the end and all MPS and MPO sites have been contracted, we do the second sweep in reverse direction, again performing SVDs and truncating MPS bonds at each site, to ensure the optimal MPS form is found. After  $n$  timesteps, the MPS-MPO time evolution yields an ADT expressed as an MPS with  $n$  sites and efficiently truncated bonds, instead of a single rank- $n$  object. The ‘grow’ phase augments the MPS until it reaches  $K$  sites, which amounts to contracting the contents of the green box in Fig. 5.2(b). After  $K$  timesteps, we enter the ‘propagate’ phase and introduce the finite memory cutoff by setting:

$$[b_k]_{\alpha', i}^{\alpha, j} = \delta_{\alpha'}^{\alpha} \delta_i^j \quad k > K, \quad (5.33)$$

The above expression follows directly from  $\eta_k = 0$  and  $I_k(j_n, j_{n-k}) = \delta_{j_{n-k}}^{j_n}$  for  $k > K$ . Plugging Eq. (5.33) into Eq. (5.28) we find the MPO propagator for  $n = K + 1$ :

$$B_{i_K, \dots, i_1}^{j_{K+1}, \dots, j_2} = \sum_{j_1} B_{i_K, \dots, i_1}^{j_{K+1}, \dots, j_2, j_1} \quad (5.34)$$

or more generally for timesteps  $n > K$ :

$$B_{i_{n-1}, \dots, i_{n-K}}^{j_n, \dots, j_{n-K+1}} = \sum_{j_{n-K}} B_{i_{n-1}, \dots, i_{n-K}}^{j_n, \dots, j_{n-K+1}, j_{n-K}} \quad (5.35)$$

i.e. only the indices  $j_n, \dots, j_{n-K+1}$  are relevant, and we can sum over the rest. In practice, we take a more efficient approach: to evolve by one timestep in the ‘propagate’ phase we apply the propagator  $B_{i_{n-1}, \dots, i_{n-K}}^{j_n, \dots, j_{n-K+1}, j_{n-K}}$  from the summand of Eq. (5.35) to the MPS with  $K$  sites in length. The MPS-MPO multiplication augments the MPS by one site corresponding to the latest timestep. The resulting intermediate MPS extends  $K + 1$  timesteps into the past:

$$A_{j_n, j_{n-1}, \dots, j_{n-K+1}, j_{n-K}} = [a_0]_{\alpha_1}^{j_n} \left( \prod_{k=1}^{K-2} [a_k]_{\alpha_{k+1}}^{\alpha_k, j_{n-k}} \right) [a_{K-1}]_{\alpha_K}^{\alpha_{K-1}, j_{n-K+1}} [a_K]^{\alpha_K, j_{n-K}} \quad (5.36)$$

To impose the finite memory cutoff, we sum over the local index  $j_{n-K}$  earliest in time. The summation is illustrated in Figs. 5.1, 5.2 as a contraction with a  $d^2$ -dimensional vector whose all elements are equal to one (shown as a semicircle) over

the leg  $j_{n-K}$ . We subsequently absorb the ‘earliest’ site  $a_K$  into the ‘second earliest’ site  $a_{K-1}$ :

$$\sum_{j_{n-K}} [a_{K-1}]_{\alpha_K}^{\alpha_{K-1}, j_{n-K+1}} [a_K]^{\alpha_K, j_{n-K}} \rightarrow [a_{K-1}]^{\alpha_{K-1}, j_{n-K+1}} \quad (5.37)$$

This contraction removes the ‘earliest’ site and yields a fully updated MPS that now extends  $K$  timesteps into the past:

$$A^{j_n, j_{n-1}, \dots, j_{n-K+1}} = [a_0]_{\alpha_1}^{j_n} \left( \prod_{k=1}^{K-2} [a_k]_{\alpha_{k+1}}^{\alpha_k, j_{n-k}} \right) [a_{K-1}]^{\alpha_{K-1}, j_{n-K+1}} \quad (5.38)$$

Therefore, each step of the ‘propagate’ phase adds and removes one site at the opposite ends of the MPS, to maintain a constant number of sites  $K$  during the rest of the propagation. Finally, we recover the physical density operator from a time evolved MPS by performing the ‘readout’ step. The ‘readout’ simply means summing over all the indices corresponding to the past states  $j_{n-1}, \dots, j_1$  and keeping only the most recent index  $j_n$ , along the same lines as we did in Eq. (5.24):

$$\rho_{j_n}(t_n) = \sum_{j_n, j_{n-1}, \dots, j_{n-K+1}} A^{j_n, j_{n-1}, \dots, j_{n-K+1}} = [a_0]_{\alpha_1}^{j_n} \left( \prod_{k=1}^{K-2} [\tilde{a}_k]_{\alpha_{k+1}}^{\alpha_k} \right) [\tilde{a}_{K-1}]^{\alpha_{K-1}} \quad (5.39)$$

where  $[\tilde{a}_k]_{\alpha_{k+1}}^{\alpha_k} = \sum_{j_{n-k}} [a_k]_{\alpha_{k+1}}^{\alpha_k, j_{n-k}}$  are the MPS tensors with summed local indices. Contracting all the  $\tilde{a}$ -matrices with the  $[a_0]_{\alpha_1}^{j_n}$  tensor recovers the density operator  $\rho_{j_n}(t_n)$  at time  $t_n$ . The steps outlined above form the basis of the time-evolving matrix product operator (TEMPO) algorithm. TEMPO has enabled us to evaluate the path sum Eq. (5.15) reformulated as MPS-MPO time evolution of ADT. We will demonstrate in the coming sections that TEMPO indeed provides an efficient way of dealing with the non-Markovian ‘curse of dimensionality’ that underpinned the exponential scaling with memory cutoff  $K$  in QUAPI.

## 5.4 Benchmarking TEMPO

We first benchmark TEMPO by applying it to problems where known results are available from other methods. Our first test problem is the exactly solvable independent boson model (IBM). It is a special case of the spin-1/2 spin-boson model Eq. (1.100) with coupling between the energy levels of the system set to zero  $\Omega = 0$ :

$$H = \frac{\epsilon}{2} \sigma^z + \frac{\sigma^z}{2} \sum_k \left( g_k a_k + g_k^* a_k^\dagger \right) + \sum_k \omega_k a_k^\dagger a_k \quad (5.40)$$

where  $\sigma^{x,z}$  are the spin-1/2 matrices, and all variables are the same as defined in Eq. (1.100). This model can be used to describe the pure dephasing of a two-level impurity embedded in a vibrational environment [147]. The IBM Hamiltonian is straightforward to diagonalize using the polaron transformation, which allows one to calculate the reduced density matrix of the system  $\rho(t)$ :

$$\rho(t) = \sum_{m,n=\pm 1} |m\rangle \langle n| [\rho(0)]_{mn} e^{-i(E_m - E_n)t} I_{mn}(t) \quad (5.41)$$



where

$$I_{mn}(t) = \begin{cases} e^{-\phi(t)} & m \neq n \\ 1 & m = n \end{cases} \quad (5.42)$$

and  $\phi(t)$  is given by

$$\phi(t) = 4 \sum_k \frac{|g_k|^2}{\omega_k^2} (1 - \cos(\omega_k t)) = 4 \int_0^\infty d\omega \frac{J(\omega)}{\omega^2} (1 - \cos(\omega t)) \quad (5.43)$$

The derivation is presented in more detail in the Appendix A.2. The reader may also find other methods of solution, for instance, in Ref. [147]. Here we take the initial state of the system at  $t = 0$  equal to:

$$\rho(0) = |\Psi_0\rangle \langle \Psi_0| \quad (5.44)$$

with  $|\Psi_0\rangle = \frac{1}{\sqrt{2}} (|\uparrow\rangle + |\downarrow\rangle)$ . From Eq. (5.41), we find the exact dynamics of  $\langle \sigma^x(t) \rangle$ :

$$\langle \sigma^x(t) \rangle = \text{Tr}_B (\sigma^x \rho(t)) = e^{-\phi(t)} \cos(\epsilon t) \quad (5.45)$$

Let us now compare TEMPO against the exact solution Eq. (5.45) for a bath at  $T = 0$  with spectral density

$$J(\omega) = 2\alpha\omega^\nu \omega_c^{1-\nu} e^{-\omega/\omega_c} \quad (5.46)$$

Fig. 5.3 shows a perfect match between TEMPO results and Eq. (5.45) for Subohmic ( $\nu = 1/2$ ), Ohmic ( $\nu = 1$ ) and Superohmic ( $\nu = 2$ ) spectral densities. We have also chosen a system-bath coupling strength  $\alpha = 0.48$ , and the cutoff frequency  $\omega_c = 8\epsilon$ . No finite memory cutoff was applied in these simulations.

We next turn to the spin-boson model (SBM) Eq. (1.100) introduced in Sec. 1.3.1 which, in general, does not have exact analytical solutions. In our second test case, we demonstrate that TEMPO can easily reproduce the results obtained using standard QUAPI. Figure 5.4 reproduces Fig. 2 from the original article by Makri and Makarov [163]. It shows the relaxation dynamics of  $\langle \sigma^z(t) \rangle$  polarization for the unbiased spin-1/2 SBM of a two-level system coupled to an Ohmic bath (characterized by the spectral density in Eq. (5.46) with  $\nu = 1$ ) at  $T = 0.2\Omega$ . While in Ref. [163] the dynamics is already converged for memory cutoff  $K = 7$  and timestep  $\delta t = 0.25/\Omega$ , we are able to perform the simulation with no memory cutoff at all. Here we also illustrate a major difference between TEMPO and QUAPI – the presence of SVD truncation and the new parameter  $\lambda_c$  that sets the SVD precision as we discard all singular values smaller than  $\lambda_c$ . We can control the accuracy of TEMPO by varying  $\lambda_c$  and Fig. 5.4 shows the convergence of TEMPO results with respect to  $\lambda_c$ . One can see that, while the dynamics is visibly different at  $\lambda_c = 10^{-2}, 10^{-3}$ , it quickly converges when the SVD precision is tuned down to lower values  $\lambda_c = 10^{-4}, 10^{-6}$ .

Finally, we compare TEMPO to the Reaction Coordinate Mapping (RCM) technique [157] for SBM in Eq. (1.100) coupled to a bath with Drude-Lorentz spectral density

$$J(\omega) = \frac{\alpha\Gamma\omega_0^2\omega}{(\omega_0^2 - \omega^2)^2 + \Gamma^2\omega^2} \quad (5.47)$$

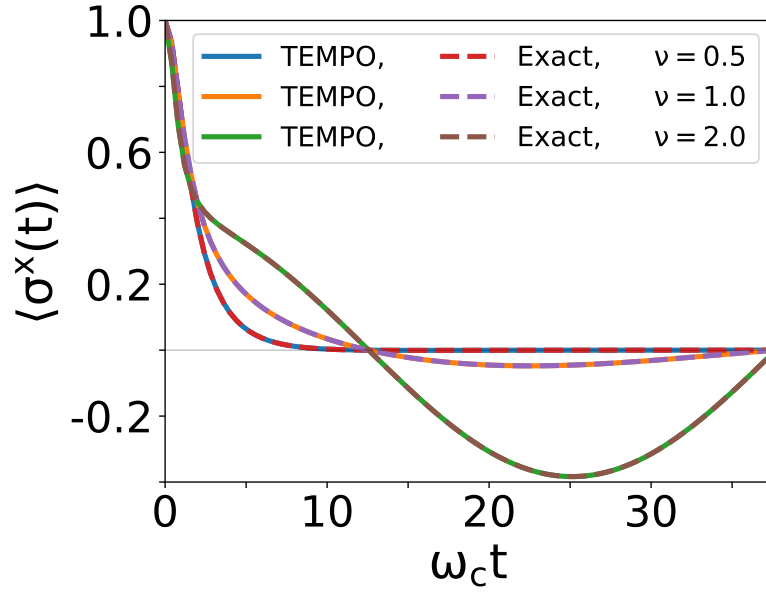


Figure 5.3: The  $\langle \sigma^x(t) \rangle$  dynamics of IBM with  $\epsilon = 1$  coupled to a harmonic bath with Subohmic ( $\nu = 1/2$ ), Ohmic ( $\nu = 1$ ) and Superohmic ( $\nu = 2$ ) spectral densities, Eq. (5.46) with  $\alpha = 0.48$ ,  $\omega_c = 8\epsilon$  and  $T = 0$ . The figure compares TEMPO results (solid lines) to the exact analytical solution Eq. (5.45) (dashed lines). Other parameters are:  $\delta t = 0.4/\omega_c$ ,  $\lambda_c = 10^{-6}$ . No finite memory cutoff was used.

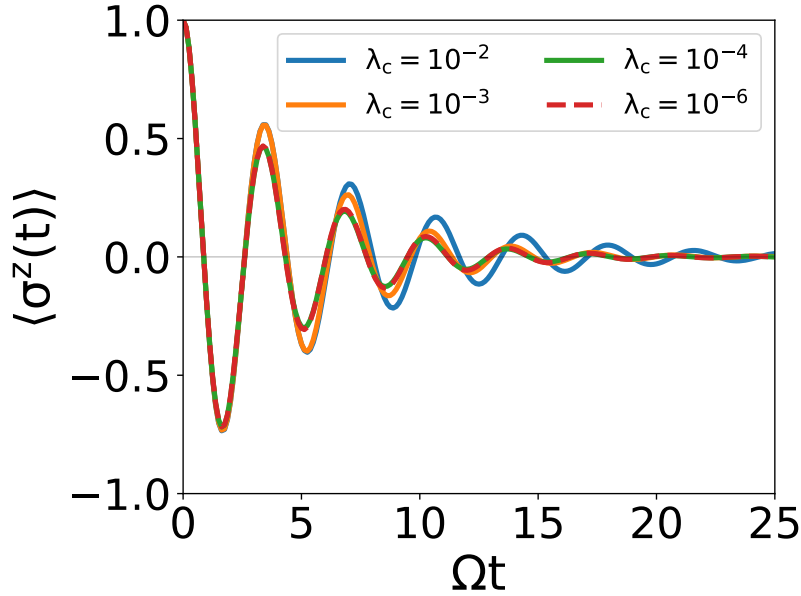


Figure 5.4: TEMPO results for the  $\langle \sigma^z(t) \rangle$  dynamics of spin-1/2 SBM with  $\Omega = 1$ ,  $\epsilon = 0$  coupled to an Ohmic bath ( $\nu = 1$ , Eq. (5.46)) with  $\alpha = 0.1$ ,  $\omega_c = 7.5\Omega$  and  $T = 0.2\Omega$ . This figure reproduces the QUAPI calculation in Fig. 2 of Makri and Makarov's original article [163]. It also demonstrates the convergence of TEMPO with increasing values of SVD precision:  $\lambda_c = 10^{-2}, 10^{-3}, 10^{-4}, 10^{-6}$ . Other parameters are:  $\delta t = 0.12/\Omega$ . No finite memory cutoff was used.

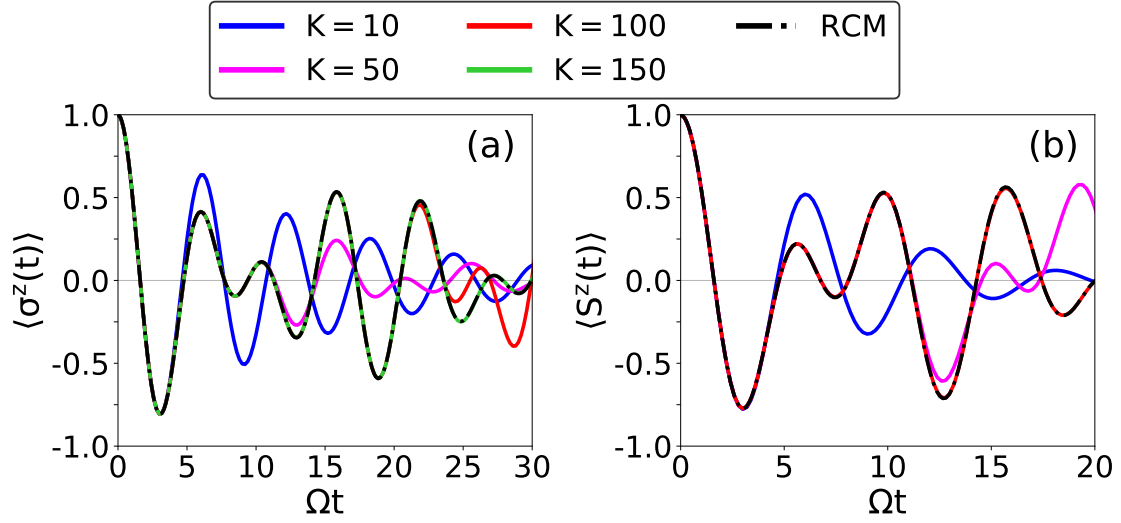


Figure 5.5: TEMPO (solid lines) and RCM (dashed lines) results for (a)  $\langle \sigma^z(t) \rangle$  dynamics of spin-1/2 SBM using finite memory cutoffs  $K = 10, 50, 100, 150$ , with  $\lambda_c = 10^{-8}$ ; (b)  $\langle S^z(t) \rangle$  dynamics of spin-1 SBM using finite memory cutoffs  $K = 10, 50, 100$ , with  $\lambda_c = 10^{-6}$ . In both cases, SBM is coupled to a Drude-Lorentz bath with spectral density Eq. (5.47) and  $\alpha = 0.08$ ,  $\Gamma = 0.05\Omega$ ,  $\omega_0 = \Omega$ ,  $T = 0.5\Omega$ . The SBM Hamiltonian is specified by  $\Omega = 1$  and  $\epsilon = 0$ . Other parameters are:  $\delta t = 0.2/\Omega$ .

which has the coupling strength  $\alpha$ , the resonance frequency  $\omega_0$ , and the bandwidth  $\Gamma$ . RCM includes a single collective mode (the reaction coordinate) of the bath into the system Hamiltonian, thus augmenting the system Hilbert space. Once all the resonant modes of the bath have been transferred to the system, the spectral density of the remaining bath is unstructured and Markovian. The dynamics of the now-augmented system is governed by a Markovian master equation that we can easily solve. One can perform RCM analytically for a bath with Drude-Lorentz spectral density, which consists of a single resonant peak. The RCM derivation of the master equation for SBM with a Drude-Lorentz bath is described in [157] and in the Appendix A.1. Simulating more sophisticated environments requires more reaction coordinates to be included into the augmented system Hilbert space, whose dimension scales exponentially with the number of reaction coordinates, soon making the simulation unfeasible. Nonetheless, RCM is known to perform well for problems with very few resonant modes [157, 297, 298], and is expected to yield highly accurate results for systems coupled to a Drude-Lorentz bath.

Treating narrow band environments is a particularly demanding task for TEMPO, since the presence of a sharp resonant peak leads to long bath correlation times, requiring large MPS bond dimensions and long memory cutoff times to capture the non-Markovian dynamics accurately. We therefore consider a Drude-Lorentz bath with a narrow bandwidth  $\Gamma$ , and use it as a challenging numerical test for TEMPO.

Figure 5.5(a) displays the  $\langle \sigma^z(t) \rangle$  dynamics generated by TEMPO and RCM for the unbiased ( $\epsilon = 0$ ) spin-1/2 SBM with an underdamped spectral density Eq. (5.47). We set the system-bath coupling strength  $\alpha = 0.08$ , bath resonance frequency  $\omega_0 = \Omega$ , bandwidth  $\Gamma = 0.05\Omega$ , and temperature  $T = 0.5\Omega$ . The simulation

required SVD precision  $\lambda_c = 10^{-8}$  and timestep  $\delta t = 0.2/\Omega$  to obtain converged results. Fig. 5.5(a) serves to illustrate the convergence of TEMPO with the memory cutoff  $K$ . With increasing values of  $K$ , TEMPO matches RCM for increasingly longer times until a certain point  $t > \tau_c = K\delta t$  where errors accumulate due to the finite memory approximation. Finally, for  $K = 150$  we find a perfect match between TEMPO and RCM throughout the entire range of dynamics. The long memory cutoff times needed to capture the correct dynamics indicate strongly non-Markovian effects present in the system. We also demonstrate that TEMPO can efficiently tackle problems with larger Hilbert space. To this end, we simulate a spin-1 SBM coupled to a Drude-Lorentz bath, increasing the local dimension from  $d^2 = 4$  to  $d^2 = 9$ . We use the same set of parameters as before, except a lower precision of  $\lambda_c = 10^{-6}$  was sufficient here. Figure 5.5(b) compares  $\langle S^z(t) \rangle$  dynamics calculated with TEMPO and RCM for different memory cutoffs  $K$ . As in the spin-1/2 case, we observe that the range of dynamics over which TEMPO is accurate extends with increasing  $K$ , until a perfect match between TEMPO and RCM is achieved for  $K = 100$ . We remark that the memory cutoffs  $K = 100 - 150$  used in Fig. 5.5 are far beyond the reach of QUAPI which is typically restricted to  $K < 20$ . The results in Fig. 5.5 thus not only confirm the accuracy of TEMPO but also exemplify a toy problem that is relatively easy to simulate with TEMPO, yet completely impossible with standard ADT calculations.

## 5.5 TEMPO results

### 5.5.1 The localization phase transition

Having benchmarked the TEMPO algorithm, we now apply it to study the localization phase transition in the spin-boson model. Here we consider the unbiased SBM given by Eq. (1.100) with  $\epsilon = 0$ , and the bath that is described by spectral density Eq. (1.102). The behaviour of this model is then determined by two dimensionless parameters:  $\Omega/\omega_c$ , which measures the coherent tunnelling rate between the  $S_z$  eigenstates of the spin particle, and  $\alpha$ , the strength of coupling between the spin particle and the harmonic bath. The total SBM Hamiltonian is also invariant under  $S_z \rightarrow -S_z$  and  $b_k \rightarrow -b_k$ . Tracing out the bath degrees of freedom gives a reduced system Liouvillian for the spin particle, which has a symmetry  $S_z \rightarrow -S_z$ . When the spectral density of the harmonic bath is Ohmic (i.e. Eq. (1.102) with  $\nu = 1$ ), SBM is known to exhibit a dissipative quantum phase transition. The transition is in the BKT universality class [299]. The transition is controlled by the system-bath coupling  $\alpha$ , and occurs at the critical value  $\alpha = \alpha_c$ . There are two phases in this model. Below the critical coupling  $\alpha < \alpha_c$ , tunnelling dominates and the system is in the delocalized phase with the  $S_z \rightarrow -S_z$  symmetry. This means that the spin particle is delocalized between its  $S_z$  eigenstates, which leads to the vanishing order parameter  $\langle S_z \rangle_{SS} = 0$  in the steady state. Above the critical coupling  $\alpha > \alpha_c$ , the system-bath coupling dominates and the system enters the localized phase. The spin particle then becomes localized in one of the  $S_z$  eigenstates, giving  $\langle S_z \rangle_{SS} \neq 0$  order parameter in the steady state, and thus breaking the symmetry.

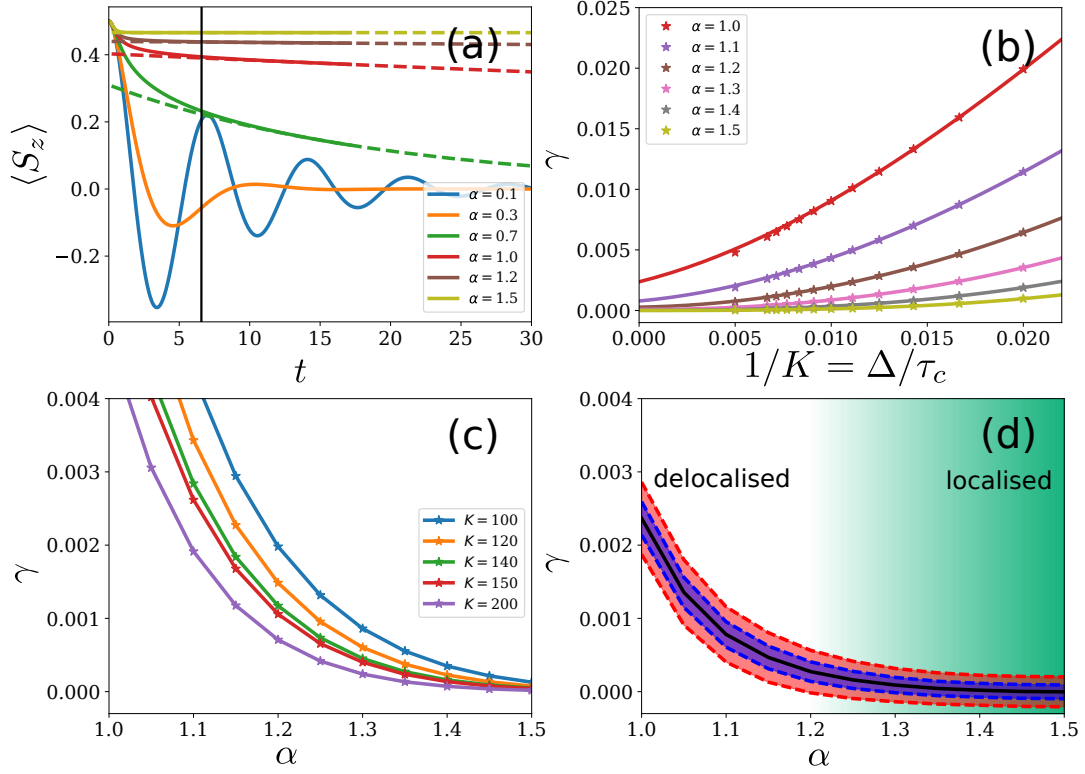


Figure 5.6: (a) The dynamics of spin-1/2 SBM in the vicinity of the localization phase transition for various couplings  $\alpha$ . The vertical black line marks the location of the finite memory cutoff at  $K = 200$ . The dashed lines indicate the exponential fits above  $\alpha = 0.5$ . (b) The decay rate  $\gamma$  extracted from the exponential fit as a function of inverse memory cutoff  $1/K$  for different couplings  $\alpha$ . (c) The decay rate  $\gamma$  as a function of the coupling strength  $\alpha$  for different values of the memory cutoff  $K$ . (d) The extrapolated decay rate  $\gamma$  in the limit  $K \rightarrow \infty$  as a function of the coupling strength  $\alpha$ , with the 68% (blue) and 95% (red) confidence intervals. All figures are for a spin-1/2 SBM with  $\Omega = 1$  and  $\epsilon = 0$  coupled to an Ohmic bath with  $\omega_c = \Omega$  and  $T = 0$ . Other parameters:  $\delta t = 0.03/\Omega$ ,  $\lambda_c = 10^{-12}$ . This figure was reproduced with permission from Ref. [296].

We study the case of a spin-1/2 particle coupled to an Ohmic bath at  $T = 0$ . In this scenario, the critical coupling is known to be  $\alpha_c = 1 + O(\Omega/\omega_c)$  [139, 300, 301]. We will demonstrate that TEMPO is able to capture the dynamics around the localization phase transition, and to locate the critical point. Fig. 5.6(a) displays the  $\langle S_z(t) \rangle$  dynamics at different couplings  $\alpha$ . The simulations were performed using an initial condition  $\langle S_z(0) \rangle = 1/2$ , SVD precision  $\lambda_c = 10^{-12}$  for the truncation of MPS bonds, timestep size of  $\delta t = 0.03/\Omega$ , and a finite memory cutoff of  $K = 200$  timesteps. For weak couplings  $\alpha < 0.5$ , we observe damped coherent oscillations around  $\langle S_z \rangle = 0$  with frequency  $\sim \Omega$ . At  $\alpha \approx 0.5$  these oscillations become overdamped and turn into an incoherent decay, well approximated by  $\langle S_z(t) \rangle \propto e^{-\gamma t}$ . As we increase  $\alpha$ , the decay rate  $\gamma$  of  $\langle S_z(t) \rangle$  decreases, and for  $\alpha > 1$  the spin particle appears close to reaching the steady state with  $\langle S_z \rangle_{SS} \neq 0$ . However,  $\gamma$  always remains finite albeit very slow, meaning that  $\langle S_z(t) \rangle$  eventually always decays to 0 in the limit of very long times  $t \rightarrow \infty$  and the true localization never happens.

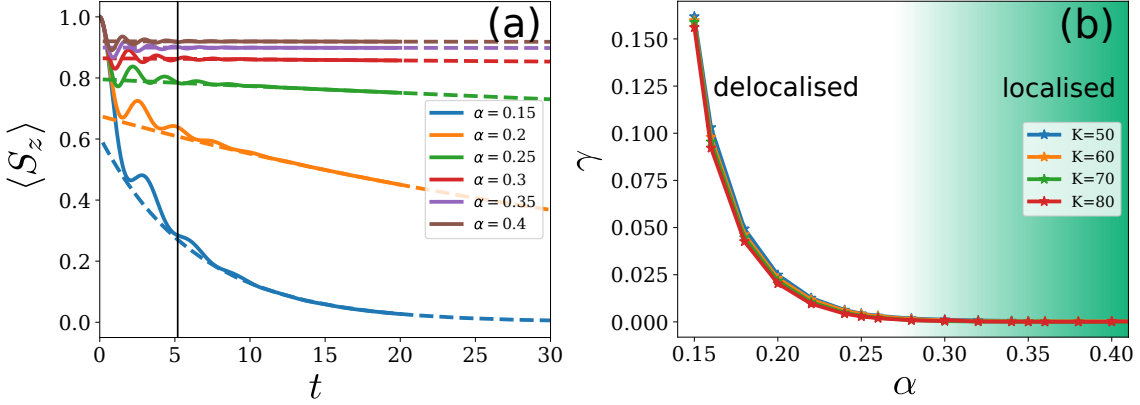


Figure 5.7: (a) The dynamics of spin-1 SBM in the vicinity of the localization phase transition for various couplings  $\alpha$ . The vertical black line marks the location of the finite memory cutoff at  $K = 80$ . The dashed lines indicate the exponential fits. (b) The decay rate  $\gamma$  as a function of the coupling strength  $\alpha$  for different values of the memory cutoff  $K$ . Both figures are for a spin-1 SBM with  $\Omega = 1$  and  $\epsilon = 0$  coupled to an Ohmic bath with  $\omega_c = \Omega$  and  $T = 0$ . Other parameters:  $\delta t = 0.065/\Omega$ ,  $\lambda_c = 10^{-8}$ . This figure was reproduced with permission from Ref. [296]

This contradiction arises due to the finite memory cutoff time  $\tau_c = K\delta t$ , indicated by the vertical black line in Fig. 5.6(a). The finite  $K$  leads to time-local dynamics in the enlarged space of  $K$  timesteps, which produces a gapped spectrum of the reduced system Liouvillian. On the other hand, the Liouvillian gap must vanish in the broken symmetry phase at  $\alpha > \alpha_c$  as we increase the memory cutoff time  $\tau_c \rightarrow \infty$ .

We can thus find the location of the critical point  $\alpha_c$  by extrapolating our results to  $K \rightarrow \infty$ . To this end, we fit an exponential function  $e^{-\gamma t}$  to  $\langle S_z(t) \rangle$  dynamics for various values of  $\alpha$  and  $K$  (dashed lines in Fig. 5.6(a)), which allows us to determine the functional dependence of the decay rate  $\gamma$  on  $1/K$  and  $\alpha$  displayed in Fig. 5.6 (b,c) respectively. We next perform extrapolation to  $K \rightarrow \infty$  by fitting a cubic polynomial to  $\gamma(1/K)$  in Fig. 5.6 (b) and extracting the constant part, which corresponds to the decay rate  $\gamma(1/K = 0)$  in the limit  $K \rightarrow \infty$ . The fitted decay rates  $\gamma$  are shown in Fig. 5.6 (b,c) by the solid lines. Fig. 5.6 (d) displays the extrapolated  $\gamma(1/K = 0)$  as a function of coupling  $\alpha$ : the black line shows the best estimate of  $\gamma(1/K = 0)$  while the red and blue lines mark the 68% and 95% confidence intervals of the fit. The extrapolated  $\gamma(1/K = 0)$  should remain finite for  $\alpha < \alpha_c$ , but vanish above the critical point  $\alpha > \alpha_c$ . The critical coupling  $\alpha_c$  can thus be identified as the smallest value of  $\alpha$  with  $\gamma(1/K = 0) = 0$ . This analysis gives us the value of  $\alpha_c \simeq 1.25$ , in agreement with the known analytical results [139, 300, 301].

To demonstrate the utility of TEMPO, we use it to simulate the localization transition in the SBM for a spin-1 particle. This problem requires a larger Hilbert space, which increases the local dimensions from  $d^2 = 4$  to  $d^2 = 9$ . The larger Hilbert space limits the memory cutoff that we can reach to  $K = 80$ ; fortunately, the results also converge for a larger timestep size  $\delta t = 0.065/\Omega$ , thus allowing us to reach similar memory cutoff times  $\tau_c = K\delta t$  as in the spin-1/2 case. The SVD

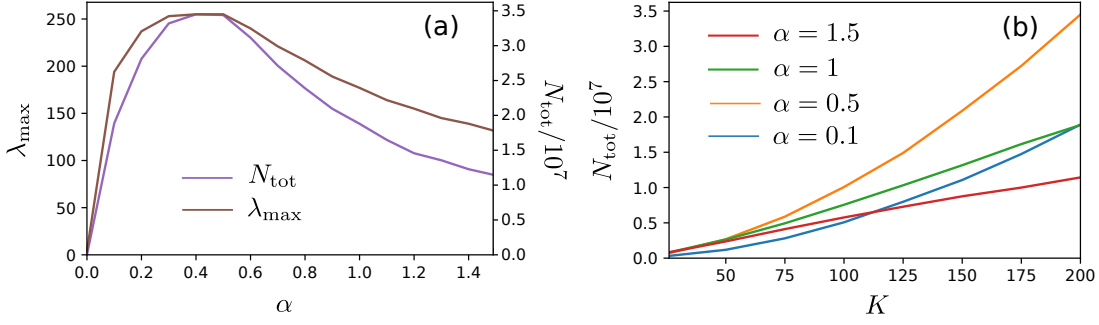


Figure 5.8: (a) The total size  $N_{\text{tot}}$  and the maximum bond dimension  $\lambda_{\text{max}}$  of the final MPS of TEMPO simulations in Fig. 5.6(a), plotted as a function of coupling strength  $\alpha$ . (b) The total size  $N_{\text{tot}}$  of the final MPS in Fig. 5.6(a), plotted as a function of memory cutoff  $K$ , for different values of coupling strength  $\alpha$ . This figure was reproduced with permission from Ref. [296].

precision needed to achieve converged results was  $\lambda_c = 10^{-8}$ , and we take an initial condition  $\langle S_z(0) \rangle = 1$ . Fig. 5.7 (a) shows the  $\langle S_z(t) \rangle$  dynamics for different values of coupling  $\alpha$ , where the vertical black line marks the memory cutoff time  $\tau_c = K\delta t$ . In contrast to the spin-1/2 case, damped oscillations persist for all values of  $\alpha$  at early times before switching to an exponential decay at later times. We fit exponentials to  $\langle S_z(t) \rangle$  as before (dashed lines in Fig. 5.7 (a)), and extract the decay rate  $\gamma$  plotted in Fig. 5.7 (b) as a function of  $\alpha$  for various values of  $K$ . The presence of oscillations introduces more uncertainty in the fits; nonetheless, this time the critical point becomes discernible without extrapolating to the  $K \rightarrow \infty$  limit. As seen in Fig. 5.7 (b), the phase transition occurs at  $\alpha_c \simeq 0.28$  where the decay rate  $\gamma$  vanishes. This result agrees well with the numerical renormalization group calculations [302, 303], but contradicts the variational ansatz results [304].

After discussing the numerical results, we also present a brief analysis of the computational cost and memory requirements of TEMPO algorithm. Our analysis is based on the simulations of the spin-1/2 SBM shown in Fig. 5.6(a). In Fig. 5.8(a) we plot the total size of the final MPS  $N_{\text{tot}}$  and its maximum bond dimension  $\lambda_{\text{max}}$  as a function of coupling strength  $\alpha$ . Notably, both  $N_{\text{tot}}$  and  $\lambda_{\text{max}}$  reach a peak near  $\alpha = 0.5$ , the point of crossover from underdamped to overdamped dynamics. On the other hand, no increase in computational requirements is seen in the vicinity of phase transition at  $\alpha_c \simeq 1.25$ . Fig. 5.8(b) shows  $N_{\text{tot}}$  plotted against  $K$  for various coupling strengths  $\alpha$ . For  $\alpha = 0.1, 0.5$ , the size of memory storage  $N_{\text{tot}} = O(K^2)$  scales quadratically with  $K$ . For  $\alpha = 1.0, 1.5$ ,  $N_{\text{tot}} = O(K)$  scales linearly in  $K$ . These observations imply a low-order polynomial scaling, which is a dramatic improvement compared to the exponential scaling  $N_{\text{tot}} = O(4^K)$  of QUAPI simulations. In particular, the improved scaling allows TEMPO to access the memory cutoffs  $K$  an order of magnitude larger than standard QUAPI can achieve.

### 5.5.2 Environment-mediated energy transfer

The next problem that we investigate with TEMPO is the excitation transfer between two spatially separated systems embedded in a common environment. This type of behaviour is relevant to a wide range of physical situations involving multiple emitters coupled to the same reservoir, for instance the exciton transfer between coupled quantum dots [292] or the long-range entanglement between qubits in waveguide-QED systems [293]. Here we consider a simplified toy model that consists of a pair of two-level systems located at positions  $r_a$  and  $r_b$ , each represented by a spin-1/2 particle:

$$H = \Omega \mathbf{S}_a \cdot \mathbf{S}_b + \sum_{\nu=a,b} \sum_{\mathbf{k}} S_{z,\nu} \left( g_{\mathbf{k},\nu} a_{\mathbf{k}} + g_{\mathbf{k},\nu}^* a_{\mathbf{k}}^\dagger \right) + \sum_{\mathbf{k}} \omega_{\mathbf{k}} a_{\mathbf{k}}^\dagger a_{\mathbf{k}} \quad (5.48)$$

Here,  $S_\nu = (S_{x,\nu}, S_{y,\nu}, S_{z,\nu})$  is the spin vector of the  $\nu$ 'th system. The spins interact with each other via a coherent isotropic Heisenberg coupling  $\Omega$ . They also both couple to the same harmonic bath, as shown in Fig. 5.9(a). The spatial separation effects are encoded in the position-dependent phase of the system-bath couplings  $g_{\mathbf{k},\nu} = g_{\mathbf{k}} e^{-i\mathbf{k} \cdot \mathbf{r}_\nu}$  for a bosonic mode with wavevector  $\mathbf{k}$ . We have assumed a linear dispersion  $\omega_{\mathbf{k}} = c|\mathbf{k}|$ , with the propagation speed of environmental excitations  $c = 1$ . We model the system-bath coupling by  $g_{\mathbf{k}} \sim \sqrt{\omega_{\mathbf{k}}}$  that arises e.g. for a quantum dot coupled to a phonon environment [147]. The spectral density of a  $D$ -dimensional harmonic bath then takes the following phenomenological form:

$$J_0(\omega) = \sum_{\mathbf{k}} |g_{\mathbf{k}}|^2 \delta(\omega - \omega_{\mathbf{k}}) = \frac{\alpha}{2} \frac{\omega^D}{\omega_c^{D-1}} e^{-\omega/\omega_c}, \quad (5.49)$$

with a high frequency cutoff  $\omega_c$  and the system-bath coupling strength  $\alpha$ . Before engaging in further analysis, we will first show that the properties of the model Eq. (5.48) allow us to map it onto SBM Eq. (1.100) for a single spin-1/2 which can be simulated with TEMPO more easily. The Hamiltonian Eq. (5.48) conserves the total  $z$ -component of the two-spin system  $[H, S_{z,a} + S_{z,b}] = 0$ . As a consequence, the system has three decoupled subspaces: one subspace consists of the two states with spins anti-aligned ( $S_{z,a} + S_{z,b} = 0$ ), while the other two subspaces each contain a single state with spins aligned ( $S_{z,a} + S_{z,b} = \pm 1$ ). The latter two subspaces are one-dimensional and thus cannot evolve in time. The two-dimensional  $S_{z,a} + S_{z,b} = 0$  subspace is then the only one with non-trivial dynamics. Therefore, we only need to consider the  $S_{z,a} + S_{z,b} = 0$  single excitation sector. We can thus transform Eq. (5.48) by subtracting any term proportional to  $S_{z,a} + S_{z,b}$  from the system-bath coupling. The transformed Hamiltonian now reads

$$H = \Omega \mathbf{S}_a \cdot \mathbf{S}_b + \frac{1}{2} (S_{z,a} - S_{z,b}) \sum_{\mathbf{k}} (|\tilde{g}_{\mathbf{k}}| a_{\mathbf{k}} + |\tilde{g}_{\mathbf{k}}| a_{\mathbf{k}}^\dagger) + \sum_{\mathbf{k}} \omega_{\mathbf{k}} a_{\mathbf{k}}^\dagger a_{\mathbf{k}}. \quad (5.50)$$

where we have defined the effective coupling

$$|\tilde{g}_{\mathbf{k}}| = |g_{\mathbf{k},a} - g_{\mathbf{k},b}| = 2g_{\mathbf{k}} \sin(\mathbf{k} \cdot \mathbf{R}/2) \quad (5.51)$$

in terms of  $\mathbf{R} = \mathbf{r}_a - \mathbf{r}_b$ . In the  $S_{z,a} + S_{z,b} = 0$  subspace, the  $\frac{1}{2}(S_{z,a} - S_{z,b})$  has the same action on the two anti-aligned spin states as  $S_z$  does on the “up” and



“down” states of a single spin-1/2. Likewise,  $\mathbf{S}_a \cdot \mathbf{S}_b$  has the same action on these anti-aligned states as  $S_x$  acting on a spin-1/2. This means that we can effectively replace  $\mathbf{S}_a \cdot \mathbf{S}_b \rightarrow S_x$  and  $\frac{1}{2}(S_{z,a} - S_{z,b}) \rightarrow S_z$  in Eq. (5.50), which yields a transformed Hamiltonian:

$$H = \Omega S_x + S_z \sum_{\mathbf{k}} (|\tilde{g}_{\mathbf{k}}| a_{\mathbf{k}} + |\tilde{g}_{\mathbf{k}}| a_{\mathbf{k}}^\dagger) + \sum_{\mathbf{k}} \omega_{\mathbf{k}} a_{\mathbf{k}}^\dagger a_{\mathbf{k}} \quad (5.52)$$

equivalent to the spin-1/2 SBM in Eq. (1.100). The modified couplings Eq. (5.51) lead to a renormalization of the effective density of states, as shown by [305, 306]:

$$J(\omega) = \sum_{\mathbf{k}} |\tilde{g}_{\mathbf{k}}|^2 \delta(\omega - \omega_{\mathbf{k}}) = 4 \sum_{\mathbf{k}} |g_{\mathbf{k}}|^2 |\sin(\mathbf{k} \cdot \mathbf{R}/2)|^2 = 2J_0(\omega)(1 - F_D(\omega R)) \quad (5.53)$$

where the actual spectral density  $J_0(\omega)$  is given by Eq. (5.49). The function  $F_D(\omega R)$  is the result of angular averaging of the phase factors  $|\sin(\mathbf{k} \cdot \mathbf{R}/2)|^2$  in  $D$ -dimensional space:

$$F_D(x) = \begin{cases} \cos(x) & D = 1 \\ B_0(x) & D = 2 \\ \text{sinc}(x) & D = 3 \end{cases} \quad (5.54)$$

where  $B_0(x)$  is a Bessel function. The form of  $F_D(\omega R)$  and the resulting dynamics thus strongly depends on the dimensionality  $D$  of the bath. At large separations,  $F_D(\omega R) \rightarrow 0$  as  $R \rightarrow \infty$  for  $D > 1$ . Therefore, higher dimensionality leads to a diminished effect of the environment mediated interaction between spins. This also implies a suppressed intensity of environmental excitations as they propagate from one spin to the other in a space with  $D > 1$ . At small separations  $R \rightarrow 0$ , one has  $F_D(\omega R) \rightarrow 1$  and thus  $J(\omega) \rightarrow 0$  for all  $D$  since the relative phase between the couplings of each spin to the bath  $\mathbf{k} \cdot \mathbf{R}$  vanishes. As a consequence, the system dynamics becomes decoupled from the bath in this limit.

One intriguing feature of our model is that its dynamics has two different timescales. The first timescale  $\tau_f \sim \omega_c^{-1}$  characterizes the dissipative dynamics due to the coupling of the spins to their local surroundings. The other timescale  $\tau_s \sim R/c$  arises due to an environment mediated spin-spin interaction, determined by the separation  $R = |\mathbf{r}_a - \mathbf{r}_b|$  between the spins. One can control the ratio of these timescales by tuning the separation  $R$ . At small separations  $R < \omega_c^{-1}$  the timescales are  $\tau_s \lesssim \tau_f$ . This means that the local dissipative dynamics and the long-range effects of the environment are mostly inseparable, and techniques such as polaron master equations [148] or standard QUAPI [307] provide accurate results in this regime. However, the regime of large separations  $R > \omega_c^{-1}$  where the two timescales  $\tau_f < \tau_s$  become widely separated, is not accessible to any existing methods and remains largely unexplored. This problem is particularly challenging as it requires both a small timestep  $\delta t \ll \omega_c^{-1}$  to simulate the local dissipative dynamics described by the fast timescale  $\tau_f$ , and a large memory cutoff time  $\tau_c = K\Delta > R$  (i.e. a large  $K$ ) to capture the environment-mediated interactions characterized by the slow timescale  $\tau_s$ . Here we show that TEMPO is able to simulate the dynamics of this model without introducing any finite memory approximation. We prepare

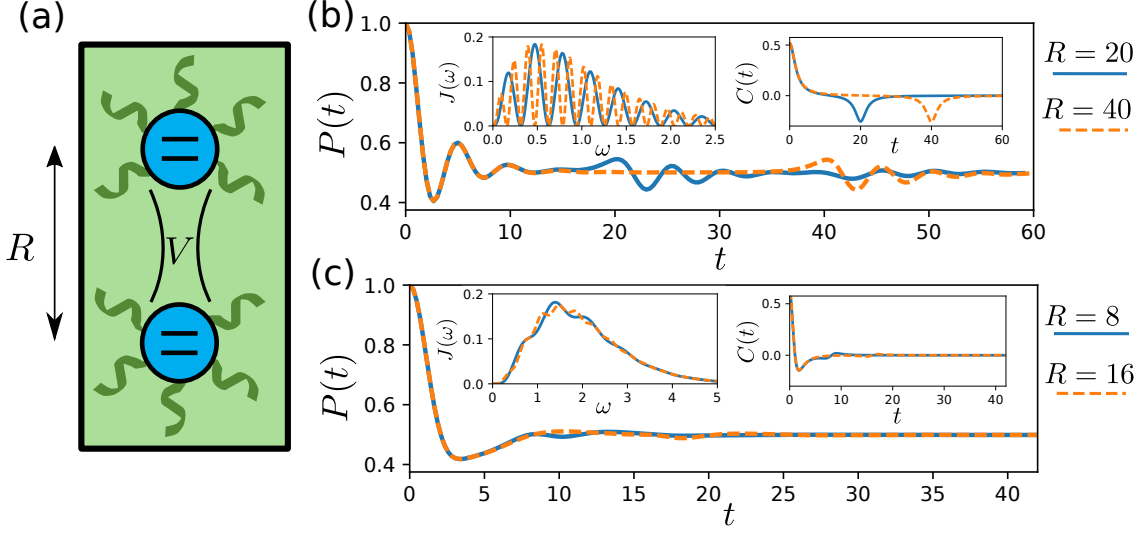


Figure 5.9: (a) Cartoon showing a pair of two-level systems interacting with each other via Heisenberg coupling  $\Omega$  and both coupled to a common environment. (b) The probability of revival  $P(t)$  as a function of time  $t$  for a one-dimensional ( $D = 1$ ) bath and spatial separations  $R = 20c/\Omega$ ,  $40c/\Omega$  between the two-level systems. The system-bath coupling strength is  $\alpha = 2$ . (c) The probability of revival  $P(t)$  as a function of time  $t$  for a three-dimensional  $D = 3$  bath and spatial separations  $R = 8c/\Omega$ ,  $16c/\Omega$  between the two-level systems. The system-bath coupling strength is  $\alpha = 1$ . The insets show the effective spectral density  $J(\omega)$  and the real part of bath correlator  $C(t)$  for each case (b,c). In our model Eq. (5.48) we choose  $\Omega = 1$ . In the spectral density Eq. (5.49) we choose  $\omega_c = 0.5\Omega$ ,  $T = 0.5\Omega$  and we set the propagation speed of excitations to  $c = 1$ . Other parameters: timestep size  $\delta t = 0.35/\Omega$  was used in (b) and  $\delta t = 0.25/\Omega$  in (c), SVD precision was  $\lambda_c = 10^{-5}$  in both panels (b,c). No memory cutoff was applied. This figure was reproduced with permission from Ref. [296].

the spins at  $t = 0$  in one of the anti-aligned states with  $\langle S_{z,a} \rangle = 1/2$ ,  $\langle S_{z,b} \rangle = -1/2$ , and initialize the bath in the thermal equilibrium state at temperature  $T$ . We then compute the probability  $P(t) = \langle S_z(t) \rangle$  of a revival, i.e. the probability of finding the spins in this state again at time  $t$ . To obtain the dynamics of model Eq. (5.48) with spectral density Eq. (5.49), we will instead simulate the mapped Hamiltonian Eq. (5.52) with the effective spectral density Eq. (5.53). Figures 5.9(b,c) display the  $P(t)$  for different  $R$  and for baths with  $D = 1$  and  $D = 3$ . The insets show the effective density of states  $J(\omega)$  and the real part of bath correlator  $C(t)$  for  $D = 1, 3$ .

In Fig. 5.9(b) we plot  $P(t)$  for a bath with  $D = 1$  and spin-spin separations  $R = 20c/\Omega$ ,  $40c/\Omega$ . The initial oscillations decay away over timescale  $\tau_f$ . The revivals then appear at  $t = \tau_s = R/c$  corresponding to the peak  $C(t = R/c)$  in bath correlators, which arises due to the strong spatial modulation seen in  $J(\omega)$ . For  $D = 1$  the propagation of environmental excitations is not suppressed by  $R$ , and so we can see that the amplitude of revivals is the same for both  $R = 20c/\Omega$ ,  $40c/\Omega$ . For  $R = 20c/\Omega$  we also observe small oscillations at  $t \approx 2R/c$  since the interaction of spins at  $t = R/c$  results in more excitations being injected into the bath, subsequently leading to a response at  $t \approx 2R/c$ . In Fig. 5.9(c) we display  $P(t)$  for a bath with

$D = 3$  and spin-spin separations  $R = 8c/\Omega, 16c/\Omega$ . The spatial modulation of  $J(\omega)$  is significantly diminished compared to the  $D = 1$  case. This results in a much smaller peak in correlations  $C(t)$  and hence a less pronounced revival in  $P(t)$  for  $R = 8c/\Omega$ . The revival for  $R = 16c/\Omega$  is even weaker, since the intensity of environmental excitations propagating between the spins is suppressed with increasing  $R$  in three dimensional space.



# Chapter 6

## Toblerone tensor networks

### 6.1 Introduction

The major accomplishment of TEMPO algorithm in Chapter 5 was a general strategy to overcome the non-Markovian ‘curse of dimensionality’ problem due to the exponential scaling with bath memory time. However, there remains an important unsolved issue: the tensor dimensions in TEMPO still grow exponentially with the system size. This inevitably restricts the applicability of TEMPO to systems that contain only a small number of particles, especially when strong particle-particle correlations are present. In essence, non-Markovian ADT calculations face two different ‘curses of dimensionality’ simultaneously: the Hilbert space of an ADT grows exponentially with both the lengthening history of past states and with the number of particles in the system. In this chapter, we propose an extension of TEMPO to many body systems in 1D by employing MPS representation to capture both temporal and spatial correlations. As it will become apparent in the course of this chapter, the resulting three-dimensional tensor network has a Toblerone geometry – hence we dub our technique Toblerone TEMPO.

Many studies of open quantum many-body systems have relied on Born-Markov approximation or similar assumptions. In Chapters 3 and 4 we have investigated coupled cavity arrays weakly interacting with a Markovian bath. An intriguing direction to explore in this context is to study coupled cavity systems subject to a structured environmental noise, in addition to the usual photon loss. For example, such noise can be engineered in superconducting circuits [16], and it naturally appears in cavity QED realisations using quantum dots [124]. An accurate and efficient many-body approach that can also capture non-Markovian dynamics would immensely broaden the scope of nonequilibrium phenomena that we can access. It would enable us to simulate the effects of different noise spectra on the physics of coupled cavity arrays. For example, one could examine the recently proposed dissipative stabilization in circuit QED experiments [36] and investigate what types of spectral density of an engineered reservoir are optimal for stabilizing strongly correlated phases against losses. One could also study cavity QED arrays in the presence of vibrational noise: in particular, the phonon-dressed resonance fluorescence and excitation-induced dephasing of the Mollow triplet, that emerges due to interaction with the phonon bath. These dephasing processes have been studied theoretically

for a single cavity in Ref. [308], and realized experimentally in Ref. [309].

Organic molecules strongly interacting with light is another actively investigated experimental platform [135, 136]. The strong light-matter coupling and the interactions between electronic states and phonons lead to the formation of organic polaritons. The structured phononic environment, arising due the vibrating molecular scaffold, generates non-Markovian polariton relaxation dynamics and significantly modifies the spectroscopic properties of these molecules [46, 137]. Toblerone TEMPO will be able to address polariton relaxation problems in many-molecule systems with a large number of vibrational modes – a very challenging problem for most other methods in existence.

Yet another interesting avenue that we will mention here concerns the relaxation dynamics of photoexcited electronic states in conjugated polymers. The relaxation dynamics in PPV polymer have been measured experimentally using various spectroscopic techniques [310–316]. The computational modelling, however, remains difficult since it needs to handle experimentally relevant polymer chain lengths, the strong exciton-phonon coupling between electronic excitations and vibrations of the internal nuclei of the molecule, as well as the damping of the internal nuclei due to to an external environment of the polymer. The recent studies have often resorted to simplified models, assuming only one vibrational mode on each site of the polymer, an external Lindblad dissipation, and no influence from the torsional modes of the polymer [317, 318].

We expect that Toblerone TEMPO will provide a powerful numerical tool for tackling these and various other problems involving many body systems interacting with non-Markovian environments. This chapter, however, will primarily focus on methodology, leaving the applications for future research.

It is worth mentioning a few examples of other attempts at developing tensor network methods for non-Markovian many body systems. Already mentioned in Chapter 1 is the technique based on time-dependent variational principle with tree tensor network states (TDVP-TTNS) [45, 46]. This approach employs tree tensor network states (TTNS) to represent a wavefunction comprising both a multipartite system and its multiple environments. It then uses the time-dependent variational principle (TDVP) to evolve it in time. TDVP-TTNS has been successfully applied to model the singlet fission in a DP-Mes molecule, and non-Markovian dynamics of polaritons in organic molecules strongly coupled to light. A useful illustration of the capacity of this method is provided by Ref. [46], who were able to simulate up to 16 molecules, with two electronic states and  $O(10^2)$  vibrational modes in each molecule. Another technique proposed shortly after TEMPO relies on a decomposition of QUAPI into a transfer MPO network, with truncations taking place along both spatial and temporal axes [319]. In Ref. [319], this technique was used to study quantum annealing of a transverse field Ising spin chain up to 64 sites, with each spin coupled to a harmonic bath. Despite its likeness to TEMPO, the tensor network decomposition in Ref. [319] was derived specifically for spin-1/2 transverse field Ising Hamiltonian, and is difficult to generalize beyond it. We expect that a TEMPO-based algorithm will be far more versatile, and not restricted to any particular system.

We begin this chapter with a reformulation of TEMPO algorithm in terms of the

process tensor framework in Sec. 6.2. In Sec. 6.3 we present the Toblerone TEMPO algorithm, and in Sec. 6.4 we benchmark Toblerone TEMPO by comparing it to the exact solution of the many-body independent boson model as well as TEMPO results for a small transverse field Ising chain coupled a harmonic bath.

In this chapter, we present work that was performed in collaboration with Gerald Fux. The TEMPO Toblerone algorithm and code were developed by Dainius Kilda and Gerald Fux. All simulations were performed by Dainius Kilda. The text and interpretation presented here is my own original work.

## 6.2 TEMPO in the process tensor framework

Before delving into the full many body problem, we revisit TEMPO and rewrite it in a more convenient and efficient representation, by exploiting the underlying symmetries of the TEMPO network. Our discussion here builds on the ideas of Jørgensen and Pollock [320] who identified an alternative form of TEMPO, motivated by the process tensor framework for describing general non-Markovian quantum processes [321]. We will discuss the connection between TEMPO and the process tensor later in the section. The representation that we introduce here will form the basis of the Toblerone TEMPO algorithm for time evolution of one-dimensional lattice systems in Sec. 6.3.

### 6.2.1 Rearranging the TEMPO network

The main idea is that the tensor network decomposition of the influence functional in Chapter 5 is not unique. Figure 6.1(a) shows the original TEMPO tensor network for  $N = 5$  timesteps, with bath influence tensors  $b_k$  each corresponding to an instant  $k$  timesteps ago from the present. It contains a set of free indices  $\mu_{1,2,3,4,5}$  attached to bath influence tensors at the top of the network, encoding memory effects at different timesteps. The indices  $\mu_{1,2,3,4,5}$  thus represent a time-nonlocal open boundary. As one can infer from Eqs. (5.28)-(5.31) describing MPO propagator of the ADT, some physical and bond indices in this network are connected only via Kronecker deltas. These indices are constrained to be equal along lines of the same colour shown in Fig. 6.1(a), each colour corresponding to a different set of Kronecker deltas. This symmetry implies that one is free to move the Kronecker deltas connecting identically-coloured legs along these lines, without changing the result of contracting the entire network. Therefore, we can shift the free indices  $\mu_{1,2,3,4,5}$  to any tensor connected to a leg of a matching colour. We choose to move  $\mu_{1,2,3,4,5}$  to the time-local bath influence tensors  $b_0$ , such that they form a time-local boundary instead. This leads to a new TEMPO network in Fig. 6.1(b), which is equivalent to the original one in Fig. 6.1(a).

To understand the index-shifting operation more clearly, let us consider an example with a simple contraction  $M_{j,\alpha,\beta} = C_l B_{i,\beta}^l A_{j,\alpha}^i$  of tensors  $C_l$ ,  $B_{i,\beta}^l = \delta_i^l b_{i,\beta}$ , and  $A_{j,\alpha}^i = \delta_j^i a_{j,\alpha}^i$ . The indices in this contraction are constrained to be equal by Kronecker deltas along the symmetry line in green, displayed in Fig. 6.2(a-c). Therefore, the result of contraction  $M_{j,\alpha,\beta}$  is invariant with respect to the shifts of Kronecker deltas connecting the green legs along this line. For example, moving

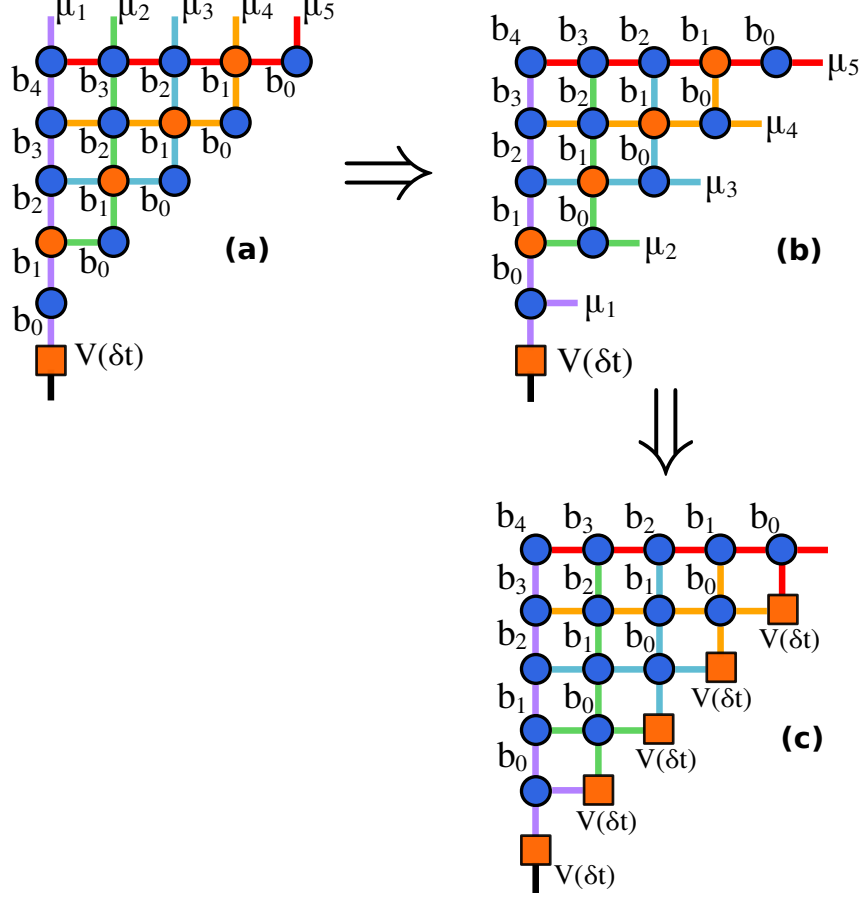


Figure 6.1: TEMPO tensor network for  $N = 5$  timesteps. (a) The original TEMPO where the free indices  $\mu_{1,2,3,4,5}$  represent a time non-local boundary; (b) TEMPO network with  $\mu_{1,2,3,4,5}$  forming a time-local boundary; (c) TEMPO network with redefined influence functions Eq. (6.6). The system propagators  $V(\delta t)$  are separated from bath influence tensors and attached to the time-local boundary. The blue circles are bath influence tensors  $b_k$ , the orange balls are bath influence tensors  $b_1$  with system propagators incorporated, and the orange squares represent the system propagators  $V(\delta t)$ . The indices in each of these TEMPO networks are constrained to be equal along lines of the same colour. Each colour corresponds to a different set of Kronecker deltas.



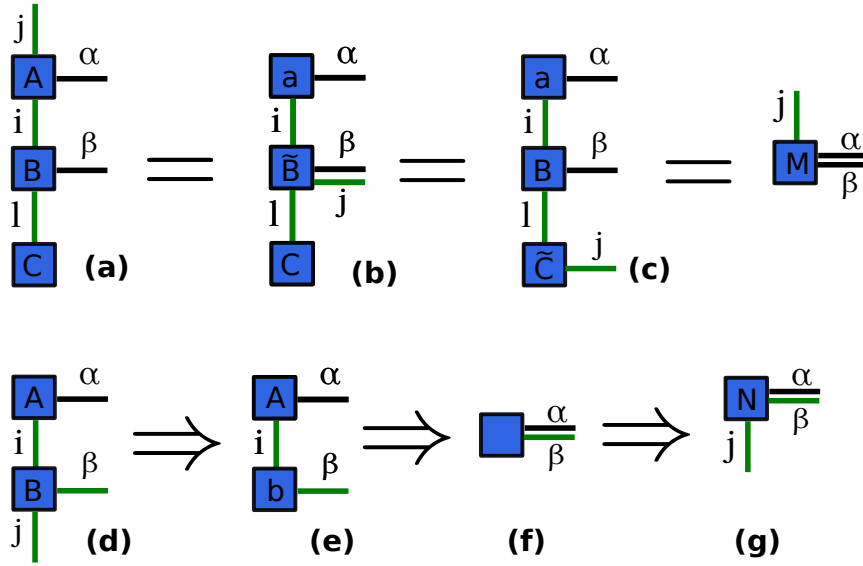


Figure 6.2: (a) Tensor contraction  $M_{j,\alpha,\beta} = C_l B_{i,\beta}^l A_{j,\alpha}^i$  of  $C_l$ ,  $B_{i,\beta}^l = \delta_i^l b_{i,\beta}$ , and  $A_{j,\alpha}^i = \delta_j^i a_\alpha^i$ . The result of contraction  $M_{j,\alpha,\beta}$  remains the same if the index  $j$  is shifted along the green symmetry line (b) from  $A$  to  $B$  or (c) from  $A$  to  $C$ . (d) Tensor contraction  $N_{j,\alpha,\beta} = A_{i,\alpha} B_{j,\beta}^i$  of  $A_{i,\alpha}$  and  $B_{j,\beta}^i = b_\beta \delta_\beta^i \delta_{\beta,j}$ . To contract  $A$  and  $B$ , we can proceed as follows: (e) remove Kronecker delta  $\delta_{\beta,j}$  carrying the index  $j$ , (f) contract  $A$  and  $\tilde{B}_\beta^i = b_\beta \delta_\beta^i$ , and (g) multiply by  $\delta_{\beta,j}$  to restore the index  $j$ .

the index  $j$  from  $A$  to  $B$ :

$$M_{j,\alpha,\beta} = C_l B_{i,\beta}^l A_{j,\alpha}^i = C_l [\delta_i^l b_{i,\beta}] [\delta_j^i a_\alpha^i] = C_l [\delta_i^j \delta_i^l b_{i,\beta}] a_\alpha^i = C_l \tilde{B}_{i,\beta}^{l,j} a_\alpha^i \quad (6.1)$$

or from  $A$  to  $C$ :

$$M_{j,\alpha,\beta} = [\delta_i^j C_l] [\delta_i^l b_{i,\beta}] a_\alpha^i = [\delta_i^j C_l] [\delta_i^l b_{i,\beta}] a_\alpha^i = \tilde{C}_l^j B_{i,\beta}^l a_\alpha^i \quad (6.2)$$

leaves the final result  $M_{j,\alpha,\beta}$  unchanged, as shown in Fig. 6.2(a-c). The exact same principle underpins the shifting of  $\mu_{1,2,3,4,5}$  indices in TEMPO network in Fig. 6.1(a).

The same symmetry can also help us to simplify some tensor contractions. We will illustrate this by considering another example. Fig. 6.2(d-g) shows the contraction of two tensors  $A_{i,\alpha}$  and  $B_{j,\beta}^i = b_\beta \delta_\beta^i \delta_{\beta,j}$ , where the tensor  $B$  has more than one Kronecker delta of the same colour. As seen from the associativity in

$$N_{j,\alpha,\beta} = A_{i,\alpha} B_{j,\beta}^i = A_{i,\alpha} [b_\beta \delta_\beta^i \delta_{\beta,j}] = [A_{i,\alpha} b_\beta \delta_\beta^i] \delta_{\beta,j} \quad (6.3)$$

the contraction result  $N_{j,\alpha,\beta}$  is then invariant whether we contract  $A$  and  $B$  immediately, or contract  $A$  and  $b$  first, and subsequently multiply the result with  $\delta_{\beta,j}$ . Thus instead of performing the contraction of  $A$  and  $B$  directly in Fig. 6.2(d), one may first remove the Kronecker delta carrying the green free index  $j$  (Fig. 6.2(e)), contract  $A$  and  $\tilde{B}_\beta^i = b_\beta \delta_\beta^i$  (Fig. 6.2(f)), and finally multiply the result by  $\delta_{\beta,j}$  (Fig. 6.2(g)). This example can be easily extended to the tensor network in Fig. 6.1: for tensors that carry more than one Kronecker delta of the same colour, the associativity allows us to remove and restore the symmetry-constrained free indices

without affecting the contraction result. We will exploit this property later in the section.

For later convenience, in Fig. 6.1(a) we have also separated the propagator Eq. (5.32) for the first timestep  $n = 1$  into a  $b_0$  tensor given by Eq. (5.30) and a system propagator  $e^{\delta t \mathcal{L}_S}$ :

$$B^{j_1, j_0} = [b_0]_{\alpha}^{j_1} [e^{\delta t \mathcal{L}_S}]^{\alpha, j_0} \quad \text{for } n = 1 \quad (6.4)$$

Crucially, the new representation with a time-local boundary in Fig. 6.1(b) also offers a convenient way to separate the system propagation from bath influence tensors at all other timesteps  $n > 1$ . To this end, we first redefine the influence functions in Eq. (5.16) by taking  $I_1(j, j') \rightarrow I_1(j, j') [V(\delta t)]_{j'}^j$ , where

$$V(\delta t) = e^{\delta t \mathcal{L}_S} \quad (6.5)$$

is the system propagator, with the system Liouvillian  $\mathcal{L}_S$  and timestep  $\delta t$ . Hence, the new definition of influence functions  $I_k(j, j')$  is

$$I_k(j, j') = e^{\phi_k(j, j')} \quad \text{for all } k \quad (6.6)$$

where each  $I_k(j, j')$  is a time-nonlocal entity that connects the time evolution of the amplitude of state  $j$  to the amplitude of state  $j'$ , a number  $k$  of timesteps ago. As before, the influence phase  $\phi_k(j, j')$  is given by Eq. (5.12) with Makri coefficients Eq. (5.13). Let us consider a generic fragment of TEMPO network in Fig. 6.1(b), displayed in Fig. 6.3(a), which can be written as

$$\begin{aligned} & [b_0]_{\beta_1, \mu_{n-1}}^{i_{n-1}} [b_1]_{\alpha_2, i_{n-1}}^{\alpha_1, \mu_{n-1}} [b_0]_{\alpha_1, \mu_n}^{j_n} \\ &= \left[ \delta_{\mu_{n-1}}^{i_{n-1}} \delta_{\beta_1}^{i_{n-1}} I_0(i_{n-1}, i_{n-1}) \right] \left[ \delta_{\alpha_2}^{\alpha_1} \delta_{i_{n-1}}^{j_{n-1}} I_1(\alpha_1, i_{n-1}) [V(\delta t)]_{i_{n-1}}^{\alpha_1} \right] \left[ \delta_{\alpha_1}^{j_n} \delta_{\mu_n}^{j_n} I_0(j_n, j_n) \right] \end{aligned} \quad (6.7)$$

By inserting the following identity resolution into Eq. (6.7), with the new index  $r_n$  running from 1 to  $d^2$ ,

$$[V(\delta t)]_{i_{n-1}}^{\alpha_1} = \delta_{r_n}^{\alpha_1} [V(\delta t)]_{i_{n-1}}^{r_n} \quad (6.8)$$

we obtain a rearranged expression for the same fragment, with the system propagator explicitly moved outside of the bath influence tensors:

$$\begin{aligned} & \left[ \delta_{\mu_{n-1}}^{i_{n-1}} \delta_{\beta_1}^{i_{n-1}} I_0(i_{n-1}, i_{n-1}) \right] \left[ \delta_{\alpha_2}^{\alpha_1} \delta_{i_{n-1}}^{j_{n-1}} I_1(\alpha_1, i_{n-1}) [V(\delta t)]_{r_n}^{\mu_{n-1}} \right] \left[ \delta_{\alpha_1}^{j_n} \delta_{\mu_n}^{j_n} \delta_{\alpha_1}^{r_n} I_0(j_n, j_n) \right] \\ &= [b_0]_{\beta_1, \mu_{n-1}}^{i_{n-1}} [V(\delta t)]_{r_n}^{\mu_{n-1}} [b_1]_{\alpha_2, i_{n-1}}^{\alpha_1, j_{n-1}} [b_0]_{\alpha_1, \mu_n}^{j_n, r_n} \end{aligned} \quad (6.9)$$

Fig. 6.3(b) shows the diagrammatic representation of Eq. (6.9). Repeating the same procedure in Fig. 6.3 for every such fragment in Fig. 6.1(b) transforms the TEMPO network in Fig. 6.1(b) into the one displayed in Fig. 6.1(c). Here, the bath influence tensors and the system propagators  $[V(\delta t)]_{j'}^j$ , are represented by blue circles and orange squares respectively. An important consequence of this rearrangement is the ability to manipulate the system and bath tensors independently, which will

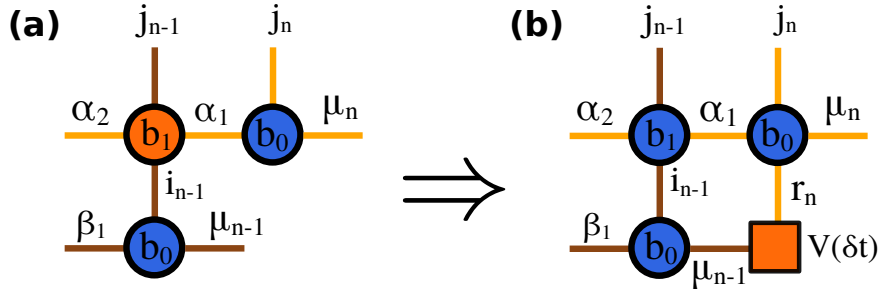


Figure 6.3: Diagrammatic representation of Eqs. (6.7), (6.9), separating the system propagator  $V(\delta t)$  from the bath influence tensor  $b_1$ . (a) Configuration with  $V(\delta t)$  contained in  $b_1$ , given by Eq. (6.7); (b) Configuration with  $V(\delta t)$  moved outside of  $b_1$ , with a new index  $r_n$ , given by Eq. (6.9).

prove highly advantageous later in this section. Overall, the bath influence tensors for each timestep  $n$  in the new TEMPO network Fig. 6.1(c) are given by:

$$\begin{cases} [b_{k,n}]_{\alpha',i}^{\alpha,j} = \delta_{\alpha'}^{\alpha} \delta_i^j I_k(\alpha, j) & 1 < n < N \\ [b_{k,n}]_{\alpha',i}^{\alpha} = \delta_{\alpha'}^{\alpha} I_k(\alpha, i) & n = N \end{cases} \quad (6.10)$$

$$\begin{cases} [b_{0,n}]_r^{\mu,j} = \delta_r^j \delta_r^{\mu} I_0(j, j) & n = 1 \\ [b_{0,n}]_{\alpha',r}^{\mu,j} = \delta_{\alpha'}^j \delta_r^j \delta_r^{\mu} I_0(j, j) & 1 < n < N \\ [b_{0,n}]_{\alpha',r}^{\mu} = \delta_{\alpha'}^{\mu} \delta_r^{\mu} I_0(\mu, \mu) & n = N \end{cases} \quad (6.11)$$

$$\begin{cases} [b_{n-1,n}]_i^{\alpha,j} = \delta_i^j I_{n-1}(\alpha, j) & 1 < n < N \\ [b_{n-1,n}]_i^{\alpha} = I_{n-1}(\alpha, i) & n = N \end{cases} \quad (6.12)$$

with influence functions defined in Eq. (6.6).

For simplicity, we have only displayed the ‘grow’ phase of TEMPO in the diagrams presented so far. Extending the same arguments to include the ‘propagate’ phase is conceptually straightforward: one can always pad the ‘propagate’ phase network in Fig. 5.2(c,d) with identity influence tensors Eq. (5.33) to obtain an equivalent tensor network that has a full triangular shape of the ‘grow’ phase. It is then easy to apply the mathematical operations described in this section to a network that contains both ‘grow’ and ‘propagate’ parts.

### 6.2.2 The process tensor approach

The alternative tensor decomposition of the influence functional in the previous subsection allows us to make a connection between TEMPO and the recently proposed process tensor framework [320, 321]. We briefly describe this framework here. Let us consider time evolution of the total system  $S + B$  governed by Liouvillian  $\mathcal{L} = \mathcal{L}_S + \mathcal{L}_B$ . As before, the Liouvillian  $\mathcal{L}_S$  generates dynamics of the bare system  $S$ , while  $\mathcal{L}_B$  includes the Hamiltonian of the bath  $B$  and the system-bath interaction. We make the same assumptions as we did in Chapter 5, including the

separable initial state  $\rho(0)\rho_B(0)$ , with the density operators  $\rho$  and  $\rho_B$  of the system  $S$  and the bath  $B$  respectively. In addition to the usual ingredients familiar from previous chapters, here we study a more general quantum process that involves a set of controlled interventions  $\{\mathcal{A}_n\}$  acting on the system at discrete times  $\{0, \delta t, 2\delta t, \dots, (N-1)\delta t\}$  during the propagation with timestep  $\delta t$ . A controlled intervention  $\mathcal{A}_n$  is generally a superoperator that, in a real experiment, could correspond to a measurement, a perturbation, a unitary gate, and various other transformations. Often  $\mathcal{A}_n$  represents the action of a system operator at some specified time  $t_n = n\delta t$ . The inclusion of intermediate transformations is particularly useful for computing dynamical quantities, such as multi-time correlation functions and spectra. In the absence of any intervention at timestep  $n$ , one can treat  $\mathcal{A}_n$  as an identity superoperator  $\mathcal{A}_n = I$ . Formally, one can write the discrete dynamics of the reduced system density matrix  $\rho_S(t)$  until the final time  $t = N\delta t$  after  $N$  timesteps as follows:

$$\rho(t) = \text{Tr}_B \left( e^{\mathcal{L}\delta t} \mathcal{A}_{N-1} e^{\mathcal{L}\delta t} \mathcal{A}_{N-2} \dots e^{\mathcal{L}\delta t} \mathcal{A}_1 e^{\mathcal{L}\delta t} \mathcal{A}_0 \rho(0) \rho_B(0) \right) \quad (6.13)$$

In practice, we typically separate the system and bath propagation using Trotter decomposition with a small timestep  $\delta t$ . As before, for ease of exposition we present our arguments using the first order Trotter splitting, but the ideas described here are easily extendable to higher order decompositions:

$$e^{\mathcal{L}\delta t} = W(\delta t)V(\delta t) + O(\delta t^2) \quad (6.14)$$

with  $V(\delta t) = e^{\mathcal{L}_S\delta t}$  and  $W(\delta t) = e^{\mathcal{L}_B\delta t}$ .

Figure 6.4 summarizes the basic idea of the process tensor approach: it shows how a quantum process with interventions in Eq. (6.13) can be expressed as an MPS-like tensor decomposition, where system, bath and controlled intervention superoperators are represented by tensors. The reader may notice that TEMPO with time-local boundary described in the last subsection already has the causal structure of the process tensor. The process tensor in Fig. 6.4 separates controlled interventions (black), free system dynamics (orange), and influence of the uncontrolled environment (blue), implying that the system and environment propagators can be computed independently. Such structure contrasts with the original TEMPO algorithm presented in Chapter 5 where system propagators were incorporated in bath influence tensors  $b_1$ . It will prove to be of critical importance to the many body extension of TEMPO later in this chapter.

Here we formulate TEMPO algorithm in a more general representation based explicitly on the process tensor. In the presence of interventions  $\{\mathcal{A}_n\}$  at intermediate times, TEMPO network in Fig. 6.1(c) remains largely the same – except the system propagators  $V(\delta t)$  are straightforwardly replaced by:

$$V(\delta t) \rightarrow \mathcal{A}_n V(\delta t) \quad (6.15)$$

at each timestep  $n$ . The resulting tensor network is displayed graphically in Fig. 6.5, where bath influence tensors, system propagators, and controlled interventions are depicted by blue circles, orange squares, and black squares respectively.

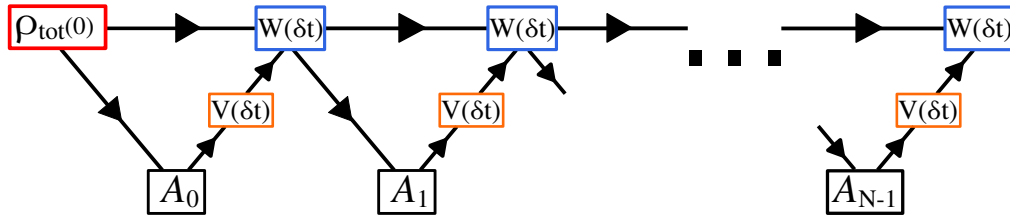


Figure 6.4: The basic idea of the process tensor formulation. A general quantum process is expressed as an MPS-like decomposition into tensors representing the free system dynamics with propagator  $V(\delta t) = e^{\mathcal{L}_S \delta t}$  (orange), the influence of an uncontrolled environment with propagator  $W(\delta t) = e^{\mathcal{L}_B \delta t}$  (blue), and controlled interventions  $\{\mathcal{A}_n\}$  (black). The process starts from the initial total system  $S + B$  density operator  $\rho_{\text{tot}}(0)$  and propagates forward in time along the arrows.

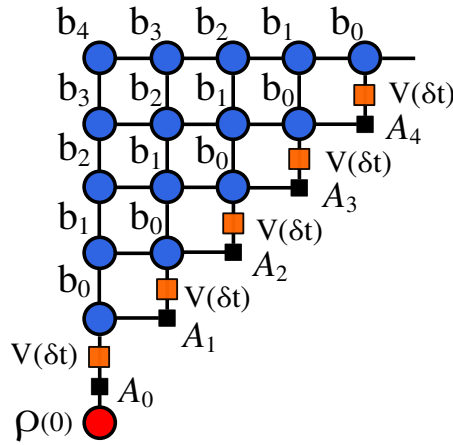


Figure 6.5: TEMPO in the process tensor framework, for  $N = 5$  timesteps. The blue circles are bath influence tensors  $b_k$ , the orange squares are system propagators  $V(\delta t)$ , and the black squares are controlled interventions  $\{\mathcal{A}_n\}$ .

To find the time-evolved density matrix  $\rho(t)$  of the system, we will first contract the bath influence tensors in Fig. 6.6(a), independently from the system tensors and interventions. Before contraction, we cast the network in a more convenient MPS-MPO form by exploiting the property described in Fig. 6.2(d-g), and temporarily removing the Kronecker delta indices marked in red. We then proceed by defining a boundary MPS marked by the red box in Fig. 6.6(b), and contracting it with an MPO defined as a column of influence tensors (green box in Fig. 6.6(b)). As Figs. 6.6(b-d) show, we continue to contract the TEMPO network in an iterative column-by-column fashion, multiplying the boundary MPS with the next column MPO in every iteration. To multiply MPS with an MPO, we employ the same protocol as we did in the original TEMPO in Chapter 5 based on the zip-up algorithm by Stoudenmire and White [201] and use SVDs to truncate the bonds to a required precision  $\lambda_c$ . This order of contractions means that the causal influence of each free leg of the time-local boundary is sequentially incorporated into the boundary MPS. The final result is the bath influence MPS displayed in Fig. 6.6(d). After contraction, we restore the red Kronecker delta legs in Fig. 6.6(e). We note in passing

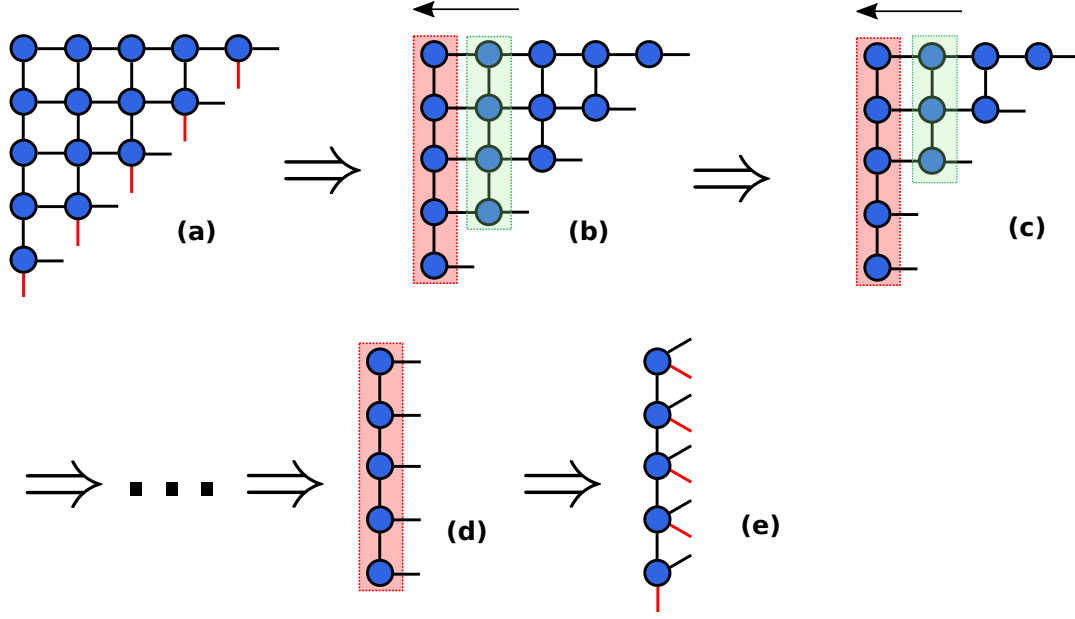


Figure 6.6: Diagrammatic contraction of bath influence tensors in Fig. 6.5, using the following steps: (a) Remove Kronecker deltas carrying the legs in red to obtain a convenient MPS/MPO representation. Contract the boundary MPS (red) with: (b) the first MPO (green); (c) the second MPO (green). Continue the iterative MPS-MPO multiplication until (d) the entire TEMPO network has been contracted into the boundary MPS. (e) Restore Kronecker deltas carrying the legs in red. The resulting object is the bath influence MPS.

that it is possible to utilize the Kronecker delta symmetries further by incorporating them in tensor contractions and singular value decompositions, to optimize the MPS-MPO multiplication in Fig. 6.6(b). This topic, however, is beyond the scope of our discussion here.

In effect, we have reduced the full TEMPO network in Fig. 6.5 to the one Fig. 6.7(a), which mimics the process tensor structure in Fig. 6.4. Contracting Fig. 6.7(a) is straightforward, and for a TEMPO network containing  $N$  timesteps it yields the reduced density matrix  $\rho(t)$  propagated until the final time  $t = N\delta t$ . The accuracy of the bath influence MPS representation determines the accuracy of  $\rho(t)$ , and is set by the  $\lambda_c$  convergence parameter. Conveniently, we may also extract  $\rho(t)$  at earlier times  $t_n$  for any timestep  $n < N$  by exploiting the fact that

$$\begin{aligned} \rho(t) &= \text{Tr}_B ([W(\delta t)V(\delta t)\mathcal{A}_{n-1}]^n \rho(0)\rho_B(0)) \\ &= \text{Tr}_B \left( [W(\delta t)]^{N-n} [W(\delta t)V(\delta t)\mathcal{A}_{n-1}]^n \rho(0)\rho_B(0) \right) \end{aligned} \quad (6.16)$$

The second equality corresponds to the tensor network in Fig. 6.7(b): to extract  $\rho(t)$  at timestep  $n < N$ , we apply the system propagators and interventions for the first  $n$  steps only, and simply trace over the remaining  $N - n$  bath influence tensors. This leaves us with a single free leg at  $n$ 'th timestep and a ‘cap’ of traced bath tensors extending above it, indicated by the purple box in Fig. 6.7(b) and a

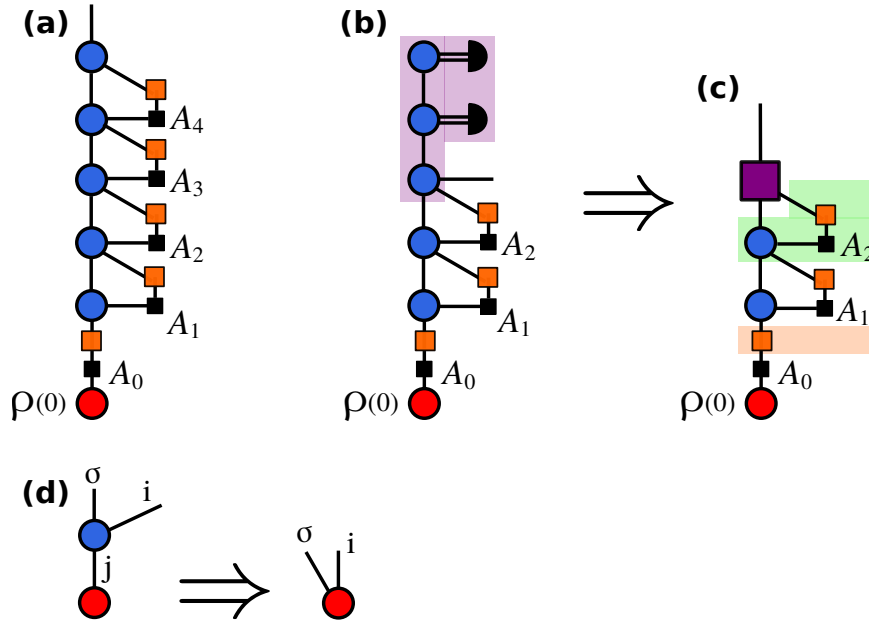


Figure 6.7: (a) Process tensor TEMPO network for  $N = 5$  timesteps from Fig. 6.5 after contracting its bath influence tensors into the bath influence MPS in Fig. 6.6. (b,c) To extract  $\rho(t)$  at earlier timesteps  $n < N$ , we trace out the bath influence tensors above the timestep  $n$  and contract them into a cap (the purple box and the purple square). The green box indicates a single timestep  $n$  of TEMPO propagation that consists of a bath influence MPS tensor, the system propagator  $V(\delta t)$ , and the control tensor  $\mathcal{A}_n$  applied during that timestep. The orange box indicates the first system propagator  $V(\delta t)$ , applied at the start of propagation. (d) The augmented density matrix object with two indices:  $i$  is the Liouville space index, and  $\sigma$  is the ancilla due to the system-bath interaction.

purple square in Fig. 6.7(c). Contracting the tensor network in Fig. 6.7(c) thus yields a time-evolved reduced density matrix  $\rho(t)$  at time  $t_n$ . The ability to extract the system state at intermediate timesteps is particularly useful as it avoids the need to contract the full network in Fig. 6.5 from scratch for every single value of  $n$ . Instead, we can treat the problem as a sequential propagation in time from timestep  $n = 1$  to  $n = N$ , where a single-step propagator is indicated by the green box in Fig. 6.7.

As seen in Fig. 6.7, each propagation step  $n < N$  results in an object with two legs in Fig. 6.7(d). We call this object an ‘augmented density matrix’  $P(t)$  to distinguish it from the density matrix  $\rho(t)$  of the system. The leg  $i$  is a physical index corresponding to the Liouville space of the reduced system, and has a dimension of  $d^2$ . The other leg  $\sigma$  is an ancilla arising due to the system-bath interaction. It corresponds to the bond index connecting timesteps  $n$  and  $n + 1$  of bath influence MPS, with the bond dimension of  $D_B$ . To recover the actual time-evolved density matrix  $\rho(t)$  after the  $n$ ’th step, all that one needs to do is apply an appropriate ‘cap’ to the augmented density matrix  $P(t)$ , which removes the ancillary bath influence index.

Before concluding this section, we test the process tensor TEMPO algorithm described in this chapter against the standard TEMPO introduced in Chapter 5.

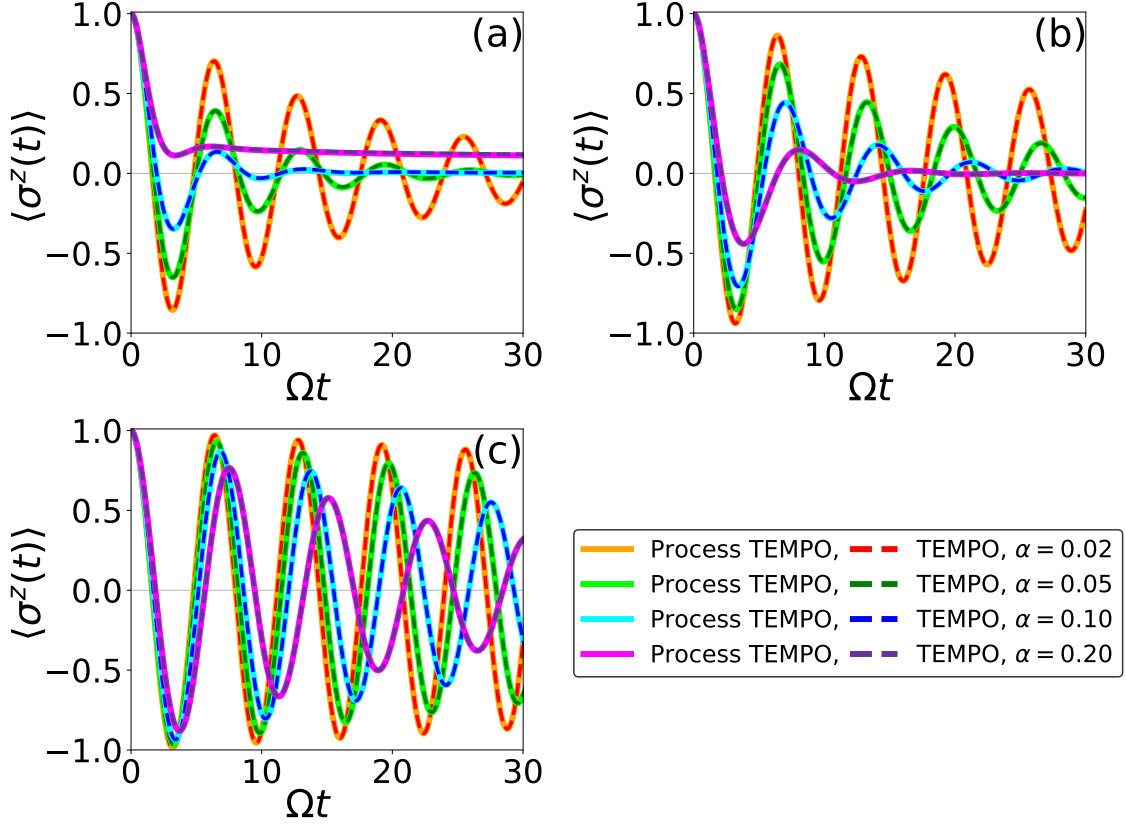


Figure 6.8: The  $\langle \sigma^z(t) \rangle$  dynamics of the spin-1/2 SBM with (a) Subohmic ( $\nu = 1/2$ ), (b) Ohmic ( $\nu = 1$ ), (c) Superohmic ( $\nu = 2$ ) spectral densities. Each panel shows results for  $\alpha = 0.02, 0.05, 0.10, 0.20$ . The figure compares process tensor TEMPO (solid lines, labelled as Process TEMPO in the legend) and standard TEMPO (dashed lines) results. We used timestep size  $\delta t = 0.1/\Omega$ , and SVD precision  $\lambda_c = 10^{-8}$ . Other parameters are:  $\omega_c = 5\Omega$ ,  $T = 0$ ,  $\Omega = 1$ , and  $\epsilon = 0$ . No finite memory cutoff was used.

To this end, we use both approaches to simulate the unbiased spin-1/2 spin boson model (SBM) given by Eq. (1.100) with  $\epsilon = 0$ . We consider a bath at  $T = 0$  described by the spectral density in Eq. (1.102). In Fig. 6.8(a,b,c) we plot the  $\langle \sigma^z(t) \rangle$  dynamics for Subohmic ( $\nu = 1/2$ ), Ohmic ( $\nu = 1$ ) and Superohmic ( $\nu = 2$ ) spectral densities respectively, as well as for different system-bath coupling strengths  $\alpha = 0.02, 0.05, 0.10, 0.20$ . In all simulations, we have taken 300 timesteps without using the finite memory cutoff  $K$ , effectively meaning  $K = 300$ . In Fig. 6.8 we observe a perfect match between the two approaches, confirming that process tensor TEMPO indeed reproduces the same results as standard TEMPO.

### 6.3 Toblerone TEMPO algorithm

After introducing the process tensor formulation of TEMPO, we are now in the position to extend the TEMPO algorithm to many body lattice systems. In the last section, we have dealt with system propagators that were simple matrices  $[V(\delta t)]_{j'}^j$ , with two, incoming and outgoing physical indices. Let us consider a different sce-



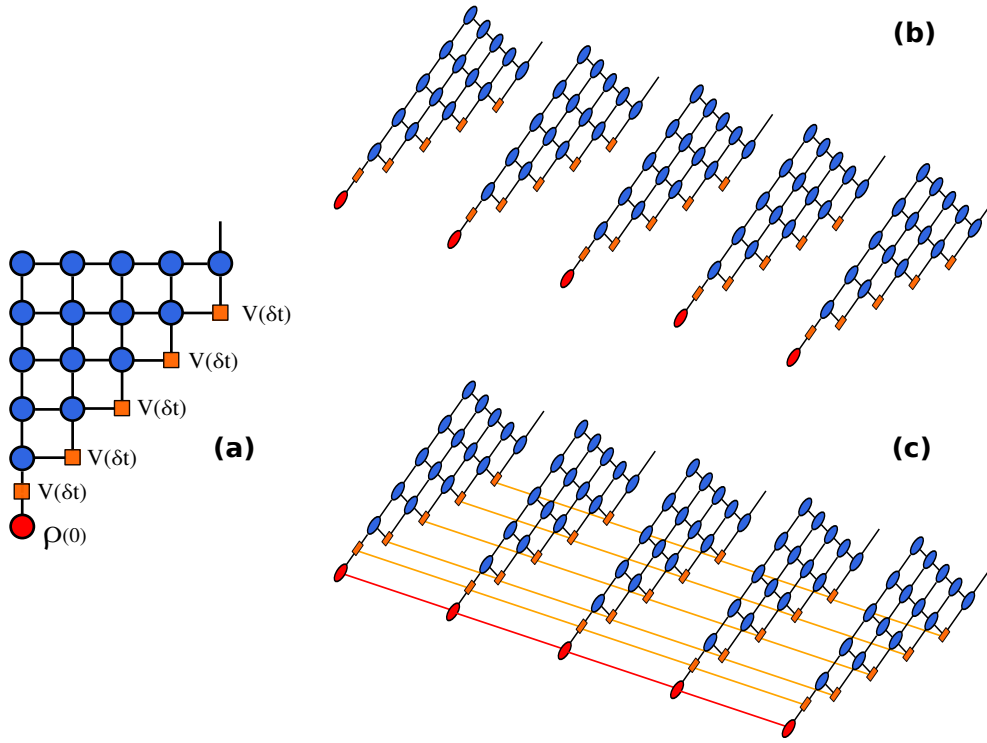


Figure 6.9: (a) The process tensor TEMPO network from Fig. 6.5 (with interventions set to  $\mathcal{A}_n = I$  for all  $n$ ). (b) A chain of  $M = 5$  non-interacting systems coupled to their respective environments. Time evolution of each individual site is represented by a TEMPO network of triangular geometry. (c) When individual sites interact and form a many-body system, the individual TEMPO triangles become connected on their diagonals and form a Toblerone tensor network. The blue, orange, and red colours correspond to bath influence tensors, system propagators, and the reduced system density matrix respectively. The red connected circles form an MPS representing the vectorized density matrix of the reduced system.

nario concerning an  $M$ -site chain of subsystems that do not interact with each other, all of them coupled to their respective environments. Throughout this chapter, we will consider the environments of different sites to be independent. We can represent the time evolution of each site by a TEMPO network with the usual triangular geometry, as shown in Fig. 6.9(b). For simplicity, here we will set controlled interventions to identity  $\mathcal{A}_n = I$  for all  $n$ .

If we switch on an interaction between the subsystems located at different sites of the chain, these individual sites become coupled with each other and form a one-dimensional many body lattice system. It is clear that a brute-force calculation of the whole system dynamics will scale exponentially with the number of sites  $M$ . To treat the many body correlations efficiently, we will adapt the MPS/MPO techniques introduced in Chapter 2. We represent the collective vectorized density operator spanning the entire lattice by an MPS along the spatial axis (red circles in Fig. 6.9(c)), whose bond indices correspond to the entanglement between different sites. The physical indices describe the local Liouville space of a each site, and run

from 1 to  $d^2$ , for a Hilbert space dimension  $d$  of each individual site. Likewise, the time evolution of different sites can no longer be described independently from each other. The system propagators  $[V(\delta t)]_j^i$  are thus replaced by an MPO propagator that consists of rank-4 tensors acting on each site of the lattice. The local legs of a rank-4 tensor correspond to the incoming and outgoing Liouville space indices (running from 1 to  $d^2$ ), whereas the bond indices arise due to the intersite coupling terms in the system Hamiltonian. Overall, the presence of intersite couplings means that the individual triangular TEMPO networks in Fig. 6.9(b) now become connected on their diagonals into a lattice. This connectivity gives rise to a 3D Toblerone-shaped tensor network, illustrated diagrammatically in Fig. 6.9(c).

Finding a time-evolved density matrix MPS of a 1D lattice thus amounts to the arduous task of contracting the entire Toblerone network in Fig. 6.9(c). At first sight, such a 3D contraction may appear extremely challenging and computationally expensive. Fortunately, in the process tensor formulation of TEMPO we may first contract the bath influence tensors on each site independently from the system MPOs. Therefore, we perform the contraction shown in Fig. 6.6 for TEMPO triangles on every lattice site. This procedure flattens all the triangles of the Toblerone network into a new structure displayed in Fig. 6.10(a), which is a standard MPS-MPO tensor network with local bath influence tensors sandwiched between the consecutive MPOs. Since the influence tensors are independent on different sites, the computational cost of this step is exactly the same as that of the process tensor TEMPO in Sec. 6.2 for a single-site system. The independence of the influence tensors also allows us calculate the ‘caps’ for each site individually, using the strategy explained in Sec. 6.2.2 and Fig. 6.7. Given a Toblerone TEMPO network containing  $N$  timesteps, we can therefore extract the evolved MPS for any intermediate timestep  $n < N$  simply by applying a ‘cap’ of traced bath tensors at each site, as shown in Fig. 6.10(b,c). Contracting the tensor network in Fig. 6.10(c) thus yields the lattice MPS at any intermediate time  $t_n$ . Similarly to Sec. 6.2.2, by using ‘caps’ one avoids a need to contract the huge Toblerone network in Fig. 6.9(c) from scratch for every single  $n$ . Instead, we can treat the problem as a sequential propagation in time from timestep  $n = 1$  to  $n = N$ , where the propagator evolving the lattice by a single step is indicated by the green box in Fig. 6.10. We note that the above approach would have been impossible using the original TEMPO representation of Chapter 5 where the system tensors were incorporated in the bath tensors  $b_1$ , and so the influence tensors on different sites were not independent. In the case of a 1D lattice, it would have inevitably required dealing with cumbersome  $b_1$  tensors of rank-6 due to the two additional MPO bond indices, leading to a much higher computational cost and a far more complicated contraction algorithm. Moreover, we would have to compute the full contraction of the Toblerone network in Fig. 6.9(c) for every single timestep  $n$ , due to the inability to use the ‘cap’ strategy.

A great conceptual advantage of the above method is that it maps the seemingly esoteric problem of contracting the 3D Toblerone tensor network in Fig. 6.9(c) onto a variant of MPS-MPO time evolution, whose general algorithmic principles are familiar from the many body simulations [38]. In our work, we will be primarily interested in systems with the nearest-neighbour spatial interactions. In such a setting, one can replace MPO propagators in Fig. 6.10 by a set of two-body gates,

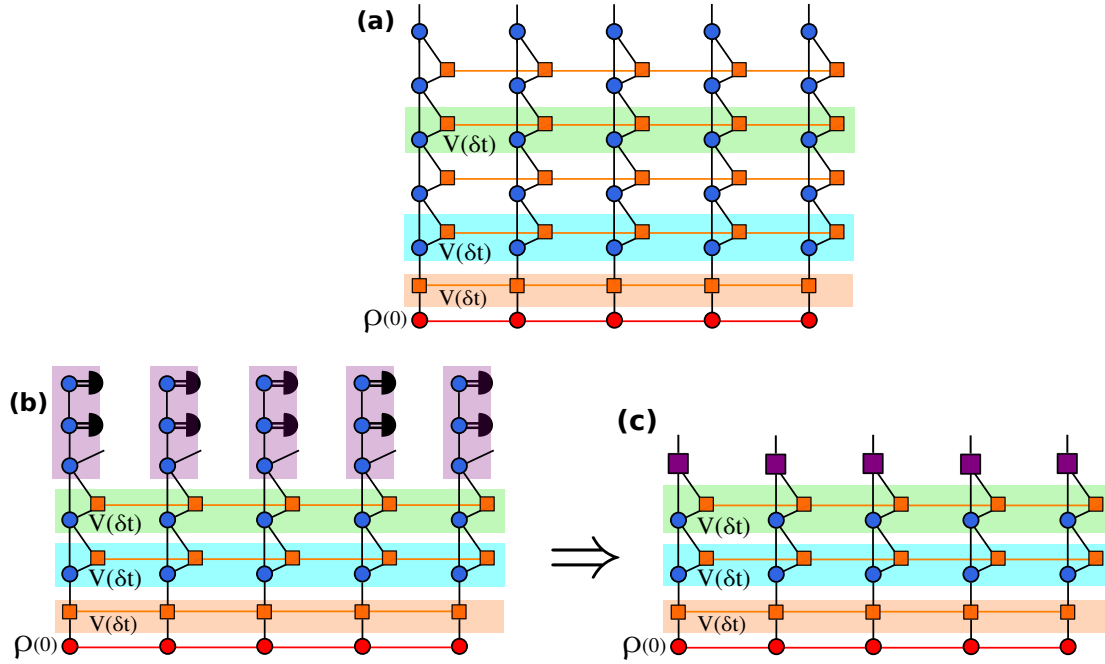


Figure 6.10: (a) The flattened Toblerone tensor network from Fig. 6.9(c) after contracting each TEMPO triangle into a bath influence MPS as shown in Fig. 6.6. The tensor network displayed is for  $N = 5$  timesteps and  $M = 5$  lattice sites. The orange box contains the first system MPO propagator  $V(\delta t)$ , applied to the initial MPS at the start of propagation. The cyan box indicates the first full timestep  $n = 1$  that consists of bath influence MPS tensors acting on each site locally, and the system MPO propagator  $V(\delta t)$  acting on all lattice sites. The first set of bath influence tensors acts on an MPS without ancilla space, and transforms it into an augmented MPS, as shown in Fig. 6.11(b,c). The green box indicates a single general timestep  $n > 1$  of TEMPO propagation, which is exactly the same as the first full timestep in the cyan box, except the bath influence tensors now act on the augmented MPS with ancilla indices. (b,c) To extract  $\rho(t)$  at earlier timesteps  $n < N$ , we trace out bath influence tensors above the timestep  $n$  and contract them into a cap (the purple box and the purple square).

as shown in Fig. 6.11(a). This simplifies the Toblerone TEMPO propagation to a modified version of the two-body-gate TEBD algorithm introduced in Sec. 2.2.3. In fact, it also makes Toblerone TEMPO algorithm easily extendable to infinite lattices, as one can simply use an infinite MPS representation and apply iTEBD algorithm of Sec. 2.2.3.

Let us now discuss the steps of time evolution in more detail. We start with some initial vectorized density matrix of an  $M$ -site lattice represented as an MPS in Vidal form (i.e. with diagonal  $\Lambda$ -matrices kept explicitly on each bond) in Fig. 6.11(b) and propagate it forward by the first set of the system TEBD gates contained in the orange box in Fig. 6.10, using the steps of TEBD algorithm in Sec. 2.2.3.

We next apply the first full timestep  $n = 1$  by contracting MPS with the contents of the cyan box in Fig. 6.10. Contracting MPS with the first set of bath influence propagators transforms it into a new object with two local indices on each site, as shown in Fig. 6.11(b,c). This object is a generalization of the augmented density

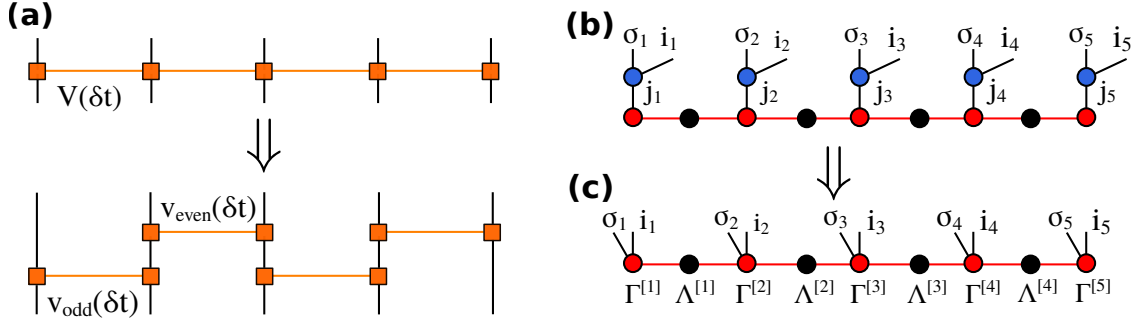


Figure 6.11: (a) For Hamiltonians with the nearest-neighbour spatial interactions, the MPO propagator  $V(\delta t)$  may be replaced by a set of two-body gates  $v_{\text{odd}}(\delta t)$  and  $v_{\text{even}}(\delta t)$  acting on odd and even bonds respectively. For simplicity, the illustration here is for the first order Trotter splitting, but the same arguments are easily extendable to the higher order decompositions. (b) Contracting the vectorized density matrix MPS with the first set of bath influence propagators transforms it into the augmented MPS with two local indices on each site:  $i_m$  is the physical Liouville space index, and  $\sigma_m$  is the ancilla due to the system-bath interaction. (c) The augmented MPS with  $M = 5$  sites in Vidal form with  $\Gamma^{[m]}$  site tensors (red circles) and  $\Lambda^{[m]}$  bond tensors (black circles), as described in Sec. 2.2.3.

matrix  $P(t)$ , described in previous section, to a lattice with  $M$  sites. We call it an ‘augmented MPS’ to distinguish it from the MPS representing the vectorized many-body density matrix  $\rho(t)$ . As before, the leg  $i_m$  is a physical index corresponding to the local Liouville space of site  $m$ , and has a dimension of  $d^2$ . Meanwhile,  $\sigma_m$  is an ancillary index of site  $m$ , corresponding to the bond index connecting timesteps  $n$  and  $n + 1$  of bath influence MPS, which has the bond dimension of  $D_B$ . As seen in Fig. 6.10, every step  $n \leq N$  of time evolution propagates the augmented MPS object rather than the vectorized density matrix MPS itself. We subsequently multiply the augmented MPS by a set of two-body TEBD propagators along the physical indices  $i_m$  at each site  $m$ . The augmented MPS is, again, updated using the steps of TEBD algorithm where the ancillary indices are treated as additional bond indices. To prevent the bond dimension from growing indefinitely, we truncate it using SVD either by keeping the  $\chi$  largest singular values, or by discarding the singular values below some fixed cutoff  $\epsilon_c$ . An update by a single two-body propagator acting on a single bond is shown diagrammatically in Fig. 6.12(c-g).

In general, to propagate the augmented MPS forward by a single timestep  $n > 1$ , we contract it with the contents of the green box in Fig. 6.10. More specifically, we contract all sites with their local bath influence propagators, and apply a set of two-body system propagators from Fig. 6.11(a) using a TEBD-like update and SVD truncation along the spatial axis. The steps of this update are illustrated graphically in Fig. 6.12. We can extract the actual density matrix MPS from the augmented MPS after  $n$  timesteps by applying a cap in the purple box in Fig. 6.10(b), which removes the ancillary indices and recovers the conventional MPS representation. Once the time-evolved vectorized density matrix MPS is available, we can use it to calculate observables as usual.

To summarize our discussion in this section, the Toblerone TEMPO algorithm

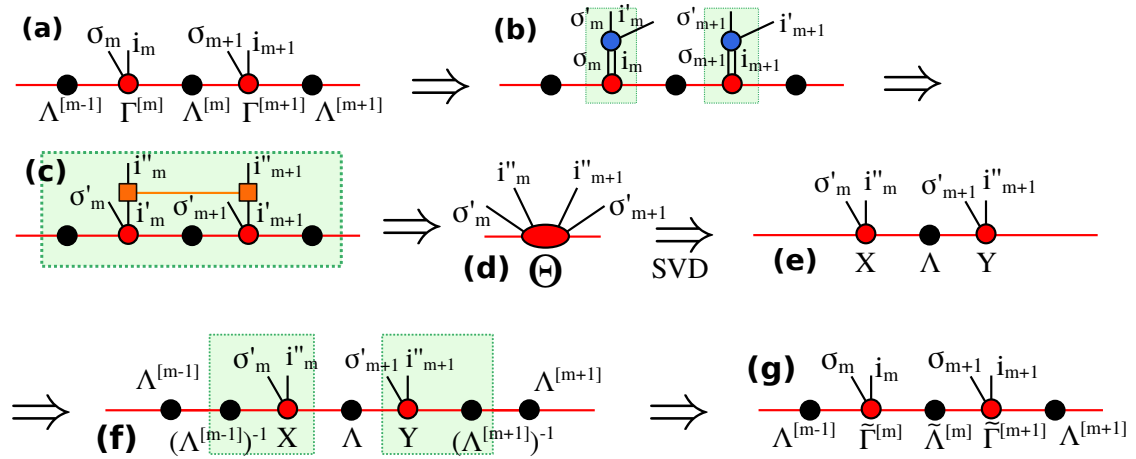


Figure 6.12: A TEBD-like update for the bond connecting sites  $m$ ,  $m+1$  of the augmented MPS. (a) The augmented MPS in Vidal form. To perform the update, we (b) contract with bath influence propagators (blue) using both the physical  $i_m$  and ancilla  $\sigma_m$  indices; (c) apply the two-body system propagator (orange) by contracting all tensors in the green box into a single  $\theta$  tensor in (d); (e) decompose  $\theta$  using SVD into the site tensors  $X$ ,  $Y$  and the bond tensor  $\Lambda$  – like in TEBD, we truncate the bond size by keeping the  $\chi$  largest singular values, or by discarding the singular values below some fixed cutoff  $\epsilon_c$ ; (f) divide  $X$ ,  $Y$  by the outer bond tensors  $\Lambda^{[m-1]}$ ,  $\Lambda^{[m+1]}$ ; (g) this restores the original Vidal form of the augmented MPS with updated site tensors  $\tilde{\Gamma}^{[m]}$ ,  $\tilde{\Gamma}^{[m+1]}$  and the bond tensor  $\tilde{\Lambda}^{[m]}$ .

consists of two phases:

1. Contracting bath influence tensors to obtain bath influence MPS for each lattice site independently. This step truncates the information about non-Markovian correlations along the temporal axis, to some fixed precision  $\lambda_c$ . The leading numerical cost is dominated by the SVDs and tensor contractions of MPS-MPO multiplication using the zip-up algorithm from Sec. 2.2.2. The cost for updating a single bond of bath influence MPS scales as  $O(D_B^3 d^6)$ . Here,  $D_B$  is the bond dimension of bath influence MPS required to maintain the precision  $\lambda_c$  for the specific bond that we are updating. The dimension  $d$  is the size of the local Hilbert space of a single lattice site.
2. Performing the TEBD-like time evolution that deals with the augmented MPS as its main object. The actual time-evolved density matrix MPS can be recovered after any timestep by applying a cap that removes the ancillary indices. This step truncates the information about many body correlations along the spatial axis, using either a fixed precision  $\epsilon_c$  or a fixed bond dimension  $\chi$ . The naive implementation carries a numerical cost of  $O(d^6 D_B^3 \chi^3)$  for updating a single bond of the augmented MPS, dominated by the SVDs of the TEBD-like update. The  $\chi$  here is either a fixed bond dimension, or a bond dimension required to maintain the fixed precision  $\epsilon_c$  for the specific bond that we are updating. For a step  $n < N$  of time evolution,  $D_B$  is the size of the bond connecting the sites of bath influence MPS corresponding to timesteps  $n$  and  $n+1$  (for  $n = N$ , we have  $D_B = 1$  as seen in Fig. 6.6).

Crucially, we can see that the numerical cost of time evolution in phase (2) depends heavily on the bond dimension  $D_B$  of the bath influence MPS, and hence on the amount of non-Markovian correlations present. The efficiency of MPS compression in phase (1) thus strongly affects the speed and the feasibility of calculations in phase (2).

## 6.4 Toblerone simulation results

We next benchmark Toblerone TEMPO by comparing it to known results available from other methods. A natural starting point is to test Toblerone TEMPO against the standard TEMPO, introduced in Chapter 5, for small lattice systems in 1D. It is important to emphasize the difference in how the two approaches treat the system-bath interaction. The standard TEMPO considers a system with only one bath. In the case of a multipartite system, either all or some of the sites will be coupled to the same bath. Meanwhile, Toblerone TEMPO describes a system with multiple baths, where each site is coupled to its own independent bath. Therefore, to make a meaningful comparison between the two methods, one needs to consider a system of  $M$  sites where only one site interacts with a bath, while the other  $M - 1$  sites are not coupled to any bath at all. In addition, since tensor dimensions in standard TEMPO scale exponentially with system size, our comparison will be restricted to small lattices.

We use standard TEMPO and Toblerone TEMPO to simulate the dynamics of a 1D spin chain with  $M = 3$  sites, described by the transverse-field Ising model where the middle site  $l = 2$  is in contact with a bosonic bath, while the other two sites  $l = 1, 3$  are coupled to the middle site but do not interact with any external environment. The Hamiltonian is given by:

$$H = \sum_{l=1}^M H_l + J^z \sum_{l=1}^{M-1} \sigma_l^z \sigma_{l+1}^z \quad (6.17)$$

Here,  $\sigma_l^{x,z}$  are Pauli matrices,  $J^z$  is the nearest-neighbour coupling between spins, and  $H_l$  is the onsite Hamiltonian for site  $l$ :

$$H_l = \begin{cases} g\sigma_l^x + \frac{\sigma_l^z}{2} \sum_k \left( g_{k,l} a_{k,l} + g_{k,l}^* a_{k,l}^\dagger \right) + \sum_k \omega_{k,l} a_{k,l}^\dagger a_{k,l} & l = 2 \\ g\sigma_l^x & l \neq 2 \end{cases} \quad (6.18)$$

where  $g$  is the transverse magnetic field along the  $x$  axis. Each bosonic mode  $k$  has a frequency  $\omega_k$  and the creation/annihilation operators  $a_k^\dagger, a_k$ . The bath modes couple to the system operator  $\sigma^z$ , and  $g_k$  is the coupling strength of the  $k$ 'th harmonic mode. We will work in units of  $J^z = 1$  throughout this section. Here we consider a harmonic bath characterized by the spectral density

$$J(\omega) = 2\alpha\omega^\nu\omega_c^{1-\nu}e^{-\omega/\omega_c} \quad (6.19)$$

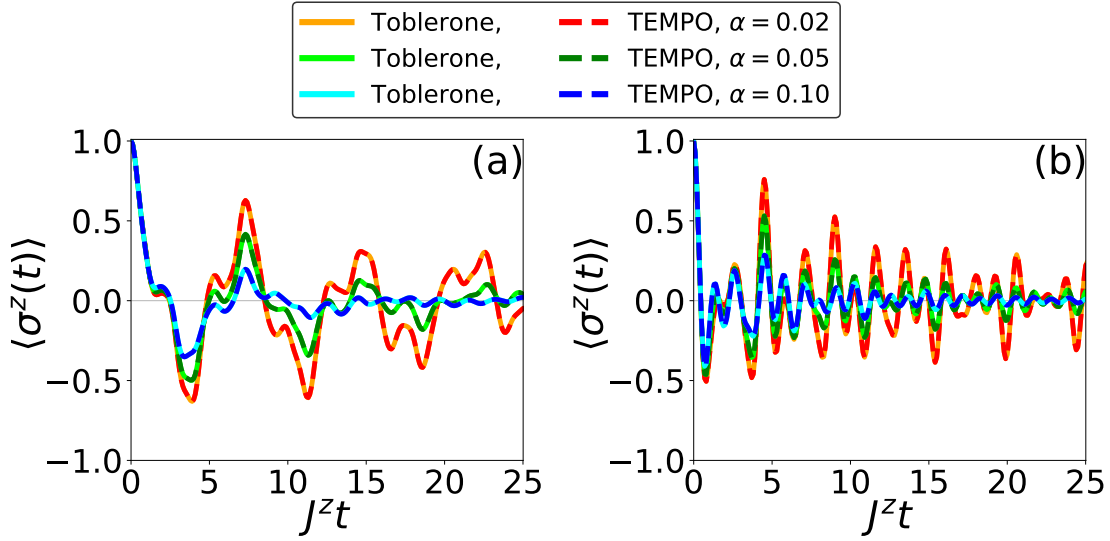


Figure 6.13: The  $\langle \sigma^z(t) \rangle$  dynamics of the transverse field Ising model Eq. (6.17), (6.18) where the middle site is coupled to an Ohmic ( $\nu = 1$ ) bath, for transverse fields (a)  $g = 1.0$ , and (b)  $g = 2.0$ . Each panel shows results for different system-bath couplings  $\alpha = 0.02, 0.05, 0.10$ . The figure compares Toblerone TEMPO (solid lines) and conventional TEMPO (dashed lines) results. TEMPO calculations used SVD precision  $\lambda_c = 10^{-7}$ . Toblerone TEMPO calculations used the fourth-order Trotter decomposition for time evolution in Fig. 6.10, SVD precision  $\epsilon_c = 10^{-4}$  for truncations on the spatial axis in Fig. 6.12, and SVD precision  $\lambda_c = 10^{-8}$  for truncations on the temporal axis in Fig. 6.6. All calculations used timestep size  $\delta t = 0.2$ . Other parameters are:  $\omega_c = 5$ ,  $T = 0$ . Energies are given in units of  $J^z = 1$ . No finite memory cutoff was used.

where  $\alpha$  is the system-bath coupling strength,  $\omega_c$  is the bath cutoff frequency, and  $\nu$  sets the weight of contribution from low-energy modes to the system-bath interaction. In our example, we will focus on a bath with Ohmic spectral density ( $\nu = 1$ ) and  $T = 0$ . In Fig. 6.13(a,b) we display the  $\langle \sigma^z(t) \rangle$  dynamics at the lattice site  $l = 2$  coupled to the bath, for transverse fields  $g = 1.0$  and  $g = 2.0$  respectively. In each case, we show the results for different system-bath couplings  $\alpha = 0.02, 0.05, 0.10$ . In all simulations, we have taken 125 timesteps without using the finite memory cutoff  $K$ , effectively meaning  $K = 125$ . We observe a perfect match between TEMPO and Toblerone TEMPO for all parameters, and throughout the entire range of dynamics. These results also illustrate that Toblerone TEMPO can be used for inhomogeneous problems where different sites are embedded in different environments.

Our second test problem is the exactly solvable many-body independent boson model (IBM). It is an extension of the independent boson model (IBM), introduced in Sec. 5.4 and Appendix. A.2, to many-body systems in 1D. More specifically, the many-body IBM describes a 1D chain of  $M$  two-level systems that interact via

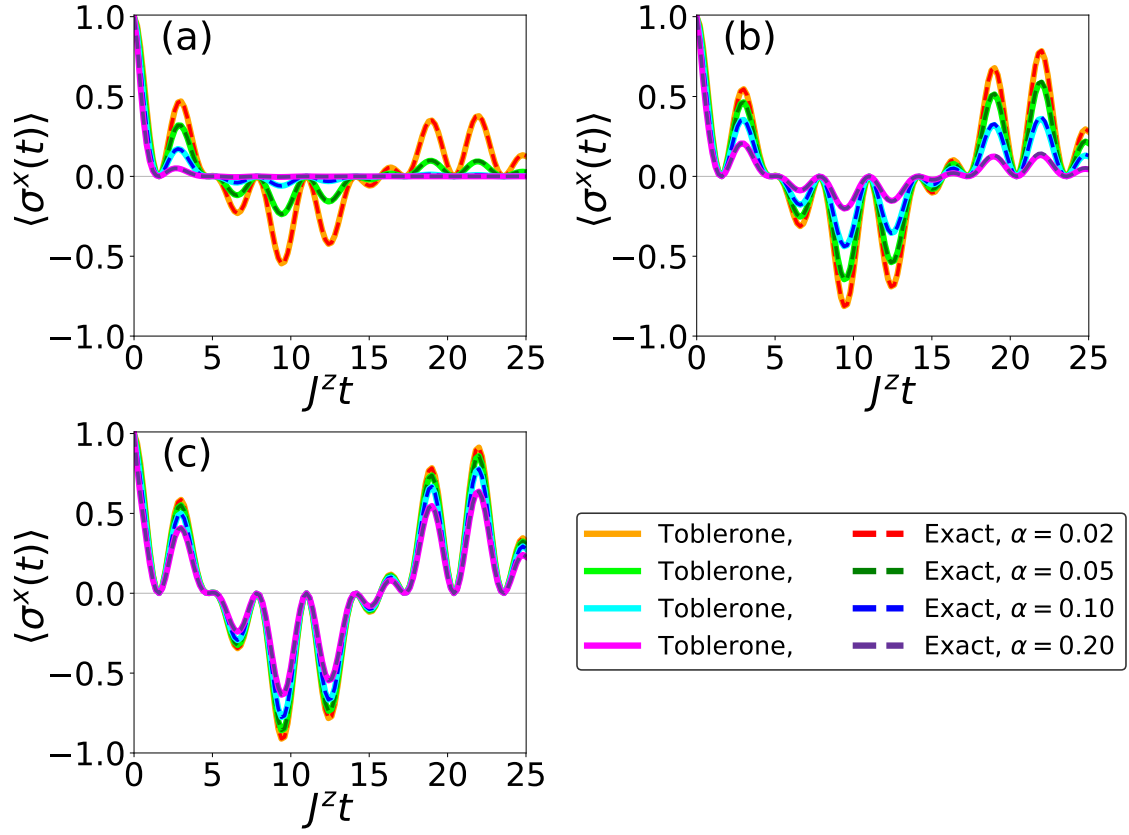


Figure 6.14: The  $\langle \sigma^x(t) \rangle$  dynamics of the many-body IBM Eq. (6.20), (6.21) where each site is coupled to a harmonic bath with (a) Subohmic ( $\nu = 1/2$ ), (b) Ohmic ( $\nu = 1$ ), (c) Superohmic ( $\nu = 2$ ) spectral densities. Each panel shows results for different system-bath couplings  $\alpha = 0.02, 0.05, 0.10, 0.20$ . The figure compares Toblerone TEMPO results (solid lines) to the exact analytical solution Eq. (6.26) (dashed lines). Toblerone TEMPO calculations used timestep size  $dt = 0.2$ , the fourth-order Trotter decomposition for time evolution in Fig. 6.10, SVD precision  $\epsilon_c = 10^{-4}$  for truncations on the spatial axis in Fig. 6.12, and SVD precision  $\lambda_c = 10^{-8}$  for truncations on the temporal axis in Fig. 6.6. Other parameters are:  $\omega_c = 5$ ,  $T = 0$ ,  $\epsilon = 0.3$ . Energies are given in units of  $J^z = 1$ . No finite memory cutoff was used.

Ising-like nearest neighbour couplings along  $z$ -axis:

$$H = \sum_{l=1}^M H_l + \frac{J^z}{2} \sum_{l=1}^{M-1} \sigma_l^z \sigma_{l+1}^z \quad (6.20)$$

where  $J^z$  is the coupling constant and  $H_l$  is the onsite Hamiltonian for site  $l$ , while  $\sigma^z$  are spin-1/2 matrices. Each site is a two-level system linearly coupled to its bosonic environment, and is described by the IBM Hamiltonian Eq. (5.40):

$$H_l = \frac{\epsilon_l}{2} \sigma_l^z + \frac{\sigma_l^z}{2} \sum_k \left( g_{k,l} a_{k,l} + g_{k,l}^* a_{k,l}^\dagger \right) + \sum_k \omega_{k,l} a_{k,l}^\dagger a_{k,l} \quad (6.21)$$

with additional site indices  $l$ . All variables have the same definitions as in Eq. (5.40) of Sec. 5.4. We consider the bosonic environments of different sites to be indepen-



dent. Similarly to the IBM in Sec. 5.4, the many-body IBM Hamiltonian Eq. (6.20) is straightforward to diagonalize using the polaron transformation, which allows us to derive the analytical solution for the reduced density matrix of the system  $\rho(t)$ :

$$\rho(t) = \sum_{\mathcal{A}, \mathcal{B}} |\mathcal{A}\rangle \langle \mathcal{B}| [\rho(0)]_{\mathcal{A}, \mathcal{B}} e^{-i(E_{\mathcal{A}} - E_{\mathcal{B}})t} \prod_l I_{l, \alpha_l, \beta_l}(t) \quad (6.22)$$

where  $\mathcal{A} = \{\alpha_l\}$  and  $\mathcal{B} = \{\beta_l\}$  are the many-body spin configurations where  $\alpha_l = \pm 1$  and  $\beta_l = \pm 1$  refer to the eigenstates  $\uparrow, \downarrow$  of a spin-1/2 at lattice site  $l$ . We have also defined

$$I_{l, \alpha_l, \beta_l}(t) = \begin{cases} e^{-\phi_l(t)} & \alpha_l \neq \beta_l \\ 1 & \alpha_l = \beta_l \end{cases} \quad (6.23)$$

with  $\phi_l(t)$  given by

$$\phi(t) = 4 \sum_k \frac{|g_{k,l}|^2}{\omega_{k,l}^2} (1 - \cos(\omega_{k,l}t)) = 4 \int_0^\infty d\omega \frac{J_l(\omega)}{\omega^2} (1 - \cos(\omega t)) \quad (6.24)$$

The derivation is presented in more detail in the Appendix A.3. For simplicity, we consider a homogeneous lattice with  $\epsilon_l = \epsilon$ ,  $J_l(\omega) = J(\omega)$  and  $\phi_l(t) = \phi(t)$ . We also take the initial state of the system at  $t = 0$  equal to:

$$\rho(0) = |\Psi_0\rangle \langle \Psi_0| \quad (6.25)$$

with  $|\Psi_0\rangle = \prod_{l=1}^M \frac{1}{\sqrt{2}} (|\uparrow_l\rangle + |\downarrow_l\rangle)$ . From Eq. (6.22), we find the exact dynamics of  $\langle \sigma_l^x(t) \rangle$  at site  $l$ :

$$\begin{aligned} \langle \sigma_l^x(t) \rangle &= \text{Tr}_B (\sigma_l^x \rho(t)) = \\ &= \begin{cases} \frac{1}{2} e^{-\phi(t)} [\cos((\epsilon - J^z)t) + \cos((\epsilon + J^z)t)] & l = 1, M \\ \frac{1}{4} e^{-\phi(t)} [\cos((\epsilon - 2J^z)t) + \cos((\epsilon + 2J^z)t) + 2\cos(\epsilon t)] & \text{else} \end{cases} \end{aligned} \quad (6.26)$$

Let us now compare Toblerone TEMPO against the exact solution Eq. (6.26) for a spin-1/2 chain with  $M = 5$  sites, each site coupled to a bath with spectral density in Eq. (6.19) and  $T = 0$ . As before, we work in units of  $J^z = 1$ . Figures 6.14(a,b,c) all show a good agreement between Toblerone TEMPO and Eq. (6.26) for Subohmic ( $\nu = 1/2$ ), Ohmic ( $\nu = 1$ ) and Superohmic ( $\nu = 2$ ) spectral densities respectively, as well as for different system-bath couplings  $\alpha = 0.02, 0.05, 0.10, 0.20$ . In all simulations, we have taken 125 timesteps without using a finite memory cutoff  $K$ , effectively meaning  $K = 125$ . The expectation values  $\langle \sigma_l^x(t) \rangle$  were evaluated at a nearest-to-the-middle lattice site  $l = 3$ .

Finally, we demonstrate that Toblerone TEMPO is also capable of treating larger systems. To this end, we simulate a 1D lattice with  $M$  sites, described by the transverse-field Ising model Eq. (6.17) where each site is additionally coupled to a bosonic bath.

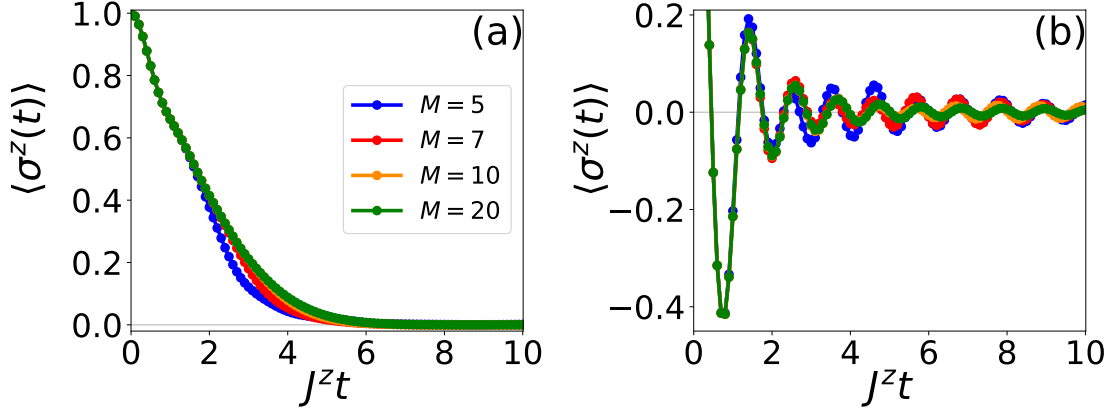


Figure 6.15: The  $\langle \sigma^z(t) \rangle$  dynamics of the transverse-field Ising model Eq. (6.17), (6.27) where each site is coupled to an Ohmic ( $\nu = 1$ ) bath for transverse fields (a)  $g = 0.7$  and (b)  $g = 2.0$ . Each panel shows results for different lattice sizes  $M = 5, 7, 10, 20$ . Toblerone TEMPO calculations used timestep size  $dt = 0.1$ , the fourth-order Trotter decomposition for time evolution in Fig. 6.10, SVD precision  $\epsilon_c = 10^{-4}$  for truncations on the spatial axis in Fig. 6.12, and SVD precision  $\lambda_c = 10^{-6}$  for truncations on the temporal axis in Fig. 6.6. Other parameters are:  $\omega_c = 5$ ,  $T = 0$ . Energies are given in units of  $J^z = 1$ . No finite memory cutoff was used.

The onsite Hamiltonian  $H_l$  at site  $l$  in Eq. (6.17) is then given by

$$H_l = g\sigma_l^x + \frac{\sigma_l^z}{2} \sum_k \left( g_{k,l} a_{k,l} + g_{k,l}^* a_{k,l}^\dagger \right) + \sum_k \omega_{k,l} a_{k,l}^\dagger a_{k,l} \quad (6.27)$$

All variables have the same definitions as in Eq. (6.18). We consider a system with all sites coupled to identical Ohmic baths at  $T = 0$ , each characterized by spectral density Eq. (6.19) with  $\nu = 1$ . In Fig. 6.15(a,b) we plot the relaxation dynamics of  $\langle \sigma^z(t) \rangle$  for  $g = 0.7$  and  $g = 2.0$  respectively, and for different lattice sizes of  $M = 5, 7, 10, 20$  sites. In each case,  $\langle \sigma^z(t) \rangle$  was evaluated at the middle site, i.e.  $l = 3, 4, 5, 10$  for  $M = 5, 7, 10, 20$  respectively. In all simulations, we have taken 150 timesteps without using the finite memory cutoff  $K$ , effectively meaning  $K = 150$ . Unlike in the previous two test cases discussed above, no analytical solutions or numerically exact results exist in literature to compare against our simulations in Fig. 6.15, to the best of our knowledge. The results in Fig. 6.15 provide a proof-of-principle example that Toblerone TEMPO can also simulate larger lattices, beyond the reach of most numerical techniques. While the development of Toblerone TEMPO is still an ongoing endeavour, we have shown here that it is already a powerful method that produces accurate results for many-body models coupled to general bosonic environments. Future work could involve further comparisons of Toblerone TEMPO against more complicated problems in Refs. [46, 319], and eventually applications to systems such as coupled cavity arrays in contact with non-Markovian noise, polaritons in organic molecules strongly coupled to light, and biomolecular systems with excitonic energy transport.

# **Part IV**

## **Conclusions**



# Chapter 7

## Conclusions and future work

In this thesis, we have explored several topics related to the development of tensor network techniques for simulating nonequilibrium steady states, dissipative quantum dynamics, and fluorescence spectra of various open quantum systems. This chapter provides a brief summary of my thesis and discusses possible research directions that could be pursued in future work.

### 7.1 Conclusions

In the first half of the thesis, we investigated driven dissipative many body physics in coupled cavity arrays. These coupled cavity systems were weakly coupled to an external bath of electromagnetic modes, and thus accurately described by Born-Markov master equations.

In Chapter 3, we extended the transfer MPO technique to calculate two-time correlations in open quantum systems. We applied this approach to compute dynamical correlation functions, and used them to extract the energy and momentum resolved fluorescence spectra of an infinite coupled cavity array in 1D. To demonstrate the information available from these spectra, we utilized them to study thermalization in driven dissipative systems. In particular, we observed that blue-detuned driving stabilizes a quasi-thermal steady state with a negative effective temperature and a maximum-energy order. In the low excitation density limit, we derived analytical results using spin-wave theory and compared them to the numerical transfer MPO results. This allowed us to interpret the form of the distribution function and the origin of quasi-thermalization. More generally, our work illustrates how calculating two-time correlations of the emitted photons provides new insights into the driven dissipative many-body physics. It will motivate both the theoretical studies on dynamical properties of coupled cavity systems and the measurement of the fluorescence spectrum in the future experiments with superconducting circuits and microwave resonators. Our results are also interesting in the context of the stabilization of negative temperature phases in recent experiments with cold atoms [250, 251], as well as the quasi-equilibrium states in various strongly interacting light-matter systems [24, 34, 239, 248].

Chapter 4 focused on the development of iPEPS-based methods to study the nonequilibrium steady states of coupled cavity lattices in 2D, and in the thermody-

namic limit. We implemented and benchmarked the iPEPO algorithm that treats a vectorized many-body density operator as an iPEPS, and uses the Simple Update iPEPS scheme to find the steady state. The iPEPO algorithm is analogous to the iTEBD method using MPS that has been successfully applied in steady state calculations of various open quantum systems in 1D. Surprisingly, we found that iPEPO algorithm is unstable, converging only in some parameter regimes while failing to find a converged steady state in others. Our negative result contradicts a recent work by Ref. [276] who used the iPEPO algorithm to calculate steady states of the dissipative XYZ and transverse field Ising models. We will discuss the possible future developments and applications of iPEPS methods to the two-dimensional steady states in the next section.

In the latter half of this thesis, we tackled problems with more general system-environment interactions, involving strong couplings and structured environments that induce non-Markovian dynamics.

In Chapter 5, we developed a powerful TEMPO algorithm based on Feynman-Vernon influence functional formalism and the augmented density tensor (ADT) representation. We reformulated the ADT time evolution as a tensor network, and employed MPS techniques to contract this network, thereby reducing the exponential scaling of standard ADT simulations to low-order polynomial. We benchmarked TEMPO by comparing it to other known results and methods: the exact analytical solution of the independent boson model, QUAPI simulation of the spin-boson model coupled to an Ohmic bath, and Reaction Coordinate Mapping of the spin-boson model interacting with a Drude-Lorentz bath. We further demonstrated the efficiency and robustness of TEMPO algorithm by applying it to study two different problems. The first one focused on the bath-induced localization phase transition of the paradigmatic spin-boson model. Understanding the dynamics and the properties of the spin-boson model in the strong coupling regime is a subject of active research [285] and is currently being explored in experiments with the superconducting circuit quantum simulators [123]. Our results have shown the potential of TEMPO in addressing this numerically challenging problem. In the second problem we simulated the excitation transfer between two spatially separated two-level systems embedded in a common environment. Using TEMPO, we have been able to capture both the small and large separation regimes of the dynamics, relevant to a wide range of physical systems, for example, the experiments with coupled quantum dots [286–291] and the long-range entanglement in waveguide QED systems [293].

The final Chapter 6 pursued the ambitious goal of extending TEMPO to many body systems interacting with non-Markovian environments. As we have seen, solving a many-body TEMPO problem amounts to contracting a quasi-3D tensor network that has a Toblerone geometry. We proposed a Toblerone TEMPO algorithm that uses MPS representation to capture both the non-Markovian memory effects and the spatial many-body correlations. In particular, we introduced a bath influence MPS describing the system-environment interaction, and showed that one may reduce the contraction of the Toblerone network to a modified TEBD algorithm that evolves the many-body density matrix MPS. We then benchmarked Toblerone TEMPO by comparing it to the analytical solution of the many-body independent boson model, as well as to TEMPO simulations of small systems. In addition, we

applied Toblerone TEMPO to simulate the transverse field Ising model on 1D lattice where each spin was coupled to a non-Markovian bath. Overall, we believe that Toblerone TEMPO will enable us to study a vast range of non-Markovian systems that are beyond the reach of the present day methods. We will discuss the possible applications in the next section.

## 7.2 Future work

We next discuss several possible research directions that could be pursued in future work related to the projects described in this thesis.

In Chapter 3, we studied coupled cavity arrays in the photon blockade regime where occupations were restricted to at most one excitation per site. The next stage of this project could investigate dynamical correlations and fluorescence spectra in problems with a larger onsite Hilbert space. In the presence of multiple onsite occupancy, one could explore nonlinear optical phenomena in coupled cavity systems, arising due to polariton-polariton scattering events between the states with different energies and momenta. The nonlinear scattering phenomena are important in various systems with strong light-matter interactions, such as microcavity polaritons [24, 322]. Investigating these phenomena could provide novel insights into the many-body physics and optical properties of coupled cavity arrays, particularly in connection to other systems featuring strong light-matter coupling. An intriguing question to ask is whether the polaritonic optical parametric oscillation (OPO), similar to the one in semiconductor microcavities [322–324], is also important to the physics of polaritons in coupled cavity systems – and whether there is a connection between polaritonic OPO and polariton crystallization [68] in coupled cavity arrays. Another question that one could address is the crossover from the limit of weakly-interacting polaritons to the limit with photon blockade in coupled cavity systems. This question is especially relevant to the formation of strongly correlated phases in synthetic photonic materials out of equilibrium, and the phase transitions between the localized and delocalized states in these materials – similar to their counterparts in various solid state systems. As the circuit QED experiments continue to grow in size, numerical simulations capable of addressing these phenomena in large-scale many body systems will be increasingly important [15, 60, 80, 86]. Tackling the problems described above will inevitably require a large local Hilbert space, thus making it necessary to improve the efficiency of both iTEBD and transfer MPO methods or devise new approaches capable of treating a large onsite basis. The possible technical developments include using improved contraction schemes for the transfer MPO network, imposing suitable gauge fixing or boundary conditions, exploiting tensor symmetries, applying local dimensionality reduction methods such as the optimal boson basis – as well as a possibility of extending the tangent space MPS methods for calculating dynamical correlations [162, 182, 236] to Liouvillian dynamics.

In Chapter 4, we have reached a conclusion that the calculation of nonequilibrium steady states of large driven dissipative lattice systems in 2D remains an unsolved problem. Future research in this area will necessarily focus on finding more

suitable and more robust strategies for solving Lindblad master equations in 2D. One possible approach is replacing the two-body updates of the iPEPO method with a global non-Hermitian variational search algorithm targetting the null eigenstate of the Liouvillian  $\mathcal{L}$  or the squared Liouvillian  $\mathcal{L}^\dagger \mathcal{L}$ . The global optimization, for instance by using the conjugate gradient method or by solving a generalized eigenvalue problem, could offer a more powerful and robust approach for calculating steady states – especially compared to a simple iPEPO algorithm that relied on a scheme essentially equivalent to an iPEPS power method with local two-body updates. Particularly appealing are the recently proposed variational iPEPS methods [210, 211] that utilized a systematic summation of contributions from different Hamiltonian coupling terms, instead of constructing a full Hamiltonian iPEPO, thereby avoiding the extremely costly contractions of iPEPS and iPEPO tensors. Extending these approaches to Liouvillian superoperators and density matrices could deliver powerful tools for simulating driven dissipative many body physics in 2D. The iPEPS simulations have made significant contributions to our understanding of the equilibrium quantum matter in 2D [213–224]. The extension of iPEPS to mixed states could open many exciting avenues for research – for instance, the two-dimensional synthetic photonic materials and the engineered topological order, already being explored in the context of circuit QED experiments [260–263]. We would also be able to study the symmetry-breaking quantum phase transitions in strongly correlated matter under drive and dissipation, which is not possible in the dissipative 1D systems. The central question here is identifying the nonequilibrium phase transitions in 2D, and their critical properties. Various models with critical behaviour can already be realized in driven dissipative Rydberg gases [268–270], and the possibilities will expand with the realization of circuit QED lattices in 2D [260–263].

Chapter 5 has led to the TEMPO algorithm – an efficient, general, and numerically exact approach for simulating non-Markovian quantum dynamics. Nonetheless, there is a number of potential technical developments that could further improve TEMPO, and we mention some of them here. For example, one could exploit the inherent symmetries present in the TEMPO tensor network due to Kronecker deltas that appear in the MPO decomposition of the ADT propagators, see Fig. 6.1. Incorporating these symmetries in tensor contractions and singular value decompositions could dramatically enhance the performance of TEMPO, and allow us to access problems with a significantly larger Hilbert space and higher bond dimensions. In addition, we could also enable applications of TEMPO to larger quantum systems by adapting widely used local basis reduction techniques such as the optimal boson basis. Although we have derived TEMPO algorithm for bosonic baths, the main idea is, in principle, applicable to other types of environments as well. Among the immediate goals is the extension of TEMPO to fermionic environments. For instance, it would enable us to simulate various impurity problems where an impurity is coupled to a Fermi Sea of electrons, and tackle systems described by Hamiltonians such as Kondo model or Anderson impurity model. The major challenge here is dealing with non-factorizing system-bath couplings that emerge in the fermionic influence functional formalism – in contrast to the product form of system-bath interaction in Eq. (1.44) for bosonic baths.

Yet another extension of TEMPO to many-body lattices interacting with bosonic



baths was pursued in Chapter 6. While we have already used Toblerone TEMPO algorithm to perform several proof of principle simulations, further improvements in efficiency are needed before we can tackle large lattice problems with at least  $O(10^2)$  sites over long timescales and treat stronger system-bath couplings than currently possible. In particular, we expect that Toblerone TEMPO will benefit greatly from the incorporation of symmetries, and the implementation of the optimal boson basis described above.

The applications of TEMPO presented in this thesis have barely scratched the surface of the vast variety of possibilities that have emerged with the development of this method. Some applications of our near-term interest include the excitonic energy transport in molecular systems, the physics of polaritons in organic molecules strongly coupled to light, as well as the simulations relevant to experimental setups with semiconductor quantum dots, superconducting circuits, and nanomechanical resonators. In the context of this thesis, Toblerone TEMPO will enable us to study coupled cavity arrays in contact with structured non-Markovian environments, in addition to the usual photon loss. For instance, one could investigate the effects of different noise spectra on the driven dissipative many body physics. Other areas that we could study in near future include the spectroscopic properties and polariton dynamics in organic molecules strongly coupled to light, and the relaxation dynamics of photoexcited electronic states in conjugated polymers. Both the properties of organic polaritons [135, 136] and the photoexcitation processes in conjugated polymers [310–316] are currently under active experimental investigation and are candidates for many applications, such as light-emitting devices, photovoltaic cells, and organic electronics. We expect that Toblerone TEMPO will provide a powerful numerical tool for tackling these and many other problems involving many-body systems embedded in non-Markovian environments.



# Part V

## Appendices



# Appendix A

## Supplementary non-Markovian calculations

### A.1 Reaction Coordinate Mapping

This section explains the basic idea behind the Reaction Coordinate Mapping (RCM) technique from [157]. For simplicity, we will focus on a spin system that interacts with a harmonic bath, and is described by the spin-boson model (SBM) defined in Eq. (1.100):

$$H = \Omega S_x + \epsilon S_z + S_z \sum_k \left( g_k a_k + g_k^* a_k^\dagger \right) + \sum_k \omega_k a_k^\dagger a_k \quad (\text{A.1})$$

where  $S^{x,z}$  are spin operators representing the N-level system,  $\Omega$  is the coherent tunnelling amplitude between the system eigenstates with energy splitting  $\epsilon$ ,  $\omega_k$  are the frequencies and  $a_k^\dagger, a_k$  are the creation/annihilation operators of the  $k$ 'th bath mode, which couples to the system with strength  $g_k$ . The bosonic bath is fully characterized by the spectral density

$$J(\omega) = \sum_k |g_k|^2 \delta(\omega - \omega_k) \quad (\text{A.2})$$

In RCM we perform the mapping

$$\lambda_{RC}(b + b^\dagger) = \sum_k \left( g_k a_k + g_k^* a_k^\dagger \right) \quad (\text{A.3})$$

where we have defined the collective mode of the environment – the reaction coordinate (RC) described by bosonic operators  $b^\dagger, b$  and frequency  $\omega_{RC} = \lambda_{RC}^{-2} \sum_k \omega_k |g_k|^2$ . The RC couples directly to the spin system with coupling strength  $\lambda_{RC} = \sqrt{\sum_k |g_k|^2}$  as well as the modes of residual harmonic environment  $a_k^\dagger, a_k$  with a new coupling strength  $f_k$ . This form of mapping ensures that the new RC operators  $b^\dagger, b$  satisfy bosonic commutation relations. The above mapping transforms SBM Hamiltonian in Eq. (A.1) into

$$H = H_0 + H_B + H_I + H_C \quad (\text{A.4})$$

We have transferred the RC from the bath Hamiltonian to the system Hamiltonian:

$$H_0 = \Omega S_x + \epsilon S_z + \lambda_{RC} S_z (b + b^\dagger) + \omega_{RC} b^\dagger b \quad (\text{A.5})$$

Other terms are defined as follows:

$$H_B = \sum_k \omega_k a_k^\dagger a_k \quad (\text{A.6})$$

is the bath Hamiltonian,

$$H_I = (b + b^\dagger) \sum_k \left( f_k a_k + f_k^* a_k^\dagger \right) \quad (\text{A.7})$$

describes the bath-RC interaction, and

$$H_C = (b + b^\dagger)^2 \sum_k \frac{|f_k|^2}{\omega_k} \quad (\text{A.8})$$

is the renormalization term. The residual environment (i.e. with RC excluded) now has the spectral density:

$$J_{RC}(\omega) = \sum_k |f_k|^2 \delta(\omega - \omega_k) \quad (\text{A.9})$$

and couples only to the RC. To complete the mapping described above, we must relate the mapped spectral density  $J_{RC}(\omega)$  Eq. (A.9) to the original one  $J(\omega)$  Eq. (A.2). This can be done by following the procedure explained in references [325], [157]: since the spectral density does not contain any information about the system but only the system-environment coupling, we can replace the spin system in both the original Eq. (A.1) and the mapped Eq. (A.4) Hamiltonians with a continuous classical coordinate  $q$  moving in a potential  $V(q)$ . By solving the classical equations of motion of this coordinate both before and after mapping, one can relate the spectral densities  $J_{RC}(\omega)$  and  $J(\omega)$ , as detailed in [157]. We consider a more specific example and take the mapped spectral density to be Ohmic  $J_{RC}(\omega) = \gamma \omega e^{-\omega/\omega_c}$  in the limit  $\omega_c \rightarrow \infty$ . As described in Ref. [157], the above procedure then finds that the mapped Ohmic  $J_{RC}(\omega)$  corresponds to the original (unmapped) Drude-Lorentz spectral density  $J(\omega)$ :

$$J(\omega) = \frac{\alpha \Gamma \omega_0^2 \omega}{(\omega_0^2 - \omega^2)^2 + \Gamma^2 \omega^2} \quad (\text{A.10})$$

with coupling strength  $\alpha$ , resonance frequency  $\omega_0$ , and bandwidth  $\Gamma$ . The parameters before and after mapping are related by  $\lambda = \sqrt{\pi \alpha \omega_0 / 2}$ ,  $\omega_{RC} = \omega_0$ ,  $\gamma = \Gamma / 2\pi \omega_0$ , and  $\omega_c = \omega_{RC} / 2\pi \gamma$ . Although RCM is not limited to Drude-Lorentz spectral densities, it allows us to derive a quasi-exact analytical solution for the reduced system dynamics since the residual bath is Markovian. Once the mapping is complete, we follow the steps outlined in [157] to derive a Born-Markov master equation for the reduced density matrix  $\rho(t)$  of the system and RC:

$$\partial_t \rho(t) = -i [H_0, \rho(t)] - [B, [\chi, \rho(t)]] + [B, \{\Theta, \rho(t)\}] \quad (\text{A.11})$$

We next explain the quantities  $B$ ,  $\chi$ ,  $\Theta$  in Eq. (A.11).  $B$  is an RC operator defined as  $B = b + b^\dagger$ . To define  $\chi$  and  $\Theta$ , we must first numerically diagonalize the composite system-RC Hamiltonian:  $H_0 |\phi_n\rangle = \epsilon_n |\phi_n\rangle$  and find the interaction picture operators

$$B(t) = e^{iH_0 t} B e^{-iH_0 t} = \sum_{m,n} B_{mn} |\phi_m\rangle \langle \phi_n| e^{i\epsilon_{mn} t} \quad (\text{A.12})$$

where the matrix elements are  $B_{mn} = \langle \phi_m | B | \phi_n \rangle$  and the energy difference is  $\epsilon_{mn} = \epsilon_m - \epsilon_n$ . We can now calculate the operators  $\chi$  and  $\Theta$  in the master equation above:

$$\begin{aligned} \chi &= \int_0^\infty d\tau \int_0^\infty d\omega J_{RC}(\omega) \cos(\omega\tau) \coth\left(\frac{\beta\omega}{2}\right) B(-\tau) \\ &\approx \frac{\pi}{2} \sum_{m,n} J_{RC}(\epsilon_{mn}) \coth\left(\frac{\beta\epsilon_{mn}}{2}\right) B_{mn} |\phi_m\rangle \langle \phi_n| \end{aligned} \quad (\text{A.13})$$

and

$$\Theta = \int_0^\infty d\tau \int_0^\infty d\omega \frac{J_{RC}(\omega)}{\omega} \cos(\omega\tau) [H_0, B(-\tau)] \approx \frac{\pi}{2} \sum_{m,n} J_{RC}(\epsilon_{mn}) B_{mn} |\phi_m\rangle \langle \phi_n| \quad (\text{A.14})$$

neglecting the imaginary Lamb shift terms. One can then solve the master equation Eq. (A.11) using standard numerical techniques.

## A.2 Independent boson model

In this appendix we briefly outline the solution of the independent boson model (IBM) using the polaron transformation. The IBM Hamiltonian describes a two-level system coupled to a bosonic bath:

$$H = \frac{\epsilon}{2} \sigma^z + \frac{\sigma^z}{2} \sum_k \left( g_k a_k + g_k^* a_k^\dagger \right) + \sum_k \omega_k a_k^\dagger a_k \quad (\text{A.15})$$

As before, we assume that the bath is made of a large number of harmonic modes, and is fully characterized by spectral density  $J(\omega) = \sum_k |g_k|^2 \delta(\omega - \omega_k)$ . Each bosonic mode  $k$  has a frequency  $\omega_k$  and the creation/annihilation operators  $a_k^\dagger, a_k$ . The  $\sigma^{z,x}$  are spin-1/2 operators, and  $\epsilon$  is the spacing between energy levels of the two-level system. The bath modes couple to the system operator  $\sigma^z$  and  $g_k$  is the coupling strength of the  $k$ 'th harmonic mode. We start our derivation by defining the polaron displacement operator:

$$D = \prod_k D_k \left( \frac{g_k}{\omega_k} \sigma^z \right) \quad (\text{A.16})$$

where  $D_k(\gamma) = \exp(\gamma a_k^\dagger - \gamma^\dagger a_k)$ . Given that  $[\gamma, a_k] = 0$ , it obeys the following properties:

$$D^\dagger(\gamma) a_k D(\gamma) = a_k - \gamma, \quad (\text{A.17})$$

$$D^\dagger(\gamma) = D(-\gamma), \quad (\text{A.18})$$

$$\langle 0 | D(\gamma) | 0 \rangle = e^{-|\gamma|^2/2}, \quad (\text{A.19})$$

$$D(\gamma) D(\lambda) = D(\gamma + \lambda) e^{(\gamma \lambda^* - \lambda^* \gamma)/2}, \quad (\text{A.20})$$

$$e^{i\omega_k t a_k^\dagger a_k} D(\gamma) e^{-i\omega_k t a_k^\dagger a_k} = D(\gamma e^{i\omega_k t}) \quad (\text{A.21})$$

We perform the polaron transformation on the full Hamiltonian:

$$H' = D H D^\dagger = H_S + H_{B0} + H_C \quad (\text{A.22})$$

where  $H_S = \frac{\epsilon}{2} \sigma^z$ ,  $H_{B0} = \sum_k \omega_k a_k^\dagger a_k$  and  $H_C = -\sum_k |g_k|^2 / \omega_k$ . The time evolution operator then becomes

$$U(t) = e^{-iHt} = D^\dagger e^{-iH't} D = D^\dagger e^{-iH_S t} e^{-iH_{B0} t} e^{-iH_C t} D \quad (\text{A.23})$$

Making the usual assumption that the initial state is separable Eq. (1.10), and taking the bath in equilibrium at  $T = 0$  with  $\rho_B(0) = |0_B\rangle \langle 0_B|$ , one can write down the time evolution of the reduced density operator of the system  $\rho(t)$ :

$$\rho(t) = \text{Tr}_B (U(t) \rho(0) \rho_B(0) U^\dagger(t)) = \sum_{mn} [\rho(0)]_{mn} \text{Tr}_B (U(t) |0_B\rangle |m\rangle \langle n| \langle 0_B| U^\dagger(t)) \quad (\text{A.24})$$

Exploiting the properties Eqs. (A.17)-(A.21) of the displacement operator, after some algebra we find

$$\rho(t) = \sum_{m,n=\pm 1} [\rho(0)]_{mn} |m\rangle \langle n| e^{-i(E_m - E_n)t} I_{mn}(t) \quad (\text{A.25})$$

where  $m = \pm 1$  and  $n = \pm 1$  correspond to the spin-1/2 eigenstates  $\uparrow, \downarrow$  respectively,  $|n\rangle = \{\uparrow, \downarrow\}$ , and the free system energies are  $E_n = \frac{n\epsilon}{2}$ . We have also defined

$$\begin{aligned} I_{mn}(t) &= \prod_k \langle 0_B | D^\dagger(\gamma_k n) e^{i\omega_k t a_k^\dagger a_k} D(\gamma_k n) D^\dagger(\gamma_k m) e^{-i\omega_k t a_k^\dagger a_k} D(\gamma_k m) | 0_B \rangle \\ &= \begin{cases} \prod_k \exp(-4|\gamma_k|^2(1 - \cos(\omega_k t))) & m \neq n \\ 1 & m = n \end{cases} \end{aligned} \quad (\text{A.26})$$

with the shorthand coefficient  $\gamma_k = g_k / \omega_k$ . We can put this expression in a more compact form:

$$I_{mn}(t) = \begin{cases} e^{-\phi(t)} & m \neq n \\ 1 & m = n \end{cases} \quad (\text{A.27})$$



with  $\phi(t)$  given by

$$\phi(t) = 4 \sum_k \frac{|g_k|^2}{\omega_k^2} (1 - \cos(\omega_k t)) = 4 \int_0^\infty d\omega \frac{J(\omega)}{\omega^2} (1 - \cos(\omega t)) \quad (\text{A.28})$$

where we have taken the continuum limit over the bath modes. We can evaluate the integral in Eq. (A.28) if a specific form of bath spectral density  $J(\omega)$  is known. For example, if  $J(\omega)$  is of the form Eq. (1.102),  $\phi(t)$  evaluates to:

$$\phi(t) = 4\sqrt{\pi} \alpha \left( [\omega_c^2 t^2]^{1/4} \cos \left( \frac{1}{2} \tan^{-1} [\omega_c t] \right) - 1 \right) \quad \text{for } \nu = 1/2 \quad (\text{A.29})$$

$$\phi(t) = \alpha \log (\omega_c^2 t^2 + 1) \quad \text{for } \nu = 1 \quad (\text{A.30})$$

$$\phi(t) = \alpha \left( 2 - \frac{2}{\omega_c^2 t^2 + 1} \right) \quad \text{for } \nu = 2 \quad (\text{A.31})$$

This step completes our derivation. The exact solution of IBM is thus given by the expression

$$\rho(t) = \sum_{m,n=\pm 1} |m\rangle \langle n| [\rho(0)]_{mn} e^{-i(E_m - E_n)t} I_{mn}(t) \quad (\text{A.32})$$

from Eq. (A.25), combined with Eq. (A.27) and Eq. (A.28).

We can now use Eq. (A.32) to extract observables. For example, starting from the initial density matrix

$$\rho(0) = |\Psi_0\rangle \langle \Psi_0| \quad (\text{A.33})$$

with  $|\Psi_0\rangle = \frac{1}{\sqrt{2}} (|\uparrow\rangle + |\downarrow\rangle)$ , we find that the dynamics of  $\langle \sigma^x(t) \rangle$  is given by:

$$\langle \sigma^x(t) \rangle = \text{Tr}_B (\sigma^x \rho(t)) = e^{-\phi(t)} \cos(\epsilon t) \quad (\text{A.34})$$

## A.3 Many-body independent boson model

This section extends the solution of independent boson model (IBM) in Appendix. A.2 to many-body systems in 1D. Let us consider a 1D chain of  $M$  two-level systems that interact via Ising-like nearest neighbour couplings along  $z$ -axis:

$$H = \sum_{l=1}^M H_l + \frac{J^z}{2} \sum_{l=1}^{M-1} \sigma_l^z \sigma_{l+1}^z \quad (\text{A.35})$$

where  $J^z$  is the coupling constant and  $H_l$  is the onsite Hamiltonian for site  $l$ , while  $\sigma^z$  are spin-1/2 matrices. Each site is a two-level system linearly coupled to its bosonic environment, and is described by the IBM Hamiltonian Eq. (A.15):

$$H_l = \frac{\epsilon_l}{2} \sigma_l^z + \frac{\sigma_l^z}{2} \sum_k \left( g_{k,l} a_{k,l} + g_{k,l}^* a_{k,l}^\dagger \right) + \sum_k \omega_{k,l} a_{k,l}^\dagger a_{k,l} \quad (\text{A.36})$$

with additional site indices  $l$ . All variables have the same definitions as in Eq. (A.15) of Appendix. A.2. We consider the bosonic environments of different sites to be independent. By analogy to Eq. (A.16), we define the many-body polaron displacement operator:

$$D = \prod_l \prod_k D_{k,l} \left( \frac{g_{k,l}}{\omega_{k,l}} \sigma_l^z \right) \quad (\text{A.37})$$

where  $D_{k,l}(\gamma) = \exp \left( \gamma a_{k,l}^\dagger - \gamma^\dagger a_{k,l} \right)$ . The polaron operator  $D$  in Eq. (A.37) obeys the same set of properties Eq. (A.17)-(A.21) as did the polaron operator in Appendix. A.2. We now perform the polaron transformation on the full Hamiltonian Eq. (A.35):

$$H' = D H D^\dagger = H_S + H_{B0} + H_C \quad (\text{A.38})$$

where the individual terms are given by

$$H_S = \sum_{l=1}^M \frac{\epsilon_l}{2} \sigma_l^z + \frac{J^z}{2} \sum_{l=1}^{M-1} \sigma_l^z \sigma_{l+1}^z \quad (\text{A.39})$$

$$H_{B0} = \sum_{k,l} \omega_{k,l} a_{k,l}^\dagger a_{k,l} \quad (\text{A.40})$$

and

$$H_C = - \sum_{k,l} |g_{k,l}|^2 / \omega_{k,l} \quad (\text{A.41})$$

The time evolution operator then becomes

$$U(t) = e^{-iHt} = D^\dagger e^{-iH't} D = D^\dagger e^{-iH_S t} e^{-iH_{B0} t} e^{-iH_C t} D \quad (\text{A.42})$$

Making the usual assumption that the initial state is separable Eq. (1.10), and taking the bath in equilibrium at  $T = 0$  with  $\rho_B(0) = |0_B\rangle \langle 0_B|$ , one can write down the time evolution of the reduced density operator of the system  $\rho(t)$ :

$$\rho(t) = \text{Tr}_B (U(t) \rho(0) \rho_B(0) U^\dagger(t)) = \sum_{\mathcal{A}, \mathcal{B}} [\rho(0)]_{\mathcal{A}, \mathcal{B}} \text{Tr}_B (U(t) |0_B\rangle |\mathcal{A}\rangle \langle \mathcal{B}| \langle 0_B| U^\dagger(t)) \quad (\text{A.43})$$

Exploiting the properties Eqs. (A.17)-(A.21) of the displacement operator, after some algebra we find

$$\rho(t) = \sum_{\mathcal{A}, \mathcal{B}} [\rho(0)]_{\mathcal{A}, \mathcal{B}} |\mathcal{A}\rangle \langle \mathcal{B}| e^{-i(E_{\mathcal{A}} - E_{\mathcal{B}})t} \prod_l I_{l, \alpha_l, \beta_l}(t) \quad (\text{A.44})$$

where we have used  $|\mathcal{A}\rangle = |\alpha_1, \alpha_2, \dots, \alpha_M\rangle$  many-body wavefunctions as our orthonormal basis.  $\mathcal{A} = \{\alpha_l\}$  and  $\mathcal{B} = \{\beta_l\}$  are the many-body spin configurations where  $\alpha_l = \pm 1$  and  $\beta_l = \pm 1$  refer to the eigenstates  $\uparrow, \downarrow$  of a spin-1/2 at lattice site  $l$ .  $|\mathcal{A}\rangle = |\alpha_1, \alpha_2, \dots, \alpha_M\rangle$  and  $|\mathcal{B}\rangle = |\beta_1, \beta_2, \dots, \beta_M\rangle$  are the many-body wavefunctions

corresponding to a particular configuration for a number  $M$  of spin-1/2 particles. The energy of the free system configuration  $|\mathcal{B}\rangle = |\beta_1, \beta_2, \dots, \beta_M\rangle$  is given by

$$E_M = \sum_{l=1}^M \frac{\epsilon_l}{2} \alpha_l + \frac{J^z}{2} \sum_{l=1}^{M-1} \alpha_l \alpha_{l+1} \quad (\text{A.45})$$

We have also defined:

$$\begin{aligned} I_{l,\alpha_l,\beta_l}(t) &= \\ &= \prod_k \langle 0_B | D^\dagger(\gamma_{k,l}\beta_l) e^{i\omega_{k,l}t} a_{k,l}^\dagger a_{k,l} D(\gamma_{k,l}\beta_l) D^\dagger(\gamma_{k,l}\alpha_l) e^{-i\omega_{k,l}t} a_{k,l}^\dagger a_{k,l} D(\gamma_{k,l}\alpha_l) | 0_B \rangle \\ &= \begin{cases} \prod_k \exp(-4|\gamma_{k,l}|^2(1 - \cos(\omega_{k,l}t))) & \alpha_l \neq \beta_l \\ 1 & \alpha_l = \beta_l \end{cases} \end{aligned} \quad (\text{A.46})$$

with the shorthand coefficient  $\gamma_{k,l} = g_{k,l}/\omega_{k,l}$ . We can put this expression in a more compact form:

$$I_{l,\alpha_l,\beta_l}(t) = \begin{cases} e^{-\phi_l(t)} & \alpha_l \neq \beta_l \\ 1 & \alpha_l = \beta_l \end{cases} \quad (\text{A.47})$$

with  $\phi_l(t)$  given by

$$\phi(t) = 4 \sum_k \frac{|g_{k,l}|^2}{\omega_{k,l}^2} (1 - \cos(\omega_{k,l}t)) = 4 \int_0^\infty d\omega \frac{J_l(\omega)}{\omega^2} (1 - \cos(\omega t)) \quad (\text{A.48})$$

where we have taken the continuum limit over the bath modes. The above equation Eq. (A.48) has the same form as Eq. (A.28) in Appendix A.2. As before, we can compute the integral in Eq. (A.48) for a specific bath spectral density  $J_l(\omega)$ . For example, evaluating Eq. (A.48) for the spectral density Eq. (1.102) gives the same Eqs. (A.29)-(A.31) as in Appendix A.2.

This step completes our derivation. The exact solution of the many-body IBM is thus given by the expression

$$\rho(t) = \sum_{\mathcal{A},\mathcal{B}} |\mathcal{A}\rangle \langle \mathcal{B}| [\rho(0)]_{\mathcal{A},\mathcal{B}} e^{-i(E_{\mathcal{A}} - E_{\mathcal{B}})t} \prod_{l=1}^M I_{l,\alpha_l,\beta_l}(t) \quad (\text{A.49})$$

from Eq. (A.44), combined with Eq. (A.47) and Eq. (A.48).

We can now use Eq. (A.49) to extract observables. For example, taking a homogeneous lattice with  $\epsilon_l = \epsilon$ ,  $J_l(\omega) = J(\omega)$  and  $\phi_l(t) = \phi(t)$ , and starting from the initial density matrix

$$\rho(0) = |\Psi_0\rangle \langle \Psi_0| \quad (\text{A.50})$$

with  $|\Psi_0\rangle = \prod_{l=1}^M \frac{1}{\sqrt{2}} (|\uparrow_l\rangle + |\downarrow_l\rangle)$ , we find that the dynamics of  $\langle \sigma_l^x(t) \rangle$  at site  $l$  is given by:

$$\begin{aligned}
\langle \sigma_l^x(t) \rangle &= \text{Tr}_B (\sigma_l^x \rho(t)) \\
&= \begin{cases} \frac{1}{2} e^{-\phi(t)} [\cos((\epsilon - J^z)t) + \cos((\epsilon + J^z)t)] & l = 1, M \\ \frac{1}{4} e^{-\phi(t)} [\cos((\epsilon - 2J^z)t) + \cos((\epsilon + 2J^z)t) + 2 \cos(\epsilon t)] & \text{else} \end{cases} \quad (\text{A.51})
\end{aligned}$$

# Part VI

## Bibliography



# Bibliography

- [1] H.-P. Breuer, F. Petruccione *et al.* *The theory of open quantum systems* (Oxford University Press on Demand, 2002).
- [2] A. Altland and B. D. Simons. *Condensed matter field theory* (Cambridge University Press, Cambridge, 2010).
- [3] M. C. Cross and P. C. Hohenberg. Pattern formation outside of equilibrium. *Rev. Mod. Phys.*, **65**, 851 (1993).
- [4] T. Vicsek and A. Zafeiris. Collective motion. *Phys. Rep.*, **517**, 71 (2012).
- [5] M. C. Marchetti, J.-F. Joanny, S. Ramaswamy, T. B. Liverpool, J. Prost, M. Rao and R. A. Simha. Hydrodynamics of soft active matter. *Rev. Mod. Phys.*, **85**, 1143 (2013).
- [6] M. C. Marchetti, Y. Fily, S. Henkes, A. Patch and D. Yllanes. Minimal model of active colloids highlights the role of mechanical interactions in controlling the emergent behavior of active matter. *Curr. Opin. Colloid Interface Sci.*, **21**, 34 (2016).
- [7] M. L. Zorn, A.-K. Marel, F. J. Segerer and J. O. Rädler. Phenomenological approaches to collective behavior in epithelial cell migration. *Biochim. Biophys. Acta Mol. Cell Res.*, **1853**, 3143 (2015).
- [8] J. Toner and Y. Tu. Flocks, herds, and schools: A quantitative theory of flocking. *Phys. Rev. E*, **58**, 4828 (1998).
- [9] R. N. Mantegna and H. E. Stanley. *Introduction to econophysics: correlations and complexity in finance* (Cambridge university press, 1999).
- [10] Z. Dogic, P. Sharma and M. J. Zakhary. Hypercomplex liquid crystals. *Annu. Rev. Condens. Matter Phys.*, **5**, 137 (2014).
- [11] M. Atatüre, J. Dreiser, A. Badolato and A. Imamoglu. Observation of faraday rotation from a single confined spin. *Nat. Phys.*, **3**, 101 (2007).
- [12] J. M. Martinis, S. Nam, J. Aumentado and C. Urbina. Rabi oscillations in a large josephson-junction qubit. *Phys. Rev. Lett.*, **89**, 117901 (2002).
- [13] J. J. Pla, K. Y. Tan, J. P. Dehollain, W. H. Lim, J. J. Morton, F. A. Zwanenbourg, D. N. Jamieson, A. S. Dzurak and A. Morello. High-fidelity readout and control of a nuclear spin qubit in silicon. *Nature*, **496**, 334 (2013).

- [14] P. Neumann, J. Beck, M. Steiner, F. Rempp, H. Fedder, P. R. Hemmer, J. Wrachtrup and F. Jelezko. Single-shot readout of a single nuclear spin. *Science*, **329**, 542 (2010).
- [15] A. A. Houck, H. E. Türeci and J. Koch. On-chip quantum simulation with superconducting circuits. *Nat. Phys.*, **8**, 292 (2012).
- [16] A. Potočník, A. Bargerbos, F. A. Schröder, S. A. Khan, M. C. Collodo, S. Gasparinetti, Y. Salathé, C. Creatore, C. Eichler, H. E. Türeci *et al.* Studying light-harvesting models with superconducting circuits. *Nat. Commun.*, **9**, 904 (2018).
- [17] M. Ludwig and F. Marquardt. Quantum many-body dynamics in optomechanical arrays. *Phys. Rev. Lett.*, **111**, 073603 (2013).
- [18] S. Gröblacher, A. Trubarov, N. Prigge, G. Cole, M. Aspelmeyer and J. Eisert. Observation of non-markovian micromechanical brownian motion. *Nat. Commun.*, **6**, 7606 (2015).
- [19] I. Yeo, P.-L. De Assis, A. Gloppe, E. Dupont-Ferrier, P. Verlot, N. S. Malik, E. Dupuy, J. Claudon, J.-M. Gérard, A. Auffèves *et al.* Strain-mediated coupling in a quantum dot–mechanical oscillator hybrid system. *Nat. Nanotechnol.*, **9**, 106 (2014).
- [20] X. Mi, J. Cady, D. Zajac, P. Deelman and J. R. Petta. Strong coupling of a single electron in silicon to a microwave photon. *Science*, **355**, 156 (2017).
- [21] R. Blatt and C. F. Roos. Quantum simulations with trapped ions. *Nat. Phys.*, **8**, 277 (2012).
- [22] K. Toyoda, Y. Matsuno, A. Noguchi, S. Haze and S. Urabe. Experimental realization of a quantum phase transition of polaritonic excitations. *Phys. Rev. Lett.*, **111**, 160501 (2013).
- [23] H. Ritsch, P. Domokos, F. Brennecke and T. Esslinger. Cold atoms in cavity-generated dynamical optical potentials. *Rev. Mod. Phys.*, **85**, 553 (2013).
- [24] J. Kasprzak, M. Richard, S. Kundermann, A. Baas, P. Jeambrun, J. Keeling, F. Marchetti, M. Szymańska, R. André, J. Staehli *et al.* Bose–einstein condensation of exciton polaritons. *Nature*, **443**, 409 (2006).
- [25] J. Preskill. Quantum computing in the nisq era and beyond. *Quantum*, **2**, 79 (2018).
- [26] S. J. Devitt, W. J. Munro and K. Nemoto. Quantum error correction for beginners. *Rep. Prog. Phys.*, **76**, 076001 (2013).
- [27] L. Chirolli and G. Burkard. Decoherence in solid-state qubits. *Adv. Phys.*, **57**, 225 (2008).



- [28] V. Giovannetti, S. Lloyd and L. Maccone. Quantum-enhanced measurements: beating the standard quantum limit. *Science*, **306**, 1330 (2004).
- [29] J. A. Jones, S. D. Karlen, J. Fitzsimons, A. Ardavan, S. C. Benjamin, G. A. D. Briggs and J. J. Morton. Magnetic field sensing beyond the standard quantum limit using 10-spin noon states. *Science*, **324**, 1166 (2009).
- [30] G. S. Engel, T. R. Calhoun, E. L. Read, T.-K. Ahn, T. Mančal, Y.-C. Cheng, R. E. Blankenship and G. R. Fleming. Evidence for wavelike energy transfer through quantum coherence in photosynthetic systems. *Nature*, **446**, 782 (2007).
- [31] P. Rebentrost, M. Mohseni, I. Kassal, S. Lloyd and A. Aspuru-Guzik. Environment-assisted quantum transport. *New. J. Phys.*, **11**, 033003 (2009).
- [32] A. B. Pun, A. Asadpoordarvish, E. Kumarasamy, M. J. Tayebjee, D. Niesner, D. R. McCamey, S. N. Sanders, L. M. Campos and M. Y. Sfeir. Ultra-fast intramolecular singlet fission to persistent multiexcitons by molecular design. *Nat. Chem.*, pages 1–8 (2019).
- [33] D. W. Snoke and J. Keeling. The new era of polariton condensates. *Phys. Today*, **70**, 54 (2017).
- [34] J. Klaers, J. Schmitt, F. Vewinger and M. Weitz. Bose-einstein condensation of photons in an optical microcavity. *Nature*, **468**, 545 (2010).
- [35] M. Mitrano, A. Cantaluppi, D. Nicoletti, S. Kaiser, A. Perucchi, S. Lupi, P. Di Pietro, D. Pontiroli, M. Riccò, S. R. Clark *et al.* Possible light-induced superconductivity in k3c60 at high temperature. *Nature*, **530**, 461 (2016).
- [36] R. Ma, B. Saxberg, C. Owens, N. Leung, Y. Lu, J. Simon and D. I. Schuster. A dissipatively stabilized mott insulator of photons. *Nature*, **566**, 51 (2019).
- [37] N. Y. Yao and C. Nayak. Time crystals in periodically driven systems. *arXiv preprint arXiv:1811.06657* (2018).
- [38] U. Schollwöck. The density-matrix renormalization group in the age of matrix product states. *Ann. Phys.*, **326**, 96 (2011).
- [39] R. Orús. A practical introduction to tensor networks: Matrix product states and projected entangled pair states. *Ann. Phys.*, **349**, 117 (2014).
- [40] M. Zwolak and G. Vidal. Mixed-state dynamics in one-dimensional quantum lattice systems: a time-dependent superoperator renormalization algorithm. *Phys. Rev. Lett.*, **93**, 207205 (2004).
- [41] J. Cui, J. I. Cirac and M. C. Bañuls. Variational matrix product operators for the steady state of dissipative quantum systems. *Phys. Rev. Lett.*, **114**, 220601 (2015).

- [42] E. Mascarenhas, H. Flayac and V. Savona. Matrix-product-operator approach to the nonequilibrium steady state of driven-dissipative quantum arrays. *Phys. Rev. A*, **92**, 022116 (2015).
- [43] A. Werner, D. Jaschke, P. Silvi, M. Kliesch, T. Calarco, J. Eisert and S. Montangero. Positive tensor network approach for simulating open quantum many-body systems. *Phys. Rev. Lett.*, **116**, 237201 (2016).
- [44] C. Joshi, F. Nissen and J. Keeling. Quantum correlations in the one-dimensional driven dissipative xy model. *Phys. Rev. A*, **88**, 063835 (2013).
- [45] F. A. Schröder, D. H. Turban, A. J. Musser, N. D. Hine and A. W. Chin. Tensor network simulation of multi-environmental open quantum dynamics via machine learning and entanglement renormalisation. *Nat. Commun.*, **10**, 1062 (2019).
- [46] J. del Pino, F. A. Schröder, A. W. Chin, J. Feist and F. J. Garcia-Vidal. Tensor network simulation of non-markovian dynamics in organic polaritons. *Phys. Rev. Lett.*, **121**, 227401 (2018).
- [47] R. Feynman and A. Hibbs. Quantum mechanics and path integrals (mcgraw hill, newyork, 1965). *Ann. Phys.*, **24**, 118 (1963).
- [48] J. Schwinger. Brownian motion of a quantum oscillator. *J. Math. Phys.*, **2**, 407 (1961).
- [49] L. V. Keldysh. Diagram technique for nonequilibrium processes. *Zh. Eksp. Teor. Fiz.*, **47**, 1018 (1964).
- [50] R. P. Feynman. Simulating physics with computers. *International journal of theoretical physics*, **21**, 467 (1982).
- [51] J. I. Cirac and P. Zoller. Goals and opportunities in quantum simulation. *Nature Physics*, **8**, 264 (2012).
- [52] S. Lloyd. Universal quantum simulators. *Science*, pages 1073–1078 (1996).
- [53] I. Bloch, J. Dalibard and W. Zwerger. Many-body physics with ultracold gases. *Rev. Mod. Phys.*, **80**, 885 (2008).
- [54] I. Bloch, J. Dalibard and S. Nascimbene. Quantum simulations with ultracold quantum gases. *Nature Physics*, **8**, 267 (2012).
- [55] I. M. Georgescu, S. Ashhab and F. Nori. Quantum simulation. *Reviews of Modern Physics*, **86**, 153 (2014).
- [56] A. Aspuru-Guzik and P. Walther. Photonic quantum simulators. *Nature physics*, **8**, 285 (2012).
- [57] A. Majumdar, A. Rundquist, M. Bajcsy, V. D. Dasika, S. R. Bank and J. Vučković. Design and analysis of photonic crystal coupled cavity arrays for quantum simulation. *Phys. Rev. B*, **86**, 195312 (2012).

- [58] G. Lepert, M. Trupke, M. Hartmann, M. Plenio and E. Hinds. Arrays of waveguide-coupled optical cavities that interact strongly with atoms. *New. J. Phys.*, **13**, 113002 (2011).
- [59] A. Majumdar, A. Rundquist, M. Bajcsy and J. Vučković. Cavity quantum electrodynamics with a single quantum dot coupled to a photonic molecule. *Phys. Rev. B*, **86**, 045315 (2012).
- [60] S. Schmidt and J. Koch. Circuit qed lattices: towards quantum simulation with superconducting circuits. *Ann. Phys.*, **525**, 395 (2013).
- [61] M. J. Hartmann, F. G. Brandao and M. B. Plenio. Strongly interacting polaritons in coupled arrays of cavities. *Nat. Phys.*, **2**, 849 (2006).
- [62] D. G. Angelakis, M. F. Santos and S. Bose. Photon-blockade-induced mott transitions and x y spin models in coupled cavity arrays. *Phys. Rev. A*, **76**, 031805 (2007).
- [63] A. D. Greentree, C. Tahan, J. H. Cole and L. C. Hollenberg. Quantum phase transitions of light. *Nat. Phys.*, **2**, 856 (2006).
- [64] F. Nissen, S. Schmidt, M. Biondi, G. Blatter, H. E. Türeci and J. Keeling. Nonequilibrium dynamics of coupled qubit-cavity arrays. *Phys. Rev. Lett.*, **108**, 233603 (2012).
- [65] A. Biella, L. Mazza, I. Carusotto, D. Rossini and R. Fazio. Photon transport in a dissipative chain of nonlinear cavities. *Phys. Rev. A*, **91**, 053815 (2015).
- [66] J. Ruiz-Rivas, E. del Valle, C. Gies, P. Gartner and M. J. Hartmann. Spontaneous collective coherence in driven dissipative cavity arrays. *Phys. Rev. A*, **90**, 033808 (2014).
- [67] T. Grujic, S. Clark, D. Jaksch and D. Angelakis. Non-equilibrium many-body effects in driven nonlinear resonator arrays. *New. J. Phys.*, **14**, 103025 (2012).
- [68] M. J. Hartmann. Polariton crystallization in driven arrays of lossy nonlinear resonators. *Phys. Rev. Lett.*, **104**, 113601 (2010).
- [69] J. Jin, D. Rossini, R. Fazio, M. Leib and M. J. Hartmann. Photon solid phases in driven arrays of nonlinearly coupled cavities. *Phys. Rev. Lett.*, **110**, 163605 (2013).
- [70] J. Jin, D. Rossini, M. Leib, M. J. Hartmann and R. Fazio. Steady-state phase diagram of a driven qed-cavity array with cross-kerr nonlinearities. *Phys. Rev. A*, **90**, 023827 (2014).
- [71] C.-E. Bardyn and A. Imamoglu. Majorana-like modes of light in a one-dimensional array of nonlinear cavities. *Phys. Rev. Lett.*, **109**, 253606 (2012).
- [72] I. Carusotto, D. Gerace, H. Tureci, S. De Liberato, C. Ciuti and A. Imamoglu. Fermionized photons in an array of driven dissipative nonlinear cavities. *Phys. Rev. Lett.*, **103**, 033601 (2009).

- [73] T. E. Lee, S. Gopalakrishnan and M. D. Lukin. Unconventional magnetism via optical pumping of interacting spin systems. *Phys. Rev. Lett.*, **110**, 257204 (2013).
- [74] T. E. Lee, C.-K. Chan and S. F. Yelin. Dissipative phase transitions: Independent versus collective decay and spin squeezing. *Phys. Rev. A*, **90**, 052109 (2014).
- [75] M. Schiró, C. Joshi, M. Bordyuh, R. Fazio, J. Keeling and H. Türeci. Exotic attractors of the nonequilibrium rabi-hubbard model. *Phys. Rev. Lett.*, **116**, 143603 (2016).
- [76] J. Jin, A. Biella, O. Viyuela, L. Mazza, J. Keeling, R. Fazio and D. Rossini. Cluster mean-field approach to the steady-state phase diagram of dissipative spin systems. *Phys. Rev. X*, **6**, 031011 (2016).
- [77] D. F. Walls and G. J. Milburn. *Quantum optics* (Springer Science & Business Media, 2007).
- [78] L. Tian and H. Carmichael. Quantum trajectory simulations of two-state behavior in an optical cavity containing one atom. *Phys. Rev. A*, **46**, R6801 (1992).
- [79] A. Imamoglu, H. Schmidt, G. Woods and M. Deutsch. Strongly interacting photons in a nonlinear cavity. *Phys. Rev. Lett.*, **79**, 1467 (1997).
- [80] M. J. Hartmann. Quantum simulation with interacting photons. *J. Opt.*, **18**, 104005 (2016).
- [81] H. Walther, B. T. Varcoe, B.-G. Englert and T. Becker. Cavity quantum electrodynamics. *Reports on Progress in Physics*, **69**, 1325 (2006).
- [82] K. M. Birnbaum, A. Boca, R. Miller, A. D. Boozer, T. E. Northup and H. J. Kimble. Photon blockade in an optical cavity with one trapped atom. *Nature*, **436**, 87 (2005).
- [83] A. Faraon, I. Fushman, D. Englund, N. Stoltz, P. Petroff and J. Vučković. Coherent generation of non-classical light on a chip via photon-induced tunnelling and blockade. *Nat. Phys.*, **4**, 859 (2008).
- [84] L. S. Bishop, J. Chow, J. Koch, A. Houck, M. Devoret, E. Thuneberg, S. Girvin and R. Schoelkopf. Nonlinear response of the vacuum rabi resonance. *Nat. Phys.*, **5**, 105 (2009).
- [85] V. Sala, D. Solnyshkov, I. Carusotto, T. Jacqmin, A. Lemaître, H. Terças, A. Nalitov, M. Abbarchi, E. Galopin, I. Sagnes *et al.* Spin-orbit coupling for photons and polaritons in microstructures. *Phys. Rev. X*, **5**, 011034 (2015).
- [86] M. Fitzpatrick, N. M. Sundaresan, A. C. Y. Li, J. Koch and A. A. Houck. Observation of a dissipative phase transition in a one-dimensional circuit qed lattice. *Phys. Rev. X*, **7**, 011016 (Feb 2017).

- [87] M. Leib, F. Deppe, A. Marx, R. Gross and M. J. Hartmann. Networks of non-linear superconducting transmission line resonators. *New Journal of Physics*, **14**, 075024 (2012).
- [88] C. Eichler, Y. Salathe, J. Mlynek, S. Schmidt and A. Wallraff. Quantum-limited amplification and entanglement in coupled nonlinear resonators. *Physical review letters*, **113**, 110502 (2014).
- [89] J. Raftery, D. Sadri, S. Schmidt, H. E. Türeci and A. A. Houck. Observation of a dissipation-induced classical to quantum transition. *Physical Review X*, **4**, 031043 (2014).
- [90] P. Roushan, C. Neill, A. Megrant, Y. Chen, R. Babbush, R. Barends, B. Campbell, Z. Chen, B. Chiaro, A. Dunsworth *et al.* Chiral ground-state currents of interacting photons in a synthetic magnetic field. *Nature Physics*, **13**, 146 (2017).
- [91] S. Hacohe-Gourgy, V. Ramasesh, C. De Grandi, I. Siddiqi and S. Girvin. Cooling and autonomous feedback in a bose-hubbard chain with attractive interactions. *Physical Review Letters*, **115**, 240501 (2015).
- [92] D. L. Underwood, W. E. Shanks, J. Koch and A. A. Houck. Low-disorder microwave cavity lattices for quantum simulation with photons. *Physical Review A*, **86**, 023837 (2012).
- [93] M. Leib and M. J. Hartmann. Bose-hubbard dynamics of polaritons in a chain of circuit quantum electrodynamics cavities. *New. J. Phys.*, **12**, 093031 (2010).
- [94] D. Rossini and R. Fazio. Mott-insulating and glassy phases of polaritons in 1d arrays of coupled cavities. *Phys. Rev. Lett.*, **99**, 186401 (2007).
- [95] M. Aichhorn, M. Hohenadler, C. Tahan and P. B. Littlewood. Quantum fluctuations, temperature, and detuning effects in solid-light systems. *Phys. Rev. Lett.*, **100**, 216401 (2008).
- [96] P. Pippan, H. G. Evertz and M. Hohenadler. Excitation spectra of strongly correlated lattice bosons and polaritons. *Phys. Rev. A*, **80**, 033612 (2009).
- [97] M. Hohenadler, M. Aichhorn, S. Schmidt and L. Pollet. Dynamical critical exponent of the jaynes-cummings-hubbard model. *Phys. Rev. A*, **84**, 041608 (2011).
- [98] M. Hohenadler, M. Aichhorn, L. Pollet and S. Schmidt. Polariton mott insulator with trapped ions or circuit qed. *Phys. Rev. A*, **85**, 013810 (2012).
- [99] S. Ferretti, L. C. Andreani, H. E. Türeci and D. Gerace. Photon correlations in a two-site nonlinear cavity system under coherent drive and dissipation. *Phys. Rev. A*, **82**, 013841 (2010).

- [100] M. Cazalilla, R. Citro, T. Giamarchi, E. Orignac and M. Rigol. One dimensional bosons: From condensed matter systems to ultracold gases. *Rev. Mod. Phys.*, **83**, 1405 (2011).
- [101] M. Girardeau. *Phys.(ny)* **1**, 516 (1960). *Phys. Rev.*, **139**, B500 (1965).
- [102] J. Cho, D. G. Angelakis and S. Bose. Simulation of high-spin heisenberg models in coupled cavities. *Phys. Rev. A*, **78**, 062338 (2008).
- [103] F. Dimer, B. Estienne, A. Parkins and H. Carmichael. Proposed realization of the dicke-model quantum phase transition in an optical cavity qed system. *Phys. Rev. A*, **75**, 013804 (2007).
- [104] C.-K. Chan, T. E. Lee and S. Gopalakrishnan. Limit-cycle phase in driven-dissipative spin systems. *Phys. Rev. A*, **91**, 051601 (2015).
- [105] T. E. Lee, H. Häffner and M. Cross. Antiferromagnetic phase transition in a nonequilibrium lattice of rydberg atoms. *Phys. Rev. A*, **84**, 031402 (2011).
- [106] A. Le Boité, G. Orso and C. Ciuti. Steady-state phases and tunneling-induced instabilities in the driven dissipative bose-hubbard model. *Phys. Rev. Lett.*, **110**, 233601 (2013).
- [107] A. Le Boité, G. Orso and C. Ciuti. Bose-hubbard model: Relation between driven-dissipative steady states and equilibrium quantum phases. *Phys. Rev. A*, **90**, 063821 (2014).
- [108] A. Tomadin, V. Giovannetti, R. Fazio, D. Gerace, I. Carusotto, H. Türeci and A. Imamoglu. Signatures of the superfluid-insulator phase transition in laser-driven dissipative nonlinear cavity arrays. *Phys. Rev. A*, **81**, 061801 (2010).
- [109] S. Diehl, A. Tomadin, A. Micheli, R. Fazio and P. Zoller. Dynamical phase transitions and instabilities in open atomic many-body systems. *Phys. Rev. Lett.*, **105**, 015702 (2010).
- [110] H. Weimer. Variational principle for steady states of dissipative quantum many-body systems. *Physical review letters*, **114**, 040402 (2015).
- [111] H. Weimer, A. Kshetrimayum and R. Orús. Simulation methods for open quantum many-body systems. *arXiv preprint arXiv:1907.07079* (2019).
- [112] A. J. Daley. Quantum trajectories and open many-body quantum systems. *Adv. Phys.*, **63**, 77 (2014).
- [113] D. Kilda and J. Keeling. Fluorescence spectrum and thermalization in a driven coupled cavity array. *Phys. Rev. Lett.*, **122**, 043602 (2019).
- [114] E. Gillman, F. Carollo and I. Lesanovsky. Numerical simulation of critical dissipative non-equilibrium quantum systems with an absorbing state. *arXiv preprint arXiv:1907.02433* (2019).

- [115] L. Bonnes, D. Charrier and A. M. Läuchli. Dynamical and steady-state properties of a bose-hubbard chain with bond dissipation: A study based on matrix product operators. *Phys. Rev. A*, **90**, 033612 (2014).
- [116] S. Finazzi, A. Le Boité, F. Storme, A. Baksic and C. Ciuti. Corner-space renormalization method for driven-dissipative two-dimensional correlated systems. *Phys. Rev. Lett.*, **115**, 080604 (2015).
- [117] R. Rota, F. Minganti, C. Ciuti and V. Savona. Quantum critical regime in a quadratically driven nonlinear photonic lattice. *Phys. Rev. Lett.*, **122**, 110405 (2019).
- [118] P. Degenfeld-Schonburg and M. J. Hartmann. Self-consistent projection operator theory for quantum many-body systems. *Physical Review B*, **89**, 245108 (2014).
- [119] S. Okubo, M. Eto, P. Degenfeld-Schonburg and M. J. Hartmann. Study of coupled qed-cavities using the self-consistent mori projector method. *Journal of Physics: Conference Series*, **568**, 012014 (2014).
- [120] M. Szymańska, J. Keeling and P. Littlewood. Nonequilibrium quantum condensation in an incoherently pumped dissipative system. *Physical review letters*, **96**, 230602 (2006).
- [121] E. G. D. Torre, S. Diehl, M. D. Lukin, S. Sachdev and P. Strack. Keldysh approach for nonequilibrium phase transitions in quantum optics: Beyond the dicke model in optical cavities. *Phys. Rev.A*, **87**, 023831 (2013).
- [122] M. Buchhold, P. Strack, S. Sachdev and S. Diehl. Dicke-model quantum spin and photon glass in optical cavities: Nonequilibrium theory and experimental signatures. *Phys. Rev.A*, **87**, 063622 (2013).
- [123] L. Magazzù, P. Forn-Díaz, R. Belyansky, J.-L. Orgiazzi, M. Yurtalan, M. Otto, A. Lupascu, C. Wilson and M. Grifoni. Probing the strongly driven spin-boson model in a superconducting quantum circuit. *Nat. Commun.*, **9**, 1403 (2018).
- [124] K. H. Madsen, S. Ates, T. Lund-Hansen, A. Löffler, S. Reitzenstein, A. Forchel and P. Lodahl. Observation of non-markovian dynamics of a single quantum dot in a micropillar cavity. *Phys. Rev. Lett.*, **106**, 233601 (2011).
- [125] S. Diehl, A. Micheli, A. Kantian, B. Kraus, H. Büchler and P. Zoller. Quantum states and phases in driven open quantum systems with cold atoms. *Nat. Phys.*, **4**, 878 (2008).
- [126] F. Verstraete, M. M. Wolf and J. I. Cirac. Quantum computation and quantum-state engineering driven by dissipation. *Nat. Phys.*, **5**, 633 (2009).
- [127] F. Koppens, D. Klauser, W. Coish, K. Nowack, L. Kouwenhoven, D. Loss and L. Vandersypen. Universal phase shift and nonexponential decay of driven single-spin oscillations. *Phys. Rev. Lett.*, **99**, 106803 (2007).

- [128] J. Medford, C. Barthel, C. Marcus, M. Hanson, A. Gossard *et al.* Scaling of dynamical decoupling for spin qubits. *Phys. Rev. Lett.*, **108**, 086802 (2012).
- [129] A. Chin, J. Prior, R. Rosenbach, F. Caycedo-Soler, S. Huelga and M. B. Plenio. The role of non-equilibrium vibrational structures in electronic coherence and recoherence in pigment–protein complexes. *Nat. Phys.*, **9**, 113 (2013).
- [130] M. K. Lee, P. Huo and D. F. Coker. Semiclassical path integral dynamics: photosynthetic energy transfer with realistic environment interactions. *Annu. Rev. Phys. Chem.*, **67**, 639 (2016).
- [131] M. Thorwart, J. Eckel, J. H. Reina, P. Nalbach and S. Weiss. Enhanced quantum entanglement in the non-markovian dynamics of biomolecular excitons. *Chem. Phys. Lett.*, **478**, 234 (2009).
- [132] S. F. Huelga and M. B. Plenio. Vibrations, quanta and biology. *Contemp. Phys.*, **54**, 181 (2013).
- [133] M. d. Rey, A. W. Chin, S. F. Huelga and M. B. Plenio. Exploiting structured environments for efficient energy transfer: the phonon antenna mechanism. *J. Phys. Chem. Lett.*, **4**, 903 (2013).
- [134] M. Mohseni, A. Shabani, S. Lloyd and H. Rabitz. Energy-scales convergence for optimal and robust quantum transport in photosynthetic complexes. *J. Chem. Phys.*, **140**, 01B609.1 (2014).
- [135] W. Barford. *Electronic and optical properties of conjugated polymers*, volume 159 (Oxford University Press, 2013).
- [136] D. Sanvitto and S. Kéna-Cohen. The road towards polaritonic devices. *Nat. Mater.*, **15**, 1061 (2016).
- [137] M. A. Zeb, P. G. Kirton and J. Keeling. Exact states and spectra of vibrationally dressed polaritons. *ACS Photonics*, **5**, 249 (2017).
- [138] A. Caldeira and A. J. Leggett. Quantum tunnelling in a dissipative system. *Ann. Phys. (N. Y.)*, **149**, 374 (1983).
- [139] A. J. Leggett, S. Chakravarty, A. T. Dorsey, M. P. Fisher, A. Garg and W. Zwerger. Dynamics of the dissipative two-state system. *Rev. Mod. Phys.*, **59**, 1 (1987).
- [140] S. Han, J. Lapointe and J. Lukens. Observation of incoherent relaxation by tunneling in a macroscopic two-state system. *Phys. Rev. Lett.*, **66**, 810 (1991).
- [141] B. Golding, M. N. Zimmerman and S. Coppersmith. Dissipative quantum tunneling of a single microscopic defect in a mesoscopic metal. *Phys. Rev. Lett.*, **68**, 998 (1992).
- [142] B. Golding, J. E. Graebner, A. B. Kane and J. Black. Relaxation of tunneling systems by conduction electrons in a metallic glass. *Phys. Rev. Lett.*, **41**, 1487 (1978).



- [143] R. Cukier and M. Morillo. Solvent effects on proton-transfer reactions. *J. Chem. Phys.*, **91**, 857 (1989).
- [144] D. Segal and B. K. Agarwalla. Vibrational heat transport in molecular junctions. *Annu. Rev. Phys. Chem.*, **67**, 185 (2016).
- [145] I. De Vega and D. Alonso. Dynamics of non-markovian open quantum systems. *Rev. Mod. Phys.*, **89**, 015001 (2017).
- [146] A. Rivas, S. F. Huelga and M. B. Plenio. Quantum non-markovianity: characterization, quantification and detection. *Rep. Prog. Phys.*, **77**, 094001 (2014).
- [147] G. D. Mahan. *Many-particle physics* (Springer Science & Business Media, 2013).
- [148] D. P. McCutcheon, N. S. Dattani, E. M. Gauger, B. W. Lovett and A. Nazir. A general approach to quantum dynamics using a variational master equation: Application to phonon-damped rabi rotations in quantum dots. *Phys. Rev. B*, **84**, 081305 (2011).
- [149] C. Roy and S. Hughes. Polaron master equation theory of the quantum-dot mollow triplet in a semiconductor cavity-qed system. *Phys. Rev. B*, **85**, 115309 (2012).
- [150] S. Jang. Theory of coherent resonance energy transfer for coherent initial condition. *J. Chem. Phys.*, **131**, 164101 (2009).
- [151] G. Cohen, E. Gull, D. R. Reichman and A. J. Millis. Taming the dynamical sign problem in real-time evolution of quantum many-body problems. *Phys. Rev. Lett.*, **115**, 266802 (2015).
- [152] H.-T. Chen, G. Cohen and D. R. Reichman. Inchworm monte carlo for exact non-adiabatic dynamics. i. theory and algorithms. *J. Chem. Phys.*, **146**, 054105 (2017).
- [153] H.-T. Chen, G. Cohen and D. R. Reichman. Inchworm monte carlo for exact non-adiabatic dynamics. ii. benchmarks and comparison with established methods. *J. Chem. Phys.*, **146**, 054106 (2017).
- [154] Y. Tanimura and R. Kubo. Time evolution of a quantum system in contact with a nearly gaussian-markoffian noise bath. *J. Phys. Soc. Jpn.*, **58**, 101 (1989).
- [155] J. Strumpfer and K. Schulten. Open quantum dynamics calculations with the hierarchy equations of motion on parallel computers. *J. Chem. Theory Comput.*, **8**, 2808 (2012).
- [156] B. Garraway. Nonperturbative decay of an atomic system in a cavity. *Phys. Rev. A*, **55**, 2290 (1997).

- [157] J. Iles-Smith, N. Lambert and A. Nazir. Environmental dynamics, correlations, and the emergence of noncanonical equilibrium states in open quantum systems. *Phys. Rev. A*, **90**, 032114 (2014).
- [158] F. A. Schröder and A. W. Chin. Simulating open quantum dynamics with time-dependent variational matrix product states: Towards microscopic correlation of environment dynamics and reduced system evolution. *Phys. Rev. B*, **93**, 075105 (2016).
- [159] A. W. Chin, Á. Rivas, S. F. Huelga and M. B. Plenio. Exact mapping between system-reservoir quantum models and semi-infinite discrete chains using orthogonal polynomials. *J. Math. Phys.*, **51**, 092109 (2010).
- [160] M. Woods, R. Groux, A. Chin, S. Huelga and M. B. Plenio. Mappings of open quantum systems onto chain representations and markovian embeddings. *J. Math. Phys.*, **55**, 032101 (2014).
- [161] Y.-Y. Shi, L.-M. Duan and G. Vidal. Classical simulation of quantum many-body systems with a tree tensor network. *Phys. Rev. A*, **74**, 022320 (2006).
- [162] J. Haegeman, J. I. Cirac, T. J. Osborne, I. Pižorn, H. Verschelde and F. Verstraete. Time-dependent variational principle for quantum lattices. *Phys. Rev. Lett.*, **107**, 070601 (2011).
- [163] N. Makri and D. E. Makarov. Tensor propagator for iterative quantum time evolution of reduced density matrices. i. theory. *J. Chem. Phys.*, **102**, 4600 (1995).
- [164] N. Makri and D. E. Makarov. Tensor propagator for iterative quantum time evolution of reduced density matrices. ii. numerical methodology. *J. Chem. Phys.*, **102**, 4611 (1995).
- [165] K. Le Hur. Entanglement entropy, decoherence, and quantum phase transitions of a dissipative two-level system. *Ann. Phys. (N. Y.)*, **323**, 2208 (2008).
- [166] M. P. Fisher and W. Zwerger. Quantum brownian motion in a periodic potential. *Phys. Rev. B*, **32**, 6190 (1985).
- [167] N. Prokof'ev and P. Stamp. Quantum relaxation of magnetisation in magnetic particles. *J. Low Temp. Phys.*, **104**, 143 (1996).
- [168] N. Prokof'ev and P. Stamp. Low-temperature quantum relaxation in a system of magnetic nanomolecules. *Phys. Rev. Lett.*, **80**, 5794 (1998).
- [169] U. Weiss. *Quantum dissipative systems*, volume 13 (World scientific, 2012).
- [170] M. B. Plenio, J. Eisert, J. Dreissig and M. Cramer. Entropy, entanglement, and area: analytical results for harmonic lattice systems. *Phys. Rev. Lett.*, **94**, 060503 (2005).

- [171] M. Cramer and J. Eisert. Correlations, spectral gap and entanglement in harmonic quantum systems on generic lattices. *New. J. Phys.*, **8**, 71 (2006).
- [172] J. Eisert, M. Cramer and M. B. Plenio. Colloquium: Area laws for the entanglement entropy. *Rev. Mod. Phys.*, **82**, 277 (2010).
- [173] M. B. Hastings. An area law for one-dimensional quantum systems. *J. Stat. Mech. Theory Exp.*, **2007**, P08024 (2007).
- [174] G. Vidal. Class of quantum many-body states that can be efficiently simulated. *Phys. Rev. Lett.*, **101**, 110501 (2008).
- [175] L. Tagliacozzo, G. Evenbly and G. Vidal. Simulation of two-dimensional quantum systems using a tree tensor network that exploits the entropic area law. *Phys. Rev. B*, **80**, 235127 (2009).
- [176] S. R. White. Density matrix formulation for quantum renormalization groups. *Phys. Rev. Lett.*, **69**, 2863 (1992).
- [177] S. R. White. Density-matrix algorithms for quantum renormalization groups. *Phys. Rev. B*, **48**, 10345 (1993).
- [178] G. Vidal. Efficient classical simulation of slightly entangled quantum computations. *Phys. Rev. Lett.*, **91**, 147902 (2003).
- [179] G. Vidal. Efficient simulation of one-dimensional quantum many-body systems. *Phys. Rev. Lett.*, **93**, 040502 (2004).
- [180] G. Vidal. Classical simulation of infinite-size quantum lattice systems in one spatial dimension. *Phys. Rev. Lett.*, **98**, 070201 (2007).
- [181] R. Orus and G. Vidal. Infinite time-evolving block decimation algorithm beyond unitary evolution. *Phys. Rev. B*, **78**, 155117 (2008).
- [182] L. Vanderstraeten, J. Haegeman and F. Verstraete. Tangent-space methods for uniform matrix product states. *SciPost Phys. Lect. Notes*, page 007 (2019).
- [183] J. J. Dorando, J. Hachmann and G. K.-L. Chan. Targeted excited state algorithms. *J. Chem. Phys.*, **127**, 084109 (2007).
- [184] D. Sénéchal, A.-M. Tremblay and C. Bourbonnais. *Theoretical methods for strongly correlated electrons* (Springer Science & Business Media, 2006).
- [185] T. D. Kühner and S. R. White. Dynamical correlation functions using the density matrix renormalization group. *Phys. Rev. B*, **60**, 335 (1999).
- [186] K. A. Hallberg. Density-matrix algorithm for the calculation of dynamical properties of low-dimensional systems. *Phys. Rev. B*, **52**, R9827 (1995).
- [187] S. R. White and A. E. Feiguin. Real-time evolution using the density matrix renormalization group. *Phys. Rev. Lett.*, **93**, 076401 (2004).

- [188] A. J. Daley, C. Kollath, U. Schollwöck and G. Vidal. Time-dependent density-matrix renormalization-group using adaptive effective hilbert spaces. *J. Stat. Mech. Theory Exp.*, **2004**, P04005 (2004).
- [189] A. Holzner, A. Weichselbaum and J. von Delft. Matrix product state approach for a two-lead multilevel anderson impurity model. *Phys. Rev. B*, **81**, 125126 (2010).
- [190] A. E. Feiguin and S. R. White. Finite-temperature density matrix renormalization using an enlarged hilbert space. *Phys. Rev. B*, **72**, 220401 (2005).
- [191] S. R. White. Minimally entangled typical quantum states at finite temperature. *Phys. Rev. Lett.*, **102**, 190601 (2009).
- [192] E. M. Stoudenmire and S. R. White. Studying two-dimensional systems with the density matrix renormalization group. *Annu. Rev. Condens. Matter Phys.*, **3**, 111 (2012).
- [193] S. Yan, D. A. Huse and S. R. White. Spin-liquid ground state of the  $s = 1/2$  kagome heisenberg antiferromagnet. *Science*, **332**, 1173 (2011).
- [194] G. K.-L. Chan and S. Sharma. The density matrix renormalization group in quantum chemistry. *Annu. Rev. Phys. Chem.*, **62**, 465 (2011).
- [195] S. Wouters and D. Van Neck. The density matrix renormalization group for ab initio quantum chemistry. *Eur. Phys. J. D*, **68**, 272 (2014).
- [196] T. H. Johnson, T. Elliott, S. R. Clark and D. Jaksch. Capturing exponential variance using polynomial resources: applying tensor networks to nonequilibrium stochastic processes. *Phys. Rev. Lett.*, **114**, 090602 (2015).
- [197] E. Miles Stoudenmire and D. J. Schwab. Supervised learning with quantum-inspired tensor networks. *arXiv preprint arXiv:1605.05775* (2016).
- [198] E. Pavarini, E. Koch and U. Schollwöck. *Emergent Phenomena in Correlated Matter: Autumn School Organized by the Forschungszentrum Jülich and the German Research School for Simulation Sciences at Forschungszentrum Jülich 23-27 September 2013; Lecture Notes of the Autumn School Correlated Electrons 2013*, volume 3 (Forschungszentrum Jülich, 2013).
- [199] D. Gottesman and M. Hastings. Entanglement versus gap for one-dimensional spin systems. *New. J. Phys.*, **12**, 025002 (2010).
- [200] N. Schuch, M. M. Wolf, F. Verstraete and J. I. Cirac. Entropy scaling and simulability by matrix product states. *Phys. Rev. Lett.*, **100**, 030504 (2008).
- [201] E. Stoudenmire and S. R. White. Minimally entangled typical thermal state algorithms. *New J. Phys.*, **12**, 055026 (2010).
- [202] F. Verstraete, M. M. Wolf, D. Perez-Garcia and J. I. Cirac. Criticality, the area law, and the computational power of projected entangled pair states. *Phys. Rev. Lett.*, **96**, 220601 (2006).

- [203] H. Kalis, D. Klagges, R. Orús and K. P. Schmidt. Fate of the cluster state on the square lattice in a magnetic field. *Phys. Rev. A*, **86**, 022317 (2012).
- [204] R. Haghshenas, M. J. O'Rourke and G. K.-L. Chan. Conversion of projected entangled pair states into a canonical form. *Phys. Rev. B*, **100**, 054404 (2019).
- [205] M. Lubasch, J. I. Cirac and M.-C. Banuls. Algorithms for finite projected entangled pair states. *Phys. Rev. B*, **90**, 064425 (2014).
- [206] J. Jordan, R. Orús, G. Vidal, F. Verstraete and J. I. Cirac. Classical simulation of infinite-size quantum lattice systems in two spatial dimensions. *Phys. Rev. Lett.*, **101**, 250602 (2008).
- [207] M. Levin and C. P. Nave. Tensor renormalization group approach to two-dimensional classical lattice models. *Phys. Rev. Lett.*, **99**, 120601 (2007).
- [208] Z.-Y. Xie, H.-C. Jiang, Q. N. Chen, Z.-Y. Weng and T. Xiang. Second renormalization of tensor-network states. *Phys. Rev. Lett.*, **103**, 160601 (2009).
- [209] Z.-Y. Xie, J. Chen, M.-P. Qin, J. W. Zhu, L.-P. Yang and T. Xiang. Coarse-graining renormalization by higher-order singular value decomposition. *Phys. Rev. B*, **86**, 045139 (2012).
- [210] L. Vanderstraeten, J. Haegeman, P. Corboz and F. Verstraete. Gradient methods for variational optimization of projected entangled-pair states. *Phys. Rev. B*, **94**, 155123 (2016).
- [211] P. Corboz. Variational optimization with infinite projected entangled-pair states. *Phys. Rev. B*, **94**, 035133 (2016).
- [212] L. Vanderstraeten, J. Haegeman and F. Verstraete. Simulating excitation spectra with projected entangled-pair states. *Phys. Rev. B*, **99**, 165121 (2019).
- [213] H.-J. Liao, Z.-Y. Xie, J. Chen, Z.-Y. Liu, H.-D. Xie, R.-Z. Huang, B. Normand and T. Xiang. Gapless spin-liquid ground state in the  $s = 1/2$  kagome antiferromagnet. *Phys. Rev. Lett.*, **118**, 137202 (2017).
- [214] T. Liu, W. Li, A. Weichselbaum, J. von Delft and G. Su. Simplex valence-bond crystal in the spin-1 kagome heisenberg antiferromagnet. *Phys. Rev. B*, **91**, 060403 (2015).
- [215] P. Corboz and F. Mila. Tensor network study of the shastry-sutherland model in zero magnetic field. *Phys. Rev. B*, **87**, 115144 (2013).
- [216] P. Corboz and F. Mila. Crystals of bound states in the magnetization plateaus of the shastry-sutherland model. *Phys. Rev. Lett.*, **112**, 147203 (2014).
- [217] P. Corboz, A. M. Läuchli, K. Penc, M. Troyer and F. Mila. Simultaneous dimerization and  $su(4)$  symmetry breaking of 4-color fermions on the square lattice. *Phys. Rev. Lett.*, **107**, 215301 (2011).

- [218] P. Corboz, M. Lajkó, A. M. Läuchli, K. Penc and F. Mila. Spin-orbital quantum liquid on the honeycomb lattice. *Phys. Rev. X*, **2**, 041013 (2012).
- [219] P. Corboz, M. Lajkó, K. Penc, F. Mila and A. M. Läuchli. Competing states in the su (3) heisenberg model on the honeycomb lattice: Plaquette valence-bond crystal versus dimerized color-ordered state. *Phys. Rev. B*, **87**, 195113 (2013).
- [220] P. Corboz, J. Jordan and G. Vidal. Simulation of fermionic lattice models in two dimensions with projected entangled-pair states: Next-nearest neighbor hamiltonians. *Phys. Rev. B*, **82**, 245119 (2010).
- [221] P. Corboz, R. Orús, B. Bauer and G. Vidal. Simulation of strongly correlated fermions in two spatial dimensions with fermionic projected entangled-pair states. *Phys. Rev. B*, **81**, 165104 (2010).
- [222] P. Corboz, S. R. White, G. Vidal and M. Troyer. Stripes in the two-dimensional t-j model with infinite projected entangled-pair states. *Phys. Rev. B*, **84**, 041108 (2011).
- [223] P. Corboz, T. M. Rice and M. Troyer. Competing states in the t-j model: Uniform d-wave state versus stripe state. *Phys. Rev. Lett.*, **113**, 046402 (2014).
- [224] B.-X. Zheng, C.-M. Chung, P. Corboz, G. Ehlers, M.-P. Qin, R. M. Noack, H. Shi, S. R. White, S. Zhang and G. K.-L. Chan. Stripe order in the underdoped region of the two-dimensional hubbard model. *Science*, **358**, 1155 (2017).
- [225] R. Orús and G. Vidal. Simulation of two-dimensional quantum systems on an infinite lattice revisited: Corner transfer matrix for tensor contraction. *Phys. Rev. B*, **80**, 094403 (2009).
- [226] T. Nishino and K. Okunishi. Corner transfer matrix renormalization group method. *J. Phys. Soc. Jpn.*, **65**, 891 (1996).
- [227] T. Nishino and K. Okunishi. Corner transfer matrix algorithm for classical renormalization group. *J. Phys. Soc. Jpn.*, **66**, 3040 (1997).
- [228] B. Bruognolo. *Tensor network techniques for strongly correlated systems*. Ph.D. thesis, lmu (2017).
- [229] M. Schiró, C. Joshi, M. Bordyuh, R. Fazio, J. Keeling and H. Türeci. Exotic attractors of the nonequilibrium rabi-hubbard model. *Phys. Rev. Lett.*, **116**, 143603 (2016).
- [230] T. C. H. Liew and V. Savona. Single photons from coupled quantum modes. *Phys. Rev. Lett.*, **104**, 183601 (May 2010).
- [231] M. Bamba, A. Imamoglu, I. Carusotto and C. Ciuti. Origin of strong photon antibunching in weakly nonlinear photonic molecules. *Phys. Rev. A*, **83**, 021802 (Feb 2011).

- [232] C. Lang, D. Bozyigit, C. Eichler, L. Steffen, J. M. Fink, A. A. Abdumalikov, M. Baur, S. Filipp, M. P. da Silva, A. Blais and A. Wallraff. Observation of resonant photon blockade at microwave frequencies using correlation function measurements. *Phys. Rev. Lett.*, **106**, 243601 (Jun 2011).
- [233] H. N. Phien, G. Vidal and I. P. McCulloch. Infinite boundary conditions for matrix product state calculations. *Phys. Rev. B*, **86**, 245107 (2012).
- [234] S. Wolff, J.-S. Bernier, D. Poletti, A. Sheikhan and C. Kollath. Evolution of two-time correlations in dissipative quantum spin systems: aging and hierarchical dynamics. *arXiv preprint arXiv:1809.10464* (2018).
- [235] M. C. Bañuls, M. B. Hastings, F. Verstraete and J. I. Cirac. Matrix product states for dynamical simulation of infinite chains. *Phys. Rev. Lett.*, **102**, 240603 (2009).
- [236] J. Haegeman, T. J. Osborne and F. Verstraete. Post-matrix product state methods: To tangent space and beyond. *Phys. Rev. B*, **88**, 075133 (2013).
- [237] P. Kirton and J. Keeling. Thermalization and breakdown of thermalization in photon condensates. *Phys. Rev. A*, **91**, 033826 (2015).
- [238] T. D. Doan, H. T. Cao, D. B. Tran Thoai and H. Haug. Condensation kinetics of microcavity polaritons with scattering by phonons and polaritons. *Phys. Rev. B*, **72**, 085301 (Aug 2005).
- [239] J. Kasprzak, D. D. Solnyshkov, R. André, L. S. Dang and G. Malpuech. Formation of an exciton polariton condensate: Thermodynamic versus kinetic regimes. *Phys. Rev. Lett.*, **101**, 146404 (Oct 2008).
- [240] Y. Sun, P. Wen, Y. Yoon, G. Liu, M. Steger, L. N. Pfeiffer, K. West, D. W. Snoke and K. A. Nelson. Bose-einstein condensation of long-lifetime polaritons in thermal equilibrium. *Phys. Rev. Lett.*, **118**, 016602 (Jan 2017).
- [241] B. Öztıp, M. Bordyuh, Ö. E. Müstecaplıoğlu and H. E. Türeci. Excitations of optically driven atomic condensate in a cavity: theory of photodetection measurements. *New J. Phys.*, **14**, 085011 (2012).
- [242] L. Sieberer, S. Huber, E. Altman and S. Diehl. Dynamical critical phenomena in driven-dissipative systems. *Phys. Rev. Lett.*, **110**, 195301 (2013).
- [243] L. M. Sieberer, M. Buchhold and S. Diehl. Keldysh field theory for driven open quantum systems. *Rep. Prog. Phys.*, **79**, 096001 (2016).
- [244] A. Polkovnikov, K. Sengupta, A. Silva and M. Vengalattore. Colloquium: Nonequilibrium dynamics of closed interacting quantum systems. *Rev. Mod. Phys.*, **83**, 863 (2011).
- [245] J. Eisert, M. Friesdorf and C. Gogolin. Quantum many-body systems out of equilibrium. *Nat. Phys.*, **11**, 124 (2015).

- [246] T. Langen, T. Gasenzer and J. Schmiedmayer. Prethermalization and universal dynamics in near-integrable quantum systems. *J. Stat. Mech. Theory Exp.*, **2016**, 064009 (2016).
- [247] J. Berges, S. Borsányi and C. Wetterich. Prethermalization. *Phys. Rev. Lett.*, **93**, 142002 (2004).
- [248] M. Aspelmeyer, T. J. Kippenberg and F. Marquardt. Cavity optomechanics. *Reviews of Modern Physics*, **86**, 1391 (2014).
- [249] W. Hsu and R. Barakat. Statistics and thermodynamics of luminescent radiation. *Physical Review B*, **46**, 6760 (1992).
- [250] P. Medley, D. M. Weld, H. Miyake, D. E. Pritchard and W. Ketterle. Spin gradient demagnetization cooling of ultracold atoms. *Physical review letters*, **106**, 195301 (2011).
- [251] S. Braun, J. P. Ronzheimer, M. Schreiber, S. S. Hodgman, T. Rom, I. Bloch and U. Schneider. Negative absolute temperature for motional degrees of freedom. *Science*, **339**, 52 (2013).
- [252] I. Carusotto and C. Ciuti. Quantum fluids of light. *Rev. Mod. Phys.*, **85**, 299 (2013).
- [253] A. C. Y. Li and J. Koch. Mapping repulsive to attractive interaction in drivendissipative quantum systems. *New. J. Phys.*, **19**, 115010 (2017).
- [254] D. C. Mattis. *The theory of magnetism made simple: an introduction to physical concepts and to some useful mathematical methods* (World Scientific Publishing Company, 2006).
- [255] G. W. Drake. *Springer handbook of atomic, molecular, and optical physics* (Springer Science & Business Media, 2006).
- [256] M. P. da Silva, D. Bozyigit, A. Wallraff and A. Blais. Schemes for the observation of photon correlation functions in circuit qed with linear detectors. *Physical Review A*, **82**, 043804 (2010).
- [257] M. O. Scully and M. S. Zubairy. *Quantum Optics* (Cambridge University Press, Cambridge, 1997).
- [258] G. Ford and R. O’Connell. There is no quantum regression theorem. *Phys. Rev. Lett.*, **77**, 798 (1996).
- [259] S. Sachdev. *Quantum phase transitions* (Cambridge University Press, Cambridge, 2007).
- [260] A. J. Kollár, M. Fitzpatrick and A. A. Houck. Hyperbolic lattices in circuit quantum electrodynamics. *Nature*, **571**, 45 (2019).



- [261] B. M. Anderson, R. Ma, C. Owens, D. I. Schuster and J. Simon. Engineering topological many-body materials in microwave cavity arrays. *Physical Review X*, **6**, 041043 (2016).
- [262] R. Umucalılar and I. Carusotto. Fractional quantum hall states of photons in an array of dissipative coupled cavities. *Physical review letters*, **108**, 206809 (2012).
- [263] C. Noh and D. G. Angelakis. Quantum simulations and many-body physics with light. *Rep. Prog. Phys.*, **80**, 016401 (2016).
- [264] E. Arévalo and L. Morales-Molina. Geometrical frustration in nonlinear photonic lattices. *Phys. Rev. A*, **98**, 023864 (2018).
- [265] Y. Salathé, M. Mondal, M. Oppliger, J. Heinsoo, P. Kurpiers, A. Potočník, A. Mezzacapo, U. Las Heras, L. Lamata, E. Solano *et al.* Digital quantum simulation of spin models with circuit quantum electrodynamics. *Physical Review X*, **5**, 021027 (2015).
- [266] O. Viehmann, J. von Delft and F. Marquardt. Observing the nonequilibrium dynamics of the quantum transverse-field ising chain in circuit qed. *Physical review letters*, **110**, 030601 (2013).
- [267] M. Kjaergaard, M. E. Schwartz, J. Braumüller, P. Krantz, J. I.-J. Wang, S. Gustavsson and W. D. Oliver. Superconducting qubits: Current state of play. *arXiv preprint arXiv:1905.13641* (2019).
- [268] M. Saffman, T. G. Walker and K. Mølmer. Quantum information with rydberg atoms. *Reviews of Modern Physics*, **82**, 2313 (2010).
- [269] I. Bouchoule and K. Mølmer. Spin squeezing of atoms by the dipole interaction in virtually excited rydberg states. *Physical Review A*, **65**, 041803 (2002).
- [270] M. D. Lukin, M. Fleischhauer, R. Cote, L. Duan, D. Jaksch, J. I. Cirac and P. Zoller. Dipole blockade and quantum information processing in mesoscopic atomic ensembles. *Physical review letters*, **87**, 037901 (2001).
- [271] H. Weimer. Variational analysis of driven-dissipative rydberg gases. *Physical Review A*, **91**, 063401 (2015).
- [272] G. Carleo and M. Troyer. Solving the quantum many-body problem with artificial neural networks. *Science*, **355**, 602 (2017).
- [273] N. Yoshioka and R. Hamazaki. Constructing neural stationary states for open quantum many-body systems. *arXiv preprint arXiv:1902.07006* (2019).
- [274] A. Nagy and V. Savona. Variational quantum monte carlo method with a neural-network ansatz for open quantum systems. *Phys. Rev. Lett.*, **122**, 250501 (2019).

- [275] H. Landa, M. Schiró and G. Misguich. Multistability of driven-dissipative quantum spins. *arXiv preprint arXiv:1905.10349* (2019).
- [276] A. Kshetrimayum, H. Weimer and R. Orús. A simple tensor network algorithm for two-dimensional steady states. *Nat. Commun.*, **8**, 1291 (2017).
- [277] M. Cheneau, P. Barmettler, D. Poletti, M. Endres, P. Schauß, T. Fukuhara, C. Gross, I. Bloch, C. Kollath and S. Kuhr. Light-cone-like spreading of correlations in a quantum many-body system. *Nature*, **481**, 484 (2012).
- [278] J. Jordan. Studies of infinite two-dimensional quantum lattice systems with projected entangled pair states. *The University of Queensland, Australia, Quuesnland* (2011).
- [279] H. W. Blöte and Y. Deng. Cluster monte carlo simulation of the transverse ising model. *Phys. Rev. E*, **66**, 066110 (2002).
- [280] A. Kshetrimayum, M. Rizzi, J. Eisert and R. Orús. Tensor network annealing algorithm for two-dimensional thermal states. *Phys. Rev. Lett.*, **122**, 070502 (2019).
- [281] J. Jordan, R. Orús and G. Vidal. Numerical study of the hard-core bose-hubbard model on an infinite square lattice. *Phys. Rev. B*, **79**, 174515 (2009).
- [282] M. J. Hartmann, F. G. Brandao and M. B. Plenio. Quantum many-body phenomena in coupled cavity arrays. *Laser. Photon. Rev.*, **2**, 527 (2008).
- [283] G. De las Cuevas, N. Schuch, D. Pérez-García and J. I. Cirac. Purifications of multipartite states: limitations and constructive methods. *New. J. Phys.*, **15**, 123021 (2013).
- [284] A. A. Gangat, I. Te and Y.-J. Kao. Steady states of infinite-size dissipative quantum chains via imaginary time evolution. *Phys. Rev. Lett.*, **119**, 010501 (2017).
- [285] K. Le Hur, L. Henriët, L. Herviou, K. Plekhanov, A. Petrescu, T. Goren, M. Schiro, C. Mora and P. P. Orth. Driven dissipative dynamics and topology of quantum impurity systems. *Comptes Rendus Physique*, **19**, 451 (2018).
- [286] T. Nakaoka, E. C. Clark, H. J. Krenner, M. Sabathil, M. Bichler, Y. Arakawa, G. Abstreiter and J. J. Finley. Direct observation of acoustic phonon mediated relaxation between coupled exciton states in a single quantum dot molecule. *Physical Review B*, **74**, 121305 (2006).
- [287] B. D. Gerardot, S. Strauf, M. J. De Dood, A. M. Bychkov, A. Badolato, K. Hennessy, E. L. Hu, D. Bouwmeester and P. M. Petroff. Photon statistics from coupled quantum dots. *Physical review letters*, **95**, 137403 (2005).
- [288] G. Ortner, R. Oulton, H. Kurtze, M. Schwab, D. Yakovlev, M. Bayer, S. Fafard, Z. Wasilewski and P. Hawrylak. Energy relaxation of electrons in in as/ga as quantum dot molecules. *Physical Review B*, **72**, 165353 (2005).

- [289] S. Rodt, V. Türeci, R. Heitz, F. Guffarth, R. Engelhardt, U. Pohl, M. Straßburg, M. Dworzak, A. Hoffmann and D. Bimberg. Lateral carrier transfer in  $\text{cd x zn } 1-x \text{ se/zns y se } 1-y$  quantum dot layers. *Physical Review B*, **67**, 235327 (2003).
- [290] A. Tackeuchi, T. Kuroda, K. Mase, Y. Nakata and N. Yokoyama. Dynamics of carrier tunneling between vertically aligned double quantum dots. *Physical Review B*, **62**, 1568 (2000).
- [291] R. Heitz, I. Mukhametzhanov, P. Chen and A. Madhukar. Excitation transfer in self-organized asymmetric quantum dot pairs. *Physical Review B*, **58**, R10151 (1998).
- [292] E. Rozbicki and P. Machnikowski. Quantum kinetic theory of phonon-assisted excitation transfer in quantum dot molecules. *Physical review letters*, **100**, 027401 (2008).
- [293] H. Zheng and H. U. Baranger. Persistent quantum beats and long-distance entanglement from waveguide-mediated interactions. *Physical review letters*, **110**, 113601 (2013).
- [294] A. Barth, A. Vagov and V. Axt. Path-integral description of combined hamiltonian and non-hamiltonian dynamics in quantum dissipative systems. *Phys. Rev. B*, **94**, 125439 (2016).
- [295] A. Strathearn, B. W. Lovett and P. Kirton. Efficient real-time path integrals for non-markovian spin-boson models. *New. J. Phys.*, **19**, 093009 (2017).
- [296] A. Strathearn, P. Kirton, D. Kilda, J. Keeling and B. W. Lovett. Efficient non-markovian quantum dynamics using time-evolving matrix product operators. *Nat. Commun.*, **9**, 3322 (2018).
- [297] J. Iles-Smith. *Excitation dynamics of strongly dissipative quantum systems* (Imperial College London, 2015).
- [298] J. Iles-Smith, A. G. Dijkstra, N. Lambert and A. Nazir. Energy transfer in structured and unstructured environments: Master equations beyond the born-markov approximations. *J. Chem. Phys.*, **144**, 044110 (2016).
- [299] S. Florens, D. Venturelli and R. Narayanan. Quantum phase transition in the spin boson model. In *Quantum Quenching, Annealing and Computation*, pages 145–162 (Springer, 2010).
- [300] A. K. Chandra, A. Das and B. K. Chakrabarti. *Quantum quenching, annealing and computation*, volume 802 (Springer Science & Business Media, 2010).
- [301] R. Bulla, N.-H. Tong and M. Vojta. Numerical renormalization group for bosonic systems and application to the sub-ohmic spin-boson model. *Phys. Rev. Lett.*, **91**, 170601 (2003).

- [302] P. P. Orth, D. Roosen, W. Hofstetter and K. Le Hur. Dynamics, synchronization, and quantum phase transitions of two dissipative spins. *Phys. Rev. B*, **82**, 144423 (2010).
- [303] A. Winter and H. Rieger. Quantum phase transition and correlations in the multi-spin-boson model. *Phys. Rev. B*, **90**, 224401 (2014).
- [304] D. P. McCutcheon, A. Nazir, S. Bose and A. J. Fisher. Separation-dependent localization in a two-impurity spin-boson model. *Phys. Rev. B*, **81**, 235321 (2010).
- [305] T. Stace, A. Doherty and S. Barrett. Population inversion of a driven two-level system in a structureless bath. *Phys. Rev. Lett.*, **95**, 106801 (2005).
- [306] D. P. McCutcheon and A. Nazir. Coherent and incoherent dynamics in excitonic energy transfer: Correlated fluctuations and off-resonance effects. *Phys. Rev. B*, **83**, 165101 (2011).
- [307] P. Nalbach, J. Eckel and M. Thorwart. Quantum coherent biomolecular energy transfer with spatially correlated fluctuations. *New. J. Phys.*, **12**, 065043 (2010).
- [308] C. Roy and S. Hughes. Phonon-dressed mollow triplet in the regime of cavity quantum electrodynamics: excitation-induced dephasing and nonperturbative cavity feeding effects. *Physical review letters*, **106**, 247403 (2011).
- [309] S. Ulrich, S. Ates, S. Reitzenstein, A. Löffler, A. Forchel and P. Michler. Dephasing of triplet-sideband optical emission of a resonantly driven inas/gaas quantum dot inside a microcavity. *Physical review letters*, **106**, 247402 (2011).
- [310] A. Ruseckas, P. Wood, I. Samuel, G. Webster, W. Mitchell, P. Burn and V. Sundström. Ultrafast depolarization of the fluorescence in a conjugated polymer. *Physical Review B*, **72**, 115214 (2005).
- [311] M. M.-L. Grage, Y. Zaushitsyn, A. Yartsev, M. Chachisvilis, V. Sundström and T. Pullerits. Ultrafast excitation transfer and trapping in a thin polymer film. *Physical Review B*, **67**, 205207 (2003).
- [312] T. E. Dykstra, E. Hennebicq, D. Beljonne, J. Gierschner, G. Claudio, E. R. Bittner, J. Knoester and G. D. Scholes. Conformational disorder and ultrafast exciton relaxation in ppv-family conjugated polymers. *The Journal of Physical Chemistry B*, **113**, 656 (2008).
- [313] J. Sperling, A. Nemeth, P. Baum, F. Šanda, E. Riedle, H. F. Kauffmann, S. Mukamel and F. Milota. Exciton dynamics in a disordered conjugated polymer: Three-pulse photon-echo and transient grating experiments. *Chemical Physics*, **349**, 244 (2008).
- [314] T. E. Dykstra, V. Kovalevskij, X. Yang and G. D. Scholes. Excited state dynamics of a conformationally disordered conjugated polymer: a comparison of solutions and film. *Chemical physics*, **318**, 21 (2005).

- [315] X. Yang, T. E. Dykstra and G. D. Scholes. Photon-echo studies of collective absorption and dynamic localization of excitation in conjugated polymers and oligomers. *Physical Review B*, **71**, 045203 (2005).
- [316] C. Consani, F. Koch, F. Panzer, T. Unger, A. Köhler and T. Brixner. Relaxation dynamics and exciton energy transfer in the low-temperature phase of meh-ppv. *The Journal of chemical physics*, **142**, 212429 (2015).
- [317] J. R. Mannouch, W. Barford and S. Al-Assam. Ultra-fast relaxation, decoherence, and localization of photoexcited states in  $\pi$ -conjugated polymers. *The Journal of chemical physics*, **148**, 034901 (2018).
- [318] W. Barford and M. Marcus. Theory of optical transitions in conjugated polymers. i. ideal systems. *The Journal of chemical physics*, **141**, 164101 (2014).
- [319] S. Suzuki, H. Oshiyama and N. Shibata. Quantum annealing of pure and random ising chains coupled to a bosonic environment. *J. Phys. Soc. Jpn.*, **88**, 061003 (2019).
- [320] M. Jørgensen and F. Pollock. Exploiting the causal tensor network structure of quantum processes to efficiently simulate non-markovian path integrals. *arXiv preprint arXiv:1902.00315* (2019).
- [321] F. A. Pollock, C. Rodríguez-Rosario, T. Frauenheim, M. Paternostro and K. Modi. Non-markovian quantum processes: Complete framework and efficient characterization. *Phys. Rev. A*, **97**, 012127 (2018).
- [322] C. Ciuti, P. Schwendimann and A. Quattropani. Theory of polariton parametric interactions in semiconductor microcavities. *Semicond. Sci. Technol.*, **18**, S279 (2003).
- [323] P. Savvidis, C. Ciuti, J. Baumberg, D. Whittaker, M. Skolnick and J. Roberts. Off-branch polaritons and multiple scattering in semiconductor microcavities. *Phys. Rev. B*, **64**, 075311 (2001).
- [324] D. Whittaker. Effects of polariton-energy renormalization in the microcavity optical parametric oscillator. *Phys. Rev. B*, **71**, 115301 (2005).
- [325] A. Garg, J. N. Onuchic and V. Ambegaokar. Effect of friction on electron transfer in biomolecules. *J. Chem. Phys.*, **83**, 4491 (1985).